THE UNIVERSITY *of* EDINBURGH

Energetic Materials at Extreme Conditions

David I.A. Millar

A thesis submitted in fulfilment of the requirements for the degree of Doctor of Philosophy to the School of Chemistry, the University of Edinburgh.

October 2010

Abstract

In order to effectively model the behaviour of energetic materials under operational conditions it is essential to obtain detailed structural information for these compounds at elevated temperature and/or pressures. The structural characterisation of the high explosives RDX and CL-20 and a series of inorganic azides [$M^{n+}(N_3)_n$] at extreme conditions is described herein.

In addition to the characterisation of a highly metastable β-form of RDX (1,3,5-trinitrohexahydro-1,3,5-triazine) at atmospheric pressure, the structure solution of a high-pressure/high-temperature polymorph is described. This form, obtained above 4.3 GPa and 450 K, has been shown to be distinct from the β-form and has therefore been denoted ε-RDX. Furthermore, ε-RDX is sufficiently metastable to allow its recovery to ambient pressure at 150 K; it only transforms to the α-form upon warming to 230 K. Finally, the ambient-temperature compression of RDX has been investigated to a maximum pressure of 23.0 GPa, using methanol:ethanol (4:1) as the pressure-transmitting medium; no phase transition was observed under these conditions, other than the α → γ transition at 3.9 GPa.

The structure of a high-pressure polymorph of CL-20 (2,4,6,8,10,12-hexanitrohexaazaisowurtzitane) has also been determined by a combination of powder and single-crystal X-ray diffraction. Compression of γ-CL-20 to above 0.7 GPa using Fluorinert (FC-77) as the pressure-transmitting medium results in a phase transition to the ζ-form, which has been found to display structural similarities with both the γ- and ε-forms. The high-pressure behaviour of CL-20, however, depends markedly on the starting polymorph and the pressure-transmitting medium selected. Compression of γ-CL-20 in MeOH:EtOH (4:1) results in the formation of a 2:1 CL-20:MeOH solvate at 0.5 GPa. This solvate is stable upon compression to $P > 5.0$ GPa. It may also be recovered to ambient pressure at 293 K. Meanwhile, no phase transition is observed during the compression of ε-CL-20 to a maximum pressure of 7.2 GPa.

Finally, a series of inorganic azides [NaN_3, CsN_3, TlN_3, NH_4N_3, AgN_3 and $Pb(N_3)_2$] has been characterised under a range of pressure and temperature conditions. Of the six compounds studied, all displayed at least one polymorphic transition – 5 new forms have been structurally characterised in this work and evidence of another 5 is presented. The combined effect of pressure and temperature results in sodium azide adopting a tetragonal structure common to larger alkali metal azides. Caesium azide has been shown to undergo three phase transitions during compression to 6.0 GPa – the structure of the first high-pressure form is

reported. A variable temperature X-ray powder diffraction study of TlN_3 has allowed the structural characterisation of the low-temperature TlN_3-IV (at 230 K) as well as providing evidence for a phase transition to a high-temperature form above 550 K. The high-pressure form III (obtained above 0.76 GPa) has also been determined by neutron powder diffraction.

Silver, ammonium and lead(II) azides have all been shown to undergo a phase transition at high pressures. Compression of silver azide (P > 0.80 GPa) removes an orthorhombic distortion observed at atmospheric pressure, resulting in the tetragonal structure adopted by CsN_3 and TlN_3 under ambient conditions. Moreover, NH_4N_3 and $Pb(N_3)_2$ have been found to undergo phase transitions at 2.6 GPa, although their high-pressure structures have still to be determined.

Declaration

I declare that this thesis was written by myself and that the work detailed herein is my own, or I have contributed substantially to such work, except where proper reference is made to the work of another author.

David I.A. Millar

Acknowledgements

There are numerous people that I would like to thank for their contributions and advice, without which the last three years would not have been quite so successful or enjoyable. I am greatly indebted to my supervisor, Professor Colin Pulham, for his knowledge and enthusiasm (both apparently unending, even at 4 a.m. at the synchrotron). Two other former 'Pulhamites' who have been immense sources of wisdom and humour (and quite often drinking partners) are Drs Iain Oswald and Helen Maynard-Casely. Thank you as well to all members of the Pulham group, past and present.

Dr Bill Marshall has also been instrumental in this research, not only providing guidance on everything related to neutron diffraction and Rietveld refinement, but also coming up with various new avenues to explore. Naturally, the success of the experiments reported herein is a reflection of the quality of the instrument scientists and technicians, with whom we have collaborated. Many thanks to Messrs Chris Barry and Duncan Francis (PEARL-HiPr, ISIS), Drs Alistair Lennie and Chiu Tang (I11, Diamond Light Source), Dr Annette Kleppe (I15, DLS) and Dr Dave Allan (I19, DLS).

In addition, I would like to thank Dr Adam Cumming (Defence Science and Technology Laboratory) for his insights into the energetics community and his keenness for a wide-ranging project. Moreover, I am gratefully indebted to Dstl for their joint studentship with EPSRC. I would also like to acknowledge STFC for provision of beamtime at ISIS and Diamond that has been vital to the success of this work.

Finally, I am hugely grateful for the love and support of my family and friends.

Contents

Chapter 1

Introduction

1 Introduction

1.1 Energetic Materials

1.1.1 Definition

Energetic materials are regarded as those with high enthalpies of formation, which can release the chemical energy stored within their molecular structures in a reproducible manner upon stimulus by heat, impact, shock, spark, *etc*, generally with the release of large quantities of hot gaseous products. A chemical explosion arises when an exothermic transformation occurs over an extremely short timescale (typically < 0.01 s). Due to the speed of the reaction, the product gases do not instantaneously expand but remain inside the chamber that held the explosive charge. The temperature in the moments succeeding explosion is commonly of the order of several thousand Kelvin – the pressure resulting from the confinement of these extremely hot combustion products in the small volume of the blast chamber can reach several thousand atmospheres.[1] This is sufficient to produce a shock-wave capable of breaking the walls of the chamber and causing damage to the surroundings. One should note, however, that the high-pressure shock-wave that passes through the energetic material itself is many orders of magnitude greater than this.

The majority of compounds classed as energetic materials contain a high proportion of oxygen and nitrogen (often as NO, NO_2 or NO_3 groups) within their structures, along with oxidisable 'fuel' elements such as carbon and hydrogen. Significant exceptions to this rule, however, are energetic compounds that contain no oxygen, for example metal azides ($M^{n+}(N_3)_n$) and nitrogen compounds such as nitrogen triiodide (NI_3). Upon initiation the explosive molecule dissociates into its atomic constituents before recombination to form small, stable molecules as shown in Reaction Scheme 1.1. The net energy of the explosion equates to the difference between the energy required to cause the fragmentation of the molecule and the energy released upon bond formation within the product gases. The nature of the products is largely dependent on the amount of oxygen available during the reaction (either within the molecular structure or from its surroundings); very rarely is an infinite supply of oxygen available during the explosion and mixed oxidation products (*i.e.* $C/CO/CO_2$) are therefore common.

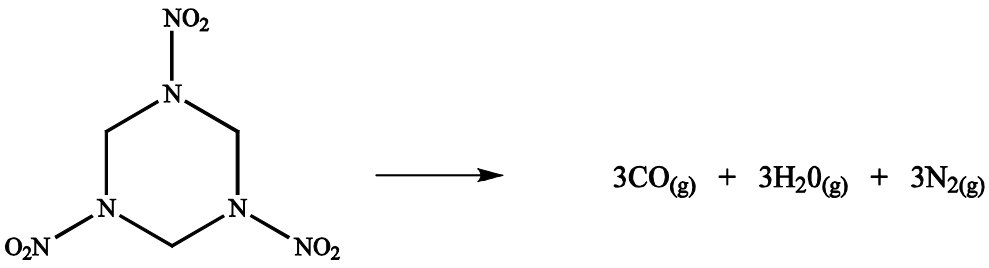

Reaction Scheme 1.1 Explosion of RDX (Section 3.1) to its gaseous products.

1.1.2 Classification

Energetic materials may be broadly classified into three categories: pyrotechnics, propellants (including gas generators) and explosives, which themselves may be further sub-divided into primary and secondary explosives. Pyrotechnic formulations undergo combustion at visibly observable rates, giving rise to coloured smoke, noise and/or brightly-coloured light. Propellants, such as ammonium perchlorate [NH_4ClO_4], contain all the oxygen necessary for their combustion within their structure. They undergo more rapid combustion than pyrotechnics but do not detonate, although burning may be violent and accompanied by sparks or flames and a hissing/crackling sound. The resultant production of large volumes of hot gas can then be utilised for the propulsion of projectiles (ranging from bullets to spacecraft) or to power turbines in torpedoes, for example.[1]

Primary explosives are sensitive to mild stimuli, such as heat or shock, causing a detonation event that gives rise to a short, strong shock-wave. Primary explosives are therefore commonly used to initiate the detonation of the less-sensitive secondary explosives. Despite many compounds displaying explosive decomposition upon initiation by a mild stimulus, very few primary explosives have been incorporated into practical and usable detonators. This is due to the rigorous constraints on thermal stability, hygroscopicity and shelf-life, that are required of a technically viable initiator.[2] The explosive properties of a range of metal azides, fulminates and styphnates (see Figure 1.1) are known, yet the majority of blasting caps utilise either lead styphnate or lead azide. In recent years, however, the toxicological and ecological hazards presented by the dispersion of minute, but cumulative, quantities of lead has motivated research into so-called ‘greener primaries’.[3] These endeavours, while worthy of merit, have so far had limited success due to the stringent quality controls placed on new detonators – lead replacements should display the same (or greater) explosive performance than the current optimum detonator, while also displaying physical and chemical stability *and* being devoid of toxic heavy metals or teratogenic perchlorates.[4]

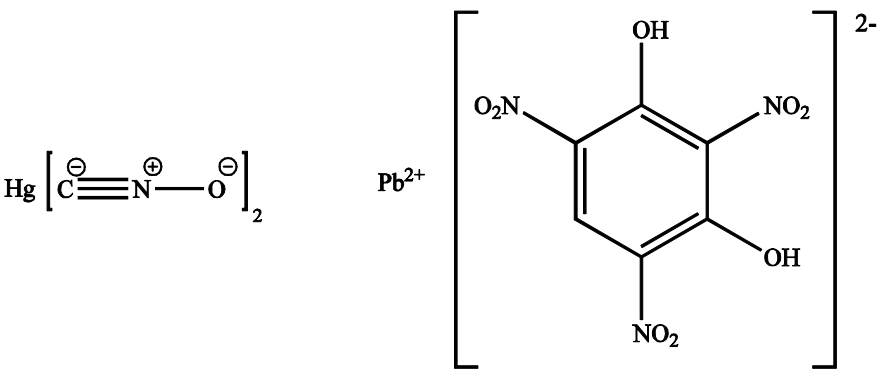

Figure 1.1 Well-known primary explosives: mercury fulminate and lead styphnate.

Secondary explosives (also referred to as high explosives) differ from primary explosives in that they are not easily detonated by heat or shock and instead require initiation by the intense shock-wave produced by a primary explosive. Once detonated however, secondary explosives create a sustained shock-wave over longer distances.

Unlike primary explosives, a raft of high explosives has been developed; many display common features however, such as the prevalence of nitro groups. The most famous explosive molecule is, of course, TNT (trinitrotoluene, see Figure 1.2(a)) which was developed at the turn of the 20th century as a replacement for picric acid, Figure 1.2(b). Picric acid was the most common military explosive of the 19th century, but its sensitivity and hazardous casting process meant that replacements were eagerly sought. After World War I, research programmes were initiated with the aim of synthesising and developing more powerful explosives, the results of which were primarily RDX and HMX. These compounds, depicted in Figure 1.2(c) and (d), remain the most widely-used explosives in current munitions.

Recent developments in explosive formulations have been more adventurous with the design of polycyclic compounds, such as CL-20 and octanitrocubane, shown in Figure 1.3. The explosive performance of CL-20, attributed to the inherent strain and the high energy-density within the molecule, has been shown to exceed that of HMX.[5] However, concerns remain over its sensitivity. Nitrocubanes meanwhile are predicted to be the most powerful explosives ever synthesised. Eaton *et al.* successfully synthesised a range of polynitrocubanes, including octanitrocubane shown in Figure 1.4, although the complicated synthetic procedure and the exorbitant cost of the raw materials ($40 000 per kg in 2000) have hindered full characterisation of its explosive performance and hence its implementation in munitions.[6]

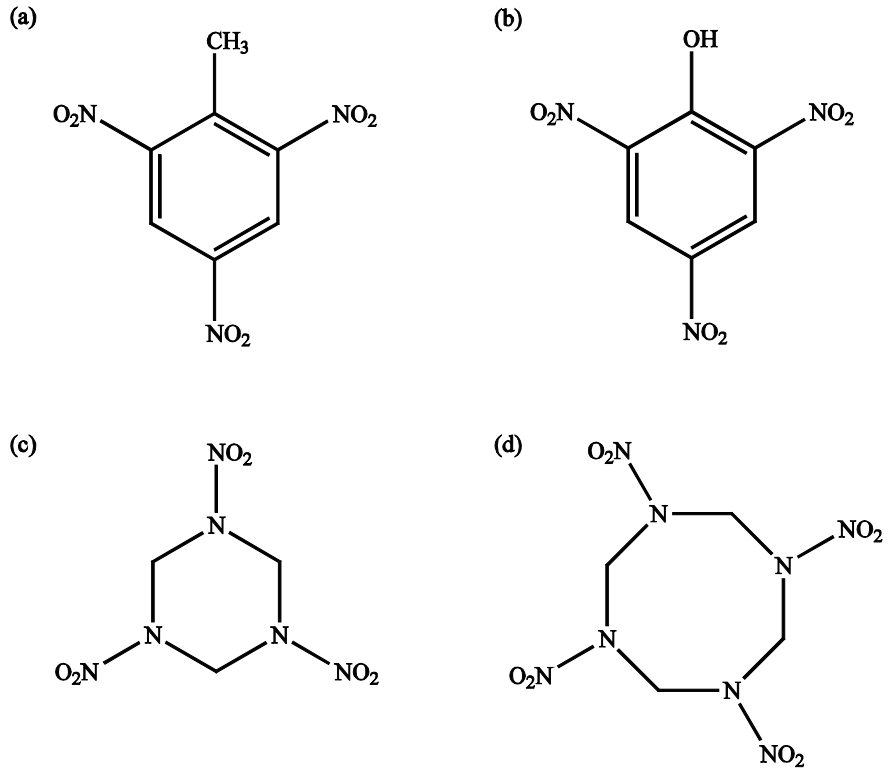

Figure 1.2 (a) the molecular structure of TNT, trinitrotoluene, presented alongside (b) picric acid, the molecule which it would come to supersede; the production of (c) RDX and (d) HMX was developed in the 1940s, but both remain widely used in current munitions.

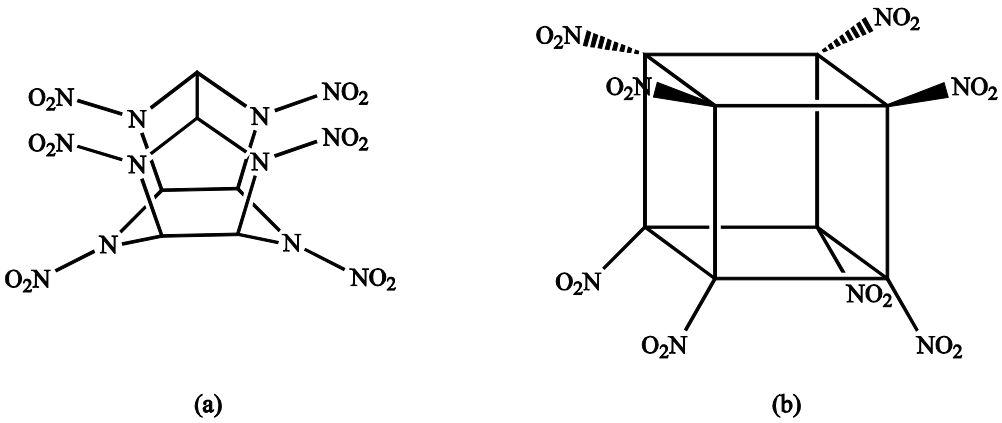

Figure 1.3 Molecular structures of the high-energy polycyclic materials (a) CL-20 and (b) octanitrocubane.

While significant research effort has been directed at improving explosive power, recent developments have also been motivated by reducing the sensitivity of energetic materials to accidental detonation. Nitro-1,2,4-triazole-3-one (NTO) is a heterocyclic compound with high energy and low sensitivity; FOX-7 (or 1,1-diamino-2,2-dinitroethene) also displays a

detonation velocity comparable to RDX but with dramatically reduced sensitivity, attributed to the high-degree of conjugation and hydrogen bonding within its crystal structure.[7] NTO and FOX-7 are illustrated in Figure 1.4. Finally, the desire for an energetic material that produces no greenhouse gases upon detonation has led to the development of another range of energetic materials, sometimes referred to as 'environmentally-friendly' explosives. While this concept may appear initially paradoxical, it has become a priority for current researchers, since the responsible disposal of these materials is now the subject of international regulation.

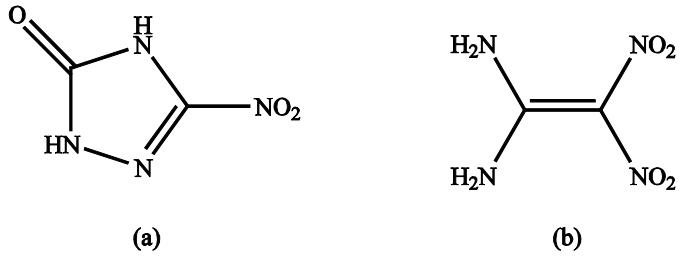

(a) (b)

Figure 1.4 Molecular structures of the insensitive munitions, NTO and FOX-7.

Recent advances in the synthesis of novel energetic materials have been thoroughly reviewed by Agrawal [8], Pagoria *et al.* [9] and Badgujar *et al.*[10]

1.1.3 Energetic Performance

It is essential that the performance and reproducibility of energetic materials are fully assessed prior to their application in munitions. Properties that are critical to energetic performance include sensitivity to detonation (by impact, friction, shock or charge); the detonation velocity (defined as the velocity of the shock-wave passing through the detonated material); thermal stability and crystal morphology.[11] The crystal density is also a critical criterion for performance assessment, since it is desirable to obtain the material in as dense a form as possible for applications where volume is limited (such as in explosive charges). Moreover the detonation velocity is, to a first approximation, proportional to the crystal density [1] and it is therefore common to use experimental densities (and calculated densities for novel materials) as an approximate index for explosive power.

The solid-state chemistry of this class of compounds often strongly influences these properties and may therefore have significant consequences for explosive performance and its reproducibility.[12] This is especially true for materials that exhibit the phenomenon of polymorphism.

1.2 Polymorphism

1.2.1 Definition

The term 'polymorphism' can have different connotations depending on the field in which it is applied. Most commonly used in genetics and molecular biology, as determined by a recent survey of the Chemical Abstracts [13], it describes the co-existence of two or more discrete phenotypes or genotypes within a sample population. It can also be used to describe the ability of a computer programming code to deal with different input sources. In chemistry and materials science however, the term is generally given to a situation in which "a substance can exist in more than one crystalline state."[14] These different crystalline states, or polymorphs, are identical in the liquid and vapour states but display different crystal structures in the solid state. Polymorphism can therefore greatly affect a range of properties such as melting/sublimation temperature, heat capacity, conductivity, solubility, density, refractive index and solid-state reactions.[15] Such is the impact of this phenomenon on materials chemistry, it has been the subject of numerous reviews and special issues within the literature, a sample of which can be found in [16-21] and references therein.

A familiar example of polymorphism is elemental carbon. Carbon can exist in numerous allotropic[1] crystalline forms: primarily graphite and diamond, although lonsdaleite (a hexagonal analogue of diamond), fullerenes (three-dimensional cages made solely of carbon atoms, for example C_{60} and C_{70}) and carbon nanotubes either exist naturally, in minute quantities, or have been synthesised by researchers.[22-26] The striking structural variety of these forms is presented in Figure 1.5 alongside a representation of amorphous carbon (displaying no long-range crystalline order) for completeness. These structural differences imbue each allotrope with dramatic differences in their chemical, physical and electrical properties. Diamond is the hardest material known and is electrically insulating, optically transparent and chemically inert. In contrast, graphite is black, soft, electrically conducting and chemically reactive.

[1] In this case, the term allotropy is more often used as the substance in question is an element.

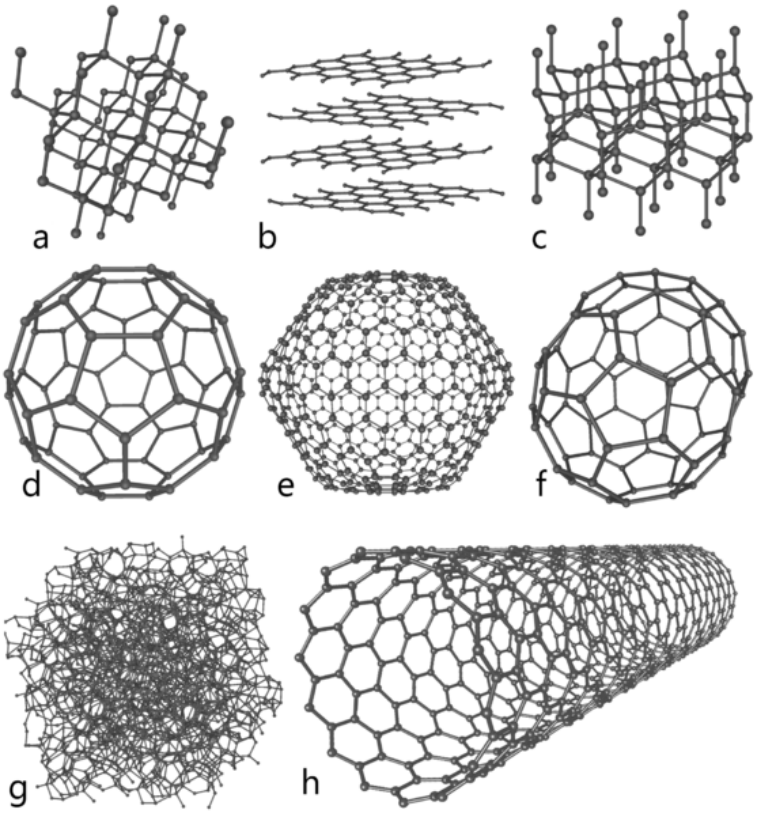

Figure 1.5 Allotropes of carbon: (a) diamond, (b) graphite, (c) lonsdaleite, (d) buckminsterfullerene, C_{60}, (e) C_{540}, an icosahedral fullerene, (f) C_{70}, fullerene, (g) amorphous carbon, and (h) single-walled carbon nanotube.

This example not only highlights the structural diversity of different polymorphs but also underscores the delicate balance between thermodynamics and kinetics during crystallisation. While thermodynamics governs the stability of a particular crystalline form, the crystallisation process itself is often dictated by kinetics. This may result in the appearance of metastable polymorphs, some of which may exhibit sufficient stability to exist for years. Under ambient conditions the most thermodynamically stable allotrope of carbon is graphite. However, due to the high energy barrier to conversion of diamond to graphite, this process is extremely slow (in effect impossible) at ambient conditions. The crystallisation of metastable polymorphs has been 'formalised' in Ostwald's Rule of Stages, which states that the metastable form will often crystallise first (a reflection of the initial kinetic control) but over time this form will transform to a more stable form (due to thermodynamics).[27]

The sometimes competing influences of kinetics and thermodynamics mean that a wide range of materials have been documented to display polymorphism. Indeed comments like McCrone's "*in general, the number of forms known for a given compound is proportional to*

the time and money spent in research on that compound" [28] suggest that polymorphism is the rule, rather than the exception. While it is no doubt the case that the *possibility* of polymorphism always exists for a given compound, the exact conditions for the crystallisation of other forms are not necessarily obvious, nor achievable. Of the *ca* 500 000 crystal structures deposited in the Cambridge Structural Database as of November 2009, 16 014 bear the tag 'polymorph'.[29] This clearly demonstrates that compounds displaying proven polymorphism are in the minority (3.3%), especially when one considers that this is a measure of the number of individual polymorphs in the database, not the number of polymorphic molecules. Despite this, the implications of polymorphism on myriad physicochemical properties underline the importance of the characterisation of all possible polymorphic modifications, particularly in an industrial setting.

1.2.2 Implications of polymorphism

Materials Science

The dramatic consequences that may arise from a polymorphic transition can be best exemplified by reference to the catastrophic deterioration of tin objects upon exposure to long durations of sub-ambient temperatures. Tin undergoes an allotropic conversion from white tin (β-Sn) to grey tin (α-Sn) at 286 K.[30] In the β-form, tin is a ductile metal that adopts a body-centred tetragonal structure ($I4_1/amd$), with a density of 7.28 Mg m^{-3}; below the transition, α-Sn is a brittle semi-conductor with a considerably less-dense, cubic structure (5.75 Mg m^{-3}, $Fd\bar{3}m$).[31] The β → α transition therefore results in a catastrophic volumetric expansion of ~ 27%, characterised by the appearance of discrete powdery efflorescences of grey tin that gradually spread and coalesce, eventually reducing the tin to powder (see Figure 1.6).[32] The defeat of the Napoleonic army in the Russian steppes and the ill-fate that befell Captain Scott and his crew on their expedition to the South Pole have both, perhaps erroneously, been attributed to this phase transition.[32]

Observations of this 'tin pest' or 'tin disease' were first reported by German and Russian scientists who noted the marked deterioration in large portions of tin organ pipes and other tin artefacts in the mid 19th century.[33, 34] This curious behaviour was only rationalised in the early 20th century as a result of Cohen's rigorous investigation of the transition temperature, its kinetics and its reversibility (the results of which were published in a series of articles in *Zeitschrift für physikalische Chemie*, for example [35, 36]). He found that the transition occurred most quickly at ~ 225 K, that it was reversible but also that samples that had previously undergone temperature-cycling underwent the β → α much more swiftly.

This observation was rationalised by the presence of grey-tin nuclei providing nucleation sites for subsequent transitions.

Figure 1.6 Total disintegration of a tin test piece after prolonged exposure to temperatures *ca* 255 K.[37]

Commercial grades of tin were shown not to undergo this disintegration however – trace impurities commonly found in such samples have been credited with retarding the $\beta \rightarrow \alpha$ transition or even stopping it altogether.[37] One may therefore assume that tin pest may be consigned to the history books and, quite literally, to museum pieces (and their conservation). However, recent European regulations restricting the use of hazardous substances have meant that lead-free solders containing 95 – 99% Sn have had to be developed.[38] This had led to a recent resurgence in research into this polymorphic transition, particularly since circuitry in cold environments (*e.g.* aerospace) risk failure in this way. Small quantities of elements that are soluble in tin (Sb and Bi, for example) have been shown to decelerate the rate of transition; insoluble elements such as Zn, Al and Mg actually promote it.[39]

Food Science

Polymorphism has also been shown to play an important role in the processing of foods based on fat molecules (triglycerides), such as margarine, ice cream and chocolate. The melting behaviour of such molecules is intrinsically linked with the sensory experience of these products, affecting texture and appearance. This is further complicated for producers of chocolate, since cocoa butter can adopt one of six polymorphs over a very narrow temperature range (289 – 309 K), only one of which has the desired characteristics.[40] If the wrong form is present, or the fat has not been crystallised (tempered) correctly, white powdery deposits form on the surface, known as fat bloom. There has therefore been

considerable industrial impetus for the structural characterisation of a range of triglycerides as well as the determination of their physical properties and the optimum conditions for their crystallisation.[41-43]

Pharmaceuticals

Despite these illustrative examples of the implications of polymorphism in materials science and food technology, polymorph screening experiments are still primarily carried out on pharmaceuticals. This is because polymorphism can lead to profound effects during processing, serious implications for patient risk and costly challenges to intellectual property.

Throughout the manufacturing process drug molecules are exposed to a range of pressure and temperature conditions, during grinding, freeze-drying and tabletting for example. It is therefore crucial to determine whether any polymorphic transitions are likely to occur under such conditions if one is to ensure the consistent and selective production of the desired form.[44] Furthermore, throughout its shelf-life a pharmaceutical product will experience fluctuations in environmental factors such as temperature and relative humidity which may also promote phase transitions. This is best illustrated by the case of Ritonavir, a protease inhibitor used in HIV treatments: the crystallisation of a thermodynamically more stable (and therefore less soluble) form of the drug two years after its introduction to the market resulted in substantial costs for its producers.[45]

Since the majority of drug molecules rely on their dissolution in the gastro-intestinal tract to allow their function within the body, it is reasonable to conclude that the bio-availability of a given polymorph is related to its solubility.[46] Two polymorphs will therefore have significantly different activities, and thus dosages must be adapted to reflect this. It is essential therefore that solubility and bio-availability are ascertained before the drug is administered.

As a result of the significant impact of these properties on the effectiveness and safety of pharmaceuticals, it has now become a legal requirement for companies to provide detailed information regarding drug polymorphs to licensing bodies such as the United States Food and Drug Administration (USFDA).

Finally, pharmaceutical companies are motivated to carry out extensive polymorph screening operations in order to protect their own intellectual property and patents. Although international patent legislation varies, challenges to patents have been successful on the basis of the discovery of new polymorphs. As demonstrated above, a new crystalline form may be

expected to exhibit very different physical, chemical or biological properties thus subverting patent protection. Therefore in order to maintain, or in certain cases lengthen, the exclusivity of the patent, it is necessary to characterise all polymorphs prior to its issuance. Bernstein's monograph contains various case studies illustrating this subject.[11]

Energetic Materials

As outlined in Section 1.1.3, the performance of an energetic material depends on a number of factors, such as sensitivity, detonation velocity and thermal stability. Since these factors are inextricably linked with the material's solid-state chemistry, polymorphism can have significant implications for explosive performance and reproducibility. Much like in the pharmaceutical industry, it is therefore essential that all polymorphs are identified, their stability (or metastability) is assessed critically, and the conditions under which they are formed are characterised. Furthermore any polymorphic transitions which may be reasonably expected to occur during storage or application should be studied – structural investigations at variable temperature and pressure have therefore been pursued more extensively in this industry than in any other. The occurrence of polymorphism in nitroglycerine, TNT, RDX and HMX, for example, is well documented (such as in [11] and references therein).

HMX (Figure 1.2(d)) is an excellent illustrative example of the role played by polymorphism in energetic materials. Four forms of HMX have been identified and structurally characterised (α, β, γ, δ), although the γ-form has been shown to be a hemihydrate, and not a true polymorph.[47-49] Investigations have shown that the sensitivities to impact follow the order δ > γ > α > β.[50] The risk of accidental detonation of the δ-, γ-, and α-forms means that only β-HMX is permitted in munitions used by the British armed forces.

Of particular note in recent years, mainly due to concerns over sensitivity, is the polymorphism of triacetone triperoxide (TATP, see Figure 1.7). TATP is an improvised explosive that can be synthesised from readily-accessible raw materials and has gained notoriety due to its alleged use in terrorist attacks. TATP is extremely sensitive to detonation, making it impractical for military and civilian munitions. This situation is exacerbated by the recent identification of six polymorphs of this material - the sensitivity and explosive characteristics of each is currently being investigated.[51]

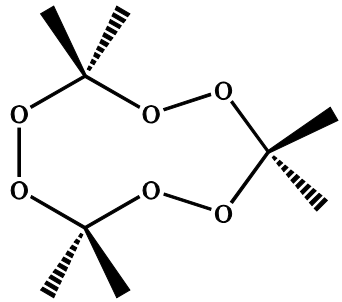

Figure 1.7 Molecular structure of triacteone triperoxide (TATP).

In many cases, the conditions experienced by energetic materials during manufacturing and storage are similar to those applied to pharmaceuticals – it is therefore essential to determine if the material is at risk of undergoing polymorphic conditions under these conditions. A catastrophic example of the sensitisation of an explosive during its shelf-life is that of ammonium nitrate. Ammonium nitrate is primarily used as a fertiliser, although it is a strong oxidiser and can therefore be incorporated into energetic formulations with hydrocarbons such as diesel or kerosene. Accounts of polymorphism of NH_4NO_3 are among the oldest of any energetic material, dating to 1903.[52] It has been shown to adopt four different polymorphic structures at atmospheric pressure, depending on temperature.[53]

Of critical importance for handling and storage of NH_4NO_3 is the phase transition between the forms IV (*Pmmn*) and III (*Pnma*) at 305 K, which is accompanied by a significant (~ 4%) volume change and the formation of dislocations in the crystal structure. Temperature-cycling through this transition, due to diurnal temperature fluctuations, resulted in large quantities of stored material caking together. Attempts to break up caked masses (using blasting explosives!) resulted in the detonation of the ammonium nitrate stockpile, causing widespread destruction and a number of deaths and injuries in the first half of the 20^{th} century.[54] It has subsequently been shown that the IV → III transition can be retarded, and even halted, by the addition of small quantities of additives such as KNO_3, $Mg(NO_3)_2$ and NiO, and thus doped ammonium nitrate is insensitive enough for use in current armaments.

Finally, crystal density has become an index for explosive power, since density is directly proportional to the detonation velocity. Polymorphs adopt different crystal packing and will therefore exhibit a range of crystal densities. It is therefore desirable to obtain the material in as dense a form as is practicable. An interesting example is provided by octanitrocubane (ONC), depicted in Figure 1.3. Only one polymorph of ONC has been reported in the literature since its successful synthesis.[6] The experimental crystal density, as determined by X-ray single-crystal diffraction, was found to 1.979 Mg m^{-3}. While comparable to other

high explosives, such as HMX and CL-20, this is lower than the theoretically predicted density of 2.06 Mg m^{-3}.[6] This is perhaps a tantalising inference to a denser polymorph that may be crystallised, providing the conditions are right. However, in the decade since ONC was first synthesised, no experimental reports on this denser form have been published.

All of the energetic materials included in this discussion so far display polymorphism under ambient conditions – although only one crystal form represents the thermodynamic minimum under these conditions, one (or various) other form is sufficiently metastable to be observed. Polymorphism, however, is not constrained to ambient conditions. As has already been intimated, particularly by the case of ammonium nitrate, different polymorphs may be adopted at different temperatures. A further thermodynamic variable which can drastically alter the relative stabilities of known polymorphs, and indeed can result in the formation of entirely new polymorphs, is pressure. This is particularly pertinent to a discussion of the polymorphism of energetic materials, which often experience pressures of several thousand times greater than atmospheric pressure during a detonation event. High-pressure polymorphism in these materials can have equally dramatic consequences for their performance and should therefore be explored equally as fully as ambient pressure studies.

In the sections that follow, a general introduction to high-pressure science is given, outlining the general concept and the motivation for the wealth of science that has been carried out at extreme conditions. This will be illustrated by examples from a range of fields, such as biotechnology and materials science. Finally, the importance of obtaining high-quality structural data on energetic materials at elevated pressures will be underscored with a discussion of previous high-pressure studies and an outline of the research presented in this work.

1.3 High Pressure

1.3.1 General Concept

The free energy of a particular system can be related to the pressure (P) and temperature (T) conditions by the following equation:

$$G = U - TS + PV$$

where G represents the Gibbs' free energy, U is the internal energy of the system, S is entropy and V is volume. Pressure therefore is a fundamental thermodynamic variable. While it is common practice to vary the temperature of a system, we are limited to a range of a few thousand degrees. This range is narrowed further if the system of interest is based on small

organic molecules that decompose at temperatures of a few hundred Kelvin. In stark contrast, high-pressure studies in the terapascal (1 000 GPa) regime have been reported recently.[55, 56] This represents a pressure range from atmospheric pressure to 1.0 TPa of the order of 10^7. Although terapascal experiments are by no means routine (they utilise high-pressure shock-waves), pressures of 0.1 – 10 GPa are regularly attained in laboratory studies and are sufficient to induce an exciting array of structural changes.

By altering the pressure of the system, we are readily able to alter its free energy. In so doing, it is possible to induce polymorphism or to divert a reaction pathway. Moreover by undertaking structural investigations at a range of pressures, we gain information on the relative contributions that inter- and intramolecular interactions make to the total free energy of a crystalline system. High-pressure structural studies also present a very rigorous test of intermolecular potentials used in molecular modelling.[57]

Descriptions of the apparatus used to generate high pressures in this study will be detailed in later sections. It is instructive, however, to include a short review of the development of this field and acknowledge the achievements that have propelled the field to the forefront of structural science.

The pioneering work by Bridgman pushed the boundaries of controlled high-pressure experiments, firstly to 7000 atmospheres (0.7 GPa) in the 1930s, then to pressures in the region of 2 GPa.[58] In this pressure regime, well-known substances began to display intriguing properties – solid H_2O transformed into its ice-VI form, which was observed to begin melting about 373 K.[59] Further technical innovation and development led to the introduction of opposed-anvil devices that had the capability of reaching pressure between 5 and 10 GPa.[60, 61]

The most important breakthrough since Bridgman's work has been the invention of the diamond-anvil cell (DAC). This elegant device, which will be discussed in detail in Section 2.2, has facilitated the generation of pressures greater than 100 GPa and has allowed the characterisation of materials *in situ* by diffraction and spectroscopy. A summary of the advances in high-pressure technology, as well as those in experimental techniques, can be found in Katrusiak's excellent review.[62] Moreover, an edition of *Reviews in Mineralogy and Geochemistry* is devoted entirely to the crystallographic characterisation of a range of materials (from small molecules to minerals) at extreme conditions.[63]

In high-pressure research, it is common to find various units used, sometimes interchangeably, as a measure of pressure. All pressures in this study will be reported in gigapascals (GPa), which may be related to other units as follows:

$$1 \text{ GPa} = 10 \text{ kbar} = 9869.2 \text{ atm.}$$

1.3.2 Previous High-Pressure Research

The impact of high-pressure research not only in the areas of physics, chemistry and materials science, but also biotechnology and food science, has been profound. A review of the recent applications of high-pressure science, which is by no means exhaustive, is given below.

Simple Elements and their Exotic Structures

The application of high pressure to simple (or *sp*-) elements has proven to be a particularly fertile research area, with many elements displaying complex crystal structures and anomalous physical properties at elevated pressures. The high-pressure behaviour of elements has been the subject of numerous reviews and for more in-depth discussion, the reader should consult [64-66] and references therein. Two examples have been selected to illustrate the structural diversity of supposedly simple elements under pressure however: sodium and oxygen.

Sodium displays a rather complex phase diagram with respect to pressure and temperature. Throughout compression at ambient temperature, the body-centred cubic (bcc) form remains stable to a maximum pressure of *ca* 65 GPa, at which point it undergoes a phase transition to a face-centred cubic (fcc) structure.[65] Compression studies carried out at elevated pressures and temperatures, however, presented evidence for the anomalous melting behaviour of sodium in the high-pressure regime. Gregoryanz *et al.* showed that the melting line reaches a maximum at *ca* 31 GPa and 1000 K and decreases steeply in its fcc phase.[67] Furthermore, this reaches a minimum at *ca* 118 GPa and 300 K, meaning it is possible to melt a sample of sodium solely by one's body heat (!), provided the sample is at sufficient pressure.[68] Using single-crystal X-ray diffraction, the authors were able to characterise seven different crystalline phases located around this minimum. Finally, above 180 GPa sodium has been shown to become optically transparent and insulating – a truly remarkable observation.[69]

To date six distinct crystalline forms of oxygen have been identified, at variable temperature and pressure. The α-, β- and γ-forms can be adopted at temperatures below 100 K at ambient

pressure. Under compression at 295 K, liquid oxygen solidifies into the β-form at 5.4 GPa before transforming to the 'orange' δ-form (9.6 GPa), which itself undergoes a phase transition to the 'red' ε-form at 10 GPa.[70] Single-crystal X-ray diffraction has shown that in the ε-form the oxygen atoms organise themselves into rhombohedral O_8 molecular units, rather than maintaining the diatomic nature of the lower pressure phases.[71] Finally, at very high pressures (*i.e.* $P > 96$ GPa) oxygen becomes metallic; this high-pressure metallic ζ-form even becomes superconducting at very low temperatures ($T_c = 0.6$ K).[72, 73] The exotic behaviour of an element that we are all familiar with in the gaseous state underscores the power that pressure has in dramatically changing not only the crystal structure of materials, but also their chemical, physical and electronic properties.

Molecular Systems

While the exotic structural behaviour displayed by elemental samples often requires pressures in the range of 10 – 100 GPa, a considerable amount of information can be gleaned by compression of organic materials to modest pressure (0.1 – 10 GPa). The development of high-pressure apparatus and the increasing brightness of X-ray sources, for example synchrotron sources (see Section 2.3.5), has facilitated the structural characterisation of weakly-scattering samples at high pressure. This is an immense accomplishment, especially when one considers the low symmetry (monoclinic or even triclinic) crystal systems that organic molecules often adopt.

The driving force behind the considerable body of work in this field is the identification, characterisation, and, ultimately, prediction of polymorphism in molecular systems. Moreover, high-pressure studies can afford detailed knowledge of intra- and intermolecular interactions and allow an appraisal of the relative contributions these interactions make to the free energy of a crystalline system. Rather than attempting to summarise the prodigious high-pressure research carried out on molecular systems, this section will instead feature illustrative examples. For a broader introduction, the reader should consult Bernstein's monograph [11], or one of the numerous review articles, such as [57, 74-76].

The high-pressure study of molecular materials can be largely partitioned into: (i) the direct compression of solid materials, generally under hydrostatic conditions; and (ii) their crystallisation at pressure, from either the liquid or solution phases. Direct compression is often a fundamental objective of high-pressure analyses, whether to obtain a measure of the compressibility of the material, to initiate polymorphic transitions, or to induce or affect chemical reactions. High-pressure crystallisations meanwhile exploit pressure as a

thermodynamic variable to cause the precipitation of high-pressure polymorphs, some of which may not be accessible by direct compression.

At the relatively modest pressure utilised in these studies (< 10 GPa), covalent bonds do not deviate significantly from their ambient pressure values. However, intermolecular interactions, such as van der Waals interactions and hydrogen bonds, are sensitive to compression. Furthermore, molecular conformations can be readily modified by the application of pressure, particularly if this results in a more efficient crystal packing at elevated pressures. By monitoring compression mechanisms and by structurally characterising high-pressure forms, it is possible to gain an understanding of how molecular crystals adapt to pressure.

Comprehensive studies of the compressibility of small molecules bearing particular functional groups or packing motifs have allowed some generalisations to be made about the effect of pressures on these materials. For example, the high-pressure polymorphism of amino acids has been extensively studied by various groups.[57, 75, 77] Phenomenological evidence from studies such as these suggests that compression is often accompanied by: the collapse of voids within the ambient pressure crystal structure; the particular sensitivity of interplanar distances to compression; a marked rigidity of hydrogen-bonded chains or layers; or the strengthening of favourable intermolecular interactions. For example, the α-form of the amino acid glycine is reported to be 20% more compressible along the direction parallel to interplanar C-H…O hydrogen bonds, when compared to intraplanar N-H…O interactions. This observation has been rationalised in terms of the minimisation of the stacking distance between layers.[78,79]

Nevertheless, significant exceptions to these rules have been reported. For example, Moggach *et al.* actually observed an *increase* in pore size upon compression of a metal-organic framework, although this has been attributed to dynamic interactions between the sample and the pressure-transmitting medium.[80]

In order to rationalise the effects of pressure, a method for the calculation of intermolecular packing energies has been developed in recent years.[81] The PIXEL method has been shown to be valid for the high-pressure phase transitions observed in salicylaldoxime [82] and serine.[83] However, the application of PIXEL calculations to the phase transition in L-serine monohydrate had unexpected results. Although a strengthening of interplanar Coulombic interactions between serine molecules was observed and the water molecules become co-ordinatively saturated with respect to hydrogen bonding, the intermolecular

interactions are reported to be weaker in the high-pressure form II.[84] In this case, the more efficient crystal packing in form II is more dominant than favourable intermolecular interactions. The maximisation of packing efficiency has also been found to be dominant in the high-pressure behaviour of a rather unusual crystal structure. Methyl 2-(carbaxol-9-yl)benzoate adopts a monoclinic structure with eight molecules in the asymmetric unit (Z' = 8), represented in Figure 1.8. Compression to 5.3 GPa, however, results in a phase transition to an orthorhombic structure with Z' = 2.[85] The stabilisation due to the dominance of the PV term at high pressures is sufficient, in fact, to outweigh the unfavourable molecular conformations adopted in the Z' = 2 structure (as determined by *ab initio* methods).

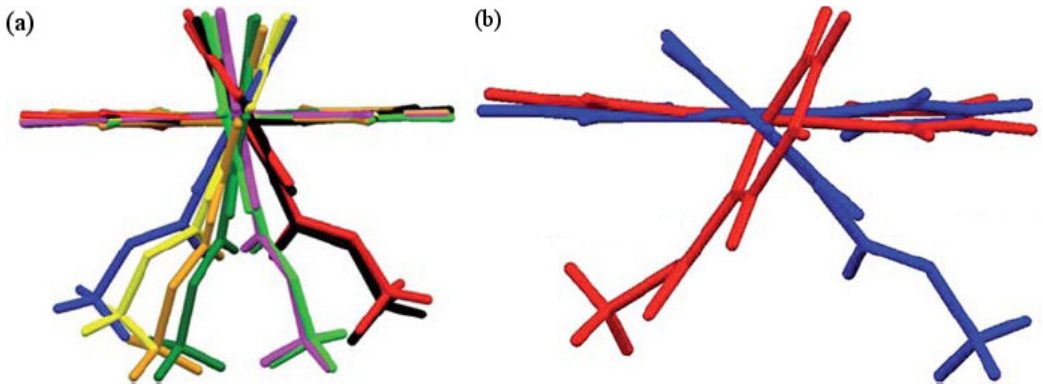

Figure 1.8 Representation of (a) the 8 molecular conformations in methyl 2-(carbaxol-9-yl)benzoate at ambient pressure and (b) the 2 conformations at 5.3 GPa.[85]

As an alternative to the direct compression of solid materials (in which pressure is applied to the ambient-pressure form), pressurisation of liquids or solutions may allow the crystallisation of high-pressure forms to be accomplished directly. In the simplest cases, crystallisation by the application of pressure to pure liquids is analogous to the crystallisation observed upon cooling. For example, the high-pressure and low-temperature forms of 1,2-dichloromethane have been shown to be isostructural.[86] It is more often the case, however, that the high-pressure and low-temperature forms are quite distinct. A variety of molecules, including benzene [87], water [59], phenols [88-90] and, most recently, nitric acid [91] have been shown to adopt different crystal structures in the high-pressure and the low-temperature regimes.

The pressure-induced crystallisation from the liquid phase is only achievable for samples that are liquid at ambient temperature or those with sufficiently low melting points (*i.e.* < 323 K) such that they may be loaded into a diamond-anvil cell in the molten state. This approach is simply not practical for samples with high melting points (such as large pharmaceutical molecules). This is further exacerbated by the general increase in melting

point at elevated pressures. An alternative to this approach is to utilise the decrease in solubility at pressure in order to crystallise high-pressure forms from saturated solutions.

Fabbiani *et al.* have exploited this phenomenon in their 'high-pressure recrystallisations' to obtain a range of novel forms (including polymorphs and solvates) of materials such as paracetamol, parabanic acid and acetamide.[92-94] This technique is perhaps still in its infancy however, since its systematic application in the search of new polymorphs is limited. For example, by simply varying the solvent or the crystallisation pressure, one may dramatically affect the kinetics and/or thermodynamics during crystallisation and hence it may be possible to obtain an array of different forms. Results of such investigations would be invaluable, not only in the identification of new polymorphs, but also in understanding the effects of temperature, pressure *and* solvent on the crystallisation process.

Biotechnology

While the high-pressure polymorphism of the amino acids has been explored extensively, the structural complexity of proteins and other biomolecules makes their high-pressure characterisation far more complicated. Despite this, the desire to understand the effect of pressure on biological systems has driven recent instrumental and methodological advances.[95, 96] For example, Girard *et al.* have developed a pneumatic diamond-anvil cell specifically for macromolecular crystallography [97], although dedicated short-wavelength synchrotron radiation still remains a pre-requisite for crystallographic studies of these complex systems.

Although the pressures in these studies are meagre in comparison to those attained in the investigation of elements, for example, biological systems are observed to exist over a pressure range spanning almost four orders of magnitude. Natural ecosystems alone are observed between atmospheric pressure (0.1 MPa) and 0.1 GPa at the deepest point of the Mariana Trench.[98] Meanwhile pressures of *ca* 1.0 GPa are routinely attained in high-pressure processing techniques, in the food industry for example (*vide infra*). Characterisation of proteins in this pressure regime therefore provides invaluable information, not only on the piezophilic (*i.e.* pressure loving) bacteria that thrive at these extreme conditions, but also on the origins of life under high pressure.[99]

More recent high-pressure experiments, however, have utilised pressure as a thermodynamic variable to artificially alter the bio-systems under investigation. Although exposure to pressures > 0.4 GPa can result in complete denaturation of proteins, intermediate pressures

(*ca* 0.2 GPa) can cause subtle changes in the quaternary structure[2], which may or may not be reversible. In a particularly exciting application, moderate high-pressure treatment is being proposed in the context of vaccine development.[100] The infectivity of the HIV-1 virus was observed to be removed completely at 0.2 GPa, for example.[101]

In addition to the modification of proteins and enzymes, high-pressure treatments have also been applied to mammalian and plant cells. Pressure-induced cellular changes have been shown to protect mammalian cells from damage occurring during cryopreservation.[98] Exposure of fresh bull semen to very gentle pressures (20 – 40 MPa, 90 – 120 mins) prior to its cryostorage was shown to preserve its viability, motility and fertility after thawing.[102] Finally, high-pressure treatment has been shown to increase biomass and grain yield in rice.[103]

Food Science

The modification of biomolecules by high-pressure treatment has also been exploited in the food processing industry to prolong shelf-life without compromising sensory or nutritional properties. Pressure (in these cases up to 1.0 GPa) has been found to influence enzymatic reaction rates and can inactivate micro-organisms, which have the potential to cause the food to spoil and can affect food safety. However, pressure-treatment does not lead to the detrimental effects on the taste or appearance associated with other preservation methods (such as heat), since pressure has limited effects on the covalent bonds within the foodstuff.

The effect of high-pressure (HP) and high-pressure/high-temperature (HPHT) processing on the colour, texture and flavour of fruit- and vegetable-based products has been reviewed in detail by Oey *et al*.[104] They highlighted the benefits of pressure treatment of a selection of foods; the firmness of fruits subjected to high pressures and temperatures, the colour of pressure-treated green vegetables, and the flavour HP fruit juices were all superior to those subjected solely to high-temperature processing. However, since HP-treatment can enhance or retard chemical and biochemical reactions, it can give rise to both desirable and undesirable products. For example, strawberry jam was reported to smell more chemical, rancid and less fruity than traditionally-processed jam.[105]

The sector of the food industry where high-pressure treatments have made a significant impact, and have already been commercialised, is in the processing of shellfish. HP treatment is particularly apposite in this case, since it is necessary to protect against shellfish-

[2] The quaternary structure arises from the combination of two or more chains, resulting in a complete unit. Quaternary interactions are simply characterised as being inter- rather than intra-chain.

borne pathogens while maintaining the appearance, flavour and texture of the raw products. The inactivation of bacterial spores in bivalve shellfish (oysters and clams, for example) can be accomplished by mild pressurisation (*ca* 0.1 GPa). Such treatment has the added benefit of shucking or opening shellfish, making this technology particularly beneficial to industry and consumers alike.[106]

Finally, in a very recent development, high-pressure treatment has been shown to eliminate the allergenicity of wheat products. Yamamoto *et al.* have presented UV and fluorescence spectra, which suggested that pressure-treatment results in a structural adaptation in alpha amylase inhibitor (α-AI), thus reducing its allergenicity.[107]

Pharmaceuticals

Throughout their manufacture, pharmaceuticals can be subjected to elevated pressures, in the milling (*i.e.* mechanical grinding) and tabletting processes. These pressures (typically less than 0.1 GPa) have been shown to be sufficient to induce either complete or partial phase transitions in pharmaceuticals.[108, 109] It is therefore critical to add pressure as a variable to the battery of screening tests in order to assess the polymorphism of these important materials fully. For a more illustrative review of the effects of pressure during the manufacture of pharmaceuticals, the reader should consult [110, 111] and references therein.

However, rather than merely playing a reactive role, by characterising undesirable polymorphic transitions during processing, high-pressure studies have recently been employed to enhance the properties of the active pharmaceutical ingredient (API). Compression studies using the diamond-anvil cell (DAC) have extended the pressure range, for which pharmaceuticals can be structurally characterised and have thus broadened the potential for the identification of new polymorphs. In select cases, these high-pressure polymorphs may display sufficient metastability to allow their recovery to ambient pressure and subsequent use as seed crystals to direct large-scale crystallisation processes. Furthermore high-pressure recrystallisation experiments developed by Fabbiani *et al.* [92-94] have been shown to be particularly successful in the production of a range of solvates as well as novel unsolvated polymorphs.

An excellent example of the different possible forms that can be obtained depending on the crystallisation technique, including direct compression and high-pressure recrystallisation, is paracetamol (Figure 1.9). Under ambient conditions, the thermodynamically most stable form is the monoclinic form I [112-114] but a metastable orthorhombic form II has also been identified.[115] In addition, an orthorhombic form III, which has proven to be an elusive

polymorph has only recently been structurally characterised by X-ray powder diffraction.[116-119]

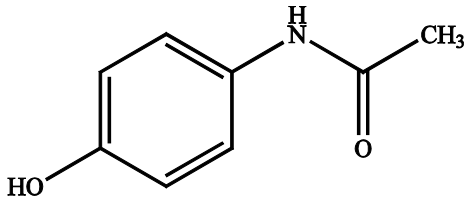

Figure 1.9 Molecular structure of paracetamol (acetaminophen).

The relatively poor compaction properties of the monoclinic form are well known – it is often necessary to include binding agents such as gelatine or starch derivatives during tabletting, thus complicating the manufacturing process.[120] In contrast, form II exhibits much more isotropic compression, thereby presenting a much more facile production.[121] There is therefore considerable interest in selectively and reproducibly obtaining form II.

Numerous methods have been shown to be successful for the crystallisation of this metastable polymorph, although techniques are often involved and not sufficiently discriminating.[122-125] In addition to these ambient pressure techniques, Boldyreva *et al.* showed that polycrystalline samples of form I could be converted to form II by compression to above 4.0 GPa.[121] However, this did not result in complete conversion and it was noted that single crystals did not undergo a phase transition in a similar pressure regime. It is clear from these observations that direct compression alone is not sufficient to obtain the desired pure form II.

High-pressure recrystallisation (DAC) experiments on paracetamol meanwhile have produced small quantities of a range of co-crystals [92, 93] and, indeed, a pure sample of form II at 1.1 GPa.[93] These observations stimulated an investigation into the possibility of the reproducible production of larger quantities of form II by the pressure-induced precipitation from concentrated solutions. Oswald *et al.* have reported the successful recovery of *ca* 0.3 g paracetamol form-II and noted that control over which form is obtained can be exercised by simple modification of the solution concentration and/or crystallisation pressure.[126]

Energetic Materials

As discussed in Section 1.1.1 a high velocity shock-wave passes through an energetic material during its detonation generating pressures of up to 50 GPa and temperatures up to 5500 K.[127] It is essential that one can model and understand the behaviour of energetic

materials under these extreme conditions. There has therefore been significant research studying the structural and physical properties of these materials at elevated temperatures and/or pressures, which has been extensively reviewed.[128-130]

Computational methods are currently employed to explore the response of energetic materials to extreme temperature and pressure conditions. These methods may provide valuable information on reaction mechanisms and rate during high energy processes such as explosive decomposition. The aim of such studies is to accurately predict and model the behaviour of current and novel energetic materials, without the need for expensive and hazardous field experiments.[131, 132] However, in order to provide detailed structural information to complement and validate these computational models, it is imperative that empirical high-pressure studies are performed. This information may be obtained by the application of either dynamic or static pressure.

Dynamic compression experiments utilise shock-waves created by firing a high-velocity projectile at the material in question. Velocities of up to 8000 ms^{-1} can be achieved by firing the projectile from either a gas gun or from an explosive charge. Pressures of up to 100 GPa can be attained upon impact. Similar results may be achieved using high-pressure plasmas (generated by the action of high-power lasers on substrates). The equation of state (see Section 2.6) of the material can be determined by the measurement of the propagation speed of the shock-wave through the material and the change of the velocity across the front (*i.e.* the velocity of the material behind the front if the material ahead of the front is at rest). In addition, recent advances in extremely ultra-fast spectroscopy have allowed the response of molecular materials to shock-wave compression to be analysed *in situ*, thus allowing any high-pressure/high-temperature phase transitions to be identified.[133] In contrast, diffraction experiments have been limited to recovered materials.

In order to ascertain the crystal structure of energetic materials at extreme conditions, it is necessary to conduct direct static compression. In these studies it is possible to generate pressures up to ~ 30 GPa and temperatures *ca* 650 K using mechanical apparatus, such as the diamond-anvil cell. The sample may then be studied *in situ* by both spectroscopic and diffraction techniques, allowing an unambiguous assessment of its compression behaviour. Thus it is possible to characterise directly any anisotropy in the compression mechanism, the development of intra- and intermolecular interactions, and the structure of any high-pressure polymorphs.

Previous high-pressure research on RDX (Figure 1.2), CL-20 (Figure 1.3) and a series of inorganic azides will be reviewed in more detail in subsequent chapters. In addition to these compounds, however, there has been a substantial body of work pertaining to the high-pressure behaviour of HMX, FOX-7 and a series of energetic ammonium compounds. This selection, while not exhaustive, illustrates not only the difficulties of performing high-pressure studies, but also the accomplishments that have been made in this field.

HMX (Figure 1.2) displays rich polymorphic behaviour at ambient temperature and pressure – three polymorphs (α, β and δ) and a hemihydrate (γ-HMX) have been structurally characterised by a combination of single-crystal X-ray and neutron diffraction.[47-49] The stability of the β-form with respect to pressure has been studied by a combination of spectroscopic [134], diffraction [135, 136] and computational methods.[137, 138] X-ray powder diffraction experiments to 45 GPa under quasihydrostatic conditions[3] identified (i) a conformational transition at 12 GPa to ε-HMX, with no abrupt volume change, and (ii) a first-order transition at 27 GPa to a further high-pressure form.[139] However, the phase transition at 27 GPa was not observed during the isentropic compression of single crystals of β-HMX.[140] Recent computational studies, which have extended the pressure range for theoretical calculations on HMX to 40 GPa, have produced conflicting accounts of the compression behaviour *ca* 27 GPa. Lu *et al.* do detect an abrupt volume change in their molecular dynamics calculations [141], but not in their DFT (density functional theory) study.[142] Similar DFT studies by Zhu *et al.* and Cui *et al.* did not show any evidence of a phase transition up to 40 GPa.[143-145]

While the majority of experimental and theoretical studies have focussed on the β-form, the stability ranges of the other forms have also been determined. Goetz *et al*. used Raman spectroscopy to show that α-HMX remains stable upon compression to 4.2 GPa, the maximum pressure studied; the γ-form transforms to the β-form at 0.55 GPa; and that δ-HMX converts to a mixture of the α- and β-forms below 0.05 GPa.[134] Finally, Gump and Peiris presented X-ray powder diffraction data suggestive of a β → δ transition upon decompression of the former from *ca* 5 GPa, highlighting the importance of conducting thorough examinations of the decompression behaviour.[135]

FOX-7 has been shown to display rich polymorphic behaviour with temperature (at ambient pressure). In addition to the ambient temperature α-form, two high-temperature forms have already been structurally characterised: β-FOX-7 results from a reversible transition from the

[3] Argon was used as the pressure-transmitting medium; Ar has an approximate hydrostatic limit of 1.9 GPa (Angel *et al*., ref. [13], Chapter 2).

α-form at 389 K [146]; γ-FOX-7 meanwhile is obtained above 435 K and subsequently can be quenched to ambient temperature.[147] In addition, Peiris *et al.* have performed a thorough investigation of the compression behaviour of the α-form to 8.2 GPa, although the significant reduction in intensity of their X-ray powder diffraction patterns at 4.5 GPa during the non-hydrostatic compression led them to suggest that the sample becomes amorphous under these conditions.[148] Neutron powder diffraction studies on FOX-7-d_4 showed the same loss of intensity.[149] No high-pressure investigation has been carried out on a recovered sample of γ-FOX-7. However, decompression of the 'amorphous' high-pressure sample results in a phase transition to the γ-form when this is conducted at elevated temperatures.[149]

Finally, Davidson *et al.* have recently characterised the high-pressure polymorphism of a series of energetic ammonium compounds (ammonium nitrate [NH_4NO_3], ammonium perchlorate [NH_4ClO_4] and ammonium dinitramide [$NH_4N(NO_2)_2$]).[150] Ammonium nitrate was found to be stable upon hydrostatic compression to the highest pressure studied (7.85 GPa). The authors note, however, that previous observations of a phase transition at *ca* 3.0 GPa were made in studies using either a non-gasketed diamond-anvil cell [151] or shock compression.[152] These results therefore highlight the effect of non-hydrostatic conditions on the occurrence of phase transitions.

Ammonium perchlorate, an energetic oxidiser used in solid rocket motors, was observed to undergo a first-order transition between 3.49 and 3.98 GPa, with a 1.8% decrease in volume. By a combination of neutron powder and X-ray single-crystal diffraction, the authors were able to determine the structure of the high-pressure form unequivocally.[150] These observations are broadly in line with previous spectroscopic and power diffraction experiments, although there is a marked variation in the transition pressure. On the basis of their Raman measurements, Brill *et al.* tentatively proposed a phase transition at *ca* 2.4 GPa [153]; shock compression resulted in significant changes in the X-ray powder diffraction pattern reported by Sandstrom *et al*. at 4.7 GPa [152]; and, Peiris *et al.* used vibrational spectroscopy and X-ray powder diffraction to characterise a sluggish phase transition, commencing at 0.9 GPa but only reaching completion at 3.0 GPa.[154] It should be stressed, however, that experimental factors such as hydrostaticity and sample purity may affect phase behaviour dramatically.

Ammonium dinitramide (ADN) is currently being developed as a rocket propellant, since it displays minimum signature characteristics and minimal environmental contaminants. A phase transition has been reported to occur during compression of ADN at 2.0 GPa, as

measured by vibrational spectroscopy and X-ray powder diffraction under non-hydrostatic conditions.[155] No such phase transition was observed (up to 4.03 GPa) in the neutron powder diffraction study by Davidson *et al.* [150], nor in recent complementary X-ray single-crystal diffraction experiments.[156]

In their comprehensive review of these energetic ammonium compounds, Davidson *et al.* have not only characterised their high-pressure behaviour but have also drawn attention to the effect of the sample conditions on the occurrence or suppression of phase transitions.

1.4 General Aims and Outline of Research

Pressure has been shown to be an extremely powerful thermodynamic variable, resulting in innumerable phase transitions. This is compounded further by the combined effects of pressure *and* temperature. Such pressure- or temperature-induced phase transitions may therefore dramatically affect the performance of an energetic material. For this reason, it is essential to characterise fully the structural response of energetic materials to extreme conditions. This study therefore aims:

- to investigate the effect of pressure, and in some cases pressure *and* temperature, on the polymorphism of a range of energetic materials;
- to identify and structurally characterise new phases *in situ*;
- to explore whether high-pressure forms can be recovered to ambient pressure, with a view to obtaining energetic materials with enhanced properties at ambient conditions.

Chapter 3 describes the characterisation of the high-pressure/high-temperature polymorphism of RDX using a combination of neutron powder and X-ray single-crystal diffraction. In addition, the structure of the highly metastable polymorph at ambient pressure is reported. Chapter 4 explores the high-pressure behaviour of CL-20 in different pressure media. In Chapters 5 and 6, a series of inorganic azides has been structurally characterised under a range of pressure and temperature conditions. Suggestions of future work pertinent to each study are made in the relevant chapters. However, general conclusions and an outlook for the study of energetic materials at extreme conditions can be found in Chapter 7.

1.5 References

1. J. Akhavan, *The Chemistry of Explosives*, Royal Society of Chemistry, Cambridge, UK, 2004, 2nd edn.
2. J. Bottaro, *Ideas to Expand Thinking About New Energetic Materials*, in *Overviews of Recent Research on Energetic Materials*, R.W. Shaw, T.B. Brill, and D.L. Thompson, Editors, 2005, World Scientific Publishing Co., Singapore.

3. M.H.V. Huynh, M.A. Hiskey, T.J. Meyer, and M. Wetzler, *Proc. Nat. Acad. Sci. USA*, 2006, **103**, 5409.
4. M.H.V. Huynh, M.D. Coburn, T.J. Meyer, and M. Wetzler, *Proc. Nat. Acad. Sci. USA*, 2006, **103**, 10322.
5. R.L. Simpson, P.A. Urtiew, D.L. Ornellas, G.L. Moody, K.J. Scribner, and D.M. Hoffman, *Propellants, Explos., Pyrotech.*, 1997, **22**, 249.
6. P.E. Eaton, R.L. Gilardi, and M.X. Zhang, *Adv. Mater.*, 2000, **12**, 1143.
7. U. Bemm and H. Ostmark, *Acta Cryst.*, 1998, **C54**, 1997.
8. J.P. Agrawal, *Prog. Energy Combust. Sci.*, 1998, **24**, 1.
9. P.F. Pagoria, G.S. Lee, A.R. Mitchell, and R.D. Schmidt, *Thermochim. Acta*, 2002, **384**, 187.
10. D.M. Badgujar, M.B. Talawar, S.N. Asthana, and P.P. Mahulikar, *J. Hazard. Mater.*, 2008, **151**, 289.
11. J. Bernstein, *Polymorphism in Molecular Crystals*, Clarendon Press, Oxford, UK, 2002.
12. J.J. Dick, *J. Phys. IV*, 1995, **5**, 103.
13. *SciFinder Scholar*, 2007, American Chemical Society.
14. S. Rosenstein and P.P. Lamy, *Am. J. Hosp. Pharm.*, 1969, **26**, 598.
15. D. Giron, *Pharm. Sci. Technol. Today*, 1998, **1**, 191.
16. T.L. Threlfall, *Analyst*, 1995, **120**, 2435.
17. G.P. Stahly, *Cryst. Growth Des.*, 2007, **7**, 1007.
18. P.R. Unwin, *Faraday Discuss.*, 2007, **136**, 409.
19. A.J. Matzger, *Cryst. Growth Des.*, 2008, **8**, 2.
20. F. Grepioni, *New J. Chem.*, 2008, **32**, 1657.
21. A.D. Bond, *Curr. Opin. Solid State Mater. Sci.*, 2009, **13**, 91.
22. C. Frondel and U.B. Marvin, *Nature*, 1967, **214**, 587.
23. H.W. Kroto, J.R. Heath, S.C. O'Brien, R.F. Curl, and R.E. Smalley, *Nature*, 1985, **318**, 162.
24. P.R. Buseck, J.T. Semeon, and R. Hettich, *Science*, 1992, **257**, 215.
25. S. Iijima, *Nature*, 1991, **354**, 56.
26. M. Monthioux and V.L. Kuznetsov, *Carbon*, 2006, **44**, 1621.
27. W. Ostwald, *Z. Phys. Chem.*, 1897, **22**, 289.
28. W. McCrone, *Polymorphism*, in *Physics and Chemistry of the Organic Solid*, D. Fox, M.M. Labes, and A. Weissberger, Editors, 1965, Wiley Interscience, New York, USA.
29. D. Braga, F. Grepioni, and L. Maini, *Chem. Commun.*, 2010, **46**, 6232.
30. E.S. Hedges and J.Y. Higgs, *Nature*, 1952, **169**, 621.
31. A.D. Styrkas, *Inorg. Mater.*, 2003, **39**, 683.
32. M. Gilberg, *AICCM Bulletin*, 1991, **17**, 3.
33. O.L. Erdmann, *J. Prakt. Chem.*, 1851, **52**, 428.
34. T. von Fritzsche, *Comptes Rendus*, 1868, **67**, 1106.
35. E. Cohen and C. van Eijk, *Z. Phys. Chem.*, 1899, **30**, 601.
36. E. Cohen and K.D. Dekker, *Z. Phys. Chem.*, 1927, **127**, 178.
37. W.J. Plumbridge, *Circuit World*, 2007, **33**, 9.
38. D. Di Maio and C. Hunt, *J. Mater. Sci: Mater. Electron.*, 2009, **20**, 386.
39. D. Di Maio and C. Hunt, *J. Electron. Mater.*, 2009, **38**, 1874.
40. S.T. Beckett, *Science of Chocolate*, Royal Society of Chemistry, Cambridge, UK, 2008, 2nd edn.
41. R.N.M.R. van Gelder, N. Hodgson, K.J. Roberts, A. Rossi, M. Wells, M. Polgreen, and I. Smith, *Crystallization and polymorphism in cocoa butter fat: in-situ studies using synchrotron radiation x-ray diffraction* in *Crystal Growth of Organic Materials*, 1995, Washington, D.C., USA.
42. K. Sato, *Chem. Eng. Sci.*, 2001, **56**, 2255.

43. S.D. MacMillan, K.J. Roberts, A. Rossi, M.A. Wells, M.C. Polgreen, and I.H. Smith, *Cryst. Growth Des.*, 2002, **2**, 221.
44. J.M. Miller, B.M. Collman, L.R. Greene, D.J.W. Grant, and A.C. Blackburn, *Pharm. Dev. Technol.*, 2005, **10**, 291
45. S.R. Chemburkar, J. Bauer, K. Deming, H. Spiwek, K. Patel, J. Morris, R. Henry, S. Spanton, W. Dziki, W. Porter, J. Quick, P. Bauer, J. Donaubauer, B.A. Narayanan, M. Soldani, D. Riley, and K. McFarland, *Org. Process Res. Dev.*, 2000, **4**, 413.
46. S.R. Vippagunta, H.G. Brittain, and D.J.W. Grant, *Adv. Drug Delivery Rev.*, 2001, **48**, 3.
47. H.H. Cady, A.C. Larson, and D.T. Cromer, *Acta Cryst.*, 1963, **16**, 617.
48. R.E. Cobbledick and R.W.H. Small, *Acta Cryst.*, 1974, **B30**, 1918.
49. P. Main, R.E. Cobbledick, and R.W.H. Small, *Acta Cryst.*, 1985, **C41**, 1351.
50. S.J.P. Palmer and J.E. Field, *Proc. R. Soc. London, Ser. A*, 1982, **383**, 399.
51. O. Reany, M. Kapon, M. Botoshansky, and E. Keinan, *Cryst. Growth Des.*, 2009, **9**, 3661.
52. F. Wallerant, *C.R. Hebd. Seances Acad. Sci.*, 1903, **137**, 805.
53. C.S. Choi, H.J. Prask, and E. Prince, *J. Appl. Crystallogr.*, 1980, **13**, 403.
54. C. Boyars, *Ind. Eng. Chem., Prod. Res. Dev.*, 1976, **15**, 308.
55. H. Nagao, K.G. Nakamura, K. Kondo, N. Ozaki, K. Takamatsu, T. Ono, T. Shiota, D. Ichinose, K.A. Tanaka, K. Wakabayashi, K. Okada, M. Yoshida, M. Nakai, K. Nagai, K. Shigemori, T. Sakaiya, and K. Otani, *Phys. Plasmas*, 2006, **13**, 052705.
56. J.H. Eggert, D.G. Hicks, P.M. Celliers, D.K. Bradley, R.S. McWilliams, R. Jeanloz, J.E. Miller, T.R. Boehly, and G.W. Collins, *Nat. Phys.*, 2010, **6**, 40.
57. S.A. Moggach, S. Parsons, and P.A. Wood, *Crystallogr. Rev.*, 2008, **14**, 143.
58. P.W. Bridgman, *The Physics of High Pressure*, Bell and Sons, London, UK, 1931.
59. P.W. Bridgman, *J. Chem. Phys.*, 1937, **5**, 964.
60. P.W. Bridgman, *Proc. R. Soc. London Ser. A*, 1950, **203**, 1.
61. P.W. Bridgman, *Proc. Am. Acad. Arts Sci.*, 1952, **81**, 167.
62. A. Katrusiak, *Acta Cryst.*, 2008, **A64**, 135.
63. R.M. Hazen and R.T. Downs, eds. *Reviews in Mineralogy and Geochemistry*, *Vol. 41*:*High-Temperature and High-Pressure Crystal Chemistry*, 2000, Mineralogical Society of America, Washington, D.C., USA.
64. U. Schwarz, *Z. Kristallogr.*, 2009, **219**, 376.
65. M.I. McMahon and R.J. Nelmes, *Chem. Soc. Rev.*, 2006, **35**, 943.
66. O. Degtyareva, *High Pressure Res.*, 2010, **30**, 343
67. E. Gregoryanz, O. Degtyareva, M. Somayazulu, R.J. Hemley, and H.K. Mao, *Phys. Rev. Lett.*, 2005, **94**, 185502.
68. E. Gregoryanz, L.F. Lundegaard, M.I. McMahon, C. Guillaume, R.J. Nelmes, and M. Mezouar, *Science*, 2008, **320**, 1054.
69. Y. Ma, M. Eremets, A.R. Oganov, Y. Xie, I. Trojan, S. Medvedev, A.O. Lyakhov, M. Valle, and V. Prakapenka, *Nature*, 2009, **458**, 182.
70. Y.A. Freiman and H.J. Jodl, *Phys. Rep.*, 2004, **401**, 1.
71. L.F. Lundegaard, G. Weck, M.I. McMahon, S. Desgreniers, and P. Loubeyre, *Nature*, 2006, **443**, 201.
72. S. Desgreniers, Y.K. Vohra, and A.L. Ruoff, *J. Phys. Chem.*, 1990, **94**, 1117.
73. K. Shimizu, K. Suhara, M. Ikumo, M.I. Eremets, and K. Amaya, *Nature*, 1998, **393**, 767.
74. E. Boldyreva, *Cryst. Growth Des.*, 2007, **7**, 1662.
75. E. Boldyreva, *Acta Cryst.*, 2008, **A64**, 218.
76. S. Moggach and S. Parsons, *CrystEngComm*, 2010, **12**, 2515.
77. P.T.C. Freire, *Pressure-Induced Phase Transitions in Crystalline Amino Acids. Raman Spectroscopy and X-Ray Diffraction*, in *High-Pressure Crystallography*, E. Boldyreva and P. Dera, Editors, 2010, Springer Netherlands.

78. A. Dawson, D.R. Allan, S.A. Belmonte, S.J. Clark, W.I.F. David, P.A. McGregor, S. Parsons, C.R. Pulham, and L. Sawyer, *Cryst. Growth Des.*, 2005, **5**, 1415.
79. E.V. Boldyreva, H. Ahsbahs, and H.P. Weber, *Z. Kristallogr.*, 2003, **218**, 231.
80. S. Moggach, T. Bennett, and A. Cheetham, *Angew. Chem. Int. Ed.*, 2009, **48**, 7087.
81. A. Gavezzotti, *Z. Kristallogr.*, 2005, **220**, 499.
82. P.A. Wood, R.S. Forgan, D. Henderson, S. Parsons, E. Pidcock, P.A. Tasker, and J.E. Warren, *Acta Cryst.*, 2006, **B62**, 1099.
83. P.A. Wood, D. Francis, W.G. Marshall, S.A. Moggach, S. Parsons, E. Pidcock, and A.L. Rohl, *CrystEngComm*, 2008, **10**, 1154.
84. R.D.L. Johnstone, D. Francis, A.R. Lennie, W.G. Marshall, S.A. Moggach, S. Parsons, E. Pidcock, and J.E. Warren, *CrystEngComm*, 2008, **10**, 1758.
85. R.D.L. Johnstone, M. Ieva, A.R. Lennie, H. McNab, E. Pidcock, J.E. Warren, and S. Parsons, *CrystEngComm*, 2010, **12**, 2520.
86. M. Podsiadlo, K. Dziubek, and A. Katrusiak, *Acta Cryst.*, 2005, **B61**, 595.
87. G.J. Piermarini, A.D. Mighell, C.E. Weir, and S. Block, *Science*, 1969, **165**, 1250.
88. D.R. Allan, S.J. Clark, A. Dawson, P.A. McGregor, and S. Parsons, *Acta Cryst.*, 2002, **B58**, 1018.
89. I.D.H. Oswald, D.R. Allan, G.M. Day, W.D.S. Motherwell, and S. Parsons, *Cryst. Growth Des.*, 2005, **5**, 1055.
90. I.D.H. Oswald, D.R. Allan, W.D.S. Motherwell, and S. Parsons, *Acta Cryst.*, 2005, **B61**, 69.
91. D.R. Allan, W.G. Marshall, D.J. Francis, I.D.H. Oswald, C.R. Pulham, and C. Spanswick, *Dalton Trans.*, 2010, **39**, 3736.
92. F.P.A. Fabbiani, D.R. Allan, A. Dawson, W.I.F. David, P.A. McGregor, I.D.H. Oswald, S. Parsons, and C.R. Pulham, *Chem. Commun.*, 2003, **39**, 3004.
93. F.P.A. Fabbiani, D.R. Allan, W.I.F. David, S.A. Moggach, S. Parsons, and C.R. Pulham, *CrystEngComm*, 2004, **6**, 504.
94. F.P.A. Fabbiani, D.R. Allan, W.G. Marshall, S. Parsons, C.R. Pulham, and R.I. Smith, *J. Cryst. Growth*, 2005, **275**, 185.
95. E. Girard, A.C. Dhaussy, B. Couzinet, J.C. Chervin, M. Mezouar, R. Kahn, I. Ascone, and R. Fourme, *J. Appl. Crystallogr.*, 2007, **40**, 912.
96. R. Fourme, E. Girard, R. Kahn, A.C. Dhaussy, and I. Ascone, *Annu. Rev. Biophys.*, 2009, **38**, 153.
97. E. Girard, R. Fourme, R. Ciurko, J. Joly, F. Bouis, P. Legrand, J. Jacobs, A.C. Dhaussy, J.L. Ferrer, M. Mezouar, and R. Kahn, *J. Appl. Crystallogr.*, 2010, **43**, 762.
98. A. Aertsen, F. Meersman, M.E.G. Hendrickx, R.F. Vogel, and C.W. Michiels, *Trends Biotechnol.*, 2009, **27**, 434.
99. I. Daniel, P. Oger, and R. Winter, *Chem. Soc. Rev.*, 2006, **35**, 858.
100. A.C. Oliveira, A.M.O. Gomes, S.M.B. Lima, R.B. Goncalves, W.D. Schwarcz, A.C.B. Silva, J.R. Cortines, and J.L. Silva, *Effects of Hydrostatic Pressure on Viruses*, in *High-Pressure Microbiology*, C.W. Michiels, D.H. Bartlett, and A. Aertsen, Editors, 2008, ASM Press, Herndon, VA, USA.
101. T. Otake, T. Kawahata, H. Mori, Y. Kojima, and K. Hayakawa, *Appl. Microbiol. Biotechnol.*, 2005, **67**, 746.
102. C. Pribenszky, M. Molnar, A. Horvath, G. Kutvolgyi, A. Harnos, O. Szenci, J. Dengg, and J. Lederer, *Reprod. Fertil. Dev.*, 2007, **19**, 181.
103. G.S. Li, C.K. Bai, J. Duan, C.L. Peng, K.N. Weng, and S.D. Liu, *Chin. J. High Press. Phys.*, 2003, **17**, 122.
104. I. Oey, M. Lille, A. Van Loey, and M. Hendrickx, *Trends Food Sci. Technol.*, 2008, **19**, 320.
105. J. Gimenez, P. Kajda, L. Margomenou, J.R. Piggott, and I. Zabetakis, *J. Sci. Food Agric.*, 2001, **81**, 1228.

106. L.W. Murchie, M. Cruz-Romero, J.P. Kerry, M. Linton, M.F. Patterson, M. Smiddy, and A.L. Kelly, *Innovative Food Sci. Emerg. Technol.*, 2005, **6**, 257.
107. S. Yamamoto, K. Takanohashi, T. Hara, S. Odani, A. Suzuki, and T. Nishiumi, *J. Phys. Conf. Ser.*, 2010, **215**, 012170.
108. H.K. Chan and E. Doelker, *Drug Dev. Ind. Pharm.*, 1985, **11**, 315
109. V.V. Boldyrev, *J. Mater. Sci.*, 2004, **39**, 5117.
110. F.P.A. Fabbiani and C.R. Pulham, *Chem. Soc. Rev.*, 2006, **35**, 932.
111. A. Llinàs and J.M. Goodman, *Drug Discovery Today*, 2008, **13**, 198.
112. M. Haisa, S. Kashino, R. Kawai, and H. Maeda, *Acta Cryst.*, 1976, **B32**, 1283.
113. D.Y. Naumov, M.A. Vasilchenko, and J.A.K. Howard, *Acta Cryst.*, 1998, **C54**, 653.
114. G. Nichols and C.S. Frampton, *J. Pharm. Sci.*, 1998, **87**, 684.
115. M. Haisa, S. Kashino, and H. Maeda, *Acta Cryst.*, 1974, **B30**, 2510.
116. P. Di Martino, P. Conflant, M. Drache, J.P. Huvenne, and A.M. Guyot-Hermann, *J. Therm. Anal. Calorim.*, 1997, **48**, 447.
117. J.C. Burley, M.J. Duer, R.S. Stein, and R.M. Vrcelj, *Eur. J. Pharm. Sci.*, 2007, **31**, 271.
118. M.A. Perrin, M.A. Neumann, H. Elmaleh, and L. Zaske, *Chem. Commun.*, 2009, **45**, 3181.
119. S. Gaisford, A.B.M. Buanz, and N. Jethwa, *J. Pharm. Biomed. Anal.*, 2010, **53**, 366.
120. P. Di Martino, A.M. Guyot-Hermann, P. Conflant, M. Drache, and J.C. Guyot, *Int. J. Pharm.*, 1996, **128**, 1.
121. E. Boldyreva, T. Shakhtshneider, H. Ahsbahs, H. Sowa, and H. Uchtmann, *J. Therm. Anal. Calorim.*, 2002, **68**, 437.
122. M. Lang, A.L. Grzesiak, and A.J. Matzger, *J. Am. Chem. Soc.*, 2002, **124**, 14834.
123. J.S. Capes and R.E. Cameron, *Cryst. Growth. Des.*, 2006, **7**, 108.
124. J.R. Mendez del Rio and R.W. Rousseau, *Cryst. Growth Des.*, 2006, **6**, 1407.
125. J.S. Capes and R.E. Cameron, *CrystEngComm*, 2007, **9**, 84.
126. I.D.H. Oswald, I. Chataigner, S. Elphick, F.P.A. Fabbiani, A.R. Lennie, J. Maddaluno, W.G. Marshall, T.J. Prior, C.R. Pulham, and R.I. Smith, *CrystEngComm*, 2009, **11**, 359.
127. Y.B. Zel'dovich and Y.P. Raiser, *Physics of Schockwave and High Temperature Hydrodynamics Phenomena*, Academic Press, New York, USA, 1966.
128. P. Politzer and J.S. Murray, eds. *Theoretical and Computational Chemistry*, *Vol. 13*:*Energetic Materials, Part 2: Detonation, Combustion*, 2003, Elsevier.
129. R.W. Shaw, T.B. Brill, and D.L. Thompson, eds. *Advanced Series in Physical Chemistry*, *Vol. 16*:*Overviews of Recent Research on Energetic Materials*, 2005, World Scientific Publishing Co., Singapore.
130. S.M. Peiris and G.J. Piermarini, eds. *Shock Wave and High Pressure Phenomena*:*Static Compression of Energetic Materials*, 2008, Springer, Berlin-Heidelberg, Germany.
131. L.E. Fried, M.R. Manaa, and J.P. Lewis, *Modeling the Reactions of Energetic Materials in the Condensed Phase*, in *Overviews of Recent Research on Energetic Materials*, R.W. Shaw, T.B. Brill, and D.L. Thompson, Editors, 2005, World Scientific Publishing Co., Singapore.
132. B.M. Rice, *Applications of Theoretical Chemistry in Assessing Energetic Materials for Performance or Sensitivity*, in *Overviews of Recent Research on Energetic Materials*, R.W. Shaw, T.B. Brill, and D.L. Thompson, Editors, 2005, World Scientific Publishing Co., Singapore.
133. D.D. Dlott, *Annu. Rev. Phys. Chem.*, 1999, **50**, 251.
134. F. Goetz, T.B. Brill, and J.R. Ferraro, *J. Phys. Chem.*, 1978, **82**, 1912.
135. J.C. Gump and S.M. Peiris, *J. Appl. Phys.*, 2005, **97**, 053513.
136. A.J. Davidson, I.D.H. Oswald, D.J. Francis, A.R. Lennie, W.G. Marshall, D.I.A. Millar, C.R. Pulham, J.E. Warren, and A.S. Cumming, *unpublished results,* 2008.

137. T.D. Sewell, R. Menikoff, D. Bedrov, and G.D. Smith, *J. Chem. Phys.*, 2003, **119**, 7417.
138. D.C. Sorescu and B.M. Rice, *J. Phys. Chem. C*, 2010, **114**, 6734.
139. C.S. Yoo and H. Cynn, *J. Chem. Phys.*, 1999, **111**, 10229.
140. D.E. Hooks, D.B. Hayes, D.E. Hare, D.B. Reisman, K.S. Vandersall, J.W. Forbes, and C.A. Hall, *J. Appl. Phys.*, 2006, **99**, 124901.
141. L.Y. Lu, D.Q. Wei, X.R. Chen, G.F. Ji, X.J. Wang, J. Chang, Q.M. Zhang, and Z.Z. Gong, *Mol. Phys.*, 2009, **107**, 2373
142. L.Y. Lu, D.Q. Wei, X.R. Chen, D. Lian, G.F. Ji, Q.M. Zhang, and Z.Z. Gong, *Mol. Phys.*, 2008, **106**, 2569
143. W. Zhu, X. Zhang, T. Wei, and H. Xiao, *Theor. Chem. Acc.*, 2009, **124**, 179.
144. H.L. Cui, G.F. Ji, X.R. Chen, W.H. Zhu, F. Zhao, Y. Wen, and D.Q. Wei, *J. Phys. Chem. A*, 2009, **114**, 1082.
145. H.L. Cui, G.F. Ji, X.R. Chen, Q.M. Zhang, D.Q. Wei, and F. Zhao, *J. Chem. Eng. Data*, 2010, **55**, 3121.
146. J. Evers, T.M. Klapötke, P. Mayer, G. Oehlinger, and J. Welch, *Inorg. Chem.*, 2006, **45**, 4996.
147. M.J. Crawford, J. Evers, M. Göbel, T. Klapötke, P. Mayer, G. Oehlinger, and J. Welch, *Propellants, Explos., Pyrotech.*, 2007, **32**, 478.
148. S.M. Peiris, C.P. Wong, and F.J. Zerilli, *J. Chem. Phys.*, 2004, **120**, 8060.
149. D.I.A. Millar, W.G. Marshall, H.E. Maynard-Casely, C.R. Pulham, and A.S. Cumming, *unpublished results,* 2010.
150. A.J. Davidson, D.R. Allan, I.D.H. Oswald, C.R. Pulham, F.P.A. Fabbiani, D.J. Francis, W.G. Marshall, R.I. Smith, A.S. Cumming, A.R. Lennie, and T.J. Prior, *High-pressure structural studies of energetic ammonium compounds* in *38th International Annual Conference of ICT, Energetic Materials: Characterisation and Performance of Advanced Systems*, 2007, Karlsruhe, Germany.
151. D.M. Adams and S.K. Sharma, *J. Chem. Soc., Faraday Trans. 2*, 1976, **72**, 2069.
152. F.W. Sandstrom, P.A. Persson, and B. Olinger, *AIP Conf. Proc.*, 1994, **309**, 1409.
153. T.B. Brill and F. Goetz, in *Papers in Aeronautics and Astronautics*, T.L. Boggs and B.T. Zinn, Editors, 1978, AIAA, Reston, VA, USA.
154. S.M. Peiris, G.I. Pangilinan, and T.P. Russell, *J. Phys. Chem. A*, 2000, **104**, 11188.
155. T.P. Russell, G.J. Piermarini, S. Block, and P.J. Miller, *J. Phys. Chem.*, 1996, **100**, 3248.
156. D.I.A. Millar, C. Barry, D.J. Francis, A.K. Kleppe, W.G. Marshall, H.E. Maynard-Casely, I.D.H. Oswald, C.R. Pulham, P.A. Szilagyi, and A.S. Cumming, *manuscript in preparation,* 2010.

Chapter 2

Experimental Techniques

2 Experimental Techniques

2.1 Complementarity of High-Pressure Techniques

High-pressure structural science is a particularly strong example of an area that relies upon the complementarity of various techniques to achieve the final aim of the structural characterisation of novel materials. Furthermore, the advances in this field are intertwined with the evolution of complex sample environments for experiments at elevated temperatures and/or pressures, as well as the development of techniques for the collection and analysis of spectroscopic and diffraction data under extreme conditions. In this work, a combination of X-ray diffraction (both single-crystal and powder), neutron powder diffraction and Raman spectroscopy has been used to identify and structurally characterise numerous phases at a range of pressure/temperature conditions. High pressures have been generated using either the Merrill-Bassett diamond-anvil cell (DAC) [1] or the Paris-Edinburgh Cell.[2] This chapter will therefore feature a detailed description of each of these instruments, with a subsequent discussion of the experimental techniques in which they have been employed.

2.2 The Merrill-Bassett Diamond-Anvil Cell

2.2.1 DAC Components

High-pressure X-ray diffraction and Raman spectroscopic studies were performed using a gasketed diamond-anvil cell (DAC). The premise for this device is relatively simple; the sample is placed between two diamond faces (culets) and is subjected to high pressures when a force pushes the opposed anvils together. The DAC utilised in this work was based on developments by Merrill and Bassett in 1974.[1] The small size (~5 cm diameter) and relative ease of use make these cells extremely versatile and perfectly suited for high-pressure X-ray diffraction studies. Prior to the development of DAC technology, high-pressure experiments were limited to using massive Bridgman-type hydraulic or piston-cylinder cells that required specialist laboratories and posed considerable safety hazards in the event of failure.[3] A photograph of the Merrill-Bassett diamond-anvil cell is presented in Figure 2.1, along with a representation of the principles of such a device.

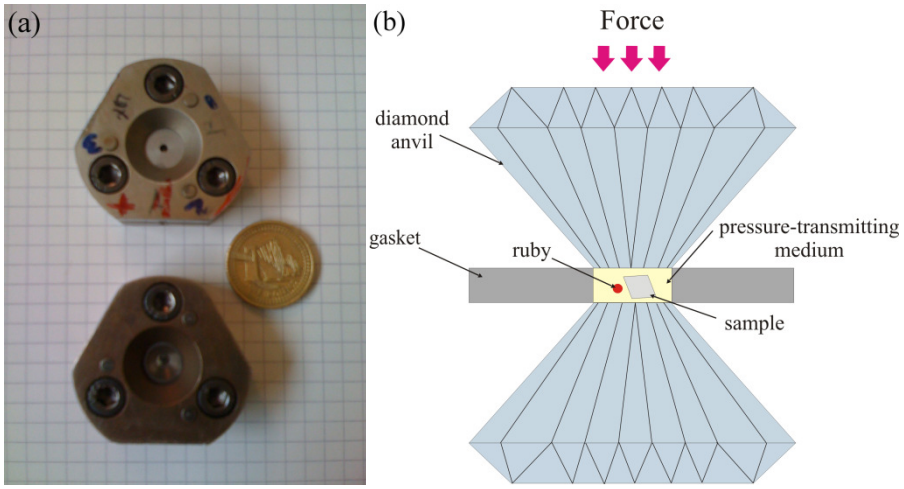

Figure 2.1 (a) photograph of the Merrill-Bassett DAC highlighting its simplicity and size (the top DAC has Be backing plates, while the diamonds are mounted on WC plates in the bottom cell); and, (b) schematic representation of the principles of the diamond-anvil cell.

Although the Merrill-Bassett diamond-anvil cell has garnered widespread recognition in the high-pressure community, the initial inspiration to utilise diamond's compressive strength to generate extreme pressures dates to the late 1940s when Lawson and Tang were able to subject samples to pressures *ca* 2.0 GPa between two halves of a cleaved diamond.[4] A team of scientists at the National Bureau of Standards (Washington, D.C., USA) meanwhile explored a parallel path by modifying Bridgman's opposed-anvil device using two gem-quality diamonds as anvils, instead of steel or tungsten carbide (WC). They were also in the extremely enviable position of being able to acquire bountiful supplies of diamonds as customs officials at the time were willing to entrust other government bodies with confiscated goods, provided that a convincing case for their use was put forward.[5] Thus Van Valkenburg and colleagues were able to construct an opposed-anvil device, in which two gem-quality diamonds were driven together by the turn of a screw, thus facilitating the visual observation of high-pressure phase transitions in a range of materials (such as KNO_3 and AgI).[6]

The ability to see the sample also brought numerous practical boons, primarily the ability to check anvil alignment and the observation of phase transitions and even sample recrystallisations. Indeed the transparency of diamond to large sections of the electromagnetic spectrum allows optical and spectroscopic analysis of the sample *in situ* and makes diamond an ideal anvil material for X-ray diffraction studies. The low atomic number (therefore minimal X-ray absorption) and the high degree of crystal perfection of gem-quality diamonds mean that it is possible to minimise any interference with the sample

diffraction. It is important to note, however, that fluorescence from the significant nitrogen impurity in Type I diamonds make them impractical for spectroscopic studies.

The significant achievement of the Merrill-Bassett DAC was its miniaturisation, allowing it to be mounted on a standard goniometer head.[1] In this cell the diamond anvils are mounted on two backing plates (platens), which are encased in a steel body, as shown in Figure 2.2. A force is then applied to the outer faces of the diamonds by tightening three screws in the steel body, which is then multiplied many times at the small inner faces (culets). The culet size is the predominant factor in determining the maximum pressure that can be achieved. In the current study, culet sizes of either 600 or 400 μm were used to reach maximum pressures of *ca* 10.0 and 25.0 GPa, respectively.

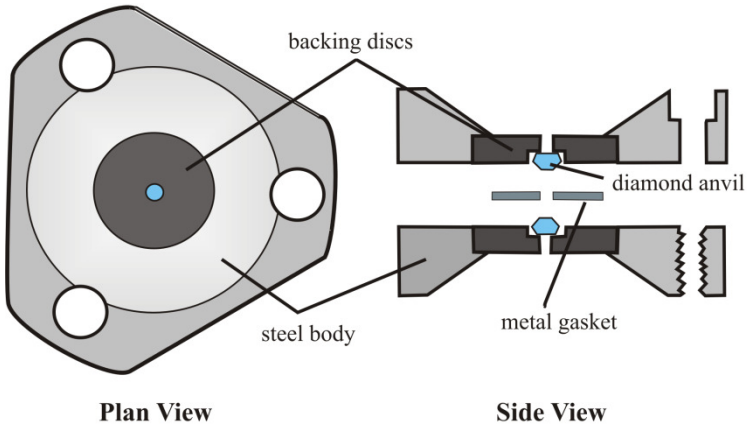

Figure 2.2 Schematic of the Merrill-Bassett diamond-anvil cell.

In their original design Merrill and Bassett exploited the tensile strength of beryllium and its transparency to X-rays for use as the backing-plates, on which to mount the diamond anvils. A major disadvantage of Be backing discs, however, is the presence of powder rings arising from X-ray scattering from the polycrystalline metal, thus contaminating the diffraction image, as shown in Figure 2.3. This is exacerbated when high flux and low divergence synchrotron X-ray beams are necessary since the Be lines become more intense and 'spottier' in appearance.[7] Moreover, the toxicity of beryllium means that great care must be taken when handling these plates.

In response to the shortcomings of Be-backed diamond-anvil cells, the Merrill-Bassett DAC has been modified to incorporate tungsten carbide or steel backing seats, which do not pose a significant safety risk. However, the opacity of these materials to X-rays means that rather than contaminating the sample diffraction pattern, an equally troublesome dilemma presents

itself – the absorption of large sections of the diffracted beam, and thus the severe restriction of the reciprocal space accessible in a high-pressure experiment. In order to overcome this, WC backing plates with wider opening angles have been designed into which a conical Böhler-Almax diamond anvil has been embedded (see Figure 2.3).[8, 9] This construction allows the full opening angle of the steel platens (80°) to be utilised, while still ensuring the anvils are adequately supported for applications at very high pressures (> 20 GPa).[7] In both cases (Be and WC), the backing plates are held within the steel body by small screws that allow alignment of the diamond anvils normal to the thrust axis [10]; parallelism can only be accounted for while mounting the anvils on the backing plates. It is essential to ensure the anvils are fully aligned and parallel – neglecting to do so risks (unnecessarily) diamond failure, especially at elevated pressures.

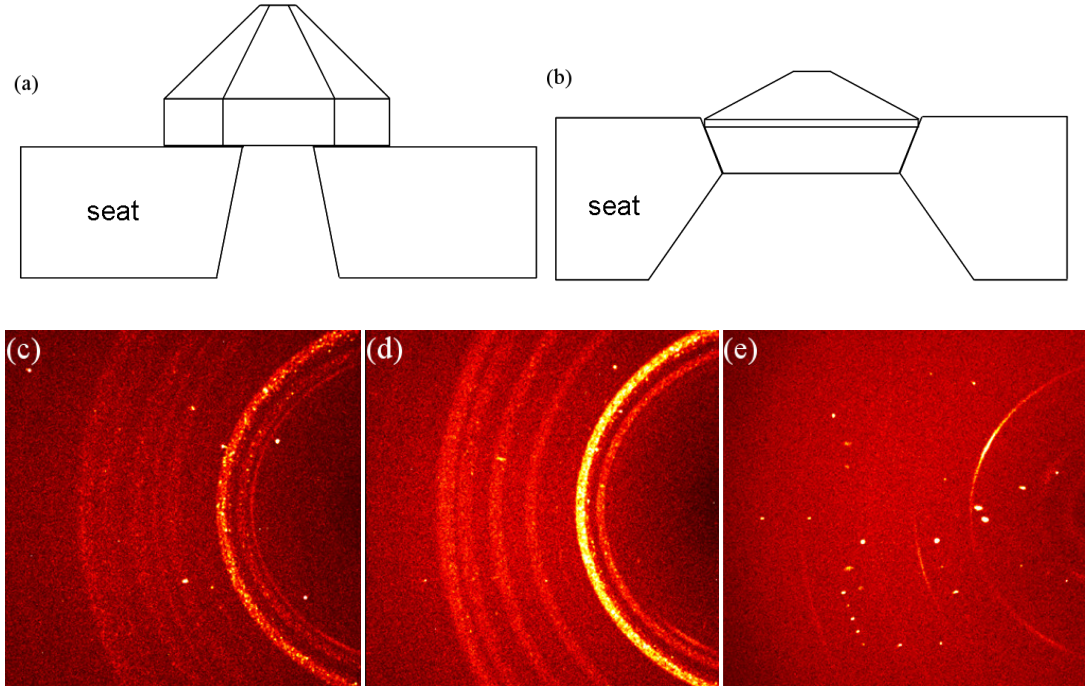

Figure 2.3 Schematic of the different backing plates and the effects each have on the quality of the diffraction data: (a) Be-backed diamond; (b) WC backing plates, with the specially cut diamonds set into the plate; (c) diffraction image collected on a laboratory source using a Be-backed diamond-anvil cell; (d) an analogous image collected using synchrotron radiation; and, (e) diffraction data collected using DAC equipped with WC backing plates. Images kindly provided by Moggach *et al.* [7]

The final constituent of the cell is the metal gasket that is sandwiched between the culets of the diamonds. The pressures attained at the diamond culets are sufficient to cause the gasket to extrude around the anvils, thus sealing the sample chamber while also providing support for the diamonds. A variety of metals, for example Re, steel and inconel (an alloy of Ni, Cr and Fe), may be used, but tungsten has high mechanical strength and thus is often the metal of choice for larger sample volumes. The nature and preparation of the gasket are also of

considerable importance. For pressure to increase, the volume of the sample chamber must decrease; normally the reduction in the thickness of the sample chamber as the anvil advances is sufficient. If the gasket is too thick however, the outwards force from the sample will exceed the friction between the anvils and the gasket and the hole will expand. Thus no pressure will be applied to the sample and there is a risk of damage to the diamonds by gasket failure.

A thin gasket will allow higher pressures to be reached and can give better control at low pressure as less force is required to seal the sample chamber initially.[11] It is therefore preferable to pre-indent the gasket by careful extrusion between the diamond anvils prior to drilling a gasket hole. This approach has the added benefits of imbuing the cell with greater stability due to the massive support from the extruded material and improving the gasket's mechanical stability by hardening. However, pre-indentation must be carried out with perfectly aligned diamonds: diamond failure is more likely to occur during pre-indentation than in the high-pressure experiment itself because the radial extrusion of the gasket material puts maximum tensile stress on the anvil tips.[12] In the majority of the work presented herein a 250 μm thick tungsten gasket was pre-indented to a *thickness* of 100 – 150 μm, which was sufficient to allow compression studies up to ~ 6.0 GPa. The compression of RDX to very high pressures (*ca* 25 GPa) necessitated the utilisation of a 150 μm W gasket that was pre-indented to a *pressure* of 30 GPa, as determined by the ruby fluorescence method (see Section 2.2.2).

It is normally desirable to ensure that the pressure applied is homogeneous and is free of any deviatoric stresses or strains because pressure, *i.e.* isotropic stress, is a thermodynamic parameter.[5] Moreover, there are a number of experimental factors which mean that non-hydrostatic conditions should be avoided wherever possible. For example, inhomogeneous strain in the crystal results in broadening of the diffraction peaks; the stresses and strains may promote or suppress phase transitions; irregularities in the relative compression of the unit cell axes may be observed; and, broadening of the ruby fluorescence R_1 line (Section 2.2.2) increases uncertainty in the pressure measurement.

In order to achieve completely hydrostatic compression, the sample must be immersed in a medium that displays hydrostatic behaviour throughout the pressure regime of interest. Furthermore the medium should not dissolve or react with the sample being studied. A range of different media have therefore been developed, the hydrostatic limits of which have been investigated by various groups.[13-16] The pressure-transmitting medium used in the majority of the studies presented in this work (a 4:1 mixture of methanol:ethanol) has been

shown to remain hydrostatic to ~9.8 GPa by Angel *et al.*, who measured the X-ray diffraction maxima from quartz single crystals in a range of media.[13] In cases where MeOH:EtOH (4:1) was found to dissolve the sample, alternatives such as a 5:1 mixture of iso:n-pentane or Fluorinert FC77, a mixture of perfluorinated hydrocarbons, were employed although these have been shown to have lower hydrostatic limits (7.4 GPa [14] and 1.0 GPa [15], respectively).

2.2.2 Pressure Measurement

Direct pressure measurement from the applied force is both inaccurate and impractical. Instead, Piermarini *et al.* demonstrated that a small chip or sphere of ruby ($Al_2O_3:Cr^{3+}$) could serve as a continuous pressure sensor within the DAC by utilising its laser-induced fluorescence.[17] Indeed the simplicity of the ruby fluorescence method for *in situ* pressure calibration is without question a contributing factor to the widespread application of diamond-anvil cell techniques and, as such, was the subject of an extensive review by Syassen in 2008.[18] The spectral lines of ruby undergo a pronounced red-shift with applied pressure; the R_1 electronic transition shows a linear dependence with pressure up to at least 20 GPa at ambient temperature [17] – this pressure scale will be used throughout the present work. At elevated temperatures, however, the fluorescence signal undergoes significant broadening and it becomes difficult to obtain a reliable measure of sample pressure. In this study, all pressure measurements *via* ruby fluorescence have been made at ambient temperature. Unless stated otherwise, spectra were collected using the 632.8 nm line from a He-Ne laser and dispersed and detected by a Jobin-Yvon LabRam 300 spectrometer, with typical precision of ± 0.05 GPa.

Another factor affecting the ruby fluorescence signal is the hydrostaticity within the sample chamber. Under hydrostatic compression the R_1 and R_2 lines remain well resolved and pressure measurement is straightforward. The R_1-R_2 separation has been shown to be strongly dependent on the presence of any deviatoric stresses within the ruby sample (*i.e.* within the sample chamber). In experiments where non-hydrostatic conditions are being investigated it is therefore common to see these spectral lines overlapping, and the uncertainty in the pressure measurement is significantly increased. A comparison of the ruby fluorescence spectra obtained under hydrostatic and non-hydrostatic conditions can be found in Figure 2.4.

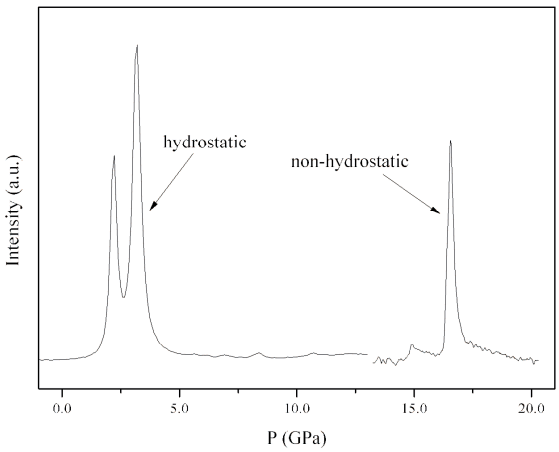

Figure 2.4 Comparison of the hydrostatic and non-hydrostatic ruby fluorescence signals, highlighting the complete reduction of the R_1-R_2 distance under non-hydrostatic conditions. It should be noted that, in this plot, the non-hydrostatic signal has been scaled to have comparable intensity to the hydrostatic signal and so the significant peak broadening observed under non-hydrostatic conditions is not apparent.

2.2.3 Sample loading

The majority of the studies undertaken in this work have been direct compression of either single crystals or polycrystalline powder. In these experiments the sample is initially loaded into the gasket hole along with a small chip or sphere of ruby. Great care must be taken in order to avoid flushing out either the sample or the ruby during the subsequent flooding of the sample chamber with the pressure-transmitting medium. In single-crystal studies it also desirable to ensure that the gasket impinges on neither the sample crystal nor the ruby. This is to avoid additional stresses being applied to either the sample or the ruby upon gasket extrusion, which would result in crystal destruction and/or greater uncertainty in the pressure calibration. Furthermore careful selection of sample crystals is pivotal for the success of a high-pressure diffraction study. Not only should high-quality single crystals be selected, it is essential to ensure that the crystal be small enough to fit inside the gasket – crystals that bridge the separation between the diamond culets will be crushed upon compression. The successful loading of a single crystal is depicted in Figure 2.5.

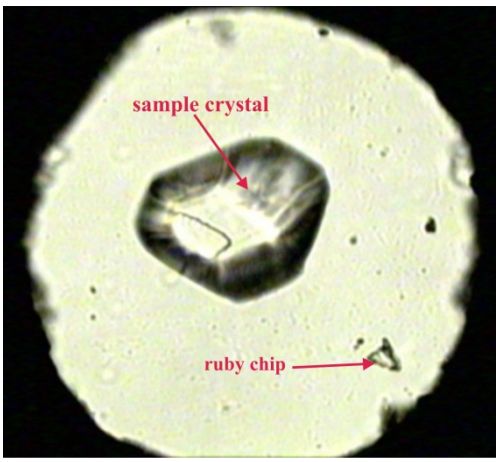

Figure 2.5 Photograph of a single crystal loaded in the DAC with ruby.

2.3 Experimental Techniques using the Diamond-Anvil Cell

2.3.1 X-ray Single-Crystal Diffraction

X-ray single-crystal diffraction is the most definitive method for the determination of atomic positions within a crystalline solid (defined as a three-dimensional array of identical unit cells with long range order and translational symmetry). Diffraction arises from the interference (both constructive and destructive) of scattered photons, which are produced by the elastic scattering of incident electromagnetic radiation by the electron density of atoms within a crystal lattice. The wavelength (or rather range of wavelengths) of X-ray radiation is comparable with interatomic separations, typically of the order of a few Ångstroms. This means that the interference of X-rays scattered by different atomic planes within the lattice will result in the observed diffraction pattern, from which it is possible to determine the relative positions of the atoms within the structure.

The condition for the constructive interference of scattered radiation (wavelength, λ) is satisfied only when the path difference is equal to $n\lambda$, where n is an integer. Bragg demonstrated that the path difference of two scattered X-rays may be expressed in terms of the separation of the lattice planes within the crystal (d) and the angle of incidence (θ).[19] As depicted in Figure 2.6, constructive interference will occur, and thus diffracted beam intensity will be observed, when $n\lambda = 2d\sin\theta$. At other angles of incidence or interplanar distances, the scattered X-rays will be partly or completely out of phase (destructive interference).

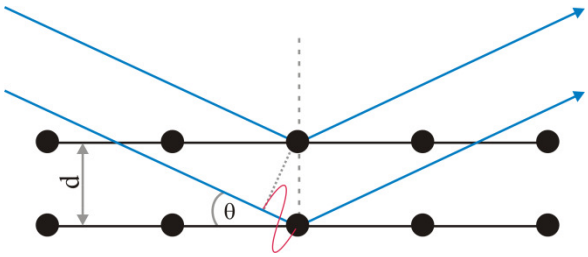

Figure 2.6 The Bragg construction for diffraction by a three-dimensional crystal lattice. In this scheme the incident X-rays (blue) are diffracted by two separate crystal planes (black), separated by a distance, *d*. For constructive interference to occur, the path difference between two diffracted beams should be an integer multiple of their wavelength (red, $n\lambda$). This situation arises only at certain scattering angles (θ); at all other angles the beams will interfere destructively.

A great deal of information (*i.e.* the unit cell indexing and space group) can be extracted directly from an observed diffraction pattern. However, while the observed intensities provide information about the amplitudes of the scattered waves, $|F_o|$, any information about the relative phases (φ) is lost. The so-called 'phase problem' presents a considerable challenge to crystallographers since both the amplitudes and phases of the scattered X-rays are required for an accurate representation of the electron density within the unit cell:

$$\rho(xyz) = \frac{1}{V}\sum_{hkl}|F(hkl)|\exp[i\varphi(hkl)]\exp\left[-2\pi i(hx+ky+lz)\right]$$

In chemical crystallography there are two main techniques for overcoming this phase problem: (i) Patterson methods, and (ii) direct methods. Patterson methods rely on either the presence of a few heavy atoms in the structure (such as in a transition metal complex) or a significant portion of the molecule in question having a well-defined and rigid geometry. In the Patterson synthesis the amplitudes of the scattered waves are replaced by their squares, $|F_o|^2$, and the phases (φ) are omitted, such that:

$$P(uvw) = \frac{1}{V}\sum_{hkl}|F(hkl)|^2\cos\left[2\pi(hu+kv+lw)\right]$$

Peaks in the resultant Patterson maps do not correspond to the electron density but rather the interatomic vectors. As each peak is proportional to the product of the atomic numbers (Z) of the atoms involved, vectors between two heavy atoms are more easily identified. The task then is to deduce the structure directly from knowledge of the distances between the atoms in the unit cell.

In direct methods, no previous knowledge of the structure is employed in structure solution – the phases of the structure factors and therefore the electron density are derived

mathematically from a set of observed X-ray intensities. The method imposes constraints that are valid for the (correct) electron density distribution (such as discrete peaks and non-negative values) to the structure factors. Since the amplitudes $|F_o|$ are known, these constraints restrict the possible phases of the structure factors and, in favourable cases, are sufficient to allow phase determination directly.

In both cases (Patterson and direct methods) the structure may be refined by calculating the residual electron density ($\Delta\rho$) – the difference between the calculated structure factors, F_c, and the observed structure factors, $|F_o|$. Such Fourier syntheses can be used to determine if any electron density has not been accurately modelled by the proposed structure, and therefore represent an effective test of whether a complete model has been reached. Moreover, it may be possible to determine hydrogen positions in high-quality data-sets.

The success of the above methods for structure solution is dependent upon the accurate determination of reflection intensities. However, this can be complicated greatly by peak overlap in X-ray powder diffraction patterns or missing reflection data, which is often the case in high-pressure experiments. In response to the limitations of these reciprocal-space methods, numerous programs such as DASH [20] and FOX [21] have been developed, which aim to generate calculated patterns based on an accurate unit cell indexing and chemical composition. In these direct-space methods, the agreement between the observed and calculated patterns is optimised using a Monte Carlo approach by varying structural parameters (for example, molecular positions and orientations as well as any torsion angles that may be present). The result of this 'simulated annealing' experiment with the lowest goodness-of-fit (χ^2) should therefore correspond to the experimental structure.

Finally, in contrast to the aforementioned methods, the most recent approach to solving the phase problem, the charge flipping algorithm, requires no information on either symmetry or chemical composition and is therefore an extremely powerful tool in structure solution. Although more details may be found in the original manuscript by Oszlányi and Sütó [22], the algorithm may be treated as a subtle adaptation to the simple Fourier cycle between the real-space electron density (ρ) and the reciprocal-space structure factors, F_o. Charge flipping exploits volumes of low electron density in the unit cell by introducing a threshold (δ) into a pixelated electron-density map. Any pixels whose electron density is below this threshold have their signs reversed, such that $\rho(r)$ becomes $-\rho(r)$, where $\rho(r) < \delta$. Temporary structure factors G_c are then calculated based on this modified electron-density map and it is the phases of these temporary structure factors that are subsequently combined with the observed amplitudes F_o to generate the new electron density. This iterative cycle is then

repeated several hundred times to obtain an accurate representation of the experimental electron density.

The particular strengths of this method are its simplicity and its truly *ab initio* character. Since the electron density is represented on a grid, no atomicity is acknowledged during structure solution and therefore no prior knowledge of the chemical composition is required. Furthermore, all structures may be solved in the space group *P*1, requiring no knowledge of the crystal symmetry – this can be determined afterwards. Charge flipping therefore represents an attractive alternative to direct-space and reciprocal-space methods, particularly in problematic cases, such as unknown composition, ambiguous space group assignment and the presence of disorder.

For a full discussion of these methodologies, the reader is invited to consult comprehensive texts on X-ray diffraction, such as those of Massa [23] and Giacovazzo *et al*.[24]

2.3.2 High-Pressure Single-Crystal X-ray Diffraction

Although diamond is transparent to X-ray radiation and every effort is made to minimise X-ray diffraction from the atomic planes within the diamonds themselves, it is inevitable that reflections due to the anvils are observed in the course of a high-pressure data collection. Furthermore depending of the orientation of the sample chamber (*i.e*. the DAC) with respect to the incident beam, one can observe powder diffraction rings due to the W gasket and Be backing discs (where used). This is exemplified in Figure 2.7, which clearly shows that in one diffraction image one can observe sample peaks, diamond reflections and W rings, and in Figure 2.8(a).

Another complexity in high-pressure data collections is imposed by shading from the steel body of the cell. While ambient pressure diffraction studies of a crystal mounted on a fibre allow the whole of reciprocal space to be sampled, this is severely restricted in high-pressure studies. A data-collection strategy to optimise completeness of high-pressure diffraction data on a CCD diffractometer was developed by Dawson *et al*.[25] This strategy has been applied in all of the high-pressure single-crystal X-ray diffraction studies presented here. Despite this optimisation, however, one can easily appreciate the severe restriction of the diffraction data accessible in high-pressure studies by comparison of the observed intensities for a high-pressure study, using the strategy outlined in [25], and an ambient-pressure study of a comparable crystal system, in Figure 2.9. In order to increase completeness further, it may be possible to load two single crystals of the same sample into DAC in different orientations (Figure 2.8(b)), although this adds further intricacy to data processing. Finally, another

popular method to improve completeness of the data is to follow the same data-collection strategy with the DAC in a different orientation, normally by rotation of the triangular cell by 120°.

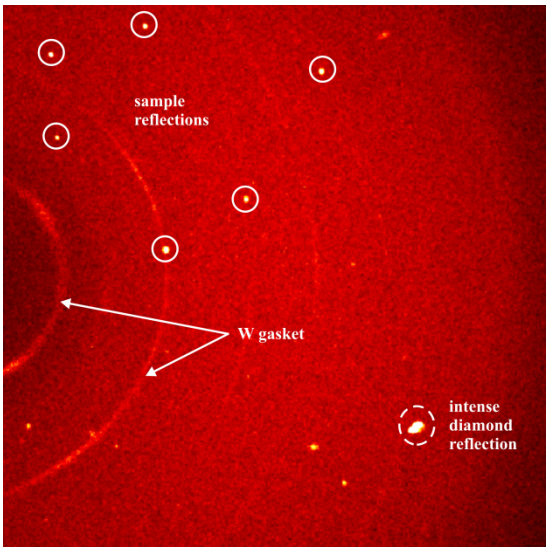

Figure 2.7 Diffraction image collected for an orthorhombic crystal ($Pca2_1$) at 5.5 GPa, showing the juxtaposition of sample reflections, tungsten powder rings and intense diamond reflections.

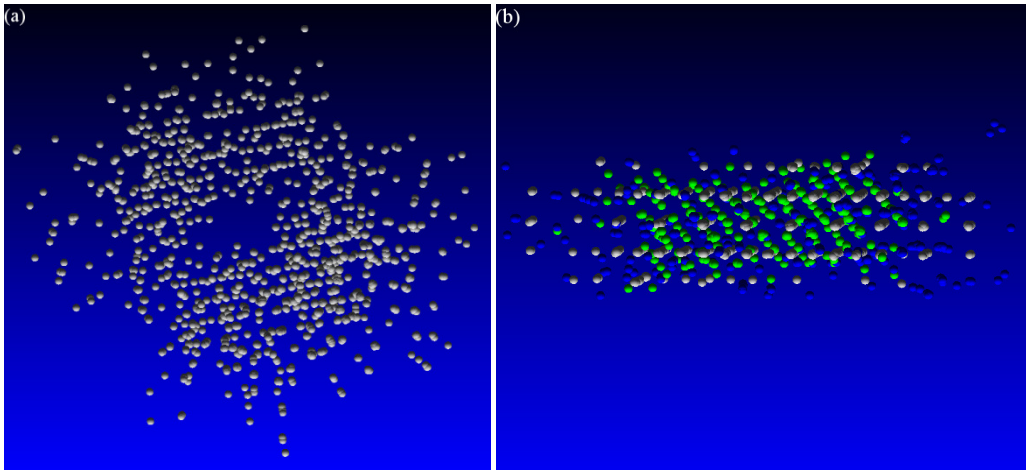

Figure 2.8 Three dimensional renderings of reciprocal lattices, created in RLATT (BrukerNonius) [26]: (a) all of the observed diffraction intensities – indexing of the sample is hampered by scattering from all the other cell components; (b) by judicious selection of the observed reflections, it is possible to separate diffraction from sample crystals (grey and green) from intensities arising from the diamond anvils, ruby and gasket (blue).

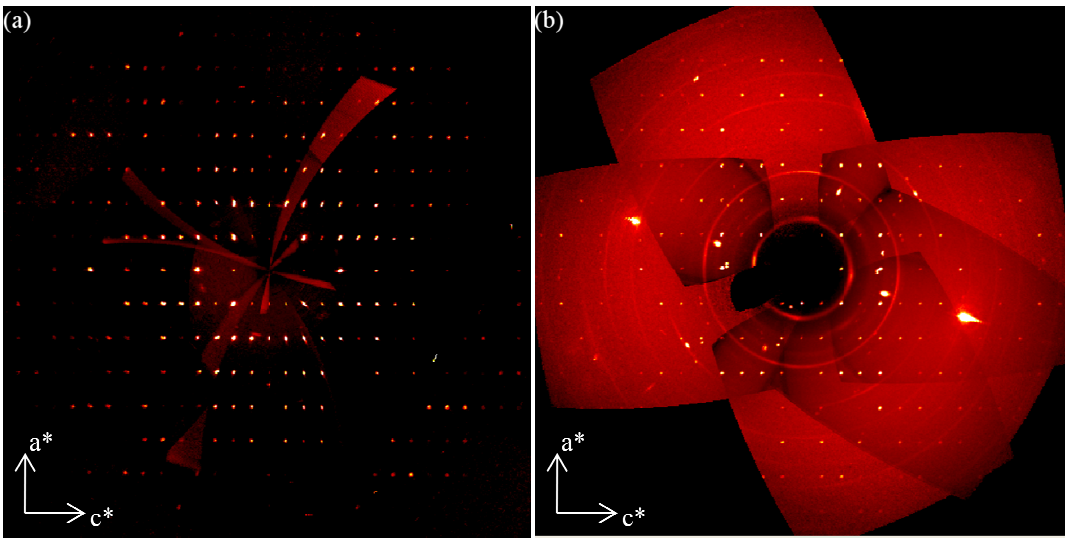

Figure 2.9 Comparison of the completeness of high-pressure data-sets with that of ambient pressure data collections: (a) calculated precession image of the *h*0*l* zone calculated for an ambient pressure data collection for a crystal on a fibre (space group $Pca2_1$); (b) the same image calculated for a high-pressure data-set on an analogous crystal system ($Pca2_1$ at ca 5.0 GPa). Precession images were calculated in the APEX-II program.[26]

In a similar way to the development of data-collection strategies, methods for harvesting the diffraction intensities from CCD images have had to be optimised. Sample reflections were harvested using a threshold algorithm applied within the APEX-II program; orientation matrices and indexing of unit cells were determined using the same program.[26] In order to address the shading of large sections of the detector during data collection, it was necessary to apply a set of dynamic masks (written by Dawson *et al.* [25]) during integration. Integration and global-cell refinement were carried out in SAINT.[27] The avoidance of harvesting data overlapped with reflections from the diamond anvils has also been shown to improve data quality.[28] Other strategies to enhance data-quality include the application of an analytical absorption correction in SHADE [29] (that rejects reflections that lie within 2° of the DAC opening angle (40°) and have poorly-resolved peak profiles); and a multi-scan absorption correction in SADABS [30], which corrects for differences in the X-ray path length arising from the different orientations of the crystal during data-collection. Finally data were merged in SORTAV in the WinGX suite of programs.[31]

In this work, structure solution from single-crystal X-ray diffraction data was carried out using either reciprocal-space methods (Sir92 [32]) or direct-space methods (FOX [21]). Once determined, structures were refined using CRYSTALS.[33] The details for each structure solution and refinement will be expanded upon in the relevant sections. It should be noted, however, that in some cases it was not possible to solve the crystal structure on the basis of the single-crystal data alone due to the low completeness of the high-pressure data-

sets. In such cases complementary data provided from X-ray powder diffraction and neutron powder diffraction proved invaluable.

2.3.3 X-ray Powder Diffraction

X-ray powder diffraction may simply be considered an extension of the single-crystal regime discussed in Section 2.3.1, but rather than one crystal being examined, powder samples contain many crystallites oriented at random. This situation results in concentric cones of diffracted intensity emanating from the sample position. These would then appear as a series of concentric rings on an area detector (such as a Mar345 Image Plate) placed normal to the X-ray beam. The development of powder diffraction rings from single-crystal diffraction spots is represented in Figure 2.10. The diffraction images may then be integrated (using calibration values individual to each instrument, such as wavelength and sample-to-detector distance) to produce a 1-dimensional plot of intensity against diffraction angle (2θ).

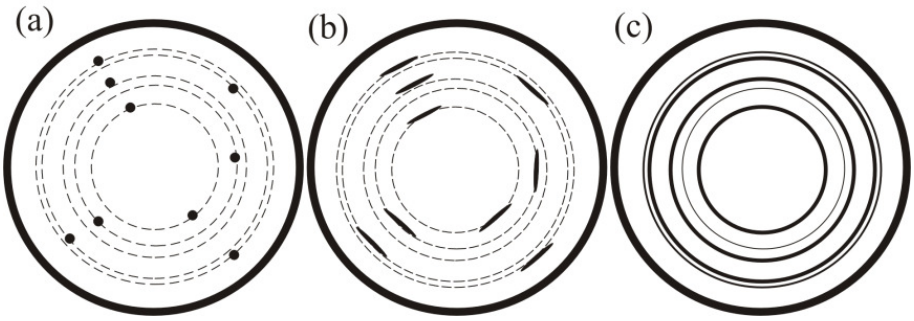

Figure 2.10 Schematic representing the development of a powder diffraction pattern, arising from the spatial averaging of numerous single crystals: (a) diffraction from a single crystal resulting in discrete spots on the image plate detector; (b) poor-quality single-crystal diffraction pattern, in which the diffracted intensities are smeared out along the Debye-Scherrer rings; and (c) 'ideal' powder pattern, in which the rings are well-resolved and each is of uniform intensity.[34]

In addition to image plate detectors, ambient-pressure X-ray powder diffraction data in this work were collected using position-sensitive devices (PSD) which measure diffracted intensity at variable angle, thus negating the need for integrating the diffraction image. Diffraction may also be carried out in either of two modes: transmission or reflection. In powder samples of sufficient volume to allow complete powder-averaging, the diffraction patterns observed in these modes should be identical. Reflection mode is often preferred for samples containing heavy atoms as this minimises the effect of X-ray absorption. This may be accounted for by the inclusion of an absorption parameter during refinement or by using thin sample capillaries. One should therefore not be discouraged from attempting to conduct a diffraction study on these materials in transmission mode.

Irrespective of the collection procedure, X-ray powder diffraction presents a quick yet definitive representation of the scattering arising from the atomic planes within the sample of interest. It is therefore an invaluable tool for assessing sample purity and for the detection of polymorphism, without the need for the sometimes arduous task of growing single crystals. Furthermore, as long as the correct structural model is used it is possible to carry out full-profile refinements of the powder diffraction patterns, thus providing important crystallographic information on the bulk sample rather than a solitary crystal. Most commonly this refinement is carried out using the Rietveld method, which facilitates the refinement of the structural model against the diffraction data directly.[35]

A powder diffraction pattern may be described as a plot of diffraction intensity (I_{obs}) against scattering angle (2θ). The Rietveld method progresses by a least-squares refinement of the structural parameters so as to minimise the difference between the calculated and observed intensities (I_{obs} vs I_{calc}). These structural parameters comprise: the structural model, a model to describe the variation in peak-widths over the observed 2θ-range, and a background model. The quality of the diffraction fit is usually quantified by two parameters: wR_p and χ^2. The weighted R-factor (wR_p) represents the minimisation of the difference between the calculated and observed patterns, while χ^2 is a comparison of wR_p to the statistically expected value R_{exp}. Throughout the course of a powder refinement, however, these values may yield erroneously low values, especially with data suffering from a high background or broadened diffraction peaks. It is often the case that visual inspection of the diffraction profile and difference curve is the best assessment for the quality of the refinement.

A secondary refinement method that does not necessitate prior knowledge of the structural model is Le Bail refinement.[36] In this method the calculated diffraction intensities (I_{calc}) are set to be equal to the observed intensities (I_{obs}), while the unit cell, background and peak profiles may be refined. Any peaks which cannot by modelled by a given Le Bail refinement routine are clear evidence that either the unit cell indexing or space group assignment (or both) is wrong. This therefore provides an extremely useful test, particularly in the initial forays into structure solution from powder diffraction. In this work, Rietveld and Le Bail refinements of the various powder diffraction patterns were carried out using GSAS.[37] Any special considerations during refinement will be highlighted in the appropriate chapters.

2.3.4 High-Pressure X-ray Powder Diffraction

Compared to high-pressure single-crystal X-ray diffraction, powder diffraction using the diamond-anvil cell does not present quite such a practical or theoretical obstacle, although for reasons discussed below (Section 2.3.5) these experiments have been carried out using

synchrotron radiation. The data presented herein were collected at the Extreme Conditions Beamline (I15) and the High-Resolution Powder Diffraction Beamline (I11) at Diamond Light Source, UK. The experimental set-up for a high-pressure X-ray powder diffraction experiment is represented in Figure 2.11. Data are collected on an image plate detector (Mar345) and are processed according to the procedure outlined for ambient pressure powder diffraction, with one exception. In some cases it may be necessary to mask out intense single-crystal reflections arising from the diamond anvils to ensure no anomalies occur in the I_{obs} vs 2θ profile. The image can then be integrated to provide the one-dimensional powder diffraction pattern using programs such as Fit2D.[38] It is also possible to mask intense powder diffraction rings due to the W gasket although should this interfere with sample peaks it is also possible to carry out Rietveld refinements, in which the tungsten diffraction pattern is incorporated. This process is represented in Figure 2.11(b) – (d).

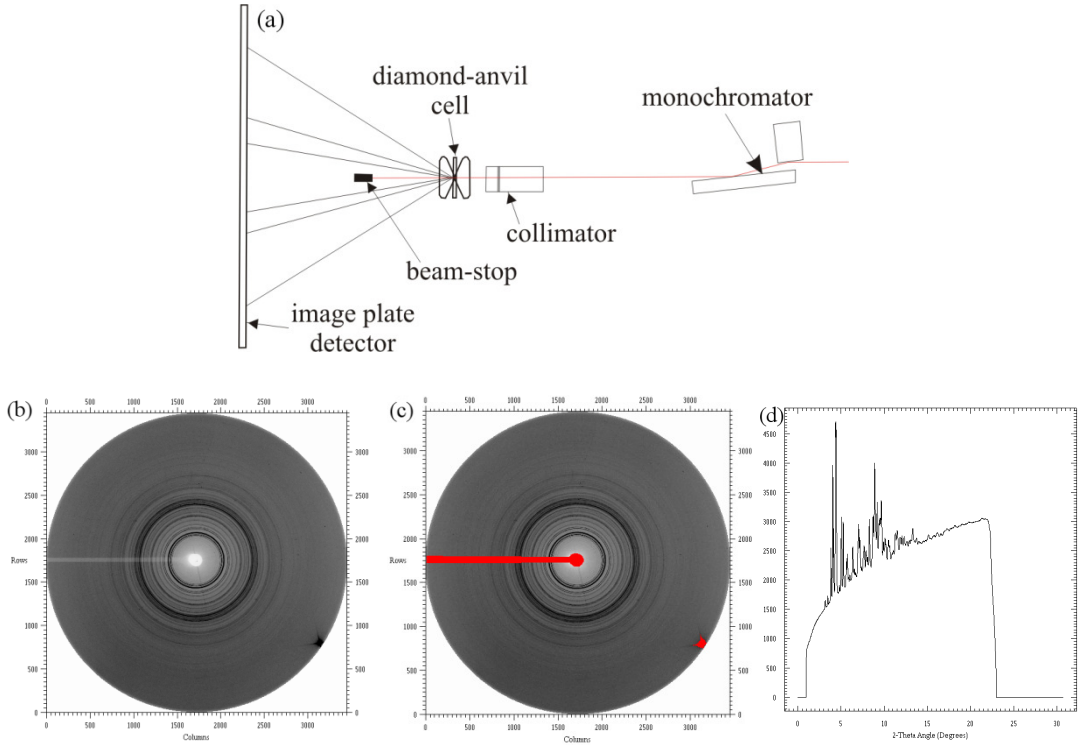

Figure 2.11 (a) schematic illustrating the key components of a high-pressure X-ray powder diffraction experiment; and (b) – (d) the stages of data reduction. The raw image collected on the Mar345 detector is shown in (b). The concentric rings correspond to the diffracted intensities from the sample; the dark spot at the edge of the image is an intense diamond reflection from the DAC. This can be masked to avoid contamination of the sample diffraction pattern - the masking process is shown in (c). It is also necessary to mask the lighter areas of the image that arise due to shading from the beam-stop. Finally the data can be integrated, in programs such as Fit2D [38], thus reducing it to a plot of diffraction intensity against scattering angle (d). The large background common to such data collections is due to Compton (inelastic) scattering from the diamonds and can be subtracted prior to data refinement.

2.3.5 X-ray Sources: Laboratory vs Synchrotron

The ambient pressure X-ray diffraction experiments detailed in this work (both single-crystal and powder) were performed using monochromatic laboratory X-ray sources at the School of Chemistry, University of Edinburgh: both Mo Kα and Cu $K\alpha_1$ radiation sources have been utilised (λ = 0.71073 and 1.54056 Å, respectively). High-pressure single-crystal data were collected at ambient temperature using Mo Kα radiation on a modified Bruker SMART APEX-II CCD diffractometer at the Centre for Science at Extreme Conditions (CSEC), University of Edinburgh. In order to allow rotation of the DAC during data collections, a shortened collimator must be used in high-pressure experiments and there was no facility to carry out these studies at sub-ambient temperatures. Details of the data collection procedures will be reserved for discussion in the relevant chapters.

In some cases, however, the restrictions applied to data completeness by the diamond-anvil cell means that it is has been necessary to use X-ray radiation of shorter wavelengths (*i.e.* $\lambda \leq$ 0.5 Å) at synchrotron sources. This improves data completeness relative to laboratory experiments by compressing the characteristic diffraction pattern into a smaller volume of reciprocal space, thus allowing a larger portion to be accessed through the 40° opening angle. Synchrotron radiation has the added benefit of increasing the incident flux that counteracts the weak diffraction from organic samples with restricted volumes and in complex sample environments, *i.e.* the DAC, in which absorption from the diamonds and backing plates reduces the intensity of measured reflections.[37] The results of high-pressure single-crystal diffraction studies conducted at synchrotron sources are not within the scope of this thesis, but the productivity of beamlines with high-pressure capabilities (such as Station 9.8 at the Daresbury Laboratory [40], Beamline I19 at Diamond Light Source [41] and ID09 and ID27 at the European Synchrotron Radiation Facility [42]) is a strong indication of the thriving research in this field.

In the current work synchrotron radiation has been essential in obtaining high-resolution powder diffraction data using the diamond-anvil cell, which is impossible using typical laboratory diffractometers. As outlined above, the short wavelengths and high flux of the synchrotron beam improve data quality significantly. Moreover it is relatively straightforward to change parameters such as the sample-to-detector distance to suit the requirements of the experiment at hand. A further experimental parameter that may be changed (although not so easily) is the wavelength selected for the experiment, thus allowing the optimisation of the data-collection strategy. Finally an important factor in diffraction studies at very high pressures (> 10 GPa) is the high degree of collimation possible, allowing

the analysis of very small sample diameters without contamination from the DAC components. In such studies, however, great care must be taken to ensure effective powder averaging of such a small sample volume.

2.3.6 Raman Spectroscopy

Scattering of light by a molecule occurs by the promotion of the molecule from its ground state to a virtual energy state and the subsequent relaxation, which results in emission of a photon (i.e. the scattered light). The vast majority of the scattered light is of the same frequency as the incident radiation (elastic; Rayleigh scattering). Raman spectroscopy, however, relies on inelastic scattering of intense monochromatic light (< 5% of cases). In such cases the molecule relaxes to a different vibrational ground state, resulting in an energy difference between the incident and scattered photons. This is perhaps best explained pictorially. In Figure 2.12 it can be seen that if the molecule relaxes to a vibrational state of lower energy than the starting level, the scattered photon will have a higher energy than the incident radiation (anti-Stokes radiation); if the $E_{virtual}$-E_{final} difference is less than the initial transition, the scattered photon will instead undergo a red-shift (Stokes).

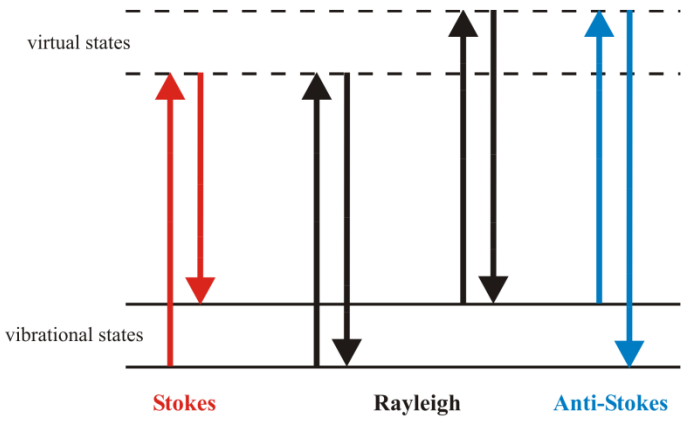

Figure 2.12 A representation of the transitions involved in Raman spectroscopy. Incident photons excite the molecule into a virtual state and the relaxation of the molecule results in emission of a 'scattered' photon. Rayleigh scattering occurs when the incident and emitted photons are of the same frequency. When the molecule relaxes to a vibrational energy level higher than the starting level, the emitted photon will be shifted to a lower frequency (Stokes). Conversely, anti-Stokes radiation has higher frequency than the incident radiation.

Generally Raman spectra are plotted such that the Rayleigh band lies at 0 cm^{-1}. On this scale, the band positions will lie at frequencies that correspond to the energy levels of different functional group vibrations, facilitating comparison with similar (but complementary) results from IR spectroscopy. The selection rule that must be satisfied for a vibrational mode to be Raman active is that there must be change in the polarisability tensor of the vibration. This is best imagined as the ease with which the electron cloud is distorted (*i.e.* polarised) and

explains the complementarity between Raman and IR spectroscopy, which relies on changes in dipole moments.

An advantage of Raman spectroscopy, particularly in high-pressure studies, is that since monochromatic light is used, any material that is transparent to visible light may be used as a sample chamber (*e.g.* glass capillaries and diamond-anvil cells). Furthermore Raman spectroscopy is sensitive to changes in the molecular symmetry and changes in the inter- and intramolecular interactions and is therefore an extremely powerful tool in the identification and characterisation of new polymorphs and the observation of phase transitions. Although not conducted in this study, it may also be appropriate to plot the general increase in frequency of a selected vibrational mode with increasing pressure. If the sample remains in the same phase, a linear shift in wavenumber is generally observed but in the event of a new spectral bands may be observed and there may be an abrupt change in the gradient of $\bar{\nu}$ *versus P* plots.

Raman spectra were collected using a LabRam instrument equipped with a 50 mW He-Ne laser (λ = 632.8 nm); typically, objectives of 10x and 20x magnifications were used.

2.4 The Paris-Edinburgh Cell

2.4.1 Construction of the Paris-Edinburgh Cell

Neutron diffraction experiments (see Section 2.5.1) require sample volumes *ca* 10^6 times larger than those required for X-ray powder diffraction, thus precluding the use of diamond-anvil cells. High-pressure neutron diffraction experiments were therefore severely limited until the advent of the Paris-Edinburgh cell (PEC), developed in 1992, which extended the pressure range to 10 – 20 GPa.[2] The popularity of the PEC arose from its (relatively) light-weight design and its portability – the Paris-Edinburgh cell weighs ~ 50 kg, in contrast to other commercial devices of the time with comparable sample volume that weighed close to 1 tonne. This portability, coupled with the fact that load can be applied to the cell by a hydraulic ram while it remains *in situ* on the beamline, greatly simplified high-pressure experiments.

The PEC is also an opposed-anvil device, like the diamond-anvil cell and the Bridgman cell. In this construction, however, the sample is compressed between anvils made of either tungsten carbide (WC) or sintered diamond, see Figure 2.13(a). Early designs utilised null-scattering TiZr toroidal gaskets located into corresponding grooves machined into the anvil faces to confine the sample and, generally, a solid pressure-transmitting medium.

Compression studies using the preferred fluid pressure-transmitting media (methanol:ethanol and iso:n-pentane) were limited to *ca* 2.0 GPa before anvil failure. It was realised that complete encapsulation of the sample and pressure-transmitting medium in two flanged hemispherical caps (TiZr) would prevent the fluid media coming into direct contact with the anvil surface.[43] In this way the anvils were shown to be protected and the available pressure range for hydrostatic studies were extended up to the freezing pressure of methanol:ethanol (*i.e.* > 9.0 GPa). The encapsulated gasket is compared to the 'standard' TiZr toroidal gasket in Figure 2.13(b).

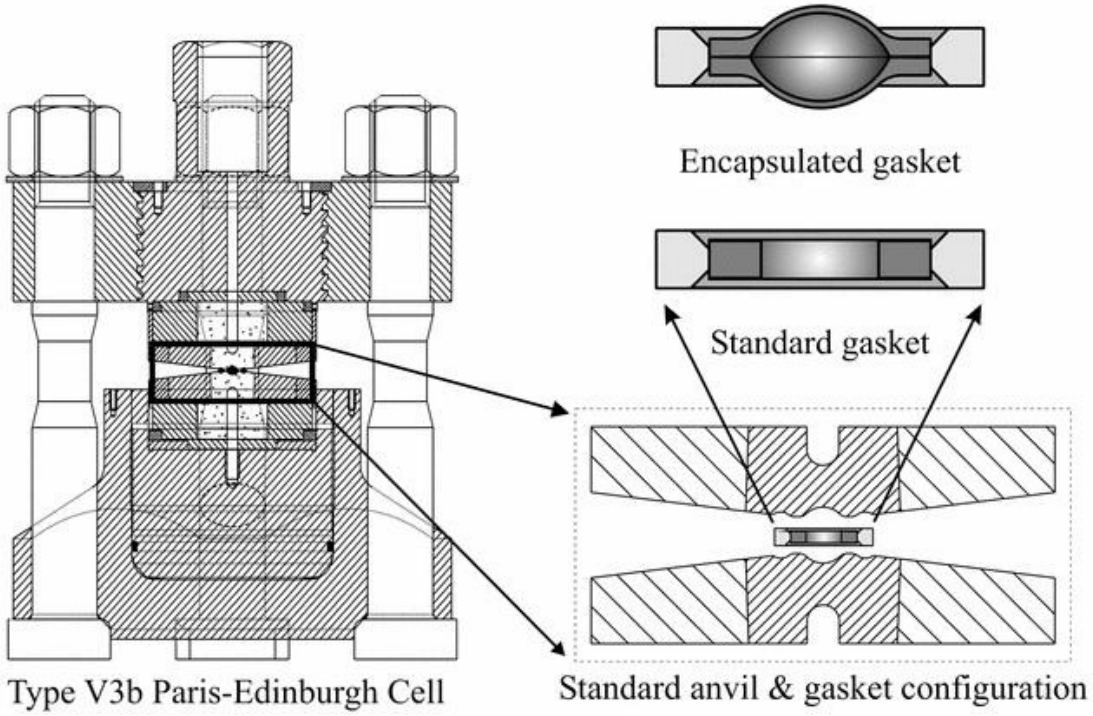

Figure 2.13 (a) Cross-section of the Paris-Edinburgh cell (V3b) and a comparison of the standard and encapsulated gaskets.[43]

2.4.2 Variable-Temperature Insert for the Paris-Edinburgh Cell

The capabilities of the Paris-Edinburgh cell have recently been enhanced by the development of a variable-temperature (v-T) insert, which has been shown to vary sample temperature between 110 and 500 K with excellent control.[44] A liquid nitrogen circuit is used to cool just the sample and the WC anvils, while temperature is increased and controlled by the incorporation of 240 W resistive heaters into the latter, see Figure 2.14. This was in an effort to reduce the volume that is heated or cooled, in order to minimise temperature response times. Cooling to 120 K from room temperature previously required 4 – 5 hours, when the whole of the PE-cell had to be cooled with liquid nitrogen. Commissioning tests on the v-T insert demonstrated its ability to cool to 100 K or warm to 473 K from ambient temperature

within 45 minutes.[44] This development has therefore not only opened up the possibility of conducting variable temperature neutron powder diffraction experiments at pressure but also presents a route for rapidly quenching high-pressure or high-pressure/high-temperature polymorphs for their recovery to ambient pressure.

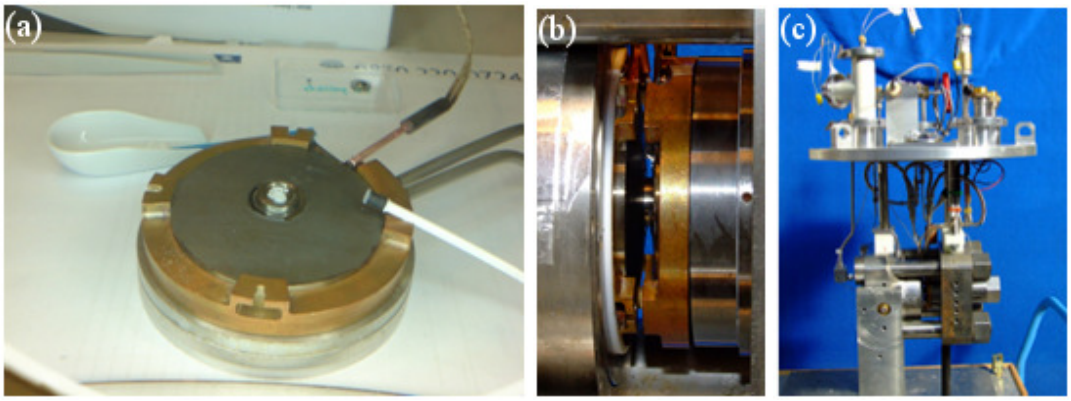

Figure 2.14 The variable-temperature insert for the Paris-Edinburgh cell: (a) the WC anvils, into which both a liquid nitrogen feed and resistive wires have been incorporated to allow rapid heating and cooling; (b) a close-up of the modified anvil within the cell; and, (c) the complete construction of a PE-cell equipped with the vT-insert, underscoring the complexity of such experiments.

2.4.3 Pressure Measurement

Unlike the diamond-anvil cell, the Paris-Edinburgh cell does not allow optical access to the sample chamber and therefore a method for pressure calibration other than the ruby fluorescence method had to be developed. Instead small quantities of internal pressure calibrants are used, typically either NaCl(s) or Pb(s). Both materials have clearly defined equations of state [45, 46], which means that the unit cell volume of the chosen calibrant (as determined by Rietveld refinement of the powder diffraction patterns) is directly related to the pressure within the gasket.

2.5 Experimental Techniques using the Paris-Edinburgh Cell

2.5.1 Neutron Powder Diffraction

While X-ray diffraction if the most widespread technique applied in the determination of crystal structures, a complementary technique using exactly the same principles is neutron diffraction. Neutrons display wave-particle duality and may therefore also be diffracted by a three-dimensional grating. The momentum of a free particle, p, is related to its wavelength, λ, by the de Broglie equation:

$$\lambda = \frac{h}{p} = \frac{h}{mv}$$

where h is Planck's constant, m = mass and v = velocity of the particle. Thus thermal neutrons with average velocities of *ca* 2500 ms^{-1} will have suitable wavelengths for diffraction from atomic planes within a crystal lattice.

In contrast to X-rays, neutrons do not interact significantly with the electron density within a crystal lattice and instead are diffracted by the nuclei of atoms. Since both nuclei and neutrons are small, significant scattering occurs only when a neutron passes close to a nucleus, and thus the total intensity of diffraction of neutrons by a crystal is low compared to that of X-rays – larger sample volumes are required to give comparable diffraction intensities. The point scattering from nuclei imbues this technique with a significant advantage however; the scattering factor does not fall off at higher angles, in stark contrast to X-ray diffraction (see Figure 2.15). This highly penetrating nature of neutrons (in contrast to X-rays) also allows the construction of rather complex sample environments, such as the Paris-Edinburgh cell. Furthermore neutron diffraction locates the atomic nuclei and not the electron density, which may be distorted due to bonding effects, and thus is far more accurate for the determination of atomic positions.

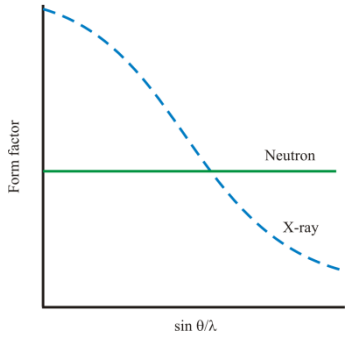

Figure 2.15 Scattering factor of X-rays and neutrons w.r.t. angle of incident.

While the scattering power of an atom with respect to X-ray radiation is directly proportional to its atomic number (Z), there is no direct relationship in neutron diffraction. Indeed neighbouring elements, and even isotopes of the same element, may have considerably different neutron scattering cross-sections – represented in Figure 2.16. This random variation has practical benefits since it is possible to select elements or alloys which display null or very little neutron scattering to construct sample environments. Vanadium (neutron scattering-length, b = -0.4) is regularly used as a sample container for ambient pressure studies; TiZr (null scatterer) is used for sample encapsulation in the Paris-Edinburgh cell. This dramatic effect also means that neutron diffraction is an extremely powerful technique for the structure solution of compounds containing a mixture of light and heavy elements, such as the inorganic azides AgN_3 and $Pb(N_3)_2$ reported in Chapters 5 and 6.

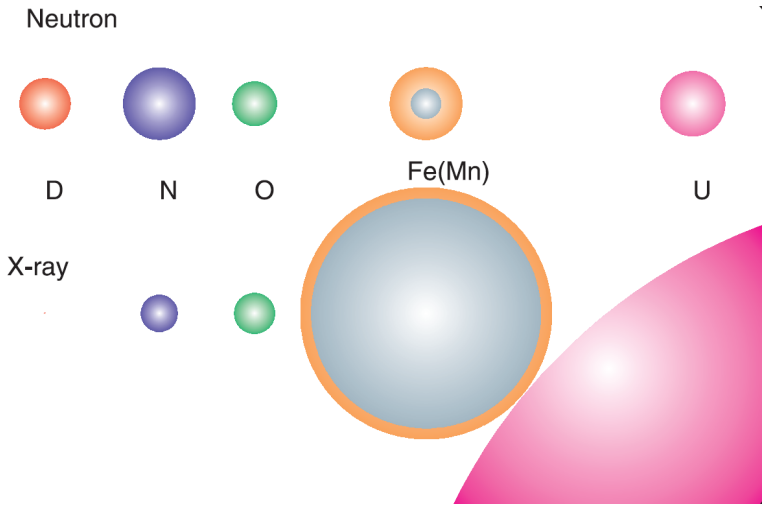

Figure 2.16 Comparison of the scattering powers of different elements with respect to neutrons and X-rays.[34]

The complementarity of X-ray and neutron diffraction is further underlined by studies aimed at the accurate determination of hydrogen positions in a range of molecular and co-ordination solids.[47] X-ray diffraction from hydrogen atoms, having just one electron, is extremely weak. This is not the case, however, in neutron diffraction, although the incoherent scattering from hydrogen normally necessitates sample deuteration.

Finally a significant advantage neutron diffraction displays over X-ray diffraction, although not explored in the present context, is the determination of magnetic structures by the interaction of the magnetic moments of the neutrons with magnetic ions within the crystal lattice. For a detailed account of neutron diffraction of magnetic materials, the reader is directed to Harrison's review.[48]

2.5.2 Neutron Sources

The nature of neutron diffraction experiments is dependent on the source of neutrons. They may be generated by fission (at nuclear reactor sources) or spallation, where short pulses of energetic protons bombard a heavy metal target causing a cascade of high-energy neutrons. At reactor sources the neutron beam is continuous and the wavelength is fixed by means of a crystal monochromator – during the diffraction experiment the detector angle is varied (angle dispersive). In contrast, at spallation sources the energetic neutrons produced must be slowed down (moderated) by collisions with atoms of comparable mass, usually H or D in water or methane, resulting in a distribution of energies impinging on the sample. The pulse of moderated neutrons is very short but stretches out in space as it moves down the flight path, with the higher energy neutrons travelling more quickly. The neutrons travel a known distance, *L*, from the source to the sample and subsequently the detector, which is positioned

at a fixed angle. The diffraction pattern is then obtained as a function of the time of flight (ToF) of the arriving neutrons (energy dispersive). Substituting the de Broglie wavelength into Bragg's law then allows the diffraction condition to be expressed in terms of ToF:

$$2d \sin \theta = \lambda = \frac{h}{p} = \frac{h}{m_n v} = \frac{ht}{m_n L}$$

$$t = \frac{2m_n L}{h} d \sin \theta$$

where t is time, m_n is the mass of the neutron, L is the length of the flight path from source to detector, h is Planck's constant, d is the spacing between the atomic planes in the crystal (d-spacing), θ is the scattering angle (fixed) and p is momentum.

It is therefore possible to collect a complete diffraction pattern using a single detector although typical ToF diffractometers utilise banks of detectors to minimise counting times. Outputs from each detector may be summed, provided each diffraction pattern is initially converted into d-spacings.

The high-pressure neutron diffraction experiments conducted in this body of work were carried out at ISIS spallation neutron and muon source, STFC Rutherford Appleton Laboratory, UK. The high-flux, medium-resolution instrument PEARL-HiPr is specifically designed for data collections using the Paris-Edinburgh cell, as shown in Figure 2.17. ToF diffraction data were collected in transverse geometry. This arrangement, in which the detectors are fixed at $83° < 2\theta < 97°$, allows access to a range of 0.5 – 4.1 Å in d-spacing, with a resolution ($\Delta d/d$) of ~ 0.8%. The individual detector element spectra are electronically summed and normalised to the incident beam monitor and the scattering from a standard vanadium calibration sample. Lastly, the diffraction pattern intensity scale was corrected for the wavelength and scattering-angle dependence of the neutron attenuation by the anvil (WC) and gasket (TiZr) materials. Full-profile Rietveld refinements were carried out using GSAS [37], while any special considerations are highlighted in the pertinent sections.

Figure 2.17 PEARL-HiPr instrument with the Paris-Edinburgh cell, in which the Paris-Edinburgh cell is mounted onto a Tomkinson flange and lowered into a vacuum tank.[49] The red arrow indicates the path of the neutrons through the instrument. Diffracted intensities can be collected by two banks of detectors; transverse geometry was used in this study. Longitudinal mode (detectors situated at $20° < 2\theta < 40°$ and $100° < 2\theta < 120°$) can also be employed to access a wider section of reciprocal space, although resolution is compromised.

2.6 Equations of State

By the structural characterisation of a material throughout its compression, it is possible to obtain a measurement of the variation of the material's density (or volume) with pressure, and sometimes temperature. Generally, static compression studies are conducted at constant temperature, thus the resulting variation of volume with pressure is termed the isothermal 'Equation of State' (EoS). Measured equations of state are usually parameterised in terms of the bulk modulus, $B_0 = -V\partial P/\partial V$, and its pressure derivatives: $B' = \partial B/\partial P$ and $B'' = \partial^2 B/\partial P^2$, which are evaluated at zero pressure. Despite actually being under finite pressure, it is generally accepted that the unit cell volume under ambient conditions may be employed as an approximation to V_0, the zero-pressure volume (which is not measurable).

There is no fundamental thermodynamic derivation of equations of state and therefore a number of approaches have been developed based on a number of assumptions about the behaviour of dense solids, which are addressed in more detail in Anderson's review.[50] The validity of such assumptions may only be assessed on whether the derived EoS accurately reproduces the experimental compression behaviour. The most commonly used formulations, and the only ones used in this study, are the Murnaghan [51], Birch-Murnaghan [52] and Vinet [53] equations.

The Murnaghan EoS is popular due to its simplicity since it can be derived from the assumption that the bulk modulus varies linearly with pressure, such that:

$$P = \frac{B_0}{B'}\left[\left(\frac{V_0}{V}\right)^{B'} - 1\right]$$

The Murnaghan EoS has been found to reproduce both *PV* data and B_0 for compressions up to about 10% (*i.e.* $V/V_0 = 0.9$) but is not recommended for use beyond this regime.[54]

Other isothermal equations of state, such as the Birch-Murnaghan, employ an assumption that the strain energy applied during compression can be expressed as a Taylor series in the finite strain, *f*. The 3rd order Birch-Murnaghan EoS is based on the Eulerian strain, $f_E = [(V/V_0)^{2/3}-1]/2$, such that:

$$P = 3B_0 f_E(1 + 2f_E)^{5/2}\left[1 + \frac{3}{2}(B' - 4)f_E + \frac{3}{2}\left(B_0 B'' + (B' - 4)(B' - 3) + \frac{35}{9}\right)f_E^2\right]$$

It may also be appropriate to truncate this expression at second order in the energy term, resulting in the 2nd order Birch-Murnaghan EoS. In this case, the coefficient of f_E must equal zero, thus requiring that B' be fixed at a value of 4.

Finally, the Vinet formalism is often applied for solids under very high compression (*i.e.* $V/V_0 = 0.6$), since it has been observed that finite strain equations of state do not accurately reproduce *PV* observations in this region.[53] The Vinet EoS is based on a general inter-atomic potential and has been particularly useful in the representation of the compression of simple solids at very high pressures.[54] The Vinet EoS can be calculated according to the following, where $f_V = (V/V_0)^{1/3}$:

$$P = 3B_0\frac{(1 - f_V)}{f_V^2}exp\left[\frac{3}{2}(B' - 1)(1 - f_V)\right]$$

In this work, the parameters for the equations of state have been determined by a least-squares fit of the *PV* data using the program EoSFit v5.2.[55] In this routine it is simpler to consider pressure as the dependent variable [$P_{calc} = EoS(V_{obs})$] and the sum of the squares of the differences between the calculated and observed pressures are minimised during the least-squares solution. It is therefore critical to the success of the fitting procedure that the experimental uncertainties in both the pressure and volume are determined.

The quality of the EoS fitting procedure is also largely dependent upon the number of data points that have been obtained for a particular phase. For example, large errors in B_0 and V_0 may arise in cases where there are very few measurements made close to atmospheric pressure. This is exacerbated in the calculation of these parameters for high-pressure polymorphs, for which it is impossible to determine the unit cell volume at ambient pressure.

It is may therefore be more appropriate to fix V_0 to be the volume determined at the lowest pressure for which structural data have been obtained. It is then necessary to offset all succeeding pressures by this value.

In all of the compression studies reported herein, equations of state have been calculated using all four of the formalisms above. The most appropriate EoS was selected by comparison of the relative uncertainties in the parameters (namely, V_0, B_0 and B') as well as the 'goodness-of-fit' of the least-squares refinement, χ^2. However, the most critical assessment of the quality of the fit is often visual inspection. Where previous EoS data have been published, the same function has been adopted to facilitate comparison between studies, except where this resulted in a considerable reduction in the quality of the fit. A summary of the equations of state derived in this work can be found alongside an assessment of the quality of the fit in each case (by means of *R* and χ^2) in Appendix 8.2.

2.7 References

1. L. Merrill and W.A. Bassett, *Rev. Sci. Instrum.*, 1974, **45**, 290.
2. J.M. Besson, R.J. Nelmes, G. Hamel, J.S. Loveday, G. Weill, and S. Hull, *Physica B*, 1992, **180-181**, 907.
3. P.W. Bridgman, *Physics of High Pressure*, Dover Publications, New York, 1971.
4. A.W. Lawson and T.Y. Tang, *Rev. Sci. Instrum.*, 1950, **21**, 815.
5. W.A. Bassett, *High Pressure Res.*, 2009, **29**, 163
6. A. Van Valkenburg, *Rev. Sci. Instrum.*, 1962, **33**, 1462.
7. S.A. Moggach, D.R. Allan, S. Parsons, and J.E. Warren, *J. Appl. Crystallogr.*, 2008, **41**, 249.
8. R. Böhler and K. De Hantsetters, *High Pressure Res.*, 2004, **24**, 391
9. R. Böhler, *Rev. Sci. Instrum.*, 2006, **77**, 115103.
10. R.M. Hazen and L.W. Finger, *Rev. Sci. Instrum.*, 1981, **52**, 75.
11. D.J. Dunstan, *Rev. Sci. Instrum.*, 1989, **60**, 3789.
12. R. Miletich, D.R. Allan, and W.F. Kuhs, *High-Pressure Single Crystal Techniques*, in *Reviews in Mineralogy and Geochemistry, 41: High-Temperature and High-Pressure Crystal Chemistry*, R.M. Hazen and R.T. Downs, Editors, 2000, Mineralogical Society of America, Washington, D.C., USA.
13. R.J. Angel, M. Bujak, J. Zhao, G.D. Gatta, and S.D. Jacobsen, *J. Appl. Crystallogr.*, 2007, **40**, 26.
14. S. Klotz, J.C. Chervin, P. Munsch, and G. Le March, *J. Phys. D: Appl. Phys.*, 2009, **42**, 075413.
15. T. Osakabe and K. Kakurai, *Jpn. J. Appl. Phys.*, 2008, **47**, 6544.
16. Y. Shen, R.S. Kumar, M. Pravica, and M.F. Nicol, *Rev. Sci. Instrum.*, 2004, **75**, 4450.
17. G.J. Piermarini, S. Block, J.D. Barnett, and R.A. Forman, *J. Appl. Phys.*, 1975, **46**, 2774.
18. K. Syassen, *High Pressure Res.*, 2008, **28**, 75
19. W.L. Bragg, *Proc. R. Soc. London, Ser. A*, 1913, **89**, 248.
20. W.I.F. David, K. Shankland, J. van de Streek, E. Pidcock, W.D.S. Motherwell, and J.C.Cole, *J. Appl. Crystallogr.*, 2006, **39**, 910.
21. V. Favre-Nicolin and R. Cerny, *J. Appl. Crystallogr.*, 2002, **35**, 734.

22. G. Oszlányi and A. Sütó, Acta Cryst., **A64**, 123.
23. W. Massa, *Crystal Structure Determination, 2nd Edition*, Springer, Berlin-Heidelberg, Germany, 2004.
24. C. Giacovazzo, H.L. Monaco, G. Artioli, D. Viterbo, G. Ferraris, G. Gilli, G. Zanotti, and M. Catti, *Fundamentals of Crystallography, 2nd Edition*, Oxford University Press, Oxford, UK, 2002.
25. A. Dawson, D.R. Allan, S. Parsons, and M. Ruf, *J. Appl. Crystallogr.*, 2004, **37**, 410.
26. Bruker-Nonius, *APEX-II*, Bruker-AXS, Madison, WI, USA, 2000.
27. Bruker-AXS, *SAINT*, Bruker-AXS, Madison, WI, USA, 2003.
28. N. Casati, P. Macchi, and A. Sironi, *J. Appl. Crystallogr.*, 2007, **40**, 628.
29. S. Parsons, *SHADE, Program for Empirical Absorption Corrections to High Pressure Data*, The University of Edinburgh, UK, 2004.
30. G.M. Sheldrick, *SADABS*, University of Göttingen, Germany, 2004.
31. L. Farrugia, *J. Appl. Crystallogr.*, 1999, **32**, 837.
32. A. Altomare, G. Cascarano, C. Giacovazzo, A. Guagliardi, M.C. Burla, G. Polidori, and M. Camalli, *J. Appl. Crystallogr.*, 1994, **27**, 435.
33. P.W. Betteridge, J.R. Carruthers, R.I. Cooper, K. Prout, and D.J. Watkin, *J. Appl. Crystallogr.*, 2003, **36**, 1487.
34. H.E. Maynard-Casely, *personal communication*, 2010.
35. H. Rietveld, *J. Appl. Crystallogr.*, 1969, **2**, 65.
36. A. Le Bail, H. Duroy, and J.L. Fourquet, *Mater. Res. Bull.*, 1988, **23**, 447.
37. R. Von Dreele and A.C. Larson, *General Structure Analysis System (GSAS)*, 1986.
38. A.P. Hammersley, S.O. Svensson, M. Hanfland, A.N. Fitch, and D. Hausermann, *High Press. Res.*, 1996, **14**, 235
39. S.A. Moggach, S. Parsons, and P.A. Wood, *Crystallogr. Rev.*, 2008, **14**, 143.
40. D.R. Allan, S. Parsons, and S.J. Teat, *J. Synchrotron Radiat.*, 2001, **8**, 10.
41. D.R. Allan, W.G. Marshall, D.J. Francis, I.D.H. Oswald, C.R. Pulham, and C. Spanswick, *Dalton Trans.*, 2010, **39**, 3736.
42. F. Datchi, V.M. Giordano, P. Munsch, and A.M. Saitta, *Phys. Rev. Lett.*, 2009, **103**, 185701.
43. W.G. Marshall and D.J. Francis, *J. Appl. Crystallogr.*, 2002, **35**, 122.
44. W.G. Marshall, D.J. Francis, C.J. Barry, O. Kirichek, C.R. Pulham, and M.G. Tucker, *manuscript in preparation*, 2010.
45. D.L. Decker, *J. Appl. Phys.*, 1971, **42**, 3239.
46. A.D. Fortes, PhD Thesis, 2004, Department of Earth Sciences, University College, London, UK.
47. M.T. Weller, P.F. Henry, V.P. Ting, and C.C. Wilson, *Chem. Commun.*, 2009, **45**, 2973.
48. R.J. Harrison, *Neutron Diffraction of Magnetic Materials*, in *Reviews in Mineralogy and Geochemistry, 63: Neutron Scattering in Earth Sciences*, H.R. Wenk, Editor, 2006, Mineralogical Society of America, Chantilly, VA, USA.
49. W.G. Marshall, *personal communication*, 2010.
50. O.L. Anderson, *Equations of State of Solids for Geophysics and Ceramic Science*, Oxford University Press, Oxford, UK, 1995.
51. F.D. Murnaghan, *Am. J. Math.*, 1937, **59**, 235.
52. F. Birch, *Phys. Rev.*, 1947, **71**, 809.
53. P. Vinet, J. Ferrante, J.R. Smith, and J.H. Rose, *J. Phys. C: Solid State Phys.*, 1986, **19**, L467.
54. R.J. Angel, *Equations of State*, in *Reviews in Mineralogy and Geochemistry, 41: High-Temperature and High-Pressure Crystal Chemistry*, R.M. Hazen and R.T. Downs, Editors, 2000, Mineralogical Society of America, Washington, D.C., USA.
55. R.J. Angel, *EOS-FIT V5.2*, Department of Geological Sciences, Virginia Tech., Blacksburg, VA, USA, 2001.

Chapter 3

Structural Studies of RDX

(1,3,5-trinitrohexahydro-1,3,5-triazine)

3 Structural Studies of RDX

3.1 Introduction

RDX (1,3,5-trinitrohexahydro-1,3,5-triazine) was first synthesised by Henning in 1899 [1], although its potential as an explosive was not explored until 1920.[2, 3] War-time impetus meant that the characterisation of RDX and the optimisation of its synthesis were both accelerated until reliable manufacturing processes were implemented in the 1940s. Bachmann's method [4] of obtaining RDX by the nitration of hexamethylenetetramine (hexamine) is still used today, although samples prepared in such a way show typical impurity levels of HMX of around 10%. Despite this, the greater thermal and chemical stability of RDX over explosives of the time led to its more widespread use in munitions during World War II.[5]

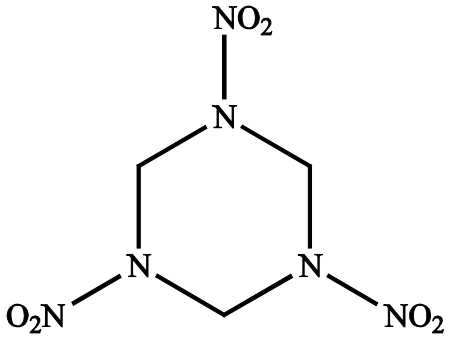

Figure 3.1 Molecular structure of RDX

Due to the sensitivity to detonation by friction or impact of pure RDX, initial efforts were aimed at desensitisation, firstly by coating RDX crystals with wax, oil or grease. The current practice, however, is to obtain 'insensitive munitions' (IMs) by embedding crystals of energetic materials in synthetic rubbers or polymer matrices (polymer bonded explosives, PBXs). RDX is the energetic component of the well-known plastic explosives C4 and Semtex, although numerous examples of PBXs have been reported.[5] The most recent development in RDX-based formulations, however, has focussed on reducing the sensitivity of PBXs to accidental detonation. Various manufacturers have promoted samples of RDX that have been observed to be less sensitive to shock initiation than neat RDX, particularly upon their inclusion in plastic explosives.[6-9] An international inter-laboratory comparison (the Reduced Sensitivity RDX Round Robin) program was therefore initiated to assess the physical properties, such as melting point and purity, as well as the impact sensitivity of seven different RDX formulations, produced by different synthetic procedures or crystallisation methods.[10] It was found that samples containing very little HMX impurity

displayed the greatest insensitivity to initiation.[11] It should be noted that synthetic and crystallisation methods are often proprietary information and are not available in the open literature. It is difficult therefore to draw conclusions on the effects these procedures have on sample quality.

The amount of research on RDX over the last 70 years is a reflection of the importance of this material. It has been the subject of a vast range of experimental and theoretical studies that include, for example, its vibrational spectroscopic properties [12-14], its molecular geometry in the gas phase [15], its decomposition mechanism [16-18], and its toxicological and environmental effects.[19-21] Despite this there is a relative paucity of detailed structural information on RDX. In fact, until 2008 only the crystal structure of the ambient polymorph had been determined, even though spectroscopic studies have presented evidence of at least three more forms depending on pressure/temperature/crystallisation conditions.

3.2 Polymorphism of RDX

The crystal structure of the stable polymorph of RDX at ambient conditions has been determined by single-crystal neutron [22] and single-crystal X-ray diffraction.[23] The α-form was found to crystallise in the orthorhombic crystal system (*Pbca*) with one molecule in the asymmetric unit. The conformation of the RDX molecule in this form (Figure 3.2) has been termed the AAE conformation based on the orientations of the three nitro groups relative to the six-membered ring: two nitro groups adopt pseudo-axial positions (A), while the third is in a pseudo-equatorial position (E). A more rigorous description of these orientations can be made by reference to the angle (δ) between the plane of the nitro group and the plane of the corresponding C-N-C ring atoms (Figure 3.3).[15]

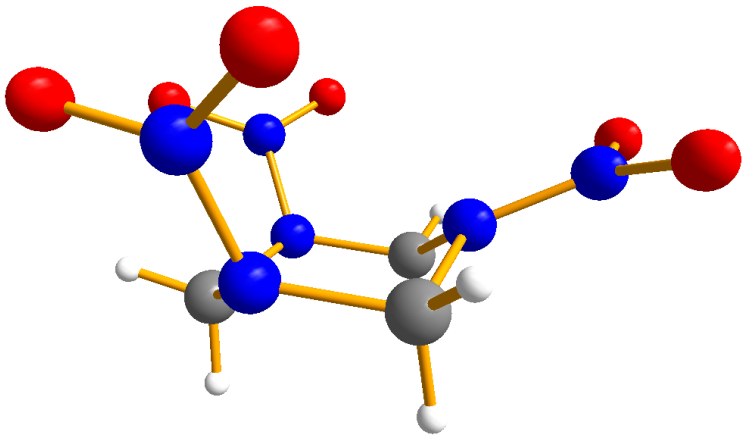

Figure 3.2 AAE molecular conformation of α-RDX

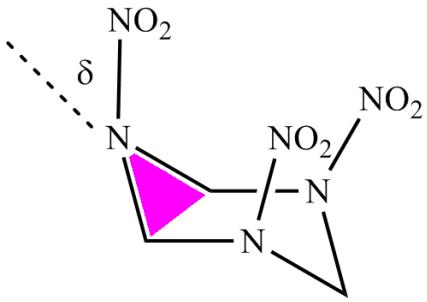

Figure 3.3 Schematic showing parameter δ used to describe orientation of the nitro groups in RDX.

In addition to the α-form, McCrone identified a highly metastable β-form obtained at ambient conditions by crystallisation from non-volatile solvents such as nitrobenzene, thymol (2-isopropyl-5-methylphenol) and even molten TNT (trinitrotoluene).[24] This form could only be isolated in small quantities and it was suggested by McCrone that "*because of its physical instability, there is no possibility of obtaining (this form) even in laboratory crystallisations… it should never be obtained on a laboratory scale*." A subsequent study by Karpowicz *et al.* [25] showed that small dendritic crystals of β-RDX could survive for several days in the absence of 'undue handling'. The β-form was also observed to transform to α-RDX upon contact with the more stable α-form or upon agitation. It was therefore asserted that the β-form is 'unlikely to survive routine handling' and is 'primarily a research curiosity'.[25]

Further spectroscopic studies have suggested that the RDX molecules in the β-form adopt essentially C_{3v} symmetry based on fewer vibrational bands being observed for β-RDX than for the α-form.[25-27] Each of these studies concluded that all of the nitro groups are equivalent and similar to the AAA conformation adopted in the solution and vapour phases. The most recent spectroscopic study on β-RDX by Infante-Castillo *et al*. has provided evidence for an α → β solid-solid phase transition at 477 K (at ambient pressure).[28] Samples of β-RDX produced in this way were not observed to undergo a reverse transition to the α-form, although no comment was made pertaining to the stability of these samples in the presence of the more stable α-form. A further aspect of this study, however, was the close agreement of the vibrational spectra and solid-state ^{15}N NMR spectrum with those calculated for the AAA conformer by DFT methods, thus providing further support for this hypothesis.[14] Unfortunately the instability of β-RDX at ambient conditions has precluded the possibility of obtaining good quality single crystals and therefore structure determination has so far proved impossible.

Various groups have examined the behaviour of RDX under variable temperature and pressure using spectroscopic and diffraction techniques.[29-35] All studies have shown that the α-form remains stable up to a pressure of ~3.9 GPa, at which point a reversible, first-order transition to a high-pressure γ-form occurs. The studies that investigated the tandem effects of pressure and temperature [31, 32, 34] found that the α → γ transition pressure did not vary with temperature, although Miller did observe that the rate of transformation did increase with temperature.

Olinger *et al.* observed that the volume decreased by approximately 1.6% over the α → γ transition with a sudden increase in the crystallographic *b*-axis but the metric symmetry remained orthorhombic. In 2006, a study by Goto *et al.* used a combination of X-ray powder diffraction and IR spectroscopy to characterise the γ-form above 4.0 GPa.[36] They proposed a structural model in which the space group (*Pbca*) is retained and the only conformational change of the molecule is a 'marginal' change in the torsion angles of the N-NO_2 groups. Nevertheless, the observation that the crystal packing is different from that in α-RDX led the authors to conclude the α- and γ-forms are indeed distinct. This structure was initially employed in the Rietveld refinements in Davidson's combined X-ray and neutron diffraction study of RDX up to ~8.0 GPa. Numerous intensity misfits, however, led the authors to conclude that this structure was incorrect and instead to propose their own structural model for γ-RDX.[37]

In accordance with previous observations, the orthorhombic crystal system was retained over this transition, although the space group symmetry was reduced from *Pbca* to $Pca2_1$. This reduction in symmetry is due to two molecules, which were formerly arranged over an inversion centre in the α-form, becoming inequivalent in order to maximise packing efficiency and to minimise unfavourable short O…O and N…O interactions. The molecular conformations of the two independent molecules in γ-RDX are shown in Figure 3.4; their respective δ angles are presented in Table 3.1 alongside those for the α-form and for isolated molecules in a range of conformations as calculated by DFT methods.[38] It is clear that one molecule adopts a conformation in which all of the nitro groups are in pseudo-axial positions (AAA). In the second molecule however, one nitro group lies in an intermediate position between axial and equatorial; this conformation has thus been termed the AAI conformation.

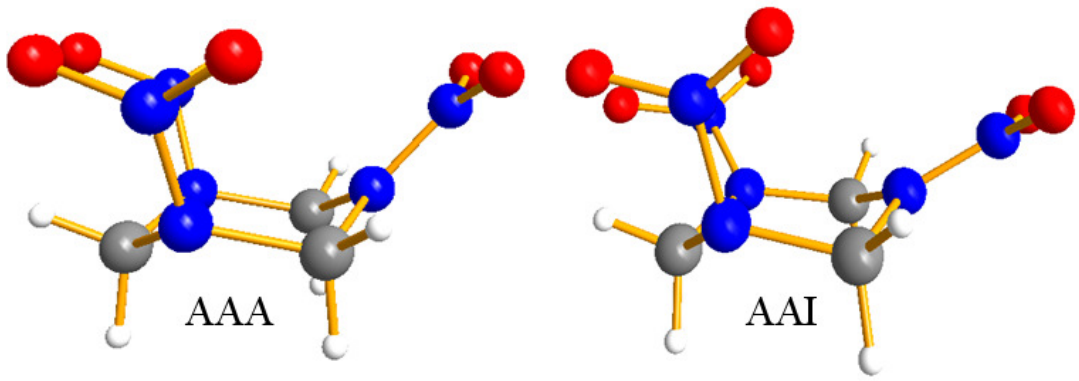

Figure 3.4 Molecular conformations of the two independent molecules in γ-RDX.

α-form	γ-form molecule 1	γ-form molecule 2	AAA*	AAE*	AAA-AAE (TS-1)*
33.4(1)	39.6(7)	36.4(9)	30.3	34.0	34.1
33.9(1)	17.3(8)	35.5(9)	30.1	34.0	33.8
-19.8(1)	-2.4(12)	9.5(11)	29.9	-37.9	1.5

Table 3.1 Values of δ (°) for different conformations of RDX. Note that values marked (*) have been calculated from ref. [38].

Figure 3.5 shows the packing arrangements in both α- and γ-RDX. This highlights that the change in molecular conformation in the γ-form allows two neighbouring molecules to effectively 'cup' one another to form dimers over a pseudo-inversion centre. This interlocking arrangement results in a *ca* 3% decrease in unit cell volume over the α → γ transition. Furthermore the high quality of data obtained for both polymorphs allowed the fitting of equations of state. The variation in volume with pressure over the stability range of the α-form was expressed as a 3rd order Birch-Murnaghan EoS with V_0 = 1640(2) Å^3, B_0 = 10.0(5) GPa, and B' = 11.3(7). The compression of the γ-form from 3.90 GPa to the highest pressure studied (7.99 GPa) was fitted using V_0 = 1632(4) Å^3, B_0 = 8.73(16) GPa, and B' = 11.26 (fixed) thus demonstrating that γ-RDX is significantly less compressible than α-RDX.[39] In the case of γ-RDX, B' was not treated as a free parameter due to the lack of low-pressure data and the relatively limited pressure range for which structural data was collected. The authors therefore used the value derived for the α-form as an appropriate approximation.

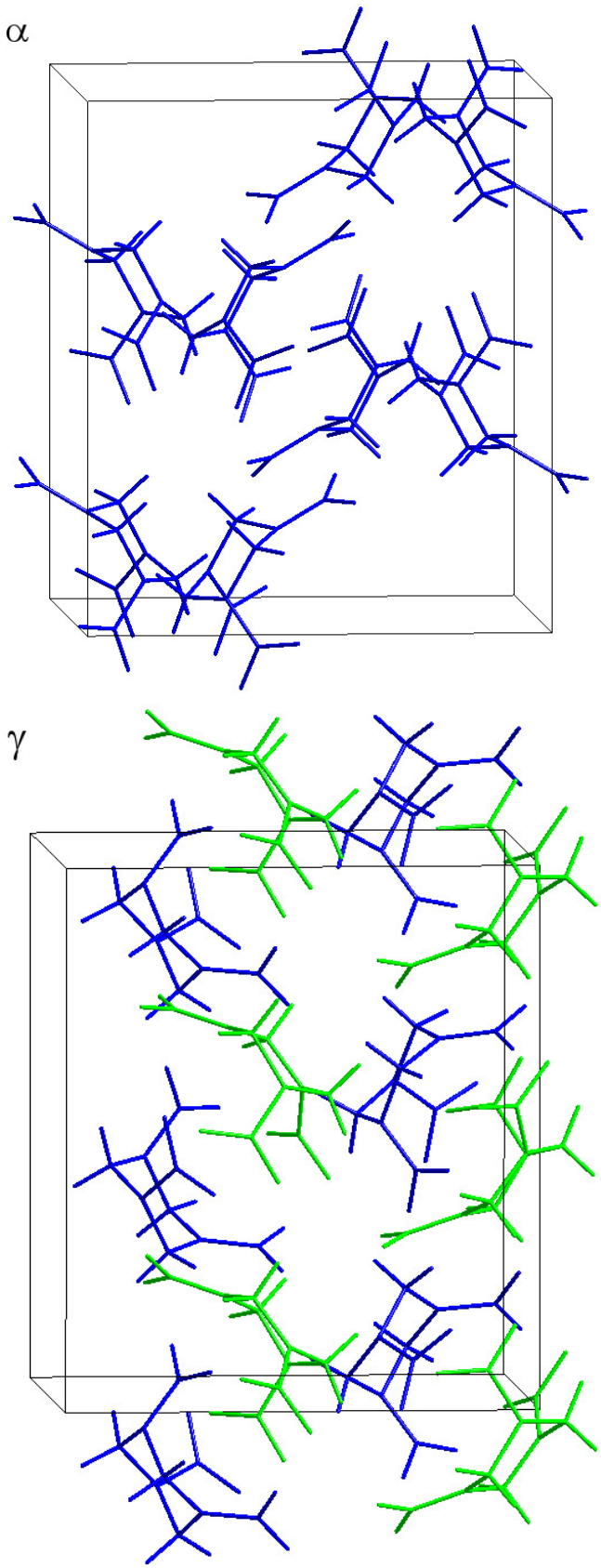

Figure 3.5 Crystal packing of α-RDX and γ-RDX, coloured by symmetry equivalence.

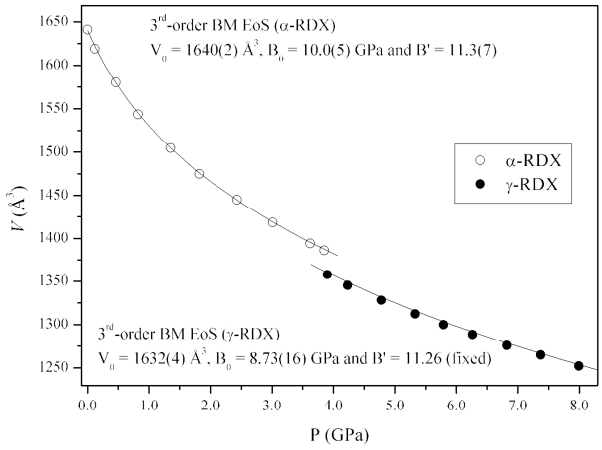

Figure 3.6 *PV* plots for the α- and γ-forms of RDX. The smooth compression of the unit cell volume with pressure has, in each case, been fitted to a 3rd-order Birch-Murnaghan EoS.[39]

Computational studies on the hydrostatic compression of RDX [40-46] have, until recently, been limited to the stability region of the α-form (i.e. $P < 3.9$ GPa). In the most recent computational study by Sorescu and Rice, however, semi-empirical atom-pairwise dispersion corrections were applied to conventional density functional theory (DFT) calculations to account for the van der Waals interactions in these molecular crystals.[47] Such calculations (termed DFT-D) were developed by Grimme [48] and have been particularly successful in reproducing experimental structures of molecular solids.[49] In their theoretical study, Sorescu and Rice were able to predict unit cell parameters within 2% of experimental data at ambient pressure. Furthermore, they investigated the evolution of the unit cell parameters upon hydrostatic compression and, in the case of RDX, were able not only to re-create the compression of α-RDX to 3.9 GPa but also to obtain excellent agreement with the experimental compression of the γ-form conducted by Davidson *et al*.[37]

By using helium as pressure-transmitting medium for their Raman measurements, Ciezak *et al.* [33, 34] have extended the pressure range for sprectroscopic studies of RDX to ~ 30 GPa. These studies confirmed the stability of γ-RDX up to ~ 18 GPa but the appearance of new vibrational bands and discontinuities in the vibrational spectra above 17.8 GPa led the authors to conclude that there was a reversible phase transition to a further high-pressure polymorph of RDX, subsequently referred to as δ-RDX. It is interesting to note that compression of single crystals to 22 GPa under non-hydrostatic conditions (resulting from the pressure-induced freezing of the mineral oil pressure-transmitting medium) does not give rise to any irreversible changes in the Raman spectrum.[35] Due to the increased overlap of peaks under non-hydrostatic conditions, the focus of this study was monitoring the spatial

variation in one selected Raman mode across the crystal in order to estimate the pressure gradient over the crystal. The mode selected in this study however (885 cm^{-1} at ambient pressure) has been shown to retain its peak-profile and intensity over the purported $\gamma \rightarrow \delta$ transition and this should therefore not be considered contradictory to the full spectroscopic analysis of RDX under very high pressures.[33]

Finally, investigations into the behaviour of RDX at elevated temperatures *and* pressures have provided evidence for another polymorph. The study by Baer *et al.* [31] using liquid nitrogen as pressure-transmitting medium observed a phase transition at $P > 3.8$ GPa and a temperature of 375 K. Miller's study [32] using Fluorinert as a pressure-transmitting medium also found this high-pressure/high-temperature polymorph at similar pressures but at a higher temperature (488 K).

Despite the differences in the conditions required to produce this form, both authors observed a simplification of the vibrational spectra, indicating a higher molecular symmetry with respect to both the α- and γ-forms. Furthermore they report that once this polymorph is formed at elevated temperatures and pressures, it can be cooled to ambient temperature and it persists on decompression 'almost to ambient pressure'. These observations led both authors to conclude that this form was the same as the metastable polymorph at ambient conditions and it has thus denoted β-RDX.

In addition to the static compression studies and the computational studies summarised above, shock compression experiments have provided complementary information on the real-time response of RDX to shock-waves at the molecular level. Patterson *et al.* were able to present Raman spectroscopic evidence for the occurrence of the $\alpha \rightarrow \gamma$ transition on the timescale of a shock compression experiment.[50, 51] This is a significant observation since it clearly demonstrates that this phase transition occurs prior to initiation, thus complicating the decomposition mechanism. These studies have since been extended to the investigation of products formed immediately after shock-wave induced decomposition by Raman and emission spectroscopy and quantum chemical calculations. Although no definitive decomposition mechanism has been determined, Patterson *et al.* propose that '*NO_2 is an important species in the initial decomposition of RDX*' and that this mechanism may, in fact, change above a threshold shock-wave pressure of *ca* 10 GPa.[52] In this higher pressure regime they suggest a more complex bimolecular decomposition mechanism between RDX and radical decomposition products.[53]

The voluminous, and at times confusing, information on the polymorphism of RDX has been summarised in Figure 3.7 that shows the regions of pressure/temperature space in which each polymorph is the stable form.

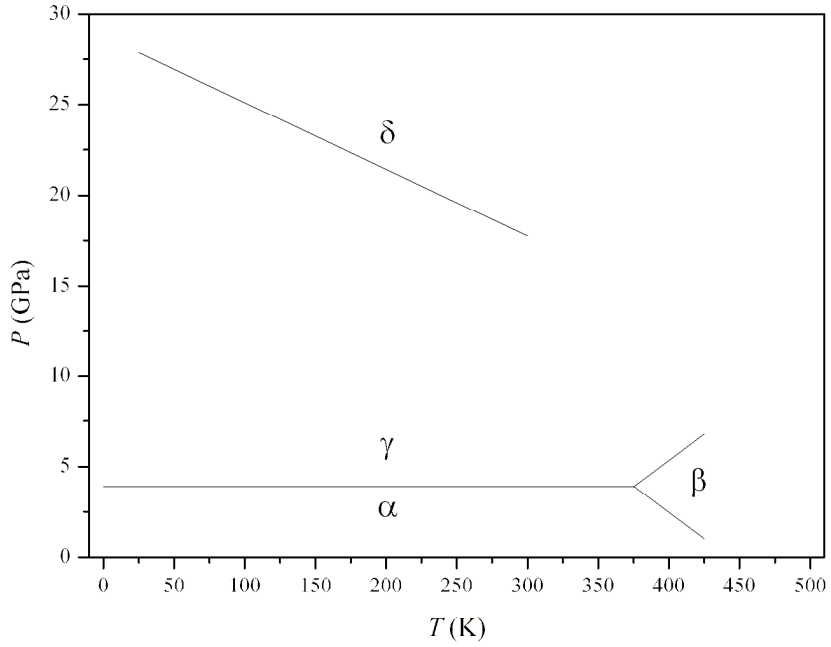

Figure 3.7 Phase diagram of RDX, taken from Ciezak *et al.* [34], with the inclusion of data from Baer *et al*. [31]

3.3 Aims

Given the confusion over the polymorphism of RDX and the paucity of detailed structural information the aims of this work were:

- to determine the structure of β-RDX at ambient conditions;
- to investigate the high-pressure/high-temperature form to determine if this was indeed the same as the β-form obtained at ambient conditions *and* to investigate the recovery of this form to ambient conditions;
- to extend the pressure range of diffraction studies to ~ 20 GPa to obtain an equation of state for RDX to this pressure and to characterise δ-RDX.

3.4 Experimental

3.4.1 Materials

Crystalline samples of RDX (SME type II; 100–300 μm) were kindly provided by W.G. Proud (Cavendish Laboratory, University of Cambridge). For neutron powder diffraction experiments, a mixture of deuterated RDX and its tetrameric oligomer HMX was prepared from deuterated paraformaldehyde and deuterated ammonia in a two-step synthesis following Bulusu's synthetic procedure [54] displayed in Reaction Scheme 2. The initial combination of paraformaldehyde and ammonia yielded the nitramine hexamethylenetetramine (hexamine), which was subsequently nitrated by concentrated nitric acid and ammonium nitrate in a complex multi-step mechanism.

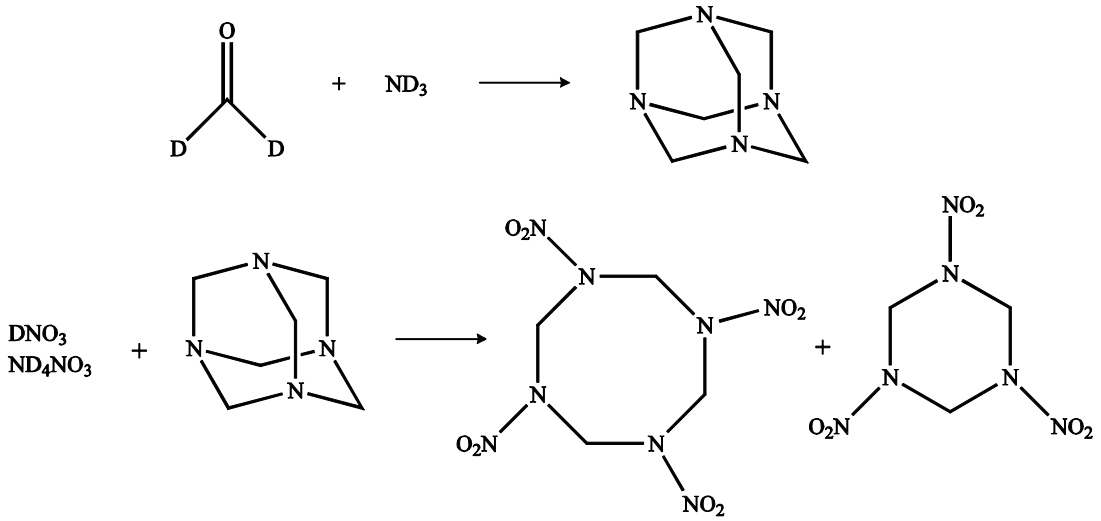

Reaction Scheme 2: The two-step synthesis of HMX and RDX. The formation of hexamethylenetetramine-d_{12} from paraformaldehyde and ammonia is followed by its nitration with nitric acid (98 – 100%) and ammonium nitrate. This resulted in an 85:15 mixture of HMX:RDX in the Bulusu synthesis.

Formation of hexamine-d_{12}: Initially, the recrystallisation of hexamine from D_2O was investigated to see if this would provide a cheaper and more facile route to hexamine-d_{12}. Infrared studies showed no evidence for hydrogen-deuterium exchange however.

Under an inert atmosphere, deuterated ammonia, ND_3, was bubbled into a solution of paraformaldehyde-d_2 ($(CD_2O)_n$, 3.28 g) in D_2O until the solution was saturated. The solvent was removed by heating and evaporation at ambient pressure; recrystallisation by azeotropic distillation with benzene gave pure hexamine in 73 % yield (2.0 g; m.p. 535 K decomp., lit. m.p. 536 K decomp.).

Nitrolysis of hexamine-d_{12}: A mixture of glacial acetic acid (CH_3CO_2D, 15 cm^3), acetic anhydride (0.25 cm^3) and paraformaldehyde-d_2 (0.35 g) was maintained at 317 K in a vessel fitted with three glass syringes. The following solutions were then added to this mixture simultaneously and uniformly over a period of 15 mins: (a) hexamine (2.0 g) in CH_3COOD (3.35 cm^3); (b) $(CH_3CO)_2O$ (5.5 cm^3); and (c) the nitrating mixture of DNO_3 (98 – 100 %, 1.89 g) and ND_4NO_3 (99 %, 1.65 g). After stirring for 15 mins, additional portions of $(CD_3CO)_2O$ (9.0 cm^3) and the nitrating mixture (DNO_3, 2.85 g; ND_4NO_3 2.63 g) were subsequently added uniformly, as before.

The reaction mixture was stirred at 317 K for an hour before dilution with D_2O and subsequent heating under reflux for 30 mins. Addition of 50 g frozen D_2O precipitated the crude product which was then collected, washed with cold H_2O and allowed to dry. This yielded 3.5g (85 %) of a mixture of HMX and RDX.

The crude mixture was stirred in 1,1-dichloroethane (300 cm^3) in order to dissolve the more soluble RDX. After filtration, the white solid was recrystallised from acetone to give the colourless crystals (3.2 g, m.p. 548 K, lit. m.p. 549 – 550 K). The RDX was then recovered from the dichloroethane extract before recrystallisation from 50 % aqueous acetone yielded the fraction in pure form (0.03 g, m.p. 468 K, lit. m.p. 478 K).

In order to increase the yield of RDX-d_6 for the structural studies outlined below it was necessary to undertake a second preparation. In this case hexamine-d_{12} was added to concentrated DNO_3 at 298 K before warming to 328 K. The RDX fraction was then precipitated with cold water before recrystallisation with acetone gave the pure solid.

Although both RDX and HMX are relatively insensitive to initiation, these are nevertheless potentially explosive materials and various safety precautions were taken to prevent initiation and explosive decomposition. Both materials were kept away from sources of ignition and care was taken to avoid the risk of detonation by friction or spark, e.g. metal spatulas. In addition appropriate safety equipment was used to minimise any risk of serious harm: all work during the nitration of hexamine was carried out behind a blast screen; Kevlar gloves and sleeves were worn to protect the hands when dealing with these materials; a reinforced face-mask was worn when close-handling of the samples was necessary. It should also be noted that all vessels which were exposed to the energetic materials were bathed in concentrated NaOH to destroy the HMX and RDX. Samples were stored in a police-licensed explosives locker.

3.4.2 High-Pressure Neutron Powder Diffraction

Neutron powder diffraction data were collected using the high flux, medium-resolution time-of-flight diffractometer PEARL-HiPr at the ISIS Neutron Facility, Rutherford Appleton Laboratory. High pressures and high temperatures were attained using a Paris-Edinburgh cell [55] with a newly commissioned variable temperature insert.[56] A lightly ground sample of RDX-d_6 (*ca* 100 mg) was loaded into an encapsulated TiZr gasket [57] with perdeuterated 4:1 methanol-ethanol as pressure-transmitting medium and a lead pellet as an internal pressure calibrant.[58] The P-E press ram pressure was monitored and varied by means of a computer-controlled hydraulic system. Time-of-flight (ToF) neutron powder diffraction data were collected using the $2\theta = 90°$ detectors with a transverse (through-anvil) scattering geometry. The resulting summed pattern was then normalised with respect to the incident beam monitor and the scattering from a standard vanadium calibration sample. Finally, the diffraction pattern intensity scale was corrected for the wavelength and scattering-angle dependence of the neutron attenuation by the anvil (tungsten carbide, WC) and gasket (titanium-zirconium alloy, TiZr) materials. Data analysis was performed by Rietveld refinement using the General Structure Analysis System (GSAS) suite of programs, in which a convolution of Gaussian (with coefficient σ_1) and Lorentzian (γ_1) functions was used to describe peak profiles (GSAS ToF profile 3).[59]

3.4.3 Ambient-Pressure Single-Crystal X-Ray Diffraction

X-ray diffraction intensities were collected using Mo-Kα radiation on a Bruker SMART APEX CCD diffractometer [60] equipped with an Oxford Cryostream-*Plus* low-temperature device.[61] Structures were solved [62] and refined by full-matrix least squares against F^2 using all data.[63] All non-hydrogen atoms were refined anisotropically. The hydrogen atoms were geometrically placed on the parent carbon.

3.4.4 High-Pressure Single-Crystal X-Ray Diffraction

High pressures were attained using the Merrill-Bassett diamond-anvil cell (DAC) [64] equipped with 600 μm culet diamonds and a 250 μm thick tungsten gasket (indented to ~100 μm) with a 300 μm diameter hole. In order to maximise the volume of reciprocal space that could be sampled it was necessary to use Böhler-Almax type diamonds and WC backing plates [65] that provide a wider opening angle than the typical beryllium-backed DACs. Initial studies focussed on the compression and subsequent heating of single crystals of α-RDX loaded in a DAC. Unfortunately, the high temperatures involved in this study led to the dissolution of the crystals in the pressure-transmitting medium (4:1 methanol:ethanol mixture). As an alternative, a high-pressure re-crystallisation route to *in situ* crystal growth

was performed. In this case, polycrystalline RDX was loaded into a DAC with MeOH:EtOH and was subsequently compressed to *ca* 5.0 GPa and heated to 500 K. Upon cooling, a crystal large enough for single-crystal X-ray diffraction was obtained at 5.7 GPa (see Section 3.5.2 for more details). Accurate determination of sample pressure was made by the ruby fluorescence method [66] using a 632.8 nm excitation line from a He-Ne laser. The fluorescence was detected by a Jobin-Yvon LabRam 300. High-pressure data sets were collected using ω-scans in 12 settings of 2θ and φ with 0.3° step-size for 60 s.[67] X-ray diffraction intensities were collected using Mo-Kα radiation on a Bruker SMART APEX II CCD diffractometer.[60] Single-crystal data were processed according to the procedure described by Dawson *et al*.[67] Integration of data sets and global cell refinement was carried out using the program SAINT [68], in which 'dynamic masks' were employed to prevent integration of areas of the detector shaded by the body of the DAC. SHADE [69] was used to reject reflections partly shaded by the DAC and absorption corrections were applied by SADABS [70] to allow for different path-lenghts of the X-rays through the crystal, depending on its orientation during the scan. Structures were solved by direct methods using SIR92 [62] and full-matrix least-squares-refinement against F^2 was carried out using CRYSTALS.[63]

3.4.5 High-Pressure X-Ray Powder Diffraction

High-pressure X-ray powder diffraction experiments were carried out using a Merrill-Bassett diamond-anvil cell (DAC) [64] equipped with 400 μm culet diamonds and a 150 μm thick tungsten gasket (pre-indented to ~20 GPa) with a 100 μm hole. Due to the cut of the diamond anvils it was necessary to use DACs fitted with Be backing plates but the high degree of collimation of the synchrotron X-ray beam (typically 30 – 50 μm) meant that this did not have a detrimental effect on data collections. Pressure measurement was made by monitoring the R_1 fluorescence line of ruby spheres.[66] Data were collected at the Extreme Conditions beamline (I15) and the High Resolution Powder Diffraction beamline (I11) at Diamond Light Source.

I15: Two experiments were carried out at beamline I15. In the first a polycrystalline sample of RDX was loaded into a DAC with methanol:ethanol (4:1) as pressure-transmitting medium. The X-ray beam (λ = 0.484693 Å) was collimated to a diameter of 50 μm and samples were exposed for 300 s. Similarly, a polycrystalline sample of RDX was loaded into a DAC with MeOH:EtOH as pressure medium in the second I15 experiment but the beam diameter was reduced to 20 μm. The wavelength for this experiment was 0.47686 Å and it

was necessary to lengthen exposure times to 1800 s due to the overall reduction in X-ray intensity.

I11: Polycrystalline RDX was loaded, with no pressure transmitting medium, into a DAC. Diffraction data were recorded using a beam of wavelength 0.485947 Å, which was slitted to 50 x 50 μm. Exposure times of 1800 s were required.

In all cases 2D diffraction patterns were collected using a Mar345 image plate and integrated using Fit2D.[71] The sample to detector distance was calibrated using either Si (I15) or CeO_2 (I11) standards. Data analysis was performed by Le Bail refinement using GSAS, in which a convolution of Gaussian (GU, GV), Lorentzian (LX, LY) and asymmetry (asym) coefficients was implemented to fit peak profiles (GSAS CW profile 2).[59]

3.4.6 DFT-MD calculations

A plane-wave density-functional theory molecular-dynamics simulation of β-RDX was carried out by Dr. A. M. Reilly using the CPMD program [72] and the PBE functional [73] augmented by a van der Waals dispersion-correction term.[74] The simulation was performed on a single unit cell, using periodic boundary conditions, at 150 K with data being collected for a total of 20 ps. The positions adopted by the atoms in the course of the simulation were analysed to produce time-averaged positions and variances that approximately correspond to the atomic positions and anisotropic displacement parameters (ADPs) determined experimentally. Further details of the analysis procedure and typical MD simulation parameters can be found elsewhere.[75]

3.5 Results and Discussion

3.5.1 β-RDX: a highly metastable polymorph at ambient conditions

Due to its observed instability, initial experiments focussed on crystallisation of RDX from nitrobenzene solution in sealed glass capillaries (o.d. ~2 mm). By thorough warming of this sealed system such that *all* of the solid was dissolved, it was possible to reduce the likelihood of seeding by residual traces of the α-form. In this way, reproducible crystallisation conditions were achieved and on cooling of a very concentrated hot solution to 298 K small crystallites were obtained which exhibited a very different morphology from α-RDX. Raman spectroscopy identified these as the β-form by comparison with previously reported spectra. [27, 28] Representative Raman spectra for the α- and β-forms are presented in Figure 3.8.

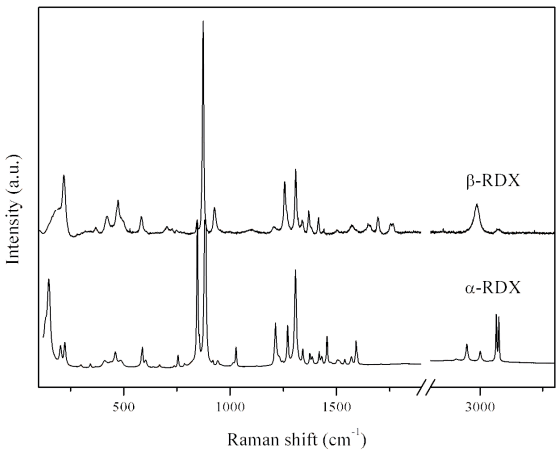

Figure 3.8 Comparison of the Raman spectra collected for α-RDX and β-RDX at ambient conditions. The spectral range between 1900 and 2800 cm^{-1} is omitted due to low spectral intensity of the vibrational modes within this region.

A single crystal was successfully grown using this same technique in a smaller diameter capillary (~0.3 mm) and single-crystal X-ray diffraction data were recorded at 273 K (see Appendix 8.1 for full structural information). The reflections were indexed to an orthorhombic unit cell ($Pca2_1$), implying 8 molecules in the unit cell and 2 independent molecules in the asymmetric unit. Structure solution and refinement showed that this was an unsolvated form of RDX. Attempts to cool the capillary resulted in freezing of the nitrobenzene and destruction of the crystal.

Subsequent crystallisation trials therefore focussed on growing single crystals that could be separated from the solvent so that low-temperature data could be collected. The most successful route proved to be when a concentrated solution of RDX in nitrobenzene on a hot glass slide was covered with an upturned glass vial to reduce the evaporation rate (see Figure 3.9). In the cases where the drop contacted the side of the upturned vial, small dendritic crystals of β-RDX were observed to form at the meniscus during evaporation. This method is very similar to the phenomenon of "contact-line crystallisation" described by Capes *et al.* for the growth of a metastable polymorph of paracetamol.[76] In this case, it has been proposed that the increased evaporation rate at the meniscus caused an increase in concentration in this region, thus permitting the nucleation of the metastable form. This form was then unable to transform to the more stable polymorph *via* a solvent-mediated transition as the solvent level dropped and the crystals were removed from solution.

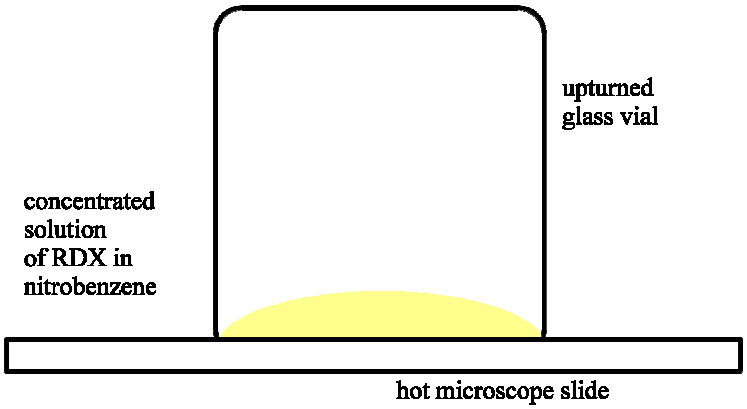

Figure 3.9 Experimental set-up for 'Contact-line Crystallisation' of β-RDX from nitrobenzene

Crystals grown in this way proved to be sufficiently metastable with respect to the α-form such that they could be manipulated and transferred to a fibre, which was subsequently mounted on the diffractometer. In this way, single-crystal X-ray diffraction data were recorded at 150 K and were consistent with the data collected at 273 K (structural information presented in Table 3.2). In the crystal structure of the β-form, both independent molecules adopt the chair conformation with all nitro groups in axial positions, resulting in approximate C_{3v} molecular symmetry (see Figure 3.10), thus supporting earlier suggestions based on vibrational spectra.[25-27] It is interesting to note that the unit cell *a*-axis actually shortens upon warming. The exact reasons for this remain unclear but a variable temperature X-ray diffraction study would be instructive.

	150 K	273 K
Space Group	$Pca2_1$	$Pca2_1$
a (Å)	15.1267(11)	15.0972(7)
b (Å)	7.4563(6)	7.5463(4)
c (Å)	14.3719(11)	14.4316(6)
V (Å^3)	1621.0(2)	1644.16(13)
D_c (Mg m^{-3})	1.820	1.795

Table 3.2 Structural information for β-RDX at 273 and 150 K.

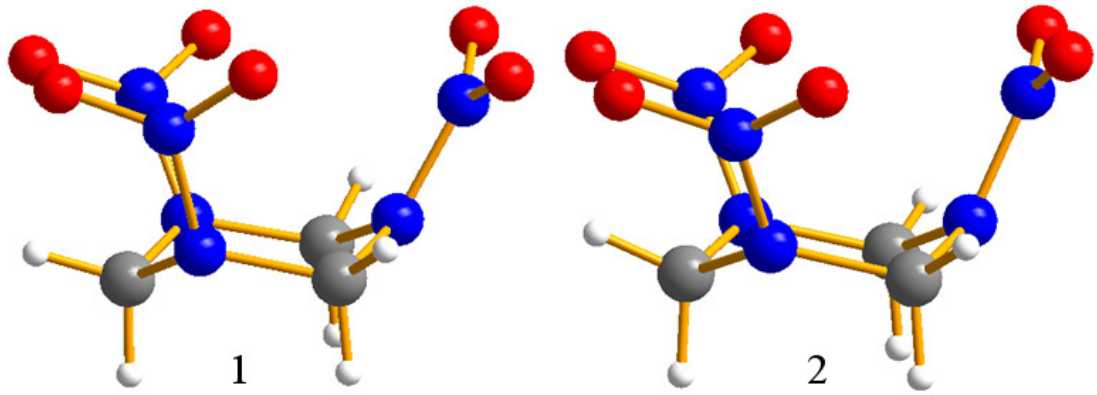

Figure 3.10 Molecular conformations of the two independent molecules in β-RDX.

The orientations of the nitro-groups can conveniently be compared by reference to the angle δ, the angle between the plane of the C-N-C ring atoms and the corresponding N-N bond.[15] The δ-values for both molecules in β-RDX are presented in Table 3.3 alongside those for α-RDX and for the *isolated* molecule in the AAA conformation as calculated using DFT methods.[38] For both molecules 1 and 2 the δ-values are very close to the calculated AAA geometry.

α-form	β-form molecule 1	β-form molecule 2	AAA*
33.4(1)	39.3(3)	33.4(3)	30.3
33.9(1)	32.4(4)	29.9(3)	30.1
-19.8(1)	28.5(4)	28.7(3)	29.9

Table 3.3 Values of δ (°) for the independent molecules in β-RDX, presented alongside those for the α-form and the AAA conformation as calculated by Vladimiroff and Rice.[38]

The packing of the molecules in β-RDX may be described as two interpenetrating lattices, one of which is composed solely of type 1 molecules and the other composed solely of type 2 molecules. Molecules within these lattices are linked by weak intermolecular C-H…O interactions. When the two independent lattices are overlayed to represent the full crystal packing (Figure 3.11) one can see similar weak C-H…O interactions occur between molecules 1 and 2 in the full lattice. This arrangement results in a slightly less dense crystal structure (1.795 Mg m^{-3} at 273 K) compared to α-RDX (1.806 Mg m^{-3} at 293 K) [22], which displays a more efficient packing of zig-zagging planes (Figure 3.5). Comparison of the α- and β-forms shows that there is no direct relationship between the two structures and that there are fewer C-H…O intermolecular interactions in β-RDX.

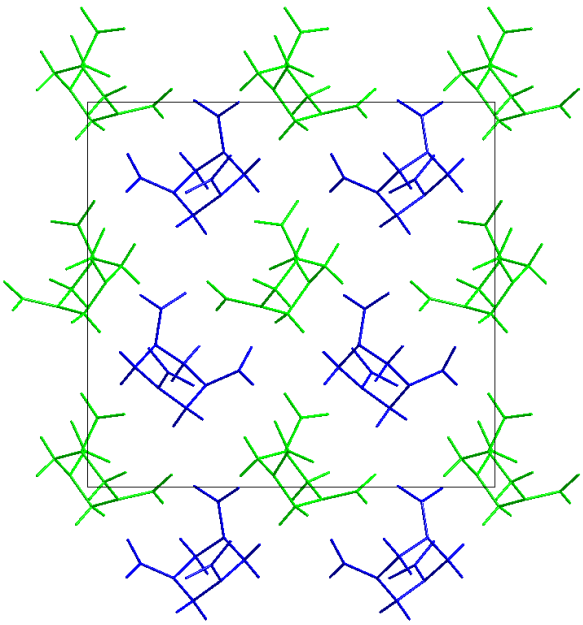

Figure 3.11 Full crystal packing in β-RDX, viewed down the *b*-axis, displaying the two interpenetrating lattices of molecules of types 1 and 2 (green and blue, respectively).

A particularly striking feature of the structure of the metastable β-form is the unusually large anisotropic displacement parameters (illustrated in Figure 3.12) associated with the nitro groups and even the ring atoms of molecule 1. These large amplitude motions (observed even at 150 K) suggest that this molecule is librating significantly about its position in the lattice and it is perhaps this that is the reason for the instability of this form with respect to the α-form. This observation prompted further investigation in order to establish the true nature of these unusual thermal ellipsoids. Initially it was suspected that a subtle static disorder may exist within the crystal structure, in which the long range order of the type 1 molecules displays a periodicity that is not commensurate with the translation symmetry defined by the crystallographic unit cell. In high-resolution single-crystal X-ray diffraction experiments, this incommensurate behaviour would be expected to result in the splitting of any single-crystal reflections dominated by scattering from type 1 molecules. Unfortunately the resolution of the data collected during the current experiment was not sufficient to identify any splitting, although slight broadening of the reflections can be seen in Figure 3.13. It would therefore be extremely useful to conduct analogous single-crystal studies exploiting the longer wavelength of, for example, a Cu-Kα source to determine conclusively whether the broadening observed in the present study was a result of the crystal quality or the occurrence of poorly-resolved satellite peaks. Furthermore, the high resolution and high incident flux of synchrotron radiation may provide additional experimental evidence for either a static or dynamic disorder model.

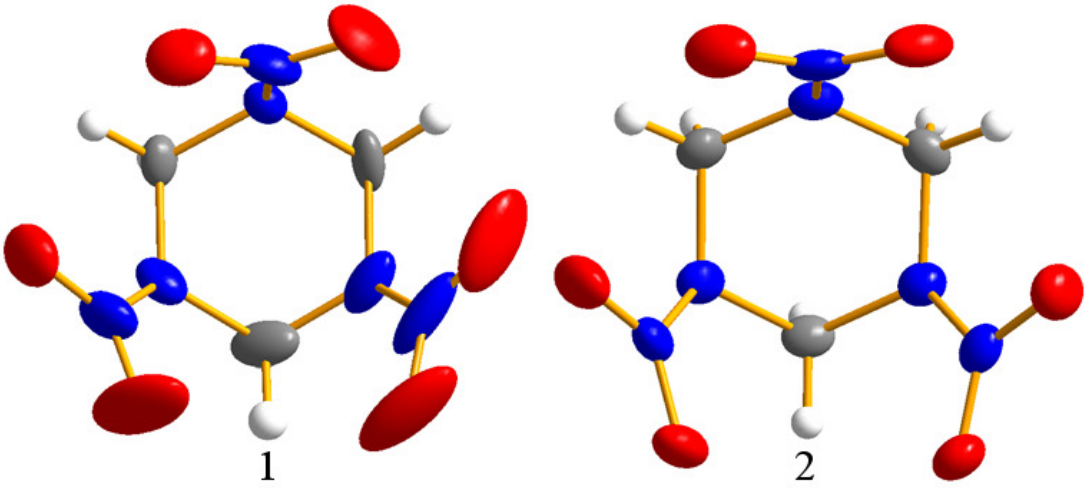

Figure 3.12 Anisotropic displacement parameters for β-RDX at 150 K.

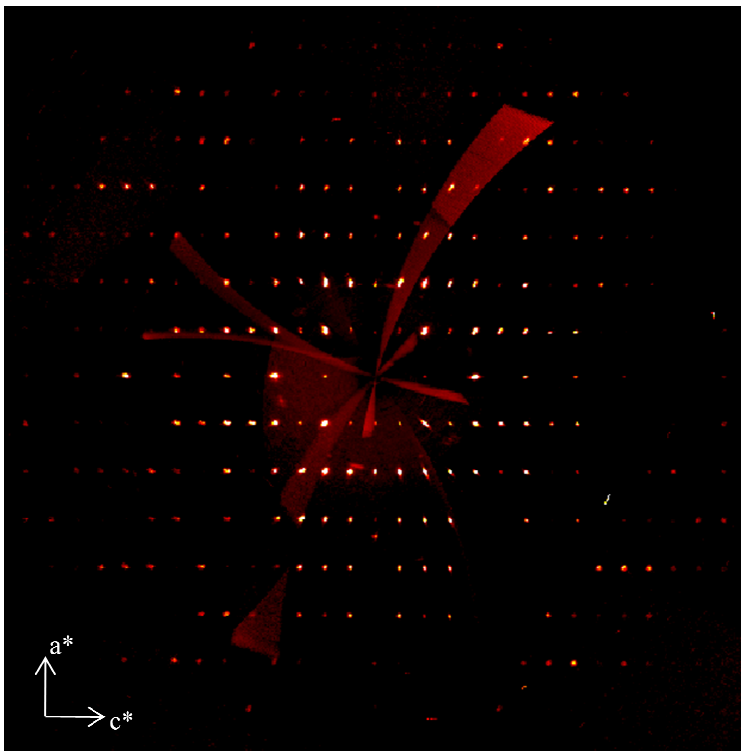

Figure 3.13 Calculated precession image of the *h*0*l* zone (produced using Bruker APEX-II software package) representing the single-crystal X-ray diffraction data collected for β-RDX at 150 K. Despite broadening of some of the reflections, it is not clear whether this is indicative of incommensurate modulation within the structure or is an experimental artefact.

In order to clarify further the disorder within β-RDX, a molecular dynamics (MD) simulation of β-RDX was carried out by Dr. A. M. Reilly (School of Chemistry, University of Edinburgh). Analysis of the motions of the molecules during the course of the simulation can be used to determine a number of 'experimental' quantities including thermal ellipsoids. The MD-derived thermal ellipsoids (plotted in Figure 3.14) have the same relative shape and

orientations as the experimental ellipsoids. The theoretically determined ADPs are smaller than the experimental values, possibly due to the inability of the MD simulation to model dispersive phonon modes and zero-point energy contributions.[77, 78] Nevertheless, the similarity of the theoretical ellipsoids with the elongated ellipsoids observed in the experimental structure suggests that this feature is not due to experimental error or static structural effects such as static disorder or incommensurate modulation as neither of these can be modelled by the MD simulation. On this basis, it is more likely that the elongation is due to some dynamic process within the unit cell.

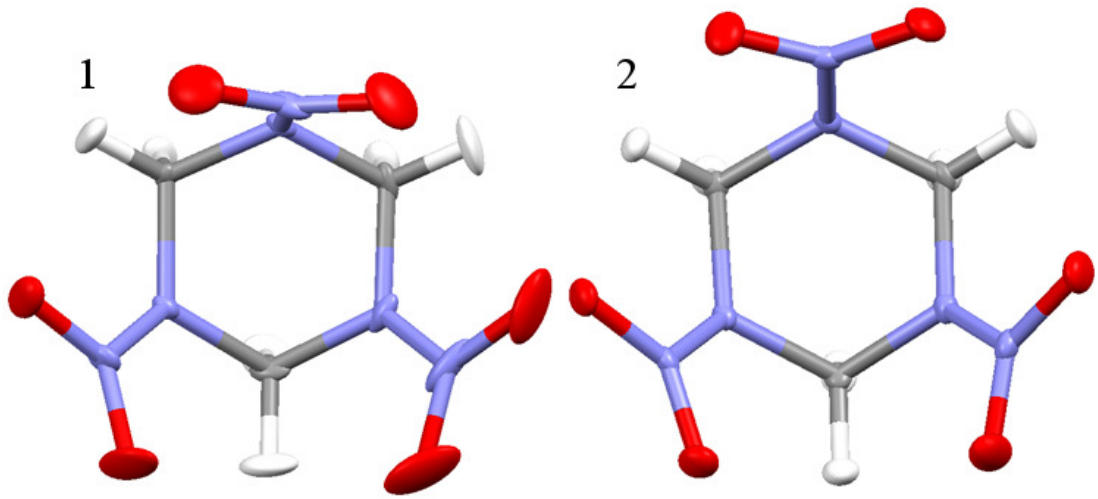

Figure 3.14 Representation of the anisotropic displacement parameters calculated for β-RDX by Molecular Dynamics Simulation.

Finally the results of this study indicate that β-RDX is rather less prone to transform to the α-form than has been previously suggested.[24] Crystals of the β-form survived gentle handling at room temperature and survived cooling to 150 K with no discernible deterioration in crystal quality (although this does not rule out a phase transition below this temperature for example). Furthermore the crystals could be manipulated in solution provided that there were no traces of the α-form present to initiate a rapid solvent-mediated transformation. Similarly, an isolated crystal of the β-form immediately transformed upon contact with a fibre or needle contaminated with residual traces of α-RDX. On this occasion a wavefront was observed to pass through the crystal leading to a marked reduction in crystal quality, indicating that this transition is reconstructive. Raman measurements conducted on these deposits confirmed that only the α-form was present after this transition was observed.

In accordance with previous conclusions [25] this instability would exclude the possibility of the presence of the β-form in RDX-containing munitions. This would therefore rule out any direct effects attributable to β-RDX on the performance of these compositions (e.g.

sensitivity to shock) although it is certainly reasonable to suggest that the reconstructive nature of this transition may adversely affect crystal quality by the introduction of shear stresses and/or crystal defects. This would have significant implications for the creation of 'hot spots' [79, 80], thereby potentially affecting performance.

It would therefore be extremely desirable to explore fully the effect of phase history on the properties of RDX, particularly sensitivity. Full-profile refinements of the powder diffraction patterns collected for samples that have undergone the β → α transition may facilitate the characterisation of shear stresses, micro strain and defect content.[81, 82] Furthermore, comparison of these powder diffraction patterns with those collected for samples of Reduced-Sensitivity (RS-RDX) will perhaps allow the direct evaluation of sensitivity based solely on diffraction data.

3.5.2 Investigation of the high-pressure/high-temperature form of RDX

Having determined the structure of β-RDX under ambient conditions, this study was extended to identify and structurally characterise the high-pressure/high-temperature form, which some authors have suggested is the same as this metastable polymorph.[31, 32] We therefore investigated this form by neutron powder diffraction using a Paris-Edinburgh cell with a newly-commissioned variable temperature insert.[56] A sample of RDX-d_6 was initially compressed in MeOD/EtOD (4:1) to obtain the γ-form at a pressure of 4.1 GPa (293 K). The sample was then heated incrementally to 423 K but no changes in the diffraction pattern were evident; only on brief warming to 448 K (30 mins) was a new pattern observed (see Figure 3.15). In order to avoid potential decomposition at these elevated temperatures, the sample was cooled initially to 323 K and then to 293 K – the new pattern persisted on cooling to ambient temperature. Subsequent decompression at 293 K showed that this form also persisted to 0.99 GPa (Figure 3.16). At the next pressure point (0.85 GPa) the characteristic diffraction pattern of α-RDX was observed. Raman spectroscopic and powder X-ray diffraction analysis on the recovered material confirmed that the sample had not undergone decomposition.

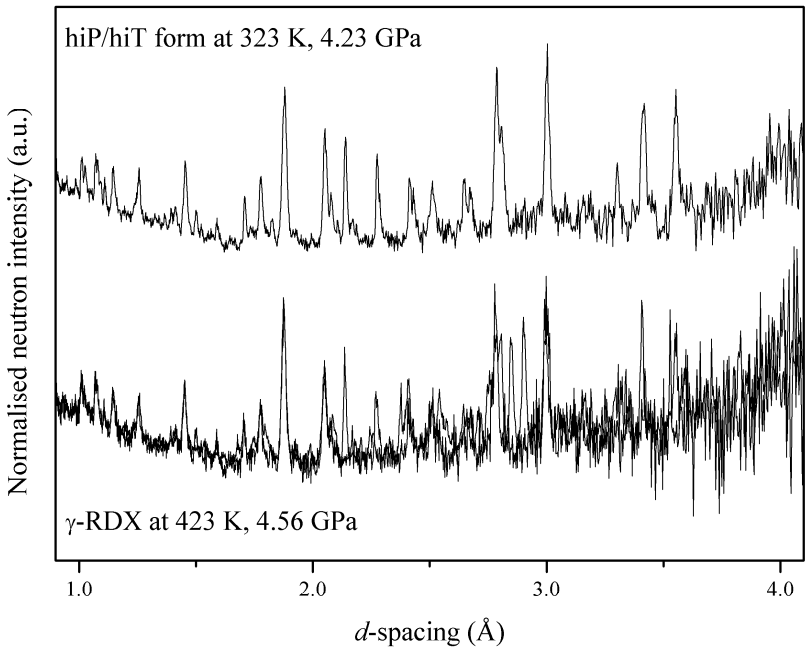

Figure 3.15 Comparison of the neutron powder diffraction patterns collected for γ-RDX-d_6 and the pattern observed for the high-pressure, high-temperature form.

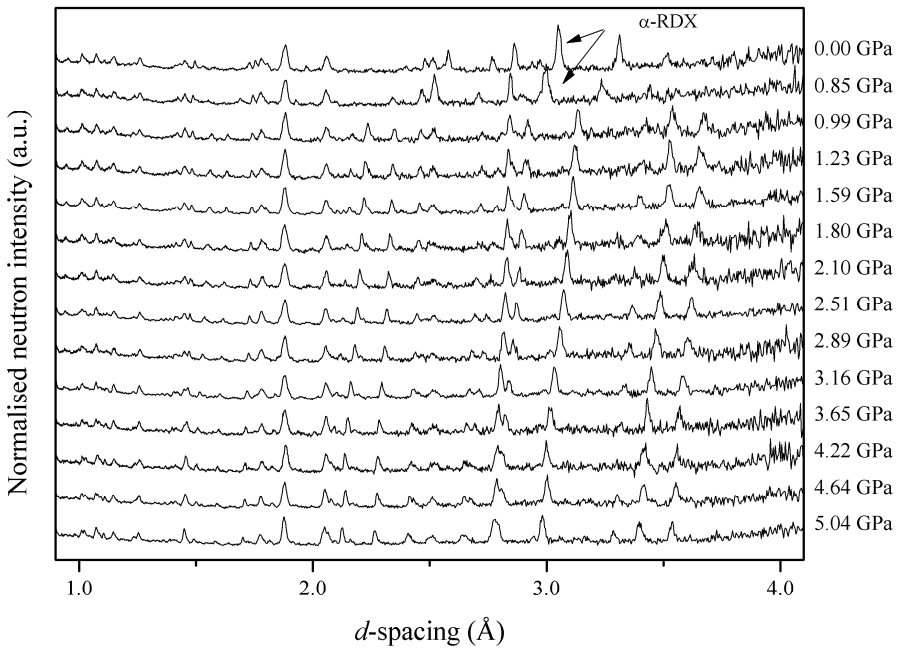

Figure 3.16 Neutron powder diffraction patterns collected during the decompression of the high-pressure/high-temperature polymorph of RDX-d_6 at ambient temperature.

Comparison of the patterns collected for this form with the calculated pattern from the crystal structure of β-RDX (Figure 3.17) allowed us to prove conclusively that the high-pressure/high-temperature polymorph of RDX is *not* the same as the metastable form at ambient conditions. Instead this represents a fifth polymorph of RDX and should therefore be re-named ε-RDX. Unfortunately indexing (and hence structure solution) was not possible on the basis of the neutron diffraction patterns collected.

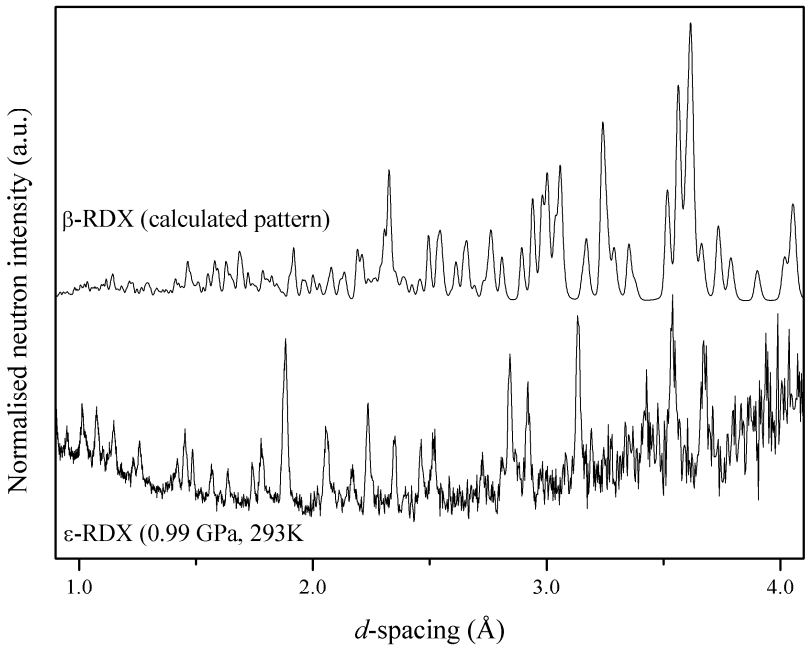

Figure 3.17 Comparison of the neutron powder diffraction pattern obtained for a sample of RDX-d_6 subjected to elevated temperatures and pressure (at 0.99 GPa and 293 K) with the simulated pattern for perdeuterated β-RDX (ambient pressure and 150 K)

These findings were mirrored in the results of a Raman spectroscopic study of RDX-h_6 contained in a diamond-anvil cell (DAC) subjected to similar temperature and pressure conditions. The Raman spectra collected for this sample were in excellent agreement with those reported by Baer *et al.*[31] Furthermore this study confirmed that, once formed, the ε-form persisted on cooling to ambient temperature and on decompression to ~ 1.0 GPa. At this pressure ε-RDX transformed to the α-form; at no point during the decompression was the γ-form observed (see Figure 3.18). In addition, the re-naming of the high-pressure/high-temperature form of RDX has been substantiated by the comparison of the Raman spectra (Figure 3.19) obtained for ε-RDX and the β-form, with which it has previously been confused. It is interesting to note that the Raman spectrum observed for β-RDX is consistent

with those published by Torres *et al.*[27], suggesting that the confusion over these distinct forms could perhaps have been remedied sooner.

In their very recent spectroscopic investigation of this form, Dreger and Gupta concur with the re-naming of this form (ε-RDX).[83] Several noticeable differences were observed between Raman spectra collected for the β- and ε-forms, particularly in the low frequencey lattice modes. It was also possible to perform compression and decompression studies of the ε-form in order to assess its structural stability. Below 0.6 GPa ε-RDX readily converted to the α-form; upon compression, however, the ε-form remained stable to 20.0 GPa, the highest pressure studied. Furthermore, the same authors conducted a parallel study on the high-pressure/high-temperature behaviour of the three forms that have been identified under these conditions (*i.e.* the α-, γ- and ε-forms).[84] Careful spectroscopic and optical measurements allowed the identification of the phase boundaries, as well as a triple point at 3.7 GPa and 466 K.

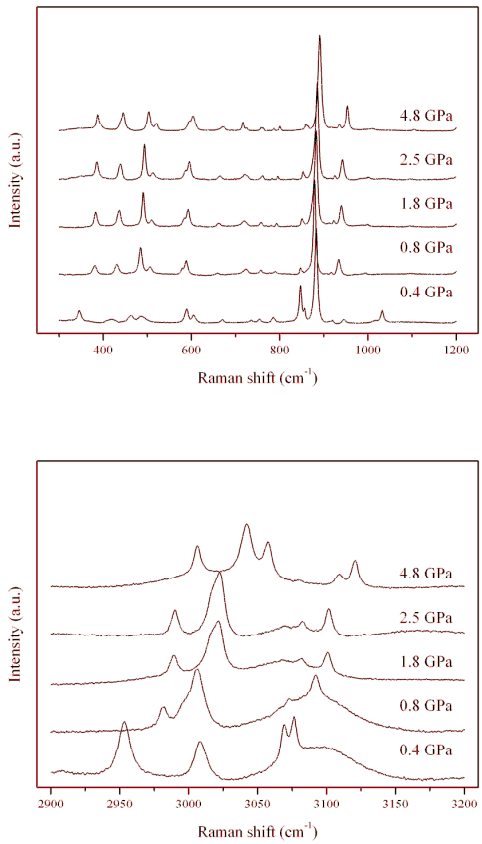

Figure 3.18 Raman decompression study of ε-RDX showing clear evidence of phase transition to the α-form between 0.8 and 0.4 GPa. The spectral intensities have been scaled for clarity and the ranges between 1200 - 1500 and 1500 - 2900 cm^{-1} have been omitted due to masking from the strong diamond signal and low sample spectral intensity, respectively.

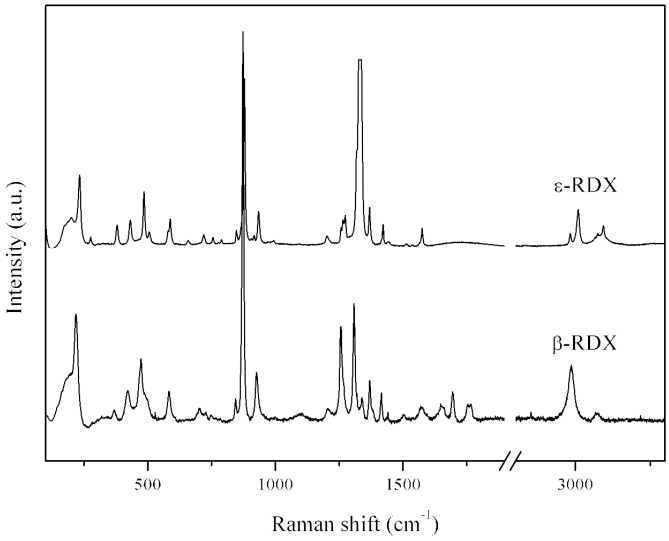

Figure 3.19 Comparison of the Raman spectra collected for β-RDX at ambient conditions and ε-RDX at 1.0 GPa and 293 K.

An important result of the complementary neutron diffraction studies on RDX-d_6 and the Raman analysis of the hydrogenous material is that the transition pressures concur within experimental error. It is therefore reasonable to conclude that the effect of deuteration on the α → γ, γ → ε, and ε → α phase transitions is negligible.

Having demonstrated that the ε-form could be obtained reproducibly, the focus of this study turned to obtaining crystals suitable for single-crystal X-ray diffraction (SXD). A single crystal of α-RDX was compressed (in a DAC) through the α → γ transition to a pressure of ~ 5.0 GPa before heating to 500 K. Unfortunately this resulted in the dissolution of the crystal in the pressure-transmitting medium (4:1 MeOH/EtOH) at these elevated temperatures.[4] For this reason, we opted to attempt the recrystallisation of RDX from solution at ~ 5.0 GPa. Whilst recrystallisation at lower pressures (i.e. up to 1.0 GPa) has been shown to be successful,[85, 86] this technique has not been used at these much higher pressures on account of pressure-induced freezing of the solvent and the low intrinsic solubilities of molecular compounds under these conditions.

Polycrystalline α-RDX was loaded into a DAC with a small quantity of MeOH:EtOH (4:1) and the pressure increased to ~ 5.0 GPa before heating to 500 K for 1 hr. At these elevated

[4] The dissolution of the crystal in MeOH:EtOH has also been reported by Dreger and Gupta (ref. [83]), who observed shattering in cases where nitrogen was employed as the pressure-transmitting medium. In contrast, crystal quality was maintained when these studies were conducted in argon. The authors do not comment on crystal quality after the ε → α transition.

temperatures the enhanced solubility of RDX in the pressure-transmitting medium and the reduced viscosity of the medium resulted, in many cases, in complete dissolution of the sample. This was overcome by loading an excess of the solute in the diamond-anvil cell. After numerous crystallisation trials, recrystallisation at 5.7 GPa produced a single crystal large enough for single-crystal X-ray diffraction.

Structure solution and refinement showed that ε-RDX crystallises in the orthorhombic crystal system ($Pca2_1$) with only one molecule in the asymmetric unit. With this structure as a starting point it was then possible to refine all of the neutron powder diffraction patterns extremely well (χ^2 values of 1.26 were typical) thus providing additional support that the structural model was correct. An illustrative example of the Rietveld refinement can be seen in Figure 3.20.

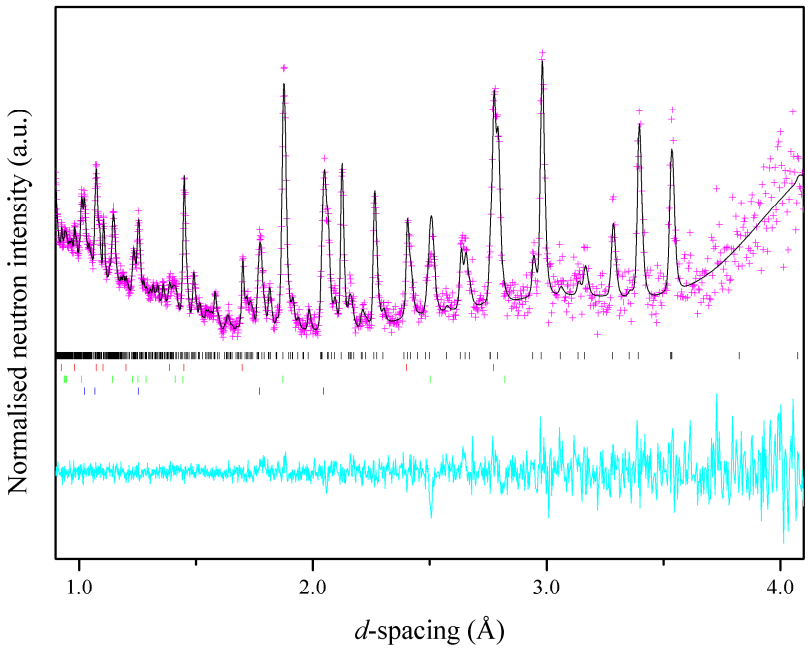

Figure 3.20 Example of the Rietveld refinement of neutron powder diffraction pattern (at 5.04 GPa and 293 K) using the structure determined for ε-RDX. The experimental data (I_{obs}) are shown in pink; the calculated pattern (I_{calc}) meanwhile is represented as a black line. The difference curve ($I_{obs} - I_{calc}$) is shown in cyan. Tick-marks for each phase are also shown for clarity: ε-RDX (black), Pb (red), WC (green) and Ni (blue).

Although there is only a small decrease in molecular volume over the γ → ε transition, and the space group is retained, comparison of the structures shows that there must be a significant rerrangement of the molecules over this transition. At a molecular level this involves a change in molecular conformation: the molecules in ε-RDX adopt the AAA

conformation shown in Figure 3.21, while the molecules in the γ-form adopt either the AAA or AAI conformation. The variation in molecular conformation amongst the different forms of RDX is highlighted by reference to the δ-angle between the plane created by the C-N-C ring atoms and that of the respective nitro groups. These values are presented in Table 3.4 alongside those for the isolated molecule calculated by DFT methods.[38]

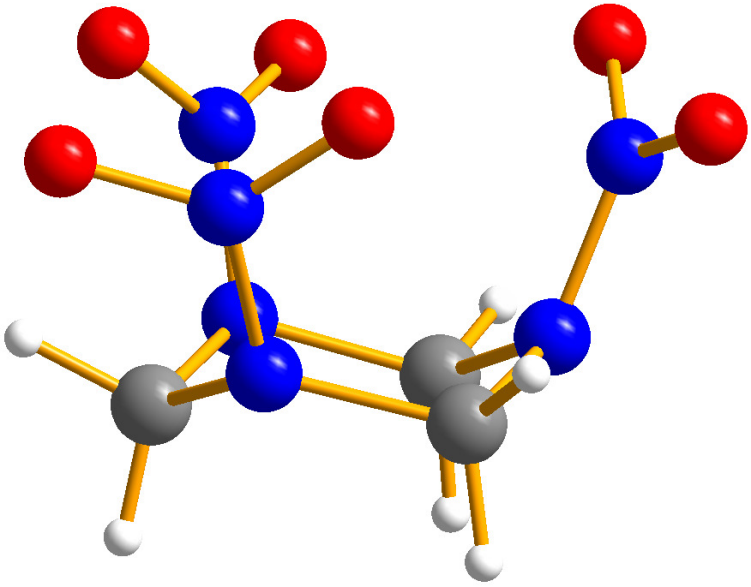

Figure 3.21 AAA molecular conformation observed in ε-RDX.

α-form	β-form molecule 1	β-form molecule 2	γ-form molecule 1	γ-form molecule 2	ε-form	AAA
33.4(1)	39.3(3)	33.4(3)	39.6(7)	36.4(9)	35.5(8)	30.3
33.9(1)	32.4(4)	29.9(3)	17.3(8)	35.5(9)	36.3(9)	30.1
-19.8(1)	28.5(4)	28.7(3)	-2.4(12)	9.5(11)	42.7(9)	29.9

Table 3.4 Values of the angle δ (°) for the molecular conformations observed in α-, β-, γ-, and ε-RDX along with the calculated values for the AAA conformation.[38]

Moreover a major reorientation of at least one of the molecules in γ-RDX must also occur in order to achieve the packing observed in the ε-form (see Figure 3.22). While the two inequivalent molecules in γ-RDX are arranged over a pseudo-inversion centre, the molecules in the ε-form (Z' = 1) adopt a head-to-tail packing arrangement.

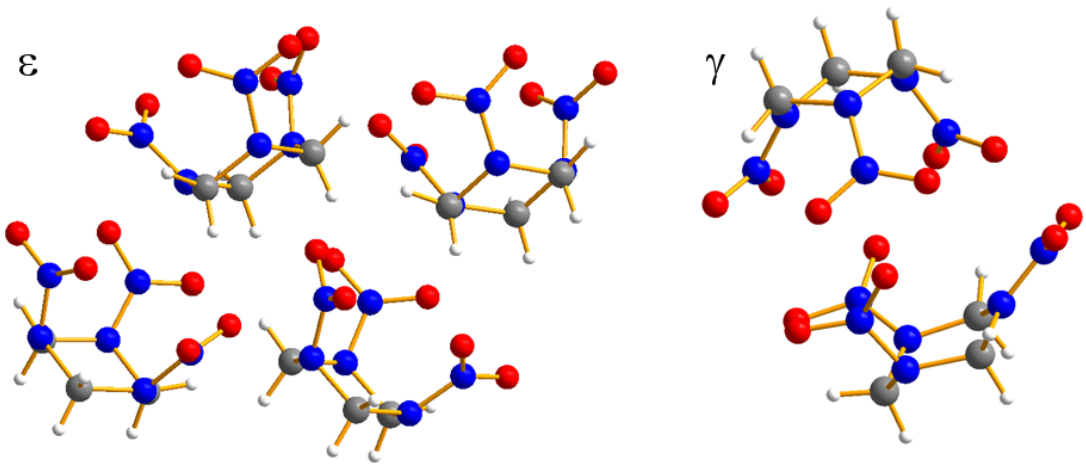

Figure 3.22 (a) 'Head-to-tail' molecular packing in ε-RDX; (b) packing of γ-RDX 'dimers' that are arranged over a pseudo-inversion centre.

The unit cell parameters obtained for ε-RDX from the neutron powder diffraction experiment are presented in Table 3.5 and in Figure 3.23(a). The smooth variation in volume with pressure is also shown in Figure 3.23(b). In order to provide an estimate of the unit cell volume, and hence crystal density, of ε-RDX at atmospheric pressure, these data have been fit to a Murnaghan[5] equation of state (EoS) with V_0 = 808(4) Å^3, B_0 = 10.3(8) GPa and B' = 7.8(3). The most exciting observation, however, is that at every pressure studied ε-RDX is denser than the α-form – this is highlighted by a plot of the molecular volumes with pressure for each polymorph (see Figure 3.24). At 3.65 GPa, the ε-form is 2.2% denser than the α-form (at 3.62 GPa) and even the extrapolated density of the ε-form at ambient pressure indicates that it has a higher density than α-RDX under the same conditions. This result has significant implications: should it be possible to recover ε-RDX to ambient pressures, one would expect this denser form to have a greater detonation velocity.

[5] Although Murnaghan EoS are generally not reliable for compression of greater than 10%, in this case it was necessary to estimate V_0 at zero pressure. Refinement of other formulations gave larger uncertainties in the EoS parameters. Meanwhile, extrapolating V_0 from a 'pressure-normalised' EoS, as outlined in Section 2.6, also introduces greater uncertainties.

P (GPa)	a (Å)	b (Å)	c (Å)	V (Å^3)	wR_p
5.04	7.0655(12)	10.6043(12)	8.8223(12)	661.00(10)	0.0295
4.64	7.0849(17)	10.6373(18)	8.8455(17)	666.64(15)	0.0521
4.33	7.1062(9)	10.6810(9)	8.8608(9)	672.55(8)	0.0239
3.65	7.1355(18)	10.7355(18)	8.8947(17)	681.37(15)	0.0545
3.16	7.1702(12)	10.8038(12)	8.9269(11)	691.53(10)	0.0287
2.89	7.1875(16)	10.8383(17)	8.9471(16)	696.99(14)	0.0459
2.51	7.2164(18)	10.8977(19)	8.9737(17)	705.72(16)	0.0468
2.10	7.2458(12)	10.9616(13)	9.0056(11)	715.27(10)	0.0296
1.80	7.2759(18)	11.0159(20)	9.0294(17)	723.71(16)	0.0522
1.59	7.2975(20)	11.0659(20)	9.0552(19)	731.24(18)	0.0604
1.32	7.3213(12)	11.1235(13)	9.0786(12)	739.35(11)	0.0290
1.23	7.3404(20)	11.1501(20)	9.0891(19)	743.91(18)	0.0490
0.99	7.3589(20)	11.2064(20)	9.1107(20)	751.33(20)	0.0492
0.85	*13.001(3)*	*11.357(3)*	*10.465(2)*	*1546.2(4)*	0.0560
0.00	*13.195(3)*	*11.597(3)*	*10.719(2)*	*1640.2(4)*	0.0422

Table 3.5 Unit cell parameters obtained during the decompression of ε-RDX at ambient temperature, as determined by neutron powder diffraction. Patterns refined using the structure of the α-form have been italicised.

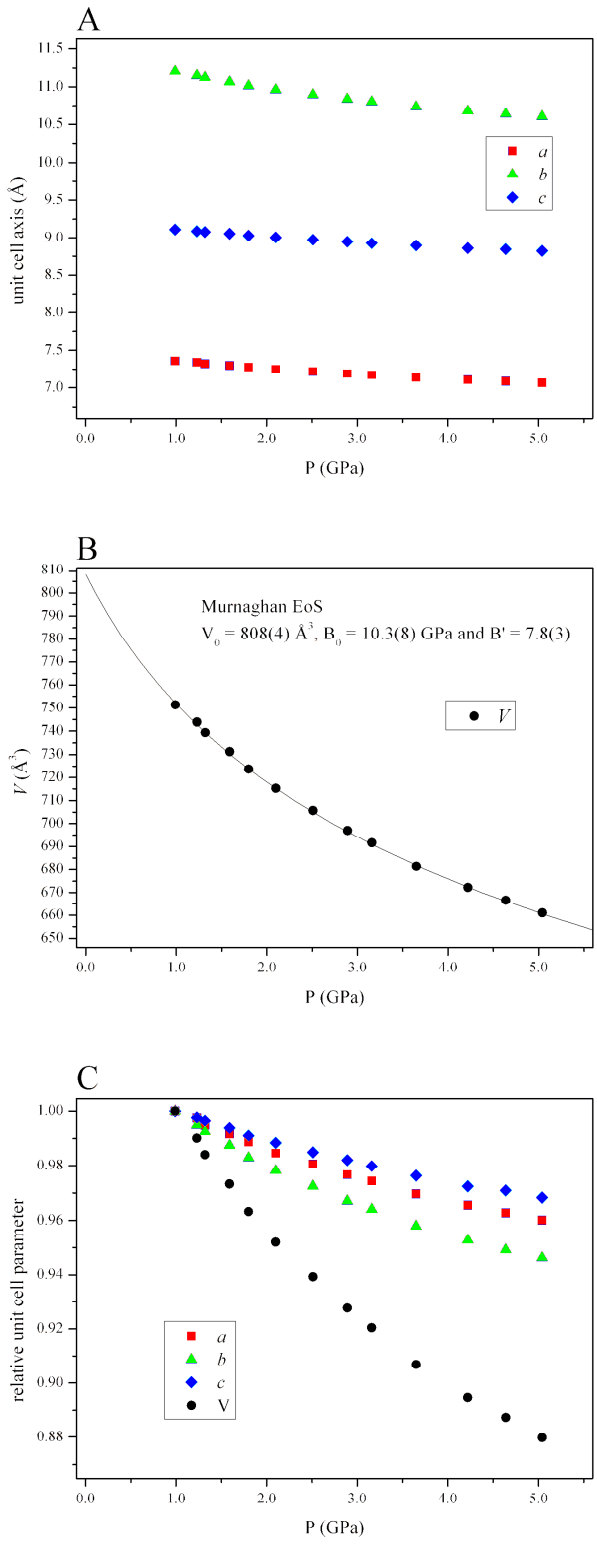

Figure 3.23 Graphical illustration of the decompression of ε-RDX: (a) plot of the unit cell axes, as determined by neutron powder diffraction; (b) the Murnaghan EoS that has been fit to the *PV*-plot; and, (c) the relative contraction of the unit cell parameters, normalised to the lowest pressure dataset (0.99 GPa).

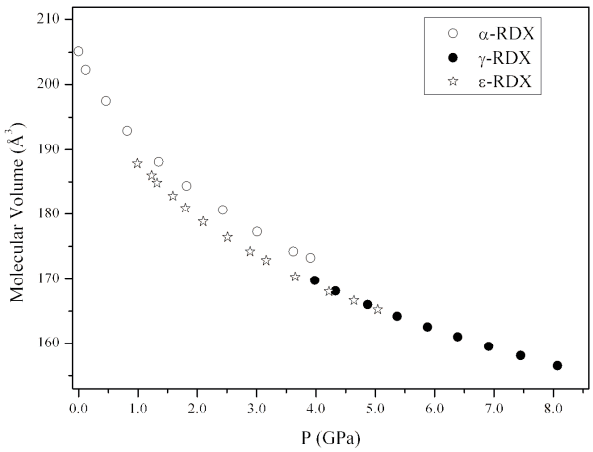

Figure 3.24 Comparison of the variation of the molecular volumes of α-, γ- and ε-RDX-d_6 with pressure.

The observation that the ε-form can be recovered almost to ambient pressure, coupled with Miller's observation that the α → ε transition is reversible at high temperatures, suggests that the ε-form is thermodynamically unstable with respect to the α-form, but may persist due to a significant kinetic barrier. If this interpretation is correct, it is reasonable to suggest that ε-RDX may be recovered to ambient pressure if the decompression were carried out at sub-ambient temperatures. Using the Paris-Edinburgh cell fitted with a variable temperature insert, a sample of ε-RDX-d_6 was formed at elevated temperatures and pressures (as described above) before the sample was gradually decompressed to ambient pressure at 150 K. Diffraction patterns were collected on warming (in 10 K intervals, Figure 3.25) and ε-RDX was observed to persist at ambient pressure up to 230 K, at which point it slowly transformed into the α-form over a period of 2 hours.

Moreover, in order to prove unequivocally that the ε-form is the denser form, the sample of α-RDX was then cooled to 220 K in order to compare the molecular volumes under exactly the same conditions. These results are shown in Table 3.6 and show clearly that the ε-form is 0.86% denser than the α-form. Furthermore it was possible to determine an expression for the volumetric thermal expansion of the ε-form over the temperature range 150 – 220 K ($\alpha_v = \partial (\ln V)/\partial T$ = [1.99(5) + 0.010(5)*(T-185)] x 10^{-4} K^{-1}). Using this expression, it was possible to obtain another estimation of the unit cell volume of ε-RDX at room temperature and ambient pressure: V_0 (293 K) = 819(2) $Å^3$ which is slightly larger than the value calculated from the Birch-Murnaghan EoS (808(4) $Å^3$). This result does, however, further substantiate the expectation that the ε-form would be the denser form at ambient temperature *and* pressure: V_0 = 1641.10 $Å^3$ for α-RDX-d_6 at 293 K.

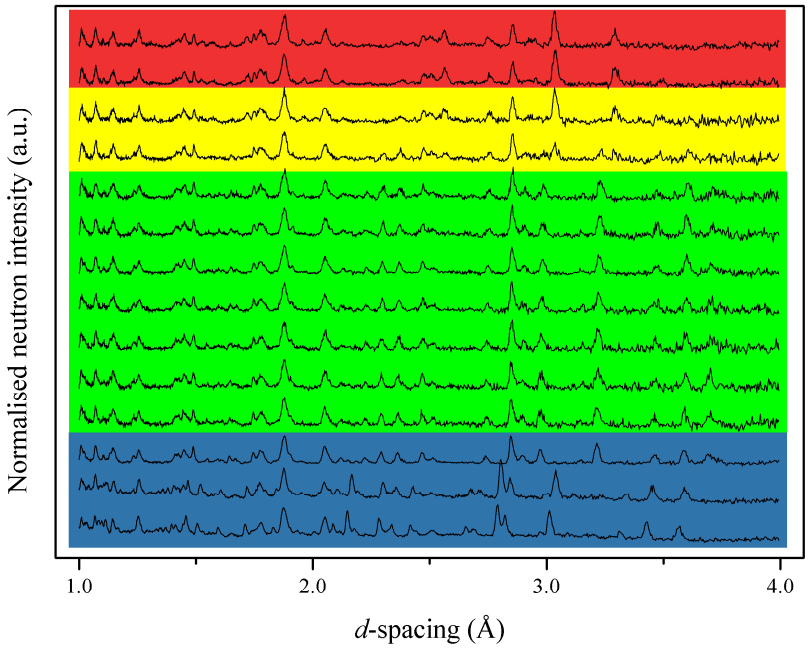

Figure 3.25 Neutron powder diffraction patterns obtained during the decompression of ε-RDX to ambient pressure at 150 K, and the subsequent warming of the sample at ambient pressure. The patterns highlighted in blue were obtained during the decompression of ε-RDX at 150 K (at 3.34, 2.47 and 0.00 GPa, respectively); the patterns shown in green represented the warming of ε-RDX at ambient pressure – data were obtained in 10 K intervals to a maximum of 220 K. Warming to 230 K, however, resulted in the formation of a mixed ε/α-phase and then a pure sample of the α-form. These patterns are shown in yellow. Finally, the sample was warmed to 240 K to ensure complete conversion to α-RDX before a pattern was collected at 220 K to facilitate comparison with the ε-form – these are shown in red. It should be noted that the patterns have been vertically scaled for clarity.

	ε-RDX	α-RDX
Space Group	$Pca2_1$	$Pbca$
a (Å)	7.519(4)	13.166(4)
b (Å)	11.643(5)	11.539(4)
c (Å)	9.177(4)	10.667(3)
V (Å^3)	803.4(4)	1620.6(5)
Z	4	8
D_c (Mg m^{-3})	1.836	1.821

Table 3.6 Comparison of the crystallographic data obtained for ε- and α-RDX at ambient pressure and 220 K.

The observation that ε-RDX can be recovered to ambient pressure and that it has been shown to be denser than the α-form under the exact same conditions has significant implications. This 'proof-of-concept' experiment has shown that the recovery of high-pressure

polymorphs is a viable route to novel materials, potentially with improved performance, and these studies are currently being extended to other energetic materials with a view to improving their performance.

3.5.3 δ-RDX: the very-high-pressure form of RDX

After the successful determination of the structures of the γ-, β-, and ε-forms of RDX [37, 87, 88], it was thought prudent to investigate the polymorphism of RDX under very high pressures (up to ~ 20 GPa). High-pressure X-ray powder diffraction experiments were carried out at the Extreme Conditions (I15) and High Resolution Powder Diffraction (I11) Beamlines at Diamond Light Source. In each case polycrystalline RDX was loaded into a Merrill-Bassett diamond-anvil cell (DAC) and pre-compressed to the maximum pressure studied. The studies undertaken at I15 used methanol:ethanol (4:1) as the pressure-transmitting medium, despite pressure-induced freezing of the pressure medium being reported to occur ~9.8 GPa at ambient temperature.[89] No medium was used in the I11 study in order to investigate any possible structural changes induced by compression to ~ 20 GPa under non-hydrostatic conditions.

Multiplots of the patterns collected at the two beamlines can be found in Figure 3.26. On initial inspection it does not appear that there are any significant changes (other than the α → γ phase transition) in the diffraction patterns over this pressure range, although peak broadening under these non-hydrostatic conditions results in much lower resolution. It is interesting to note that both the α- and γ-polymorphs are present in the diffraction pattern collected at 5.8 GPa in the I15 experiment. This implies that there is a signicant pressure gradient within the sample in this experiment (of ~ 2.0 GPa) as α-RDX has never been observed to exist beyond 3.9 GPa.[29-31, 37]

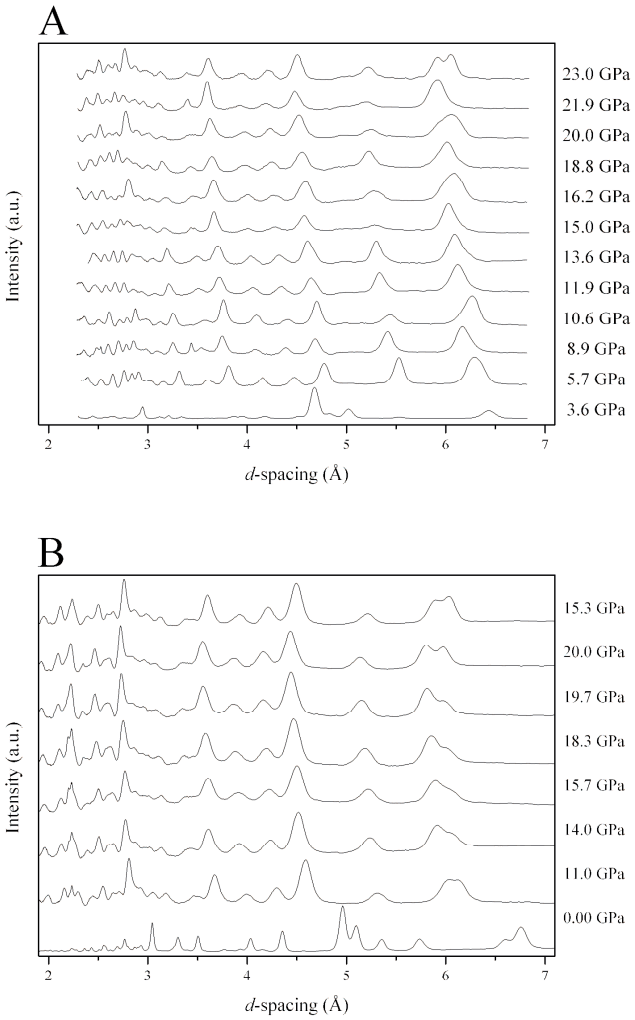

Figure 3.26 Series of diffraction patterns (scaled vertically) collected during the decompression of RDX: (a) from 23.0 GPa using MeOH:EtOH (4:1) on the Extreme Conditions Beamline (I15); (b) from 20.0 GPa on the High Resolution Powder Diffraction Beamline (I11), where no pressure medium was employed. In both experiments the diffraction pattern collected at the lowest pressure was successfully refined using the α-RDX structural model; all other patterns were indexed to the γ-form.

It was possible to perform Le Bail refinements on all of the patterns collected using the unit cell indexing of either the α-form (for patterns collected below 3.9 GPa) or the γ-form (all other patterns) confirming that no phase transitions to the reported δ-form occurred within the pressure range of this work. Unfortunately the low resolution of the powder patterns meant that Rietveld refinements were not sufficiently stable; it was therefore not possible to refine atomic positions, but inspection of the data showed that all peaks were modelled satisfactorily and that there were no extraneous peaks that may be indicative of a significant change in molecular geometry and/or molecular packing. The unit cell parameters are presented as a function of pressure in Table 3.7. The significant variation in the compression

behaviour of the different samples is particularly evident when all of the unit cell data are presented on one plot, as in Figure 3.27(a)-(d), which includes the unit cell compression of a sample of RDX-d_6 as determined by neutron powder diffraction.[37]

P (GPa)	a (Å)	b (Å)	c (Å)	V (Å^3)	wR_p	R_p	χ^2
2.9	*12.852(4)*	*11.115(3)*	*10.188(3)*	*1455.4(8)*	0.0838	0.0584	1.133
5.8	*12.705(11)* 12.732(5)	*11.002(9)* 9.513(3)	*9.953(7)* 11.133(4)	*1391.2(14)* 1348.4(7)	0.2300	0.1407	29.65
6.7	12.680(4)	9.639(3)	10.979(3)	1341.8(6)	0.1143	0.0704	6.640
8.8	12.566(4)	9.486(3)	10.858(3)	1294.2(7)	0.1255	0.0791	7.033
10.0	12.495(4)	9.408(4)	10.782(4)	1267.5(8)	0.1856	0.1064	13.91
10.8	12.443(4)	9.349(4)	10.723(4)	1247.4(7)	0.1517	0.1001	8.869
13.1	12.283(6)	9.223(5)	10.569(5)	1197.3(10)	0.2197	0.1131	10.57
3.6	*12.844(3)*	*11.010(3)*	*10.046(10)*	*1420.6(5)*	0.1323	0.0957	0.540
5.7	12.622(10)	9.542(11)	11.023(12)	1331.8(15)	0.1757	0.1146	7.125
8.9	12.474(7)	9.372(8)	10.824(8)	1265.4(16)	0.1702	0.1055	6.955
10.6	12.550(6)	9.433(7)	10.840(6)	1283.3(14)	0.1292	0.0945	3.304
11.9	12.309(8)	9.255(10)	10.732(12)	1222.7(14)	0.2164	0.1392	10.06
13.6	12.385(7)	9.284(9)	10.588(90	1217.5(13)	0.2610	0.1570	14.63
15.0	12.182(9)	9.174(9)	10.574(8)	1181.6(19)	0.1543	0.1052	5.162
16.2	12.229(10)	9.093(10)	10.576(10)	1176.1(20)	0.1657	0.1129	6.353
18.8	12.126(10)	9.108(10)	10.479(10)	1157.4(20)	0.1093	0.0864	3.370
20.0	12.130(6)	8.989(6)	10.452(5)	1139.7(11)	0.0903	0.0622	2.205
21.9	11.987(90	8.988(9)	10.365(9)	1116.7(19)	0.1210	0.0897	3.606
23.0	12.083(5)	8.976(5)	10.395(5)	1127.4(10)	0.1436	0.0933	5.045

Table 3.7 Unit cell parameters (a, b, c and V) as determined by Le Bail refinement of the X-ray powder diffraction patterns collected during compression of RDX in MeOH:EtOH. The two compression studies have been separated for clarity. The patterns that have been refined using the α-structure have been italicised, with the pattern at 5.8 GPa being refined as a mixed phase of α- and γ-RDX.

P (GPa)	a (Å)	b (Å)	c (Å)	V (Å^3)	wR_p	R_p	χ^2
15.3	12.052(8)	8.947(7)	10.362(7)	1117.4(14)	0.1247	0.0826	1.267
20.0	11.924(9)	8.861(9)	10.160(9)	1073.5(16)	0.1703	0.1024	2.311
19.7	11.976(8)	8.827(9)	10.188(9)	1077.0(10)	0.1177	0.0769	1.001
18.3	12.038(10)	8.901(10)	10.282(11)	1101.7(19)	0.2104	0.0987	3.024
15.7	12.126(10)	8.958(9)	10.354(13)	1124.6(20)	0.0848	0.0572	0.748
14.0	12.116(9)	9.012(10)	10.355(10)	1130.6(18)	0.3019	0.1691	7.884
11.0	12.271(6)	9.184(7)	10.569(7)	1191.0(8)	0.1237	0.0847	1.185
0.0	*13.195(4)*	*11.593(3)*	*10.706(3)*	*1637.6(7)*	0.1384	0.0974	0.404

Table 3.8 Unit cell parameters (a, b, c and V) as determined by Le Bail refinement of the X-ray powder diffraction patterns collected during compression of RDX in the absence of pressure-transmitting medium. In this experiment, the sample was pre-compressed to 15.3 GPa before the pressure was increased to 20.0 GPa. Subsequent data collections were performed upon decompression.

In order to compare to the equation of state determined for RDX-d_6, the variation in unit cell volume with pressure in each case was fitted to a 3rd-order Birch-Murnaghan EoS, in which V_0 was fixed to the value determined by Oswald *et al*.[39] These are presented as insets in the respective *PV* plots, Figure 3.28. Following the procedure described by Oswald *et al*., equations of state were also refined by fixing B' to be the value determined for the γ-form at lower pressure (*i.e.* 11.26). However, this resulted in unsatisfactorily large uncertainties in the parameters V_0 and B_0 and visual inspection of the data showed that this did not accurately describe the compression behaviour. A direct comparison of the EoS for RDX-h_6 (this study) and RDX-d_6 can also be found in Figure 3.28(c).

Close inspection of the compression behaviour shown in Figure 3.27 and Figure 3.28 shows that there is a marked difference between the study in which no pressure-transmitting medium was employed and the compressions conducted in MeOH:EtOH (I15). The unit cell volumes determined in the non-hydrostatic compression (I11) are consistently lower than those measured at I15, especially at pressures greater than 10 GPa. This is particularly striking evidence of the effect of non-hydrostatic conditions on the crystal structure of the material under investigation. The development of deviatoric strains under these conditions will result in a pressure gradient across the cell. Therefore, the pressures experienced by the sample at the centre of the gasket (*i.e*. the volume being sampled during the X-ray diffraction experiment) will, most likely, be greater than those recorded by the fluoresence of a ruby chip placed near the gasket edge.[90] Furthermore, the broadening of the ruby fluorescence signal under non-hydrostatic compression greatly increases the uncertainty in the pressure

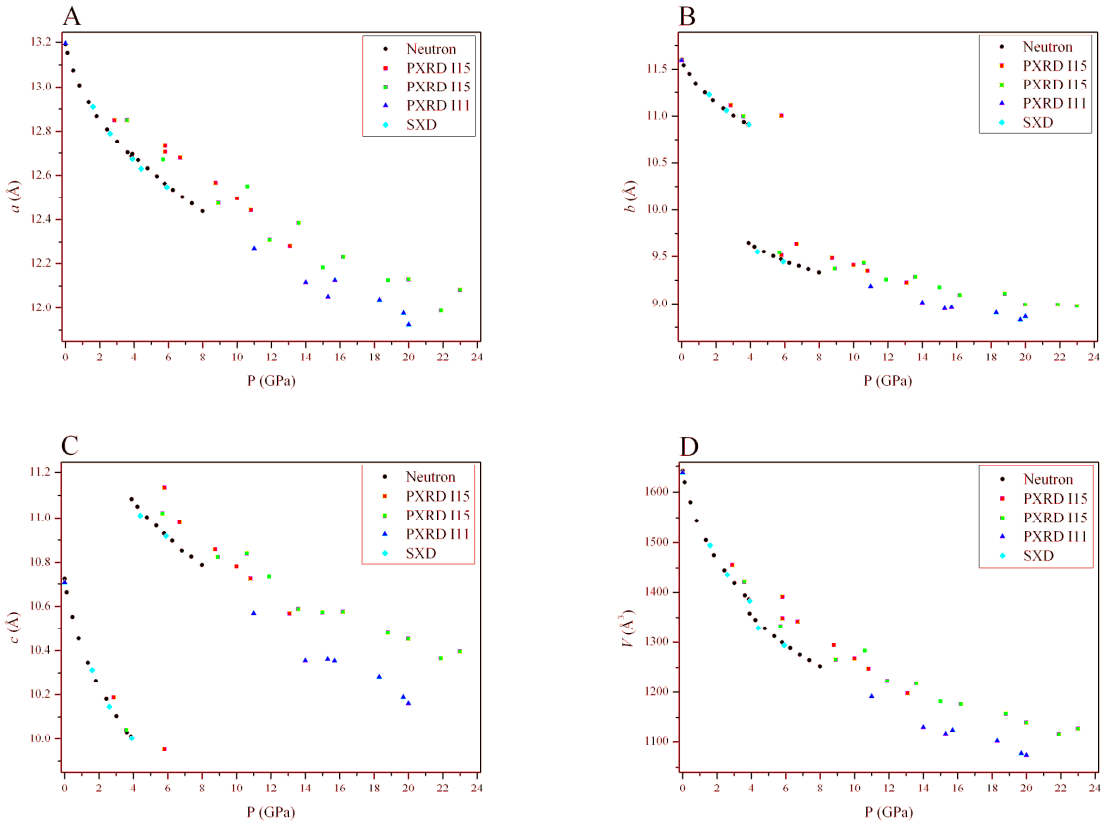

Figure 3.27 Variation in RDX unit cell parameters with pressure, as determined by Rietveld refinement of the X-ray powder diffraction patterns collected during both studies (with MeOH:EtOH and without pressure-transmitting medium). In addition, the unit cell compression of RDX-d_6 as determined by neutron powder diffraction [37] has been included, along with single-crystal X-ray data (SXD) collected on an APEX-II laboratory source (Mo Kα) [60], using MeOH:EtOH as pressure-transmitting medium.

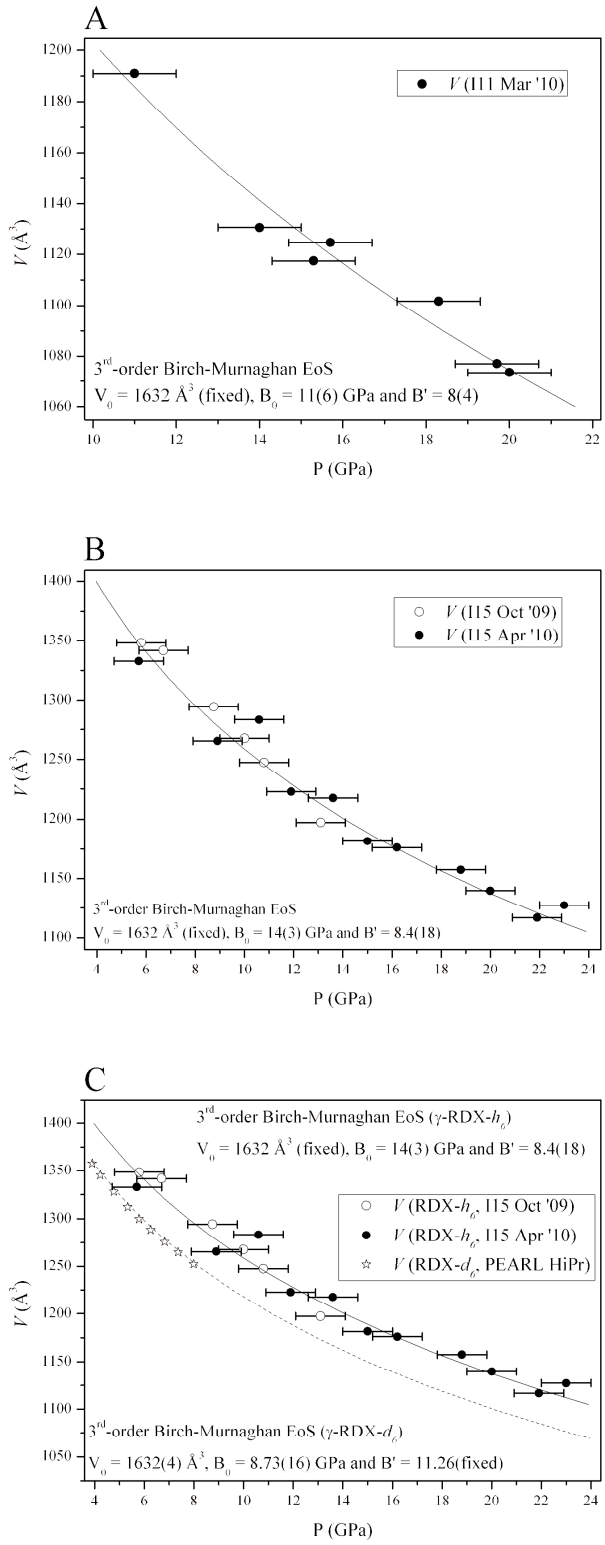

Figure 3.28 Compression of γ-RDX: (a) powder X-ray diffraction (PXRD) study conducted on RDX-h_6 (no pressure-transmitting medium); (b) PXRD study of RDX-h_6 compressed in MeOH:EtOH; and, (c) comparison of the EoS obtained for RDX-h_6 with that for RDX-d_6 reported in [39]. An uncertainty of ±1.0 GPa in the pressure measurements of the current study was used in the least squares refinement of the EoS; errors in V were smaller than the data symbols shown here.

measurement. It was therefore necessary to include a pressure error of ± 1.0 GPa in the least squares refinement of the equations of state (this has been reflected in the *PV*-plots below).

In addition, one may suggest that the influence of the pressure-transmitting medium at these elevated pressures may have greater consequences than has previously been anticipated. For example, it may be the case that the frozen pressure medium results in a pressure-hardening of the sample:medium matrix. An alternative interpretation is that the pressure medium may in fact be interacting with the sample, thus augmenting the sample's inherent resistance to compression. However, it should be noted that no extraneous peaks were observed in the patterns collected during compression indicating that solvate formation did not occur, certainly in the bulk material.

While the bulk moduli determined for the X-ray diffraction experiments are within error of each other [11(6) and 14(3) GPa], it is interesting to note that the B_0 reported by Oswald e*t al.* is significantly smaller [8.73(16) GPa] than the I15 study. This indicates that RDX is perhaps more resistant to compression than previously suggested, particularly in this higher pressure regime. This clearly underlines the importance of conducting compression studies to the highest possible/practicable pressures in order to gain an accurate representation of the structural response to pressure. This is especially true for high-pressure studies of energetic materials since these compounds may experience pressures in the range 10 – 100 GPa during detonation. However, in order to obtain more precise determinations of the bulk modulus (as well as V_0 and B'), it is still essential to obtain high quality diffraction data at minimal pressure. It is clear, therefore, that the current study should complement the existing compression data.

Nevertheless, the most important result of this study is that no evidence of a phase transition to δ-RDX was observed *ca* 18 GPa. It is certainly possible, however, that this phase transition may have been suppressed by the non-hydrostatic conditions, particularly if the transition involves a significant degree of molecular rearrangement. In their spectroscopic study of RDX (at pressures comparable to those recorded in this work), Ciezak *et al.* employed helium[6] as the pressure-transmitting medium, thus ensuring hydrostatic conditions in this pressure regime.[33, 34] At these elevated pressures, however, it may be possible that the helium pressure-transmitting medium may actually have an implict role in the $\gamma \rightarrow \delta$ transition by interacting with or even permeating the crystal lattice. Such a phenomenon has

[6] Helium has been shown to maintain hydrostaticity beyond 20 GPa, despite its pressure-induced solidification at 12.1 GPa. (Klotz *et al*., ref. [14] Chapter 2).

even been observed in MeOH:EtOH recently, whereupon a methanol solvate was formed by the application of pressure alone.[91]

Despite this marked difference in compression behaviour, the current study also complements Ciezak's spectroscopic investigation since it not only highlights the importance of choosing the pressure medium that is most suitable for the desired pressure range but also intimates that the role of the pressure medium should not be underestimated. It would therefore be extremely valuable to conduct a diffraction study of RDX to 20 GPa using He as the pressure medium in order to characterise the $\gamma \rightarrow \delta$ transition fully.

3.6 Conclusions

The structural data presented herein represent a signifcant contribution to the understanding of RDX under extreme conditions and will be valuable to scientists with a wide range of research interests: not only energetic materials but also those interested in understanding molecular compounds under extremes of temperature and/or pressure and the development of high-pressure technology and expertise.

The structure of the highly metastable β-RDX at ambient conditions has been determined – a significant achievement given the elusive nature of this polymorph. Although β-RDX has also been shown to be very prone to transform to the more stable α-form and hence is unlikely to be found in RDX munitions, the reconstructive nature of this transition may have significant implications for sensitivity and performance. The phase history of RDX samples may therefore be an important factor influencing the sensitivity of these samples to initiation.

Furthermore it has been shown that the β-form at ambient conditions is distinct from the high-pressure/high-temperature polymorph with which it has previously been confused. This form has now been re-named ε-RDX and has been structurally characterised by complementary X-ray single-crystal and neutron powder diffraction. The internationally unique capability of rapid heating and cooling *in situ* on the PEARL beamline (a technical development stimulated, in part, by this research programme) was exploited for the recovery of the ε-form to ambient pressure. Structural characterisation at ambient pressure (220 K) has also shown unequivocally that ε-RDX is denser than the α-form and would therefore be expected to exhibit a greater detonation velocity. This result is illustrative of the unrivalled opportunity that high-pressure techniques present for the recovery of novel materials with improved performance without the need for changing molecular structures.

X-ray diffraction studies of RDX have been extended to a pressure of ~20 GPa. Other than the $\alpha \rightarrow \gamma$ transition at 3.9 GPa, no phase transitions were observed although significant

differences in the compressibility of RDX were observed depending on whether a pressure-transmitting medium was used. Given this observation it is reasonable to suggest that δ-RDX may be observed in systems using different media and the pressures at which the γ → δ transition occurs may also be dependent on pressure media.

Finally, this study now allows the crystallographic data for the four polymorphs of RDX that have been structurally characterised to be summarised in Table 3.9.

	α-RDX	β-RDX	γ-RDX [37]	ε-RDX
Space Group	*Pbca*	$Pca2_1$	$Pca2_1$	$Pca2_1$
a (Å)	13.166(4)	15.1267(11)	12.5650(19)	7.519(4)
b (Å)	11.539(4)	7.4563(6)	9.4769(6)	11.643(5)
c (Å)	10.667(3)	14.3719(11)	10.9297(9)	9.177(4)
V (Å^3)	1620.6(5)	1621.0(2)	1301.5(2)	803.4(4)
Z	8	8	8	4
T (K)	220	150	293	220

Table 3.9 Crystallographic data for the four structurally characterised polymorphs of RDX. The data presented for the α-, γ- and ε-forms pertain to perdeuterated samples, while data collections for the β-form were performed on RDX-h_6. All data collections were performed at ambient pressure, except for γ-RDX – these data are correct at 5.2 GPa.

3.7 Suggestions for Further Work

The structural characterisation of the highly metastable β-form of RDX has presented the opportunity to explore, by diffraction methods, the effect that this form and the reconstructive β → α transition have on the crystal quality of commercial samples of RDX. This has obvious implications for performance, particularly sensitivity. It would therefore be extremely valuable to conduct whole powder pattern modelling on high-resolution powder diffraction data collected for not only the β-form but also samples of the α-form that have previously undergone the β → α transition. Comparison of these patterns with data collected for commercial samples of RDX would highlight any factors that may adversely affect performance, such as crystal defects. Such studies may also provide an experimental rationale for the observed insensitivity of RS-RDX, especially if one could reconcile this behaviour with the synthetic procedure. Finally, sensitivity studies should be conducted on these samples in order to provide a definitive assessment of the effect the β-form has on RDX sensitivity.

It would also be extremely valuable to conduct single-crystal X-ray diffraction studies on β-RDX using synchrotron radiation, particularly at very low temperatures. This would certainly facilitate the accurate determination of any disorder that exists within the structure

and will provide high-quality experimental evidence to complement the molecular dynamics simulations conducted in this study. High-temperature powder diffraction studies would also allow the verification of the spectroscopic observations of Infante-Castillo *et al*., who have reported an α → β solid-solid phase transition at 477 K.[28] Comparison of the powder diffraction patterns collected in this way with the simulated pattern calculated using the β-structure would either confirm their assertion or provide evidence for yet another polymorph of RDX. Finally, should it be possible to load a single crystal of β-RDX into a diamond-anvil cell, a high-pressure study of this metastable form may result in further polymorphic transitions that may not be accessible by the compression of α-RDX.

The recovery of ε-RDX to ambient pressure, its stability on warming to 220 K and its greater density (compared to the α-form) means that this represents a tantalising opportunity for revolutionising RDX munitions by the incorporation of a more powerful polymorph. In order to make ε-RDX viable for use in explosive formulation it will be necessary to explore the stabilisation of this high-pressure/high-temperature form, perhaps by the inclusion of an additive as has been successful in the desensitisation of ammonium nitrate (see Section 1.2.2). This doping approach, however, will be far from trivial since the ε-form has only ever been formed at extreme conditions, thus requiring the dopant be included in the sample before it is compressed and heated. Such an addition may dramatically affect the phase behaviour at elevated temperatures and pressures and it is, therefore, extremely difficult to predict the outcome of this experiment. An alternative approach would be to recover a sample of ε-RDX to ambient pressure (at low temperature) by the approach detailed in this work and subsequently perform doping at ambient pressure. This stabilised sample of ε-RDX could then potentially be used to seed batches of RDX to promote the large-scale crystallisation of ε-RDX. Of course, should this be successful, it will be necessary to conduct thorough testing of its thermal stability (primarily with respect to the α-form) as well as its sensitivity and detonation characteristics.

The structural characterisation of the β- and ε-forms at ambient pressure (150 K) now means that it will be possible to conduct density functional theory (DFT) calculations to determine the relative energies of these polymorphs with respect to α-RDX. These calculations will also provide an insight into the barriers to conversion that exist between the forms at ambient pressure. Furthermore, these values may be compared to the theoretically derived energy barriers published by Vladimiroff and Rice.[38]

In addition to the calculation of the relative energies under the same conditions, it would be extremely useful to conduct PIXEL calculations (see Section 1.3.2) to rationalise the phase

transitions at elevated temperatures and pressures.[92] Not only would these calculations provide an important insight into the reversible α → γ transition (at 3.9 GPa), but they would also shed light on the formation of the ε-form at elevated temperatures and pressures. Moreover, the large hysteresis during the decompression of ε-RDX is of particular interest, especially since an ε → γ transition is not observed. It would therefore be extremely interesting to assess the barriers to re-conversion of the ε-form to either γ- or α-RDX.

Finally, an X-ray powder diffraction study of RDX compressed to *ca* 20 GPa in helium is already planned. By re-creating the conditions under which δ-RDX has been observed spectroscopically, it is hoped that structural information on this form can be obtained. This would be a significant achievement as it would not only extend dramatically the pressure range for which the structural characterisation has been achieved for any energetic material but would also represent the completion of the (current) RDX phase diagram.

3.8 References

1. Henning, *German Patent, 104, 280*, 1899
2. Herz, *Swiss Patent, 88, 759*, 1920
3. Herz, *Chem. Zentr.*, 1921, **92**, 926.
4. W.E. Bachmann and J.C. Sheehan, *J.Am. Chem. Soc.*, 1949, **71**, 1842.
5. J. Akhavan, *The Chemistry of Explosives*, Royal Society of Chemistry, Cambridge, UK, 2004, 2nd edn.
6. A. Freche, J. Aviles, L. Donnio, and C. Spyckerelle, *Insensitive RDX (I-RDX)* in *Insensitive Munitions and Energetic Materials Symposium*, 2000, San Antonio, TX, USA.
7. P. Sjöberg, H. Hytti, R. Strandberg, A. Kariniemi, and M. Muilu, *PBX with Insensitive RDX - A New EIDS Substance for Underwater Use* in *International Annual Conference of ICT*, 2002, Karlsruhe, Germany.
8. T. Halvorsen, *Improved RDX, Properties and Processability* in *International Annual Conference of ICT*, 2002, Karlsruhe, Germany.
9. I.J. Lochert, R.M. Dexter, and B.L. Hamshere, *Evaluation of Australian RDX in PBXN-109*, Defence Science and Technology Organisation, Edinburgh, SA, Australia, DSTO-TN-0440, 2002.
10. D. Watt, F. Peugeot, R. Doherty, M. Sharp, D. Topler, and D. Tucker, *Reduced Sensitivity RDX- Where are we?* in *International Annual Conference of ICT*, 2004, Karlsruhe, Germany.
11. R.M. Doherty and D.S. Watt, *Propellants, Explos., Pyrotech.*, 2008, **33**, 4.
12. J.A. Ciezak and S.F. Trevino, *J. Phys. Chem. A*, 2006, **110**, 5149.
13. L. Pacheco-Londoño, W. Ortiz-Rivera, O. Primera-Pedrozo, and S. Hernández-Rivera, *Anal. Bioanal.Chem.*, 2009, **395**, 323.
14. R. Infante-Castillo, L. Pacheco-Londoño, and S.P. Hernández-Rivera, *Spectrochim. Acta, Part A*, 2010, **76**, 137.
15. I.F. Shishkov, L.V. Vilkov, M. Kolonits, and B. Rozsondai, *Struct. Chem.*, 1991, **2**, 57.
16. Y. Oyumi and T.B. Brill, *Combust. Flame*, 1985, **62**, 213.
17. T.R. Botcher and C.A. Wight, *J. Phys. Chem.*, 1994, **98**, 5441.

18. D. Chakraborty, R.P. Muller, S. Dasgupta, and W.A. Goddard, *J. Phys. Chem. A*, 2000, **104**, 2261.
19. E.P.H. Best, K.N. Geter, H.E. Tatem, and B.K. Lane, *Chemosphere*, 2006, **62**, 616.
20. X. Pan, B. Zhang, J.N. Smith, M.S. Francisco, T.A. Anderson, and G.P. Cobb, *Chemosphere*, 2007, **67**, 1164.
21. M. Vila, S. Lorber-Pascal, and F. Laurent, *Environ. Pollut.*, 2007, **148**, 148.
22. C.S. Choi and E. Prince, *Acta Cryst.*, 1972, **B28**, 2857.
23. P. Hakey, W. Ouellette, J. Zubieta, and T. Korter, *Acta Cryst.*, 2008, **E64**, o1428.
24. W.C. McCrone, *Anal. Chem.*, 1950, **22**, 954.
25. R.J. Karpowicz, S.T. Sergio, and T.B. Brill, *Ind. Eng. Chem. Prod. Res. Dev.*, 1983, **22**, 363.
26. R.J. Karpowicz and T.B. Brill, *J. Phys. Chem.*, 1984, **88**, 348.
27. P. Torres, L. Mercado, I. Cotte, S.P. Hernandez, N. Mina, A. Santana, R.T. Chamberlain, R. Lareau, and M.E. Castro, *J. Phys. Chem. B*, 2004, **108**, 8799.
28. R. Infante-Castillo, L.C. Pacheco-Londoño, and S.P. Hernández-Rivera, *J. Mol. Struct.*, 2010, **970**, 51.
29. B. Olinger, B. Roof, and H. Cady, in *Symposium International Sur Le Comportement Des Milieux Denses Sous Hautes Pressions Dynamiques*, 1978, Paris, France.
30. C.S. Yoo, H. Cynn, W.M. Howard, and N. Holmes, *Equations of State of Unreacted High Explosives at High Pressures* in *Proceedings of the 11th International Detonation Symposium*, 1998, USA.
31. B.J. Baer, J. Oxley, and M. Nicol, *High Pressure Res.*, 1990, **2**, 99.
32. P.J. Miller, S. Block, and G.J. Piermarini, *Combust. Flame*, 1991, **83**, 174.
33. J.A. Ciezak, T.A. Jenkins, Z. Liu, and R.J. Hemley, *J. Phys. Chem. A*, 2007, **111**, 59.
34. J.A. Ciezak and T.A. Jenkins, *Propellants, Explos., Pyrotech.*, 2008, **33**, 390.
35. Z.A. Dreger and Y.M. Gupta, *J. Phys. Chem. B*, 2007, **111**, 3893.
36. N. Goto, H. Fujihisa, H. Yamawaki, K. Wakabayashi, Y. Nakayama, M. Yoshida, and M. Koshi, *J. Phys. Chem. B*, 2006, **110**, 23655.
37. A.J. Davidson, I.D.H. Oswald, D.J. Francis, A.R. Lennie, W.G. Marshall, D.I.A. Millar, C.R. Pulham, J.E. Warren, and A.S. Cumming, *CrystEngComm*, 2008, **10**, 162.
38. T. Vladimiroff and B.M. Rice, *J. Phys. Chem. A*, 2002, **106**, 10437.
39. I.D.H. Oswald, D.I.A. Millar, A.J. Davidson, D.J. Francis, W.G. Marshall, C.R. Pulham, A. Cumming, A.R. Lennie, and J.E. Warren, *High Pressure Res.*, 2010, **30**, 280
40. T.D. Sewell, *J. Appl. Phys.*, 1998, **83**, 4142.
41. D.C. Sorescu, B.M. Rice, and D.L. Thompson, *J. Phys. Chem. B*, 1999, **103**, 6783.
42. T.D. Sewell and C.M. Bennett, *J. Appl. Phys.*, 2000, **88**, 88.
43. P.M. Agrawal, B.M. Rice, L. Zheng, and D.L. Thompson, *J. Phys. Chem. B*, 2006, **110**, 26185.
44. E.F.C. Byrd and B.M. Rice, *J. Phys. Chem. C*, 2007, **111**, 2787.
45. M.W. Conroy, I.I. Oleynik, S.V. Zybin, and C.T. White, *J. Appl. Phys.*, 2008, **104**, 113501.
46. M.S. Miao, Z.A. Dreger, J.M. Winey, and Y.M. Gupta, *J. Phys. Chem. A*, 2008, **112**, 12228.
47. D.C. Sorescu and B.M. Rice, *J. Phys. Chem. C*, 2010, **114**, 6734.
48. S. Grimme, *J. Comput. Chem.*, 2006, **27**, 1787.
49. V. Barone, M. Casarin, D. Forrer, M. Pavone, M. Sambi, and A. Vittadini, *J. Comput. Chem.*, 2009, **30**, 934.
50. J.E. Patterson, Z.A. Dreger, and Y.M. Gupta, *J. Phys. Chem. B*, 2007, **111**, 10897.
51. Z.A. Dreger, J.E. Patterson, and Y.M. Gupta, *J. Phys.: Conf. Ser.*, 2008, **121**, 042012.

52. M. Miao, Z.A. Dreger, J.E. Patterson, and Y.M. Gupta, *J. Phys. Chem. A*, 2008, **112**, 7383.
53. J.E. Patterson, Z.A. Dreger, M. Miao, and Y.M. Gupta, *J. Phys. Chem. A*, 2008, **112**, 7374.
54. S. Bulusu, J. Autera, and T. Axenrod, *J. Labelled Compd. Radiopharm.*, 1980, **17**, 707.
55. J.M. Besson, R.J. Nelmes, G. Hamel, J.S. Loveday, G. Weill, and S. Hull, *Physica B*, 1992, **180-181**, 907.
56. W.G. Marshall, D.J. Francis, C.J. Barry, O. Kirichek, C.R. Pulham, and M.G. Tucker, *manuscript in preparation*, 2010.
57. W.G. Marshall and D.J. Francis, *J. Appl. Crystallogr.*, 2002, **35**, 122.
58. A.D. Fortes, PhD Thesis, 2004, Department of Earth Sciences, University College, London, UK.
59. R. Von Dreele and A.C. Larson, *General Structure Analysis System (GSAS)*, 1986.
60. Bruker-Nonius, *APEX-II*, Bruker-AXS, Madison, WI, USA, 2000.
61. J. Cosier and A.M. Glazer, *J. Appl. Crystallogr.*, 1986, **19**, 105.
62. A. Altomare, G. Cascarano, C. Giacovazzo, A. Guagliardi, M.C. Burla, G. Polidori, and M. Camalli, *J. Appl. Crystallogr.*, 1994, **27**, 435.
63. P.W. Betteridge, J.R. Carruthers, R.I. Cooper, K. Prout, and D.J. Watkin, *J. Appl. Crystallogr.*, 2003, **36**, 1487.
64. L. Merrill and W.A. Bassett, *Rev. Sci. Instrum.*, 1974, **45**, 290.
65. S.A. Moggach, D.R. Allan, S. Parsons, and J.E. Warren, *J. Appl. Crystallogr.*, 2008, **41**, 249.
66. G.J. Piermarini, S. Block, J.D. Barnett, and R.A. Forman, *J. Appl. Phys.*, 1975, **46**, 2774.
67. A. Dawson, D.R. Allan, S. Parsons, and M. Ruf, *J. Appl. Crystallogr.*, 2004, **37**, 410.
68. Bruker-AXS, *SAINT*, Bruker-AXS, Madison, WI, USA, 2003.
69. S. Parsons, *SHADE, Program for Empirical Absorption Corrections to High Pressure Data*, The University of Edinburgh, UK, 2004.
70. G.M. Sheldrick, *SADABS*, University of Göttingen, Germany, 2004.
71. A.P. Hammersley, S.O. Svensson, M. Hanfland, A.N. Fitch, and D. Hausermann, *High Press. Res.*, 1996, **14**, 235
72. CPMD, 2008, IBM Corp. 1990-2008 and MPI für Festkörperforschung Stuttgart 1997-2001.
73. J.P. Perdew, K. Burke, and M. Ernzerhof, *Phys. Rev. Lett.*, 1996, **77**, 3865.
74. M. Elstner, P. Hobza, T. Frauenheim, S. Suhai, and E. Kaxiras, *J. Chem. Phys.*, 2001, **114**, 5149.
75. A.M. Reilly, PhD Thesis, 2009, School of Chemistry, University of Edinburgh.
76. J.S. Capes and R.E. Cameron, *Cryst. Growth. Des.*, 2006, **7**, 108.
77. A.M. Reilly, S. Habershon, C.A. Morrison, and D.W.H. Rankin, *J. Chem. Phys.*, 2010, **132**, 094502.
78. A.M. Reilly, S. Habershon, C.A. Morrison, and D.W.H. Rankin, *J. Chem. Phys.*, 2010, **132**, 134511.
79. D.D. Dlott and M.D. Fayer, *J. Chem. Phys.*, 1990, **92**, 3798.
80. L.N. Erofeev, Y.P. Tarasov, Y.B. Kalmykov, Y. Shu, V.V. Dubikhin, and G.M. Nazin, *Russ. Chem. Bull.*, 2001, **50**, 1000.
81. P. Scardi and M. Leoni, *Acta Cryst.*, 2002, **A58**, 190.
82. M. Herrmann, *Part. Part. Syst. Charact.*, 2005, **22**, 401.
83. Z.A. Dreger and Y.M. Gupta, *J. Phys. Chem. A*, 2010, **114**, 7038.
84. Z.A. Dreger and Y.M. Gupta, *J. Phys. Chem. A*, 2010, **114**, 8099.
85. F.P.A. Fabbiani, D.R. Allan, W.I.F. David, S.A. Moggach, S. Parsons, and C.R. Pulham, *CrystEngComm*, 2004, **6**, 505.

86. F.P.A. Fabbiani, D.R. Allan, S. Parsons, and C.R. Pulham, *CrystEngComm*, 2005, **7**, 179.
87. D.I.A. Millar, I.D.H. Oswald, D.J. Francis, W.G. Marshall, C.R. Pulham, and A.S. Cumming, *Chem. Commun.*, 2009, **45**, 562.
88. D.I.A. Millar, I.D.H. Oswald, C. Barry, D.J. Francis, W.G. Marshall, C.R. Pulham, and A.S. Cumming, *Chem. Commun.*, 2010, **46**, 5662.
89. R.J. Angel, M. Bujak, J. Zhao, G.D. Gatta, and S.D. Jacobsen, *J. Appl. Crystallogr.*, 2007, **40**, 26.
90. Y. Shen, R.S. Kumar, M. Pravica, and M.F. Nicol, *Rev. Sci. Instrum.*, 2004, **75**, 4450.
91. D.I.A. Millar, W.G. Marshall, H.E. Maynard-Casely, C.R. Pulham, and A.S. Cumming, *unpublished results,* 2010.
92. A. Gavezzotti, *Z. Kristallogr.*, 2005, **220**, 499.

Chapter 4

High-Pressure Structural Studies of CL-20

(2,4,6,8,10,12-hexanitrohexaazaisowurtzitane)

4 High-Pressure Structural Studies of CL-20

4.1 Introduction

2,4,6,8,10,12-hexanitrohexaazaisowurtzitane (HNIW, more commonly known as CL-20 after the China Lake Research Facility, USA) was first synthesised in the late 1980s [1] although the detailed synthetic procedure was only published in 1998.[2] CL-20 is a polycyclic nitramine with six nitro groups bonded to an isowurtzitane cage (see Figure 4.1). The low ratio of carbon atoms to nitramine moieties, combined with the inherent strain in the isowurtzitane cage and the increased density (with respect to its monocyclic analogue) have led to CL-20 being characterised as "the densest and most energetic explosive known."[3] It is not surprising therefore that a significant amount of research has been aimed at assessing its explosive performance [4], sensitivity [5] and thermal properties.[6-8] Furthermore spectroscopic and diffraction techniques have been used to explore the rich polymorphism of CL-20.

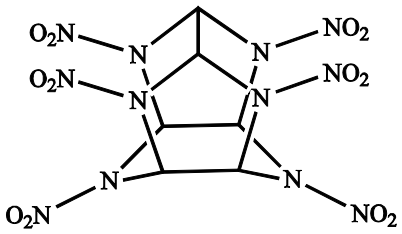

Figure 4.1 Molecular structure of CL-20.

4.2 Polymorphism of CL-20

4.2.1 Ambient-Pressure Studies

Four forms of CL-20 (α, β, γ, and ε) have been characterised at ambient conditions using FTIR spectroscopy and/or single-crystal X-ray diffraction [9-12], although it was only with the publication of the synthetic procedure that detailed structural information entered the open literature.[2] It is important to note, however, that the α-form is actually stabilised by varying amounts of water (0.25 – 0.57) [2, 13, 14] and is therefore not a true polymorph of CL-20 but a hydrate. Since it is common in the literature not to remove the water from the α-form prior to analysis, references to 'α-CL-20' should be taken to mean the 'α-hydrate' unless otherwise specified.

Of the 24 possible conformers elegantly summarised by Foltz *et al.* [6], steric hindrance and the mutual repulsion of the nearest oxygen atoms mean that only eight conformers are considered to be stable. Four of the most stable conformations, as determined by DFT

calculations [15], are represented in Figure 4.2 and it is interesting to note that three of these correspond to the molecular conformations found in the four structurally characterised forms: α and γ share the molecular conformation shown in II, β-CL-20 has been found to adopt the conformation I, while the ε-form exhibits conformation III.

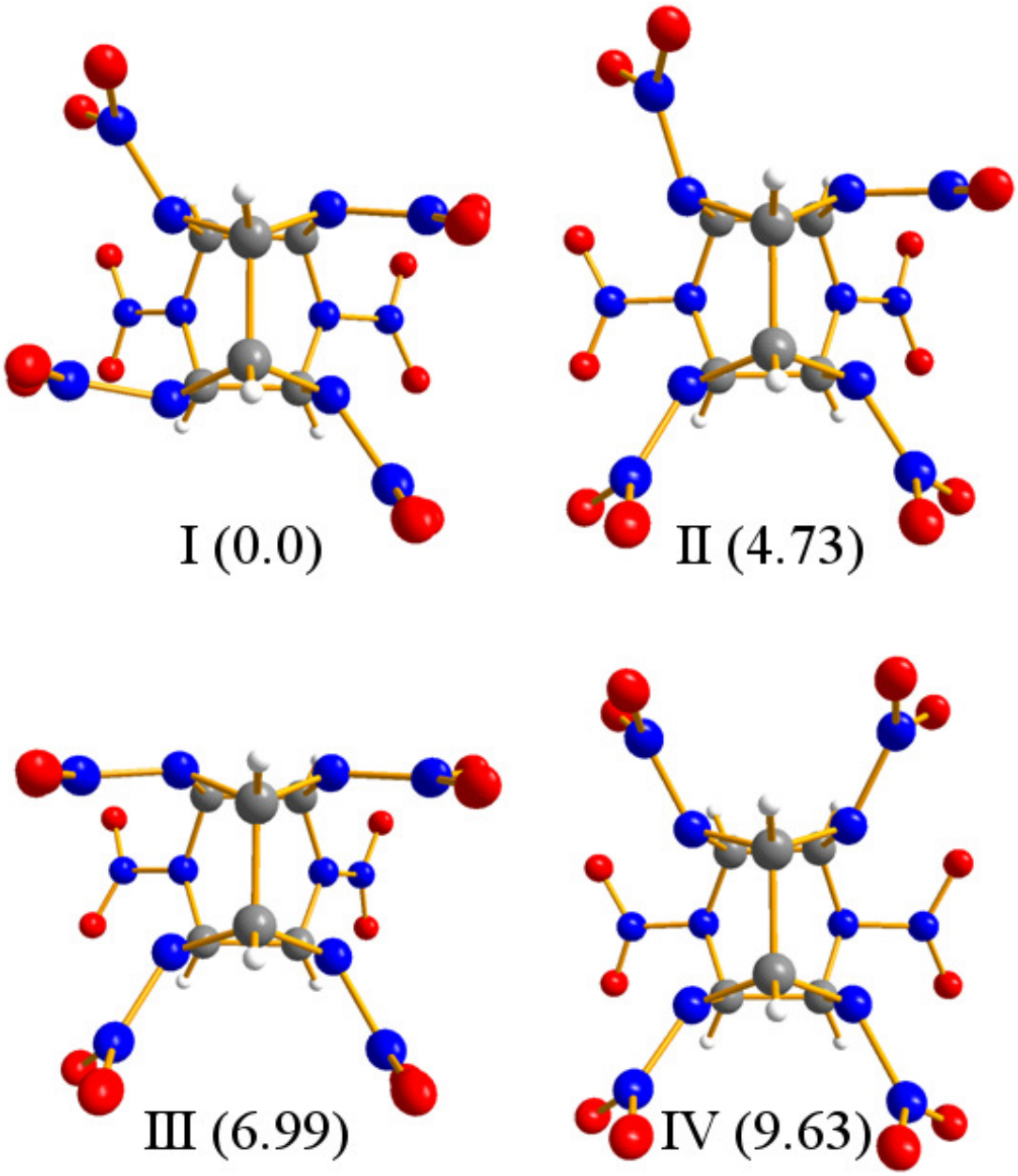

Figure 4.2 The most stable molecular conformations (including the relative energies, in kJ mol^{-1}, calculated by Kholod *et al*. [15]), three of which represent the molecular conformations of the known forms of CL-20. The conformation shown in I is adopted by β-CL-20, II is exhibited in both α- and γ-CL-20, while the ε-form adopts conformation III. It has also been proposed that the high-pressure ζ-form adopts the conformation shown in IV.

	α-CL-20[1]	β-CL-20[2]	γ-CL-20	ε-CL-20
Space Group	*Pbca*	$Pb2_1a$	$P2_1/n$	$P2_1/n$
a (Å)	9.485(2)	9.676(2)	13.231(3)	8.852(2)
b (Å)	13.225(4)	13.006(4)	8.170(2)	12.556(3)
c (Å)	23.673(3)	11.649(4)	14.876(3)	13.386(3)
β (°)			109.17(2)	106.82(2)
V (Å^3)	2969.5(11)	1466.0(10)	1518.9(8)	1424.2(8)
Z	8	4	4	4
D_c (Mg m^{-3})	1.981	1.985	1.916	2.044

Table 4.1 Summary of the crystallographic data for the four forms of CL-20 isolated at ambient temperature and pressure, as determined by Nielsen et al.[2] [1]α-CL-20 in this study refers to 1:0.25 CL-20:H_20. [2]A more conventional selection of $Pca2_1$ was made by Jacob *et al.* in their private communication to the CSD.[13]

This rich polymorphism at ambient conditions presents a significant complication for the commercial applications of CL-20 as a high explosive and for its industrial scale-up. For example, conversion to lower density phases will lead to volume expansion and stress-cracking with implications for sensitivity.[6] There has therefore been a considerable amount of research on characterising these forms, [16] their respective optimum crystallisation conditions [17-19], and their relative stabilities.[20] Thermal analyses [6, 7], kinetic studies using vibrational spectroscopy [8, 21] and DFT calculations [15, 22] have concluded that the ε-form is the most thermodynamically stable polymorph under ambient conditions, although measurements on the α-hydrate were complicated by the inclusion of water molecules.[23-25]

While ε-CL-20 has been shown to be the thermodynamically most stable form, and is therefore often precipitated as the final product of the synthetic procedure, it is possible to obtain the other polymorphs by re-crystallisation methods. For example, high quality crystals of the β-form were obtained by recrystallisation of the crude product in benzene [2] and high-boiling solvents, such as octane.[26] The crystallisation of the α-form, with varying degrees of hydration, is most commonly achieved by recrystallisation from concentrated nitric acid [2] but it has recently been shown to be possible to obtain large crystals of the α-form by the slow evaporation of a 'solution of γ-CL-20 dissolved in wet ethyl acetate'.[24] The water molecules may be removed from the α-CL-20 by prolonged heating ca 373 K, although Russell *et al.* comment that the direct preparation of anhydrous samples of the α-form has not been achieved.[20]

Upon heating, the α-, β-, and ε-forms all undergo an endothermic transition to the γ-form in the range 428 – 471 K.[27] Indeed, spectroscopic analysis of the high-temperature conversion of a sample of β-CL-20 contaminated with some of the α-form confirmed that this resulted in a phase transition to the γ-form, and not to a reported δ-form.[7] Irrespective of the starting polymorph, this high-temperature γ-form is then sufficiently stable to be recovered to ambient temperature.

4.2.2 High-Pressure Studies

Previous high-pressure studies have been reported for the ε-form (the most thermodynamically stable form at ambient conditions) and the γ-form. No experimental studies on the compression of the α- or β-forms have so far been published although the β-form has been included in the most recent computational study by Sorescu *et al.*[28]

ε-CL-20

The compression of polycrystalline ε-CL-20 has been studied by both X-ray powder diffraction [29-31] and Raman spectroscopy.[32] In their diffraction study, Gump *et al.* observed no phase transitions within the pressure range studied (up to 5.6 GPa at ambient temperature). The compression of the unit cell axes was not uniform, with the *b*-axis being ~ 2% more compressible over the whole pressure range. The ε-form was also observed to persist to 5 GPa (the maximum pressure studied) when the compression was carried out at 348 K and at 413 K, provided the sample was initially pressurised (to ~ 0.4 GPa) before heating to avoid the ε → γ thermal transition at ambient pressure.

The pressure range for this investigation was later extended by Ciezak *et al.* who used vibrational spectroscopy to examine the response of ε-CL-20 to compression to 27 GPa. Intensity changes and discontinuities in the pressure shifts of the vibrational modes led the authors to conclude that a sluggish transition from the ε-form to the γ-form occurred between 4.5 and 6.4 GPa. The authors also noted the existence of another transition that begins near 14.8 GPa but is not completed until 18.7 GPa. This phase transition results in the fifth polymorph of CL-20: ζ-CL-20.

γ-CL-20

The high-pressure ζ-form (obtained above 18 GPa by compression of the ε-form) has been shown to exist at much lower pressure when the γ-form is used as the starting material. The behaviour of γ-CL-20 under extreme conditions has been much more fully explored than for the ε-form. Russell *et al.* [20] used optical microscopy and infrared spectroscopy to assemble a pressure/temperature phase diagram in which the stability regions of all five forms of CL-

20 have been plotted along with the reversibility of the polymorphic transitions and the thermal decomposition region at elevated pressures. These results have been summarised in Figure 4.3.

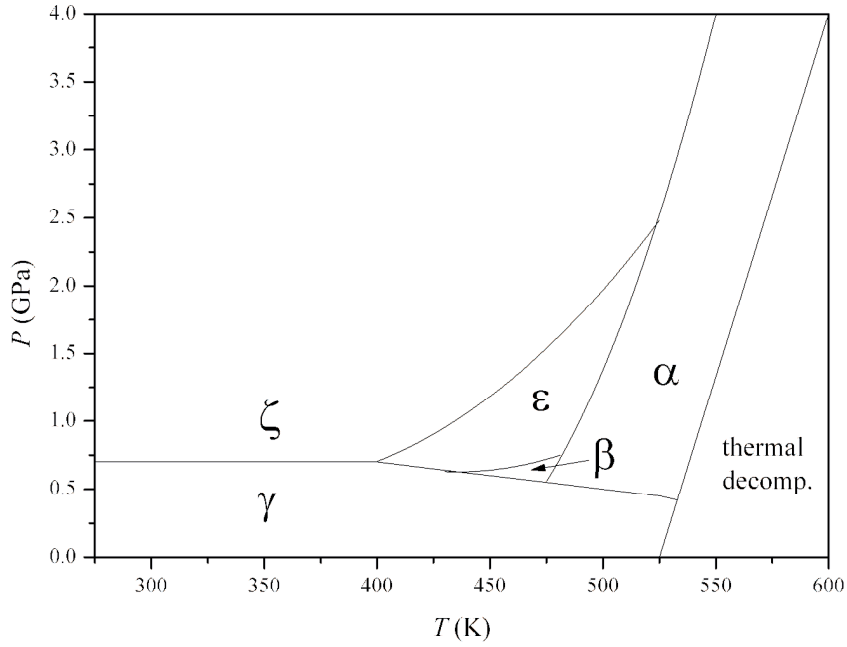

Figure 4.3 The pressure/temperature phase diagram for γ-CL-20 as determined by Russell *et al*. based on FTIR and optical polarising microscopy measurements using γ-CL-20 as starting material.

Moreover, Russell *et al.* investigated the high-pressure transition from γ-CL-20 to the ζ-form using energy dispersive X-ray powder diffraction.[12] In a further study, single crystals of the γ-form were also observed by optical microscopy to undergo a rapid and reversible transition to the ζ-form at 0.7 GPa and survive intact.[20] Comparison of the IR spectra for this high-pressure form with those for the α-, β-, and ε-forms confirmed that this was indeed a fifth form of CL-20. They observed fewer bands in the IR spectrum of ζ-CL-20 and therefore suggest that the ζ-form adopts a molecular conformation with higher symmetry. This observation is consistent with the results of DFT calculations on the different possible molecular conformations of isolated molecules of CL-20 - the fourth stable conformation depicted in Figure 4.2, in which all of the nitro groups adopt *exo*-orientations, has been proposed to correspond to the high-pressure ζ-form.[15] The pressure-induced transition to the ζ-form was also observed at 0.7 GPa in the diffraction study by Gump *et al*. They note that the '*X-ray patterns for this phase are similar to those of the ε phase, but not exactly the same*.'[29]

4.3 Aims

The importance of a detailed knowledge of the structure of CL-20 under extreme conditions has motivated an investigation into the high-pressure behaviour of both the ε- and γ-forms. The primary aims were therefore:

- to study the compression of ε-CL-20, in order to probe the nature of the proposed ε → γ transition;
- to obtain high-quality diffraction data to facilitate the calculation of an improved equation of state of ε-CL-20; and
- to compress γ-CL-20 into the high-pressure ζ-form in order to structurally characterise the fifth form of CL-20.

4.4 Experimental

4.4.1 Materials

Crystalline samples of ε-CL-20 were obtained from Dstl. Powder samples and single crystals of the γ-form were prepared by heating the ε-form to *ca* 470 K and by crystallisation from hot benzene, respectively. The phase purity of such samples of γ-CL-20 was confirmed by Raman spectroscopy and X-ray powder diffraction.

4.4.2 High-Pressure X-ray Powder Diffraction

High-pressure X-ray powder diffraction experiments were carried out using a Merrill-Bassett diamond-anvil cell (DAC) [33] equipped with 600 μm culet diamonds and a 250 μm thick tungsten gasket (pre-indented to a thickness of 100-150 μm) with a 300 μm hole. Pressure measurement was made by monitoring the R_1 fluorescence line of ruby spheres.[34] Compression of ε-CL-20 was undertaken using methanol:ethanol (4:1) as a pressure-transmitting medium; γ-CL-20 was compressed using Fluorinert FC-77 and MeOH:EtOH as pressure media. Data were collected at the Extreme Conditions Beamline (I15) at Diamond Light Source (λ = 0.48469 Å). The X-ray beam was collimated to a diameter of 50 μm and samples were exposed for 60 s. 2D diffraction patterns were collected using a Mar345 image plate, processed using FIT2D.[35] The powder diffraction data were utilised by the program FOX [36] that employed direct space global optimisation methods for structure solution of ζ-CL-20. Full-profile Rietveld refinements were carried out on all powder diffraction patterns using GSAS, in which a convolution of Gaussian (GU, GV), Lorentzian (LX, LY) and asymmetry (asym) coefficients was implemented to fit peak profiles (GSAS CW profile 2).[37]

4.4.3 High-Pressure Neutron Powder Diffraction

High-pressure neutron powder diffraction data were collected using the PEARL/HiPr diffractometer at the UK spallation neutron source, ISIS, at the STFC Rutherford Appleton Laboratory. Due to the complexity of the synthetic procedure, it was not possible to obtain a deuterated sample of CL-20 for these studies. It was therefore necessary to load a lightly ground sample of CL-20-h_6 into an encapsulated TiZr gasket [38] with perdeuterated methanol:ethanol (4:1) as pressure medium and Pb as pressure calibrant. The capsule assembly was then compressed with a type V3b Paris-Edinburgh (P-E) press equipped with standard single toroid anvils with cemented WC cores (Ni binder).[39] The P-E press ram pressure was monitored and varied by means of a computer-controlled hydraulic system.

Time-of-flight (ToF) neutron powder diffraction data were collected using the $2\theta = 90°$ detectors with a transverse (through-anvil) scattering geometry. The resulting summed pattern was then normalised with respect to the incident beam monitor and the scattering from a standard vanadium calibration sample. Lastly, the diffraction pattern intensity scale was corrected for the wavelength and scattering-angle dependence of the neutron attenuation by the anvil (WC) and gasket (TiZr) materials. Full-profile Rietveld refinements of the ToF neutron powder diffraction patterns were carried out using the GSAS package, in which a convolution of Gaussian (with coefficient σ_1) and Lorentzian (γ_1) functions was used to describe peak profiles (GSAS ToF profile 3).[37]

4.4.4 High-Pressure Single-Crystal X-ray Diffraction

High pressures were attained using a Merrill-Bassett diamond-anvil cell (DAC) [33] equipped with 600 μm culet diamonds and a 250 μm thick tungsten gasket (indented to ~100 μm) with a 300 μm diameter hole. In order to maximise the volume of reciprocal space that could be sampled it was necessary to use Böhler-Almax type diamonds and WC backing plates [40] that provide a wider opening angle than the typical beryllium backed DACs. Single crystals of γ-CL-20 were loaded into a DAC with either Fluorinert FC-77 or MeOH:EtOH (4:1) as the pressure-transmitting medium. Accurate determination of sample pressure was measured by the ruby fluorescence method [34] using a 632.8 nm excitation line from a He-Ne laser. The fluorescence was detected by a Jobin-Yvon LabRam 300. High-pressure data sets were collected using ω-scans in 12 settings of 2θ and φ with 0.3° step-size for 30 s.[41] X-ray diffraction intensities were collected using Mo-Kα radiation on a Bruker SMART APEX II CCD diffractometer.[42] Single-crystal data were processed according to the procedure described by Dawson *et al*.[41] Integration of data sets and global cell refinement was carried out using the program SAINT [43], in which 'dynamic masks'

were employed to prevent integration of areas of the detector shaded by the body of the DAC. SHADE [44] was used to reject reflections partly shaded by the DAC and absorption corrections were applied by SADABS [45] to allow for different path-lenghts of the X-rays through the crystal, depending on its orientation during the scan. In the case of ζ-CL-20, structure solution *via* direct methods was not possible and it was therefore necessary to use the program FOX [36] that employs direct space global optimisation methods. All other structures were solved by direct methods using SIR92 [46] and full-matrix least-squares-refinement against *F* were carried out using CRYSTALS.[47] All non-hydrogen atoms were refined anisotropically. The hydrogen atoms were geometrically placed on the parent carbon.

4.4.5 Ambient-Pressure Single-Crystal X-ray Diffraction

X-ray diffraction intensities were collected by Dr F. White (Crystallography Service, University of Edinburgh) using Cu-Kα radiation on an Oxford Diffraction SuperNova dual wavelength diffractometer equipped with an Atlas CCD detector and an Oxford Cryostream-*Plus* low-temperature device (100 K).[48] Data were integrated and a multi-scan absorption correction was applied using the CrysAlis Pro software package.[49] Structures were solved [46] and refined by full-matrix least squares against F^2 using all data.[47] All non-hydrogen atoms were refined anisotropically. The hydrogen atoms were geometrically placed on the parent carbon.

4.5 Results and Discussion

4.5.1 Compression of ε-CL-20

The initial focus of this study was to obtain high-quality X-ray powder diffraction data on ε-CL-20 in order to extend the pressure range of previous diffraction studies [29-31] to ~ 7 GPa thus allowing the critical examination of the proposed transition to the γ-form observed spectroscopically.[32] Polycrystalline ε-CL-20 was loaded into a diamond-anvil cell with methanol:ethanol (4:1) as the pressure-transmitting medium. X-ray powder diffraction patterns collected during the compression experiment at the Extreme Conditions Beamline (I15), Diamond Light Source, are shown in Figure 4.4. It was possible to carry out Rietveld refinements on all of the patterns collected (up to the maximum pressure studied) using the ε-CL-20 structural model – Figure 4.5 shows the quality of the Rietveld refinement for the pattern collected at 7.22 GPa. This is conclusive proof that the ε-form remains stable in this pressure regime and does not undergo a phase transition between 4.5 and 6.4 GPa as has been previously asserted.[32]

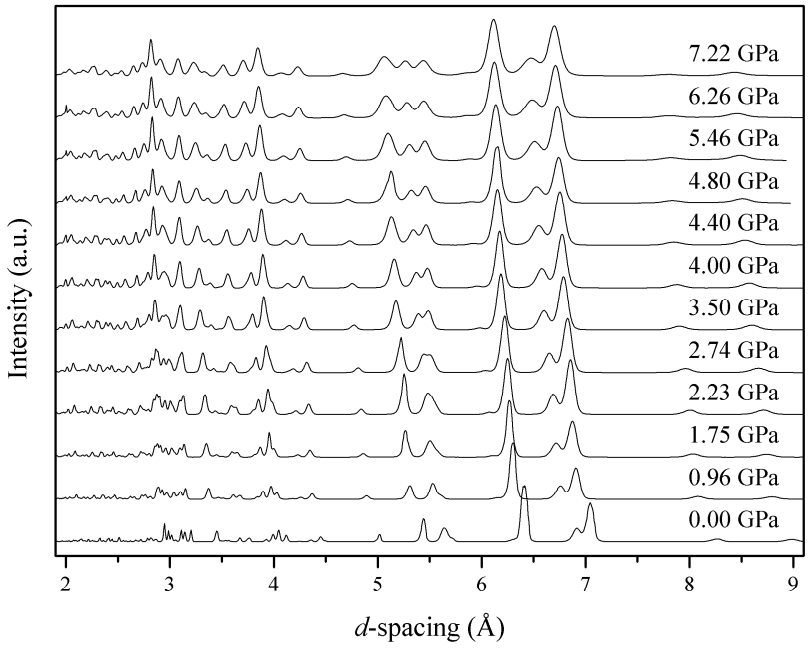

Figure 4.4 Series of X-ray powder diffraction patterns collected during the compression of ε-CL-20 to a maximum pressure of 7.22 GPa.

The variations in the unit cell parameters (*a*, *b*, *c*, *β* and *V*) are tabulated in Table 4.2 and represented graphically in Figure 4.6. The compression behaviour of the unit cell axes is broadly in agreement with that observed by Gump *et al.*: the *b*-axis is most compressible (~ 7%) and the differences in the compressibility of the *a*- and *c*-axes is within the experimental error of both studies. It is interesting to note that the gradient of the relative contraction of the unit cell volume (Figure 4.6(c)) appears to decrease *ca* 5.0 GPa. This may be indicative of a subtle adaptation of either the compression mechanism or, indeed, the structure itself in this pressure regime. Since it has been possible to perform full-profile Rietveld refinements of all the subsequent patterns using the ε-structure, it would appear that this is not evidence of a phase transition. Furthermore, characteristic diffraction peaks arising from the γ-form were not observed.

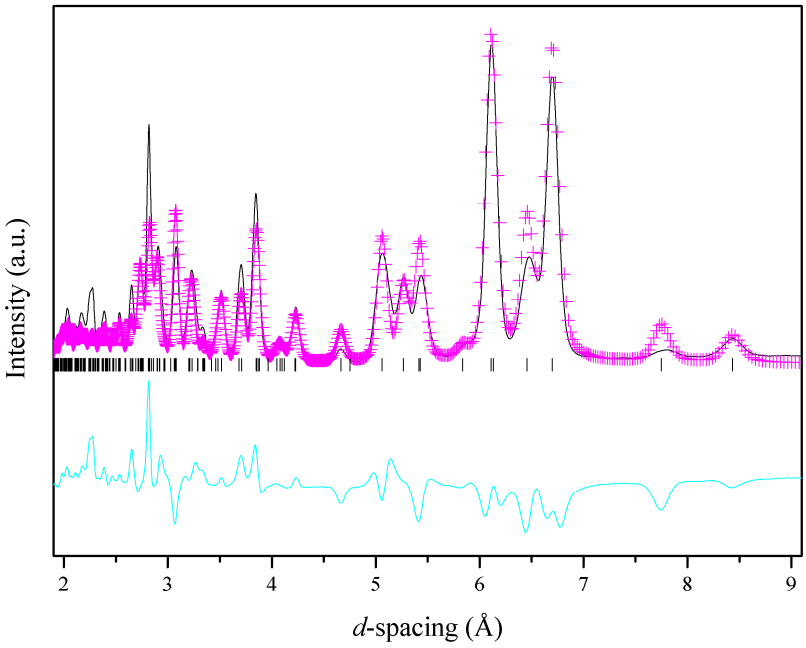

Figure 4.5 Rietveld refinements of the X-ray powder diffraction pattern collected at 7.22 GPa (using ε-CL-20 as the structural model, black tick marks). The experimental data (I_{obs}) are represented as pink crosses, the calculated pattern (I_{calc}) is shown in black and the difference (I_{obs} - I_{calc}) in cyan.

Previous observations of a phase transition to the γ-form at this pressure have been limited to discontinuities in the d$\bar{\nu}$/dP plots and the appearance of new spectral bands in the vibrational spectra. Upon close inspection of these data, however, it is suggested that these features have resulted simply from the resolution of peaks due to the relative hardening or softening of the vibrational modes at elevated pressures. Nevertheless, the change in the gradient of the relative contraction of the unit cell volume, coupled with this spectroscopic evidence, suggests that there is a modification to the intermolecular interactions at these pressures. Further investigation of the ε-form in this pressure regime would therefore be particularly worthwhile.

The compression of the unit cell volume has been fitted to a 3rd-order Birch-Murnaghan equation of state (EoS) with V_0 = 1431.8 Å^3 (fixed), B_0 = 9.5(22) GPa and B'_0 = 27(8). The high-quality of the Rietveld refinement of the pattern collected at 0.0 GPa in this study meant that it was possible to fix V_0, in order to increase the precision of the other parameters. The value of the isothermal bulk modulus (B_0) is smaller than that determined experimentally by Gump *et al.* [31] and the value calculated by Sorescu *et al.*, who used

molecular dynamics simulations [50] (13.6(20)[7] and 15.58 GPa, respectively). However, the pressure derivative (B') is larger (11.7(32) and 9.37, respectively). This indicates that the unit cell volume initially decreases more rapidly in the current study before becoming more resistant to compression.

P (GPa)	a (Å)	b (Å)	c (Å)	β (°)	V (Å^3)	wR_p
0.00	8.8667(3)	12.6020(5)	13.3912(6)	106.891(2)	1431.77(13)	0.049
0.96	8.7010(10)	12.2946(13)	13.1268(16)	106.332(7)	1347.6(4)	0.097
1.75	8.6596(11)	12.2013(16)	12.0443(15)	106.090(10)	1324.2(2)	0.213
2.23	8.6420(14)	12.1552(18)	13.008(2)	105.963(9)	1313.7(5)	0.151
2.74	8.6089(16)	12.077(2)	12.938(2)	105.750(10)	1294.7(7)	0.145
3.50	8.565(2)	11.971(3)	12.845(3)	105.401(14)	1269.9(7)	0.174
4.00	8.540(2)	11.919(3)	12.794(2)	105.24(2)	1256.7(3)	0.229
4.40	8.529(2)	11.873(4)	12.764(5)	105.00(3)	1248.5(11)	0.243
4.80	8.514(4)	11.825(5)	12.734(5)	104.82(3)	1239.5(11)	0.230
5.46	8.503(4)	11.788(6)	12.711(6)	104.62(3)	1233.0(11)	0.259
6.26	8.491(5)	11.743(6)	12.689(9)	104.47(3)	1225.2(14)	0.233
7.22	8.477(6)	11.700(7)	12.658(7)	104.39(3)	1216.1(17)	0.238

Table 4.2 Variation in the unit cell parameters of ε-CL-20 with pressure.

[7] Although the experimental values are within the limits of experimental error of each other, it is believed that the current study does indeed represent a smaller value of B_0. However, it would be extremely desirable to obtain more compression data, particularly in the low pressure (0 – 1 GPa) regime, in order to increase the precision of this value.

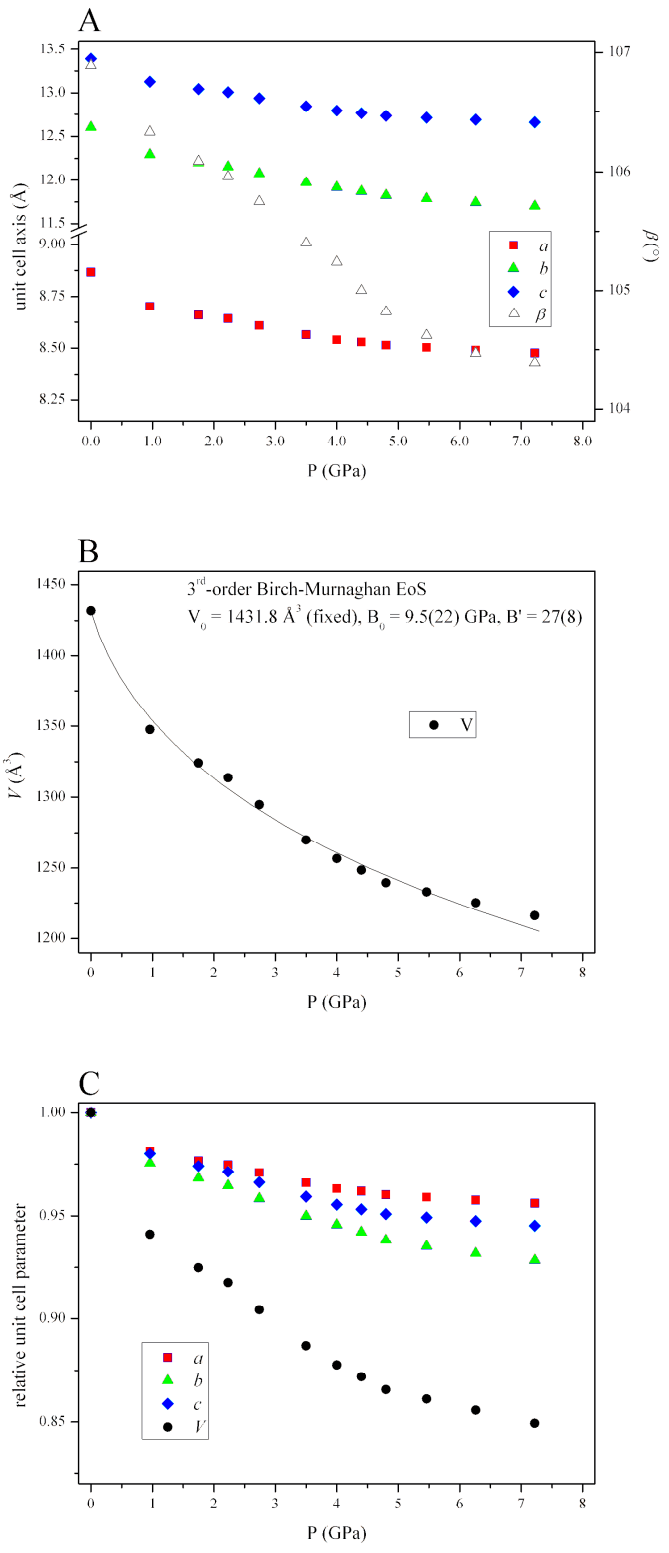

Figure 4.6 (a) Compression of the unit cell parameters (*a*, *b*, *c* and *β*) of ε-CL-20; (b) compression of the unit cell volume, fitted to a 3rd-order Birch-Murnaghan EoS; and, (c) relative contraction of the unit cell parameters.

A more significant observation, however, is that the unit cell volume is larger throughout this study than in any other experimental or theoretical study previously reported. In addition to the equations of state determined by Gump *et al.* and Sorescu *et al.*, recent DFT-D calculations have been conducted by Sorescu and Rice to determine the unit cell parameters at elevated pressure. These data are also presented in Figure 4.7.

The exact reason for this discrepancy is currently unclear. Gump and Peiris have assimilated three experimental compression studies into one table and it has therefore not been possible to plot each compression individually.[31] This would have facilitated the analysis of the relatively large scatter in the data and the identification of any experimental factors that could have contributed to this large variance. Furthermore, the determination of the unit cell parameters was based on indexings obtained from Gaussian fits of individual diffraction peaks (to determine *d*-spacings) rather than Rietveld refinement of the whole diffraction pattern (as in the present work). This is reflected in the relative errors of the two studies: the average uncertainty in the unit cell volume in Gump's study was ± 6.65 Å^3 compared to ± 0.76 Å^3 in this work.

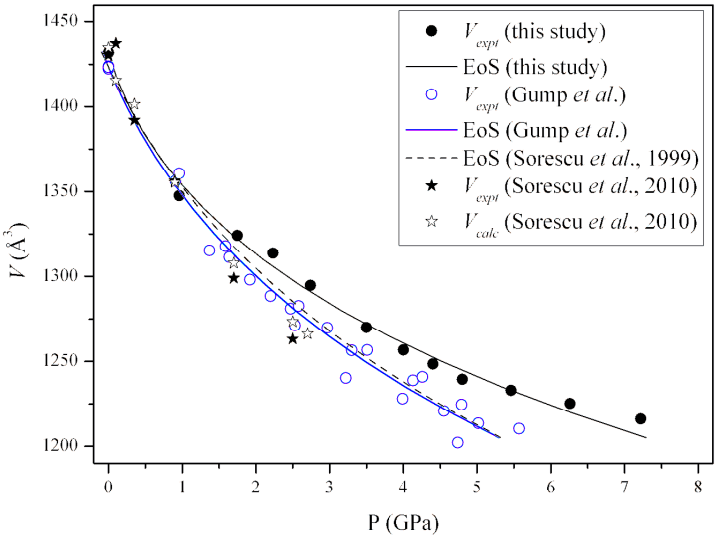

Figure 4.7 Plot of the compression of ε-CL-20: (a) this study, in which ε-CL-20 was compressed in MeOH:EtOH, (b) Gump *et al.* [31], using silicone fluid as pressure-transmitting medium, (c) theoretical equation of state determined by Sorescu *et al.* (1999) [50], and (d) *PV* data published by Sorescu *et al.* (2010), including experimental data from Pinkerton.[28]

The results of these studies and, more importantly, the discrepancies between this work and previous diffraction experiments conducted by Gump *et al.*[30, 31] highlight the importance of maintaining hydrostaticity throughout compression. Thus the selection of pressure-

transmitting medium is critical to the outcome of the experiment. While the pressure medium used in this work (4:1 mixture of MeOH:EtOH) has been shown to remain hydrostatic to 9.8 GPa (*i.e*. above the limit of this compression experiment), Gump *et al*. employed Dow Corning 200 Fluid (silicone oil) that has a hydrostatic limit of *ca* 1.0 GPa.[51] It is therefore suggested that the equation of state calculated for ε-CL-20 in the present study should be considered more reliable, since the possibility of deviatoric stresses arising from non-hydrostatic conditions can be discounted.

4.5.2 Compression of γ-CL-20

Compression in Fluorinert FC-77

The compression of the γ-form was initially investigated by X-ray powder diffraction. Polycrystalline γ-CL-20 was loaded into a diamond-anvil cell (DAC) with Fluorinert (FC-77) as the pressure transmitting-medium. Diffraction data were collected to a maximum pressure of 1.52 GPa at the Extreme Conditions Beamline (I15), Diamond Light Source. An example of the high quality of the data is presented in Figure 4.8. The γ-form was observed to persist on compression to 0.72 GPa, but at the next pressure point, 1.44 GPa, a significant change was observed in the powder diffraction pattern, indicative of a phase transition to the high-pressure ζ-form. This is shown in Figure 4.9.

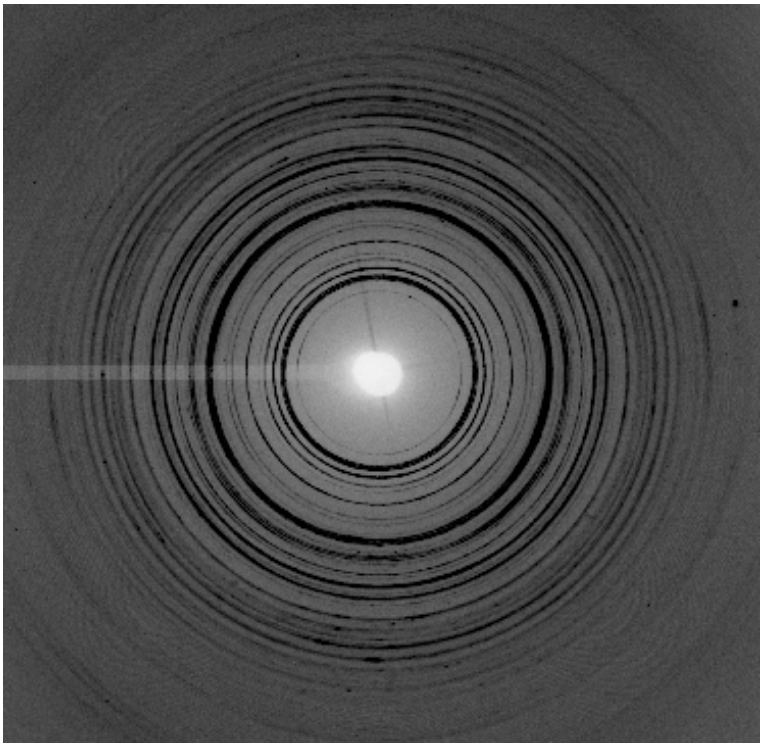

Figure 4.8 Raw powder diffraction data collected for ζ-CL-20 (1.44 GPa) at I15, DLS.

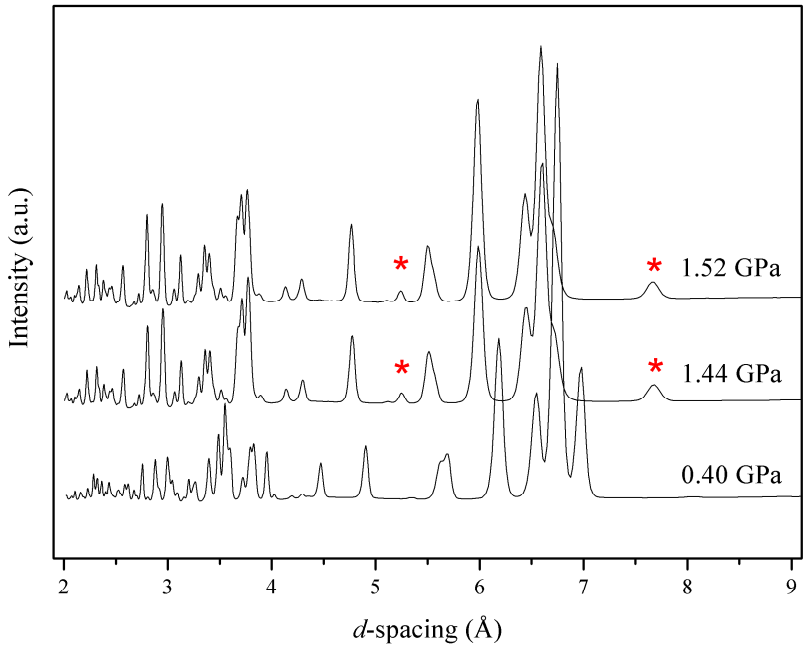

Figure 4.9 Comparison of the integrated X-ray powder diffraction patterns collected for γ-CL-20 (0.40 GPa) and ζ-CL-20 (1.44 and 1.52 GPa). The red asterisks show the diagnostic peaks of the ζ-form.

Despite the high quality data, attempts to index these patterns gave several possible solutions, none of which allowed structure solution. However, an important observation was that the difference between the X-ray powder diffraction patterns collected for γ- and ζ-CL-20 was subtle. Combined with previous optical observations [12], this suggested that hydrostatic compression of a single crystal through the γ → ζ transition might retain the integrity of the crystal, i.e. the phase transition is not reconstructive.

Crystals of the γ-form were grown from hot benzene and were loaded into a DAC, again using FC-77 as pressure medium (see Figure 4.10). The crystal was initially compressed to ~0.05 GPa to check crystal quality and the diffraction data were of sufficient quality to allow a full structural refinement of the γ-form. On compression to ~1.20 GPa, it was possible to index a set of reflections to a monoclinic cell [$P2_1/n$, a = 12.8244(8), b = 7.9029(8), c = 14.3622(6) Å and β = 111.205(4)°]. A second data-set was collected at 3.30(5) GPa with longer exposure times in order to improve data quality. It is common in high-pressure crystallography that data-sets suffer from low completeness due to shading from the steel body of the diamond-anvil cell. The completeness of both these datasets was ~60% and this, coupled with the complexity of the molecular structure, meant that structure solution *via* direct methods was not possible. Instead the indexing solutions obtained from the single-

crystal studies were used as a starting point for the structure solution from the powder diffraction patterns using the program FOX that employs direct space global optimisation methods.[36] This structural model was then refined (with no restraints) against each of the single-crystal datasets to give the molecular conformation shown in Figure 4.11.

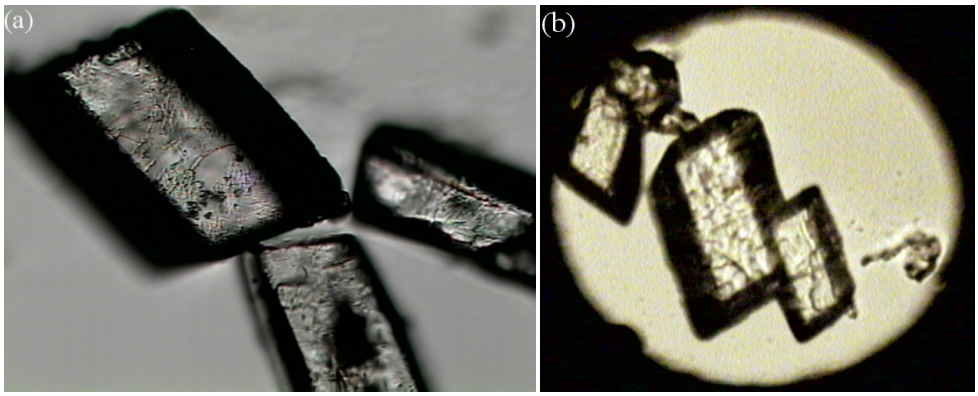

Figure 4.10 Single crystals of γ-CL-20: (a) at ambient conditions, and (b) loaded in DAC.

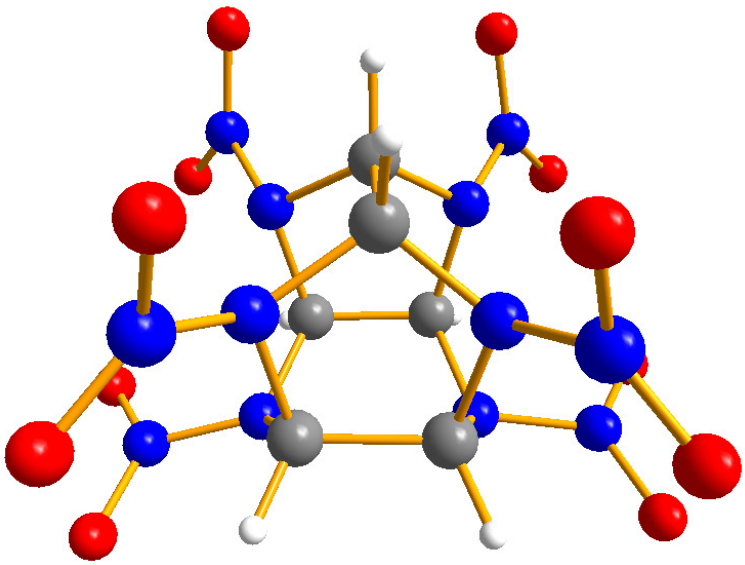

Figure 4.11 Molecular conformation of ζ-CL-20 obtained at 3.30(5) GPa.

Further confirmation that the crystal structure was correct was obtained by performing full-profile Rietveld refinements on all of the collected powder diffraction patterns, including those kindly provided by Gump and Peiris.[52] During the refinements restraints were applied to the geometry of the nitro groups, whilst the positions of the cage atoms were constrained to those obtained from the single-crystal refinements. Figure 4.12 shows an example of the quality of the Rietveld refinements for the patterns collected on the ζ-form.

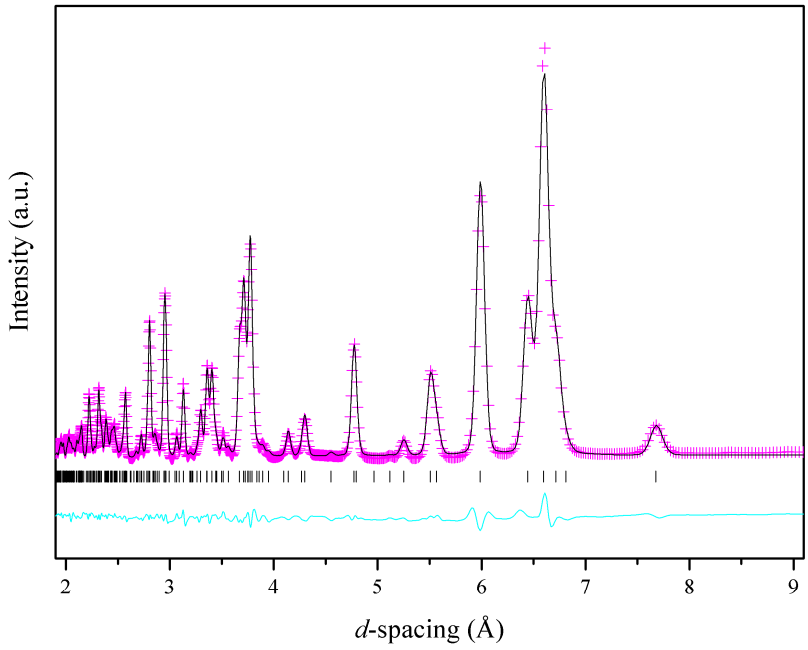

Figure 4.12 Fit of the Rietveld refinement of the ζ-CL-20 model (black tick marks) to the X-ray powder diffraction pattern recorded at 1.44(5) GPa. The experimental data (I_{obs}) are represented in pink, while the calculated pattern (I_{calc}) is shown as a black line. The difference curve ($I_{obs} - I_{calc}$) is shown in cyan.

In order to facilitate the comparison of the high-pressure ζ-form with the starting γ-form, the molecular conformations (determined from single-crystal diffraction) are presented together in Figure 4.13. This highlights that while the isowurtzitane cage does not change, the *exo*- and *endo*- spatial arrangement of the nitro groups with respect to the cage is different in the two forms. The ζ-form clearly adopts the conformation in which all of the nitro groups are *exo* with respect to the five- and six-membered rings, which is consistent with conclusions made on the basis of fewer bands being observed in the IR spectra.[12] Furthermore, this is the molecular conformation suggested by DFT calculations.[15] Given the relatively small energy differences between the most stable molecular conformation (0.0 – 9.63 kJ mol^{-1}), it is perhaps not surprising that compression of the γ-form will induce a phase transition to a conformation that allows more efficient crystal packing, as is exemplified in this case by a contraction of volume across the γ → ζ transition.

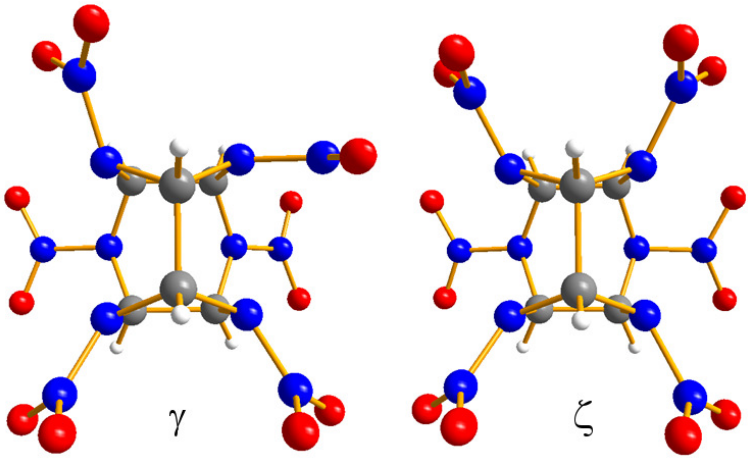

Figure 4.13 Molecular conformations of ζ- and γ-CL-20, showing that while the isowurtzitane cage does not change, the relative orientation of the nitro groups is different between the two polymorphs.

The packing in ζ-CL-20 retains the 'face-to-face' arrangement observed in the γ-form (where all five-membered rings of the cage are oriented about the same axis, see Figure 4.14). However, the closer packing and more symmetrical molecular conformation of the ζ-form allows a network of weak C-H…O interactions whereas these interactions form a chain in the γ-form. This network arrangement is more like that observed in ε-CL-20, which displays 'edge-to-face' packing. In this way, the ζ-form may be considered to display structural similarities with both γ- and ε-CL-20.

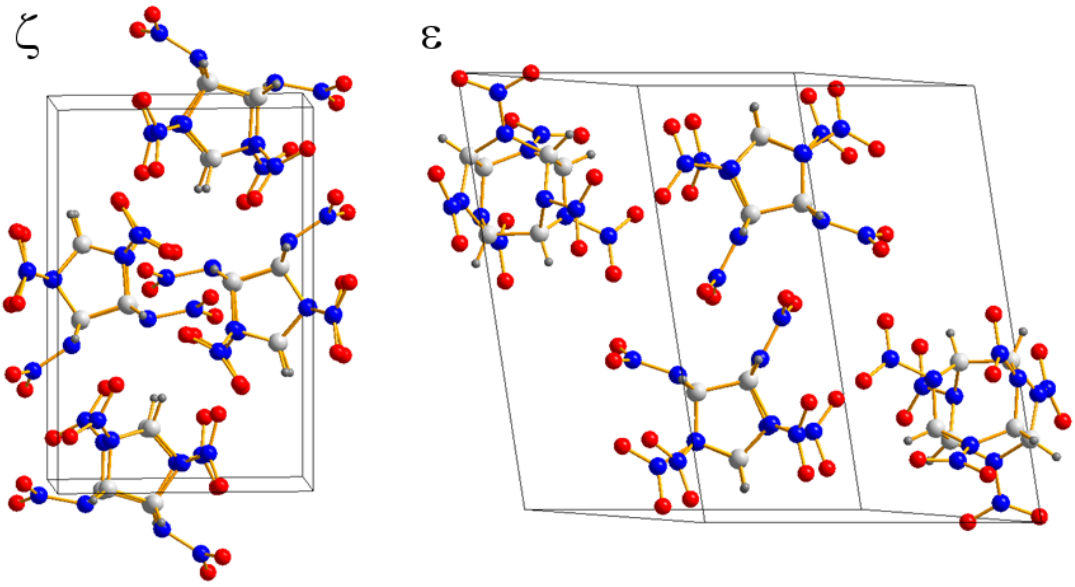

Figure 4.14 (a) The 'face-to-face' packing observed in ζ-CL-20; (b) the 'edge-to-face' packing of the ε-form. In both cases the unit cells are oriented such that the five-membered rings are viewed from above. Both polymorphs exhibit networks of intermolecular C-H…O interactions, in which each molecule interacts with two neighbouring molecules.

The structure solution of the high-pressure ζ-CL-20 is a significant achievement, given the complexity of the molecular conformation. These studies were limited, however, to relatively low pressures, due to the low hydrostatic limit of the pressure-transmitting medium in this study (Fluorinert is not considered to be hydrostatic at pressures greater than 1.2 GPa [53]). It was therefore thought prudent to carry out this compression in another medium in order to investigate the compression of γ-CL-20 to ~ 5 GPa. This would provide valuable information such as the density of ζ-CL-20 to compare to the ε-form at similar pressures as well as an equation of state for the high-pressure ζ-form.

Compression in Methanol:Ethanol

In order to provide complementary structural data, a neutron powder diffraction study was conducted at the PEARL-HiPr beamline (ISIS) using a Paris-Edinburgh Cell. In this case, the maximum pressure studied was 5.16 GPa, representing a significant extension of the pressure range over which this form has been studied previously. However, in order to maintain hydrostaticity in this pressure regime it was necessary to use a perdeuterated mixture (4:1) of methanol and ethanol as the pressure-transmitting medium.

A multiplot of the neutron powder diffraction patterns collected during this study is presented in Figure 4.15. It should be noted that the significant complexity of the synthetic procedure meant that it was not possible to obtain perdeuterated samples of γ-CL-20 for this study. As a result, the neutron powder diffraction patterns collected in this study exhibit a higher background than would normally be desired, due to the incoherent scattering from the hydrogen atoms (20 mol %) within the CL-20-h_6 sample. Despite this, there is clear evidence of a phase transition occurring between the first two patterns, collected at 0.10 and 0.57 GPa, respectively. For example, peaks at 2.3 and 3.8 Å in the pattern collected for the γ-form disappear from the pattern at 0.57 GPa. Furthermore, the peaks with strong intensities at 3.1 and 3.2 Å in the higher pressure pattern are simply not evident in the original pattern. Upon compression to 5.16 GPa, no further changes in the diffraction patterns indicative of a phase transition were observed. Unfortunately mechanical failure of the gasket resulted in sample detonation, causing damage to the WC anvils (see Figure 4.16) and thus curtailing the experiment. It was therefore not possible to investigate the decompression behaviour in this instance.

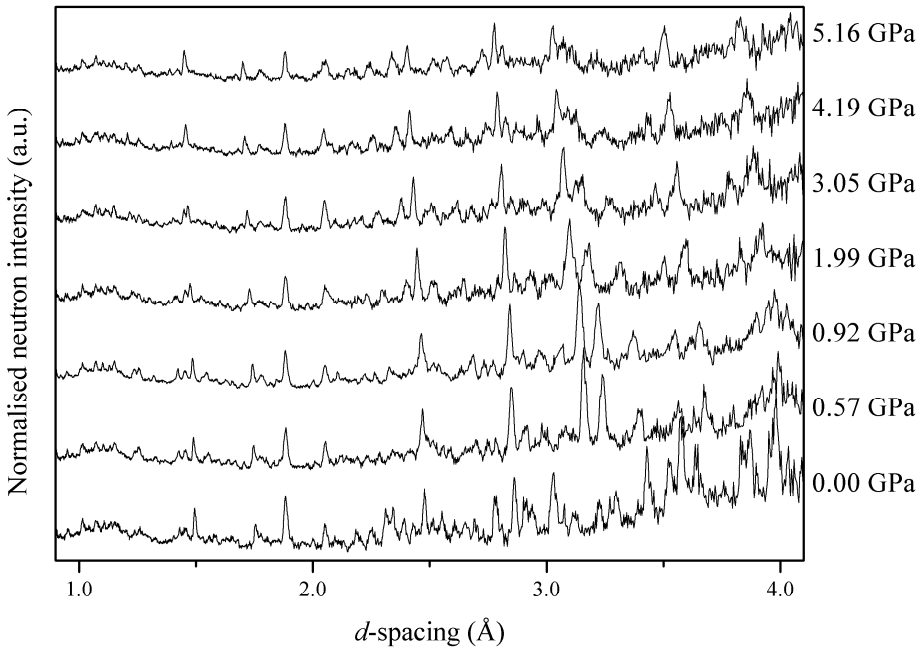

Figure 4.15 Multiplot of the neutron powder diffraction patterns collected during compression of γ-CL-20 in MeOD/EtOD.

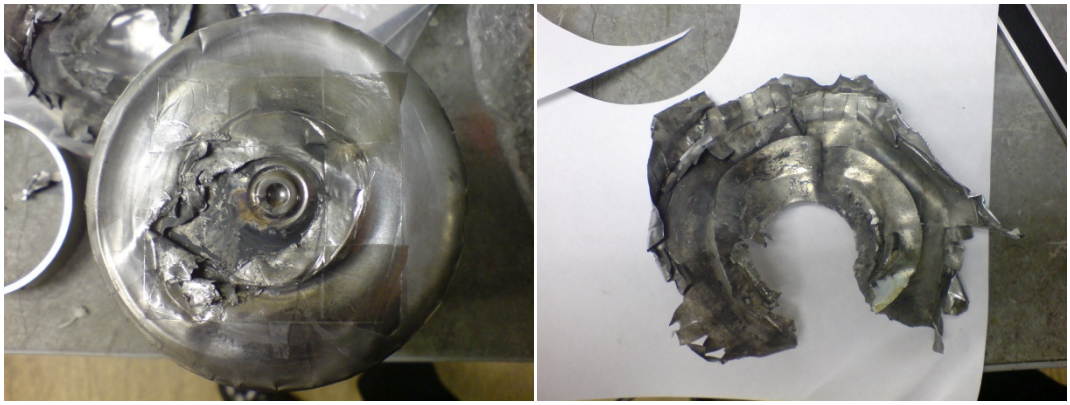

Figure 4.16 Photographs of the damage to the WC anvils due to the mechanical failure of the gasket and subsequent detonation of the sample. It should be noted that the PE-cell is contained in a metal vacuum tank and the whole experiment is conducted in an interlocked hutch. The experiment was rigorously assessed to ensure compliance with Health and Safety requirements; no members of the experimental team were in danger during the course of this experiment.

After confirming sample purity by Rietveld refinement of the initial pattern, refinement of the higher-pressure patterns was undertaken, with rather surprising results. Using the structural model of the ζ-form determined from the X-ray diffraction experiments described above, it was not possible to attain convergence. The quality of the Rietveld fit to the pattern collected at 3.05 GPa is shown in Figure 4.17. The marked differences between the observed

and calculated patterns are clear indications that the structural model used in this refinement is incorrect. In other words, the structure adopted upon compression of γ-CL-20 in MeOD/EtOD is *not* the same as that adopted when compression is performed in Fluorinert. This is a significant observation since it implies that the structural response of this material under compression is dependent upon the pressure-transmitting medium used. This, in addition to the importance of hydrostaticity discussed previously, underscores the complexity of high-pressure studies and the necessity for the publication of accurate experimental details.

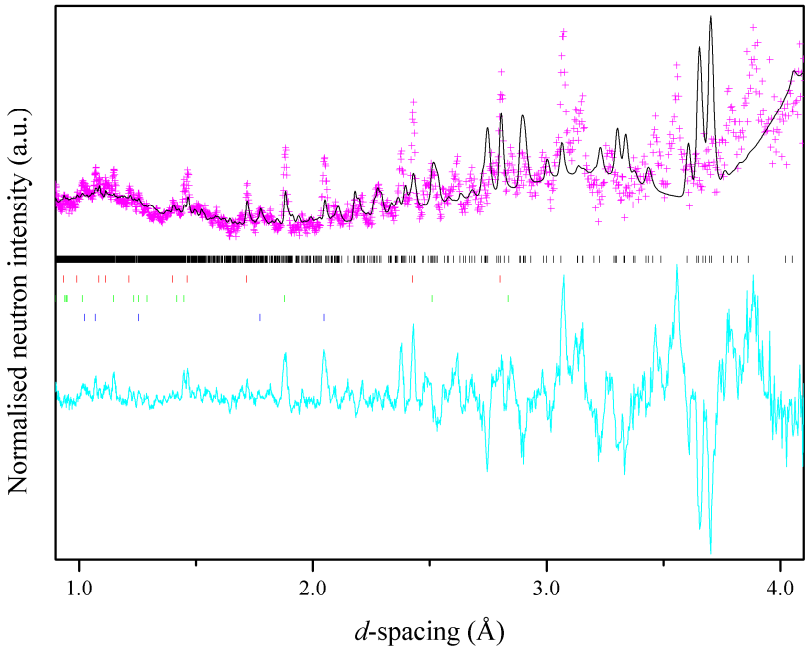

Figure 4.17 Rietveld refinement of the neutron powder diffraction pattern collected at 3.05 GPa using ζ-CL-20 structural model (black tick marks), along with the Pb pressure marker (red tick marks) and the diffracted intensities from the WC anvils and Ni binder (green and blue, respectively). Numerous mismatches are evident in this refinement and it is clear that the ζ-form is not adopted under these conditions.

This observation stimulated further investigations into the compression of γ-CL-20 in methanol:ethanol using single-crystal X-ray diffraction in order to provide a direct comparison with the analogous experiments using Fluorinert. It was decided that, in order to maximise data completeness in this experiment, two small crystals would be loaded into the diamond-anvil cell (DAC) in different orientations (as described in Section 2.2.3). In this way, two single crystals of the γ-form (produced by re-crystallisation of ε-CL-20 from hot benzene, as above) were loaded into a DAC, along with a small ruby chip to act as pressure

calibrant. Subsequent addition of the pressure-transmitting medium (4:1 MeOH:EtOH), however, resulted in the immediate formation of bubbles on the surface of the crystals. After a period of *ca* 20 mins the interaction between crystal and medium had progressed to such an extent that crystallinity was completely destroyed. This dramatic effect is shown in Figure 4.18.

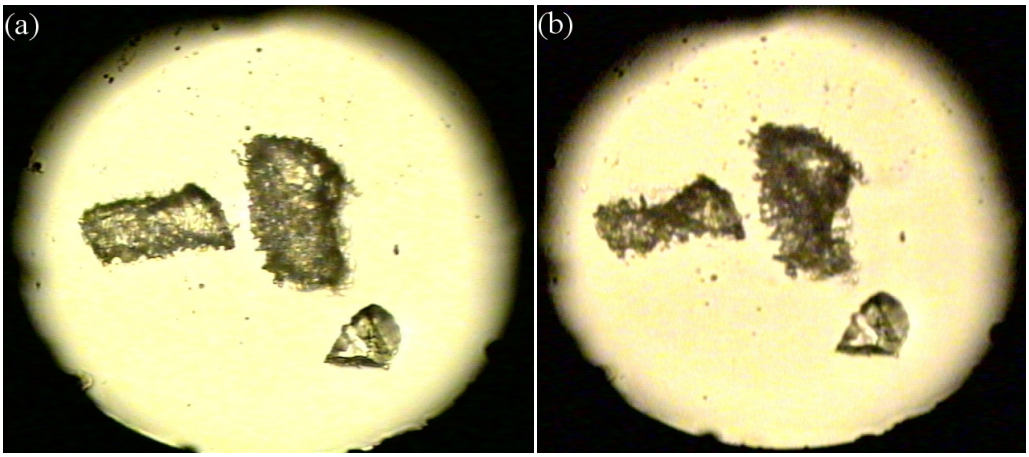

Figure 4.18 Photographs of single crystals loaded into a DAC with MeOH:EtOH as pressure-transmitting medium: (a) immediately after closure of the cell; and (b) after 20 mins, highlighting the complete destruction of the crystals. The ruby chip can be found in the bottom right quadrant of the sample chamber in both photographs.

In order to retain sufficient crystallinity to allow single-crystal diffraction, it was necessary to load a larger crystal (*ca* 150 x 75 x 50 μm) into the DAC. Thus, despite surface effects attributable to the interaction of the sample crystal with the medium, it was possible to obtain a data-set at 0.05 GPa of sufficient quality to allow a satisfactory structural refinement of γ-CL-20 ($P2_1/n$). Compression of this crystal to 0.5 GPa resulted in a distinct change in crystal morphology (see Figure 4.19), in accordance with the transition pressure determined in the neutron powder diffraction study. At this pressure, it was possible to index a set of reflections to an orthorhombic unit cell (*Pbca*, a = 9.6472, b = 13.1663, c = 23.3562 Å) and the quality of the data was such that structure solution was possible *via* direct methods.[46]

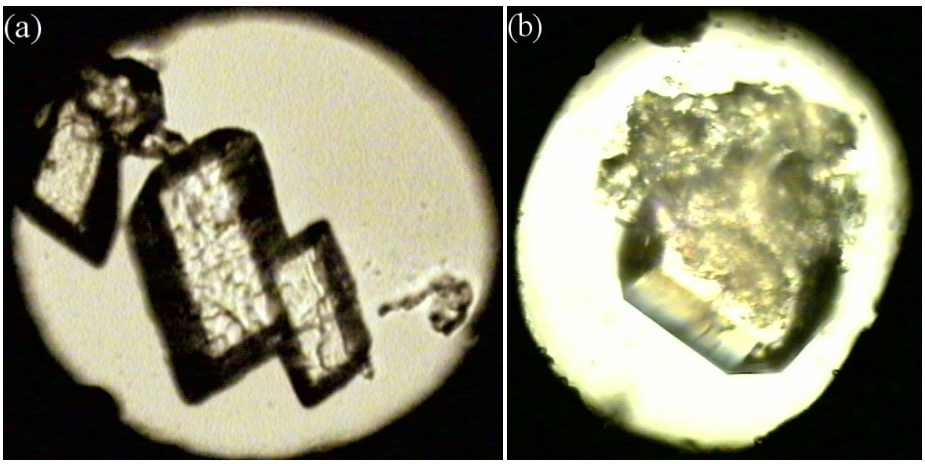

Figure 4.19 Comparison of the crystal morphology of the γ-form at ambient conditions and after compression to 0.5 GPa in MeOH:EtOH.

It is interesting to note that the unit cell dimensions, the crystal packing and the conformation of the CL-20 molecule in this form (shown in Figure 4.20) correspond extremely well those observed for α-CL-20, the hydrated form under ambient conditions. Crucially, however, the relatively low completeness (80%) of the high-pressure data-set meant that it was not possible to model the residual electron-density sufficiently to determine whether this was indeed the same form, that is a hydrate, or in fact a solvate of ethanol and/or methanol. This was further complicated by the suspected disorder of the solvent molecules within the crystal lattice. It was therefore hoped that this form was sufficiently metastable to allow its recovery to ambient pressure and its extraction from the DAC. Thus high-quality, low-temperature X-ray single-crystal diffraction data may be obtained.

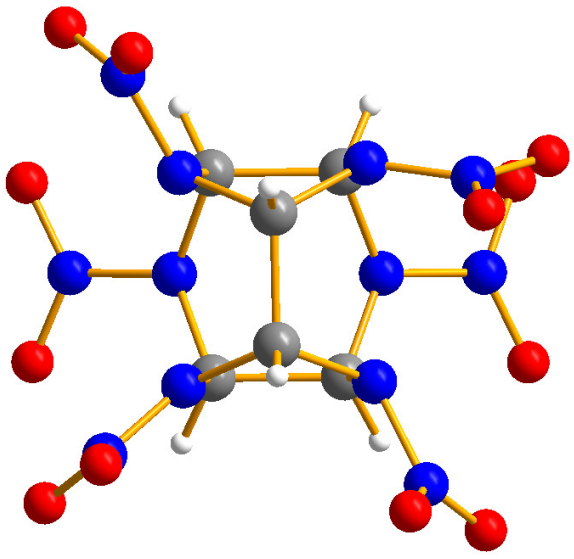

Figure 4.20 Comparison of the molecular conformation after compression of γ-CL-20 to 0.5 GPa in MeOH:EtOH.

Decompression of the sample to ambient pressure did not result in any visual indications of deterioration in crystal quality. Hence it was possible to obtain an orthorhombic unit cell indexing (*Pbca*) from a data collection performed (at 293 K) while the crystal was still confined to the DAC. Indeed the crystal was sufficiently stable to be manipulated and mounted on a fibre for data-collection at 100 K. The conformation of the CL-20 molecule and the crystal packing at this temperature were both consistent with the structure refinement at 0.5 GPa, confirming that neither decompression nor cooling had resulted in a phase transition.

Furthermore, the quality of the data was such that it has been possible to describe more accurately the solvent disorder within the structure. In contrast to the α-form, with which this structure shares a common molecular conformation and packing motif, the crystallised solvent is not water, but rather methanol. Moreover, the CL-20:MeOH ratio has been determined to be 1:0.5. The α-CL-20 structure reported by Golovina *et al.* [14] has been determined to contain a CL-20 to H_2O ratio of 1:0.57; meanwhile, in the studies by Nielsen *et al.* and Jacob *et al.* this was found to be 1:0.25.[2, 13] It should also be noted that the methanol molecules may adopt one of two orientations with respect to the rest of the unit cell, with approximately equal probability. Thus it has been necessary to model this disorder by the inclusion of two carbon atoms (with occupancy of 0.5) located at 180° to one another about the central oxygen atom, which resides on an inversion centre.

Despite these differences, however, the methanol molecules are broadly located in similar positions to those occupied by water molecules in the α-structures. Primarily, the solvent molecules are organised into channels running parallel to the *a*-axis at (*x*, *y*, 0) and (*x*, *y*, 0.5), as shown in Figure 4.21, with two whole molecules per unit cell in each channel. The positions of the solvent molecules in the crystal lattice coincide with voids within a lattice constructed solely from α-CL-20 molecules, as shown in Figure 4.21(c).

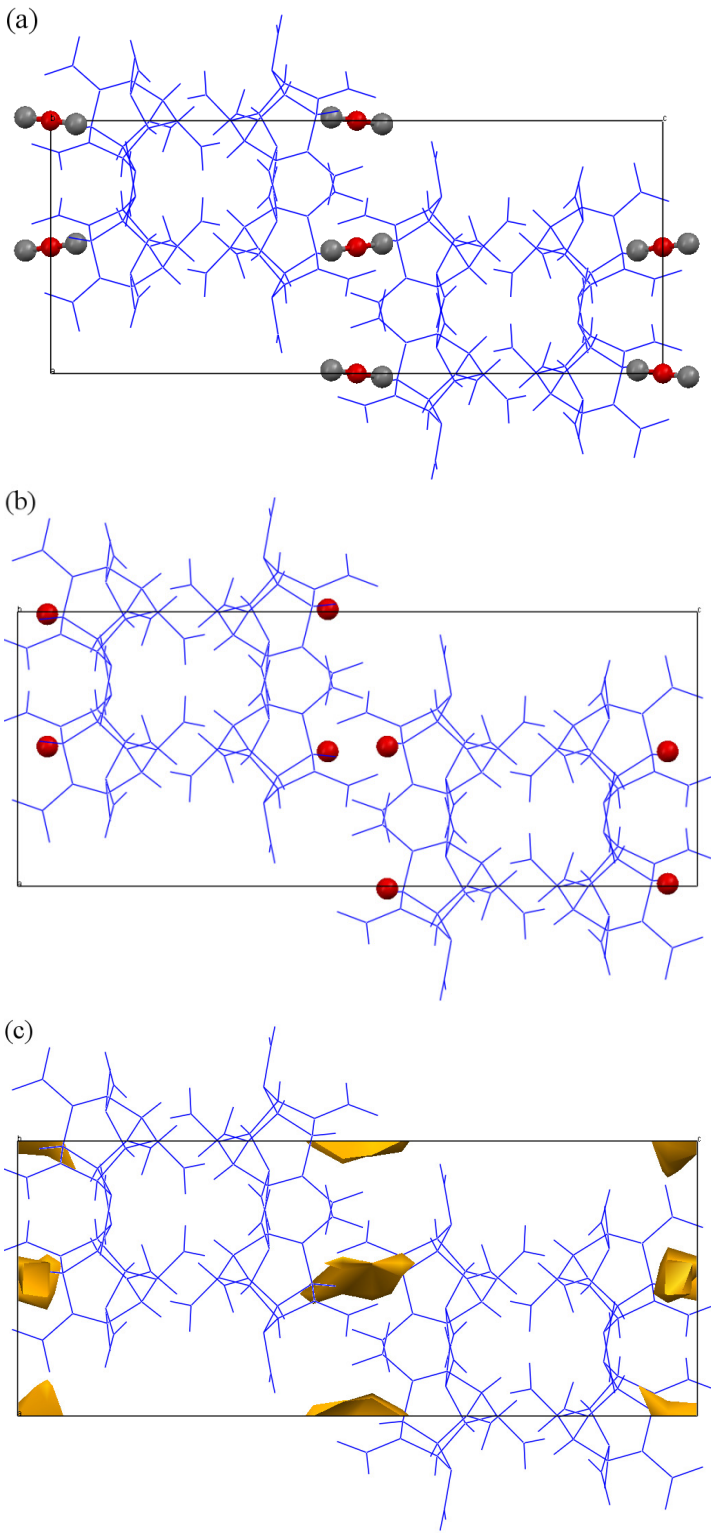

Figure 4.21 Comparison of the crystal structure of (a) the CL-20:MeOH solvate determined in this work with, (b) the α-CL-20 structure published by Jacob *et al.* In addition, void analysis of the dehydrated α-lattice has been conducted by manually deleting the water molecules from the structure reported by Jacob *et al.* and using a probe radius of 0.75 Å. These voids are shown in yellow in (c).

The inclusion of methanol molecules into this α-framework also has significant implications for the crystal density. It is interesting to note that, of the previously published structures of α-CL-20, the greatest crystal density (1.98 Mg m^{-3} at 295 K) is displayed by the structure reported by Nielsen *et al*. with a CL-20:H_2O ratio of 1:0.25, indicating perhaps that the swelling of the crystal lattice to incorporate more solvent molecules is not compensated by the added mass per unit cell. Golovina *et al.* and Jacob *et al.* both report a room temperature crystal density of 1.97 Mg m^{-3} for their 1:0.57 and 1:0.25 hydrates, respectively. In the current study, the crystal density has been determined to be 2.001 Mg m^{-3} at 100 K (as determined from full structure refinement) and 1.93 Mg m^{-3} at 293 K (based on unit cell indexing obtained from the diamond-anvil cell data-collection). Although it would be desirable to conduct an ambient-temperature data collection on a crystal mounted on a fibre, this clearly suggests that the methanol solvate is less dense than the hydrates. However, the room temperature density exceeds that of the γ-form (1.916 Mg m^{-3} at 293 K).[2] This has significant implications for its application as an energetic material, however, since a material's detonation is, to a first approximation, proportional to its crystal density.[54] This would perhaps indicate that CL-20 with solvent inclusions would be less powerful, although other factors, such as sensitivity for example, contribute to an overall assessment of energetic performance.

A summary of the pertinent crystallographic information from the data collections performed in this study is presented in Table 4.3, alongside information reported in the literature for α-CL-20.

	CL-20:MeOH		CL-20:H_2O		
Stoichiometry	2:1	2:1	1:0.57 [14]	1:0.25 [2]	1:0.25 [13]
Space Group	*Pbca*	*Pbca*	*Pbca*	*Pbca*	*Pbca*
a (Å)	9.773(2)	9.6445(5)	9.603(3)	9.485(2)	9.546(1)
b (Å)	13.346(3)	13.2186(7)	13.304(3)	13.225(4)	13.232(1)
c (Å)	23.925(5)	23.3407(8)	23.653(1)	23.673(3)	23.634(2)
V (Å^3)	3120.6(10)	2975.6(2)	3021.9(2)	2969.5(11)	2985.3(10)
D_c (Mg m^{-3})	1.93	2.001	1.97	1.98	1.97
T (K)	293	100	295	295	295

Table 4.3 Crystallographic information for the 'α-like' structure determined in this study at 293 and 100 K, presented alongside the published information for α-CL-20.

Using the structure of the CL-20:methanol solvate determined in this study, it was then possible to perform full-profile Rietveld refinements of the neutron powder diffraction

patterns collected during the compression of γ-CL-20 in MeOD:EtOD. It should be noted, however, that some intensity mismatches can be observed throughout. For example, the quality of the Rietveld refinement conducted on the pattern obtained at 5.16 GPa is shown in Figure 4.22. Inspection of the reflections most affected by the apparent intensity mismatches (for example, the (026) peak at ca 3.2 Å), suggests there exists a subtlety to the solvent disorder that has not been modelled sufficiently. Unfortunately, the relatively poor resolution of the neutron powder patterns and the restricted access to reciprocal space due to the Paris-Edinburgh cell (such studies are limited to a *d*-spacing range of 1 – 4.2 Å), have meant that it has not been possible to qualitatively assess the location of the methanol molecules within the lattice. In addition, given the large number of atoms in the asymmetric unit (39), it was thought prudent not to refine the atomic co-ordinates as this would introduce far more variables than would be appropriate for data of this quality. Despite this, all of the refinements conducted in this study have been stable and the unit cell parameters determined at each pressure have been tabulated (Table 4.4) and plotted below (see Figure 4.23).

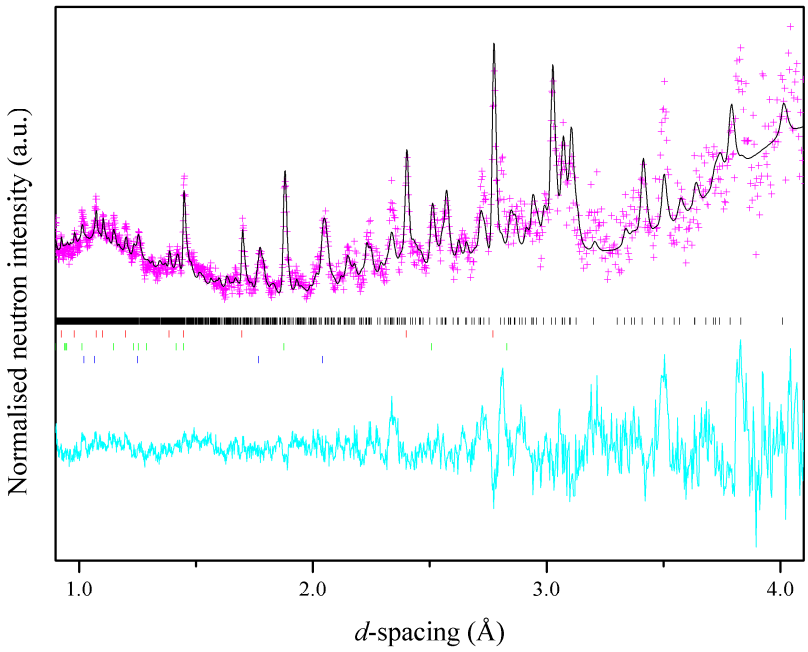

Figure 4.22 Plot of the Rietveld refinement of the pattern collected at 5.16 GPa using the structure determined for the CL-20:methanol solvate. The experimental data (I_{obs}) are represented as pink crosses, the calculated pattern (I_{calc}) is shown in black and the difference (I_{obs} - I_{calc}) in cyan. Tick-marks for each phase are also shown for clarity: CL-20:MeOD (black), Pb (red), WC (green) and Ni (blue).

P (GPa)	a (Å)	b (Å)	c (Å)	β (°)	V (Å^3)	wR_p
0.00	13.167(2)	8.1351(14)	14.839(2)	109.078(13)	1502.2(3)	0.026
0.57	9.594(3)	13.090(5)	23.267(7)		2922.0(11)	0.043
0.92	9.532(3)	13.001(5)	23.154(7)		2869.2(11)	0.040
1.99	9.395(4)	12.770(5)	22.898(7)		2747.3(12)	0.043
3.05	9.296(4)	12.610(5)	22.725(7)		2663.9(11)	0.042
4.19	9.205(4)	12.478(6)	22.557(8)		2590.8(13)	0.046
5.16	9.149(5)	12.387(6)	22.425(8)		2541.5(14)	0.052

Table 4.4 Variation of the unit cell parameters throughout compression of CL-20 in MeOD:EtOD to 5.16 GPa, indicating the transition from the pure γ-form to the CL-20:MeOD solvate.

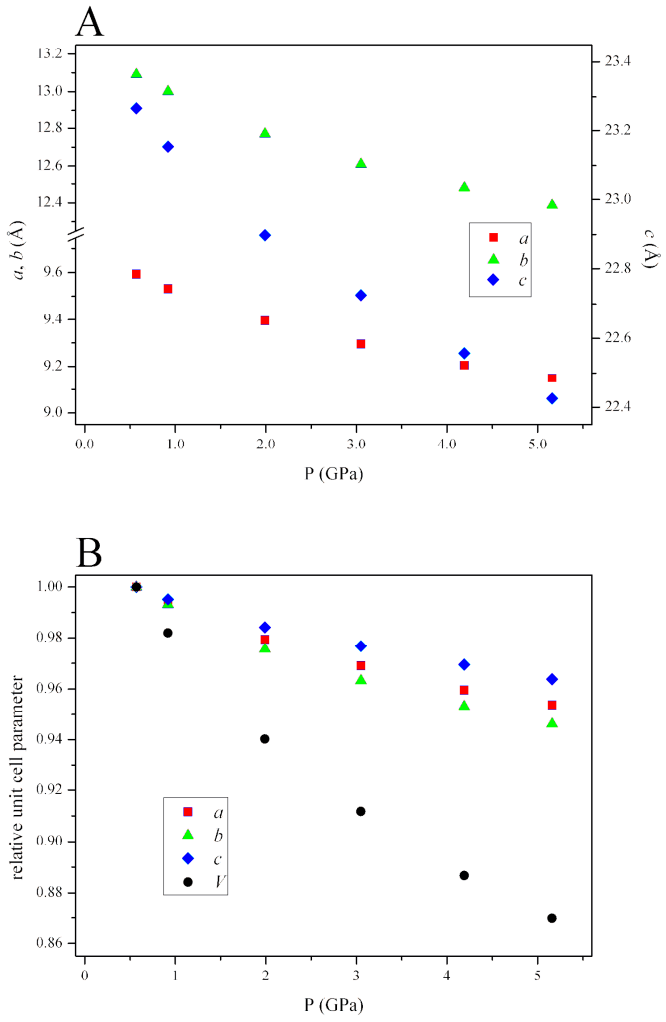

Figure 4.23 (a) The compression, and (b) the relative compression of the unit cell parameters of the CL-20:methanol solvate up to the maximum pressure (5.16 GPa).

The relative compression of the unit cell parameters shows that the *c*-axis, the direct normal to the alternating layers of methanol and CL-20 molecules, is least compressible, while the

b-axis is most compressible. Although the difference in the relative compression of these axes is small (*ca* 2% at 5.16 GPa), it perhaps underlines the important role of the methanol molecules in filling voids in the lattice. If these voids were not filled by solvent molecules, one may expect the *c*-axis to be, in fact, the most sensitive to high pressure since compression often manifests itself in the collapse of such voids and a shortening of inter-planar distances.

Furthermore, it is interesting to note that, as a whole, the CL-20:methanol structure displays similar compressibility to the pure ε-form. The smooth contraction of the unit cell volume (up to 5.16 GPa) has been fitted to both a 3rd-order Birch-Murnaghan and a Vinet EoS, as shown in Figure 4.24. In both cases, the unit cell volume at zero pressure has been fixed to the value determined by single-crystal X-ray diffraction at 293 K since CL-20-h_6 samples were used in both diffraction experiments. The coefficients of the Birch-Murnaghan EoS have been determined as V_0 = 3120.6 Å^3 (fixed), B_0 = 4.6(5) GPa and B' = 27(4). Visual inspection of this fit, however, clearly shows that this does not adequately describe the contraction of the unit cell volume, particularly at higher pressure. In this case, a much more satisfactory fit is obtained with a Vinet EoS with V_0 = 3120.6 Å^3 (fixed), B_0 = 6.6(5) GPa and B' = 13.6(8). If the Vinet equation of state is regarded as being more accurate, this suggests that the methanol solvate is marginally more compressible than the pure ε-form. In the current study, the bulk modulus of ε-CL-20 has been determined to be 9.5(22) GPa.

It should be noted, however, that calculation of the EoS based solely on the neutron powder diffraction data results in marked differences in the bulk modulus and its pressure-derivative, B'. Since no decompression study was carried out in this instance, no ambient pressure refinement has been possible. Instead, the EoS has been determined by fixing V_0 to be the unit cell volume at the first pressure where this form was observed, *i.e.* 2922.0 Å^3 at 0.57 GPa. Then, in line with the procedure outlined in Section 2.6, all succeeding pressures have been normalised to this pressure. The 3rd-order Birch-Murnaghan and Vinet equations of state determined in such a way are displayed in Figure 4.24(b). The coefficients have been found to be B_0 = 17.2(10) GPa and B' = 10.1(12) for the 3rd-Order Birch Murnaghan EoS; and, B_0 = 17.5(8) GPa and B' = 9.2(8) for the Vinet EoS. In contrast to the values above, the bulk moduli calculated in this way indicate that this structure is significantly less compressible than the ε-form. It is therefore of immediate interest to conduct a rigorous compression (and decompression) study of this form, preferably by high-resolution X-ray powder diffraction, in order to obtain a high-quality EoS for this material.

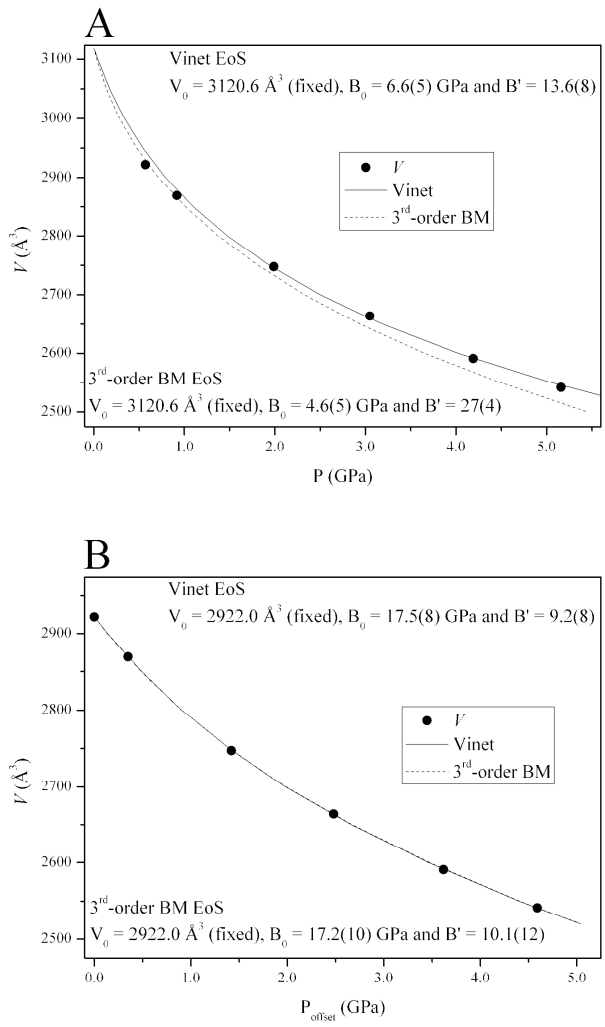

Figure 4.24 (a) Variation of unit cell volume of CL20:MeOH with pressure, including V_0 determined by X-ray single-crystal diffraction and a representation of the Vinet and 3rd-order Birch-Murnaghan equations of state; (b) the compression of the unit cell volume determined during the neutron powder diffraction experiment. In this case, pressures have been normalised to 0.57 GPa.

In addition to a re-examination of the compression behaviour of this methanol solvate, it would be highly desirable to conduct further analysis on the recovered material to determine quantitatively the degree of solvation, as well as the positions of the solvent molecules within the lattice. Current studies are therefore focussed on the spectroscopic (IR/Raman and NMR) and gravimetric (CHNO analysis and mass spectrometry) analysis, in addition to obtaining the desired high-quality diffraction data.

These studies should then be extended to explore the possibility of obtaining solvates and co-crystals of CL-20 at ambient conditions. For example, it may be possible to obtain a CL-20:methanol solvate at ambient pressure, which displays a different stoichiometry or a different molecular conformation for example. This would perhaps have significant

implications for crystal density and sensitivity. Moreover, in studies analogous to the recrystallisation of pharmaceuticals at pressure, the formation of co-crystals at elevated pressures should also be explored. Finally, an analysis of the thermal stability of such co-crystals must be undertaken. For example, crystal quality may be adversely affected by gradual desolvation during storage and, as a result, the material may actually become more sensitive. Furthermore, the desolvation products should be characterised as fully as possible in order to ascertain the resultant polymorph.

4.6 Conclusions

The structural data presented herein are illustrative of a significant advance in the structural characterisation of this important class of materials under extreme conditions. The level of complexity of the CL-20 molecule extends the limits to which high-pressure techniques may be applied, and highlights the need for employing a range of different methods for structure solution. These results will be of importance not only to the energetics community, for whom the high-pressure polymorphism of CL-20 has been a long-standing problem, but also to those solid-state chemists and physicists wishing to model the behaviour of this important class of nitramines.

The structure of the high-pressure ζ-form has been determined by a combination of single-crystal and powder X-ray diffraction. Compression of γ-CL-20 to $P > 0.72$ GPa in Fluorinert has been observed to result in a conformational change of the nitro groups with respect to the five- and six-membered rings. This change in molecular conformation imbues the high-pressure ζ-form with a higher degree of molecular symmetry and results in a crystal structure with similarities to both the γ- and ε-forms.

In a dramatic example of the effect the pressure-transmitting medium may have on the structural properties of a system, compression of γ-CL-20 in MeOH:EtOH has been found to result in the formation of a CL-20:MeOH (2:1) solvate, simply by the application of pressure. Furthermore, once formed (above 0.5 GPa), this solvate remains stable upon compression to at least 5.2 GPa *and* can be recovered to ambient pressure at ambient temperature. Although the methanol solvate has been found to be less dense than the ε-form, this result clearly highlights the opportunity that co-crystallisation techniques (at ambient conditions as well as at elevated pressure) present in the structure/property modification of these important materials.

Finally, the importance of the starting polymorph has also been illustrated by conducting a high-pressure X-ray powder diffraction investigation of the compression of ε-CL-20 to a

maximum pressure of 7.22 GPa. At no point was a pressure-induced phase transition to the γ-form observed, contrary to previous spectroscopic studies.[32] Furthermore, the equation of state describing the hydrostatic compression of ε-CL-20 has been determined. The significance of this result should not be overlooked, since previous EoS data have been determined under non-hydrostatic conditions.[31] It may be suggested therefore that the current study represents a more useful experimental account of the effects of pressure on the crystal structure and hence provides a more rigorous test of computational predictions.

4.7 Suggestions for Further Work

While the hydrostatic compression of the thermodynamically most stable form under ambient conditions, ε-CL-20, has been rigorously investigated to 7.22 GPa, no high-quality equations of state exist for the other forms of CL-20. High-pressure studies of the α- and β-forms are therefore imperative. As was evident in the compression study of the other metastable form, γ-CL-20, this may result in further phase transitions to novel polymorphs. It would also be extremely valuable to extend the pressure range for which the ζ-form has been structurally characterised. However, this will naturally be complicated by the hydrostatic limit of the Fluorinert pressure-transmitting medium (*ca* 1.0 GPa).

As has been illustrated by the compression of γ-CL-20 in MeOH:EtOH, the effect of the pressure-transmitting medium should not be underestimated. It is therefore suggested that compressions be conducted in a range of pressure media to ensure any structural effects of non-hydrostaticity and sample/medium interactions have been accounted for. It should also be noted that decompression often yields important information, particularly on the relative stability of high-pressure forms and kinetic barriers to their re-transformation. It is essential therefore that detailed decompression studies are undertaken and the recoverability of high-pressure polymorphs to ambient pressure is explored.

In this study, the application of pressure alone has been sufficient to produce the ζ-form and a CL-20:MeOH solvate. As has been shown to be extremely successful in the structural characterisation of ε-RDX (Section 3.5.2), the combined effects of temperature *and* pressure on CL-20 should also be explored. Given the rich polymorphism under ambient conditions, one would expect such studies to produce further polymorphs of CL-20, some of which may be recoverable to ambient pressure. Moreover, any recovered high-pressure forms would be expected to be denser, and therefore more powerful, than the starting polymorph.

The formation of a CL-20:MeOH solvate at 0.5 GPa also presents a significant opportunity for the development of these materials by co-crystallisation. The ability of CL-20 to form a

methanol solvate and hydrates of different stoichiometries clearly suggests that voids large enough to accommodate small molecules exist within the structure. This feature should therefore be exploited fully by the investigation of CL-20 co-crystals under ambient conditions, as well as at elevated pressure. For example, it would be interesting to compare the structures of the methanol solvate produced in this work with one that may be crystallised at atmospheric pressure. Given the dramatically different thermodynamic conditions under which they have been formed, one may reasonably expect differences to arise between the structures, for example in solvent location or stoichiometry.

Moreover, the inclusion of small molecules in the crystal lattice would certainly result in changes in the crystal density and, crucially, sensitivity. Co-crystallisation may therefore be viewed as an opportunity to tailor munitions at the molecular level, provided their structures, stability and energetic performance have been thoroughly investigated.

4.8 References

1. A.T. Nielsen, *Synthesis of Caged Nitramine Explosives* in *Joint Army, Navy, NASA, Air Force (JANNAF) Propulsion Meeting*, 1987, San Diego, USA.
2. A.T. Nielsen, A.P. Chafin, S.L. Christian, D.W. Moore, M.P. Nadler, R.A. Nissan, D.J. Vanderah, R.D. Gilardi, C.F. George, and J.L. Flippen-Anderson, *Tetrahedron*, 1998, **54**, 11793.
3. R.S. Miller, in *Decomposition, Combustion and Detonation Chemistry of Energetic Materials*, 1995, Pittsburgh, USA.
4. R.L. Simpson, P.A. Urtiew, D.L. Ornellas, G.L. Moody, K.J. Scribner, and D.M. Hoffman, *Propellants, Explos., Pyrotech.*, 1997, **22**, 249.
5. H. Bazaki, S. Kawabe, H. Miya, and T. Kodama, *Propellants, Explos., Pyrotech.*, 1998, **23**, 333.
6. M.F. Foltz, C.L. Coon, F. Garcia, and A.L. Nichols III, *Propellants, Explos., Pyrotech.*, 1994, **19**, 19.
7. M.F. Foltz, C.L. Coon, F. Garcia, and A.L. Nichols III, *Propellants, Explos., Pyrotech.*, 1994, **19**, 133.
8. V.V. Nedelko, N.V. Chukanov, A.V. Raevskii, B.L. Korsounskii, T.S. Larikova, O.I. Kolesova, and F. Volk, *Propellants, Explos., Pyrotech.*, 2000, **25**, 255.
9. R.Y. Yee, M.P. Nadler, and A.T. Nielsen, in *JANNAF Propulsion Meeting*, 1990, Anaheim, USA.
10. K.J. Kraeutle, in *JANNAF Propulsion Meeting*, 1988, Huntsville, USA.
11. K.J. Kraeutle, in *JANNAF Proceedings*, 1990, Cheyenne, USA.
12. T.P. Russell, P.J. Miller, G.J. Piermarini, and S. Block, *J. Phys. Chem.*, 1992, **96**, 5509.
13. G. Jacob, L. Toupet, L. Ricard, and C. G, *Private Communication to the CSD*, 1999.
14. N. Golovina, A. Raevskii, N. Chukanov, B. Korsounskii, L. Atovyman, and S. Aldoshin, *Rossijskij Khimicheskij Zhurnal*, 2004, **48**, 41.
15. Y. Kholod, S. Okovytyy, G. Kuramshina, M. Qasim, L. Gorb, and J. Leszczynski, *J. Mol. Struct.*, 2007, **843**, 14.
16. P. Goede, N.V. Latypov, and H. Östmark, *Propellants, Explos., Pyrotech.*, 2004, **29**, 205.
17. J.H. Kim, Y.C. Park, Y.J. Yim, and J.S. Han, *J. Chem. Eng. Jpn.*, 1998, **31**, 478.

18. D.M. Hoffman, *Propellants, Explos., Pyrotech.*, 2003, **28**, 194.
19. M.H. Lee, J.H. Kim, Y.C. Park, J.H. Hwang, and W.S. Kim, *Ind. Eng. Chem. Soc*, 2007, **46**, 1500.
20. T.P. Russell, P.J. Miller, G.J. Piermarini, and S. Block, *J. Phys. Chem.*, 1993, **97**, 1993.
21. J. Li and T.B. Brill, *Propellants, Explos., Pyrotech.*, 2007, **32**, 326.
22. G. Zhou, J. Wang, W.D. He, N.B. Wong, A. Tian, and W.K. Li, *J. Mol. Struct. THEOCHEM*, 2002, **589-590**, 273.
23. X.J. Xu, W.H. Zhu, and H.M. Xiao, *J. Phys. Chem. B*, 2007, **111**, 2090.
24. N. Chukanov, V. Zakharov, B. Korsunskii, A. Raevskii, V. Nedelko, S. Vozchikova, T. Larikova, N. Golovina, and S. Aldoshin, *Russ. J. Phys. Chem. A*, 2009, **83**, 29.
25. N. Chukanov, V. Dubovitskii, V. Zakharov, N. Golovina, B. Korsunskii, S. Vozchikova, V. Nedelko, T. Larikova, A. Raevskii, and S. Aldoshin, *Russ. J. Phys. Chem. B*, 2009, **3**, 486.
26. D.I.A. Millar, H.E. Maynard-Casely, and C.R. Pulham, *unpublished results,* 2010.
27. T.P. Russell, P.J. Miller, G.J. Piermarini, and S. Block, *J. Phys. Chem.*, 1992, **96**, 5509.
28. D.C. Sorescu and B.M. Rice, *J. Phys. Chem. C*, 2010, **114**, 6734.
29. J.C. Gump and S.M. Peiris, *Proc. Int. Det. Symposium, USA*, 2006, 1045.
30. J.C. Gump, C.A. Stoltz, and S.M. Peiris, *AIP Conf. Proc.*, 2007, **955**, 127.
31. J.C. Gump and S.M. Peiris, *J. Appl. Phys.*, 2008, **104**, 083509.
32. J.A. Ciezak, T.A. Jenkins, and Z. Liu, *Propellants, Explos., Pyrotech.*, 2007, **32**, 2774.
33. L. Merrill and W.A. Bassett, *Rev. Sci. Instrum.*, 1974, **45**, 290.
34. G.J. Piermarini, S. Block, J.D. Barnett, and R.A. Forman, *J. Appl. Phys.*, 1975, **46**, 2774.
35. A.P. Hammersley, S.O. Svensson, M. Hanfland, A.N. Fitch, and D. Hausermann, *High Press. Res.*, 1996, **14**, 235
36. V. Favre-Nicolin and R. Cerny, *J. Appl. Crystallogr.*, 2002, **35**, 734.
37. R. Von Dreele and A.C. Larson, *General Structure Analysis System (GSAS)*, 1986.
38. W.G. Marshall and D.J. Francis, *J. Appl. Crystallogr.*, 2002, **35**, 122.
39. J.M. Besson, R.J. Nelmes, G. Hamel, J.S. Loveday, G. Weill, and S. Hull, *Physica B*, 1992, **180-181**, 907.
40. S.A. Moggach, D.R. Allan, S. Parsons, and J.E. Warren, *J. Appl. Crystallogr.*, 2008, **41**, 249.
41. A. Dawson, D.R. Allan, S. Parsons, and M. Ruf, *J. Appl. Crystallogr.*, 2004, **37**, 410.
42. Bruker-Nonius, *APEX-II*, Bruker-AXS, Madison, WI, USA, 2000.
43. Bruker-AXS, *SAINT*, Bruker-AXS, Madison, WI, USA, 2003.
44. S. Parsons, *SHADE, Program for Empirical Absorption Corrections to High Pressure Data*, The University of Edinburgh, UK, 2004.
45. G.M. Sheldrick, *SADABS*, University of Göttingen, Germany, 2004.
46. A. Altomare, G. Cascarano, C. Giacovazzo, A. Guagliardi, M.C. Burla, G. Polidori, and M. Camalli, *J. Appl. Crystallogr.*, 1994, **27**, 435.
47. P.W. Betteridge, J.R. Carruthers, R.I. Cooper, K. Prout, and D.J. Watkin, *J. Appl. Crystallogr.*, 2003, **36**, 1487.
48. J. Cosier and A.M. Glazer, *J. Appl. Crystallogr.*, 1986, **19**, 105.
49. Oxford Diffraction Ltd, *CrysalisPRO Software*, Abingdon, UK, 2010.
50. D.C. Sorescu, B.M. Rice, and D.L. Thompson, *J. Phys. Chem. B*, 1999, **103**, 6783.
51. R.J. Angel, M. Bujak, J. Zhao, G.D. Gatta, and S.D. Jacobsen, *J. Appl. Crystallogr.*, 2007, **40**, 26.
52. J.C. Gump and S.M. Peiris, *personal communication*, 2009.
53. T. Varga, A.P. Wilkinson, and R.J. Angel, *Rev. Sci. Instrum.*, 2003, **74**, 4564.

54. J. Akhavan, *The Chemistry of Explosives*, Royal Society of Chemistry, Cambridge, UK, 2004, 2nd edn.

Chapter 5

Structural Investigation of a Series of Inorganic Azides

Part 1: NaN_3, CsN_3 and TlN_3

5 Structural Investigation of a Series of Inorganic Azides (Part 1)

5.1 General Introduction to Inorganic Azides

5.1.1 Azides as Energetic Materials

Inorganic azides [general formula $M^{n+}(N_3)_n$] have been widely used as energetic materials on account of their rapid decomposition to produce large amounts of nitrogen gas according to Equation (1):

$$M^{n+}(N_3)_n\,(s) \rightarrow M\,(s) + {}^{3n}/_{2}\,N_2\,(g) \qquad (1)$$

Upon initiation by stimulus, such as heat or impact, the heavy metal azides such as $Pb(N_3)_2$ and AgN_3 transition to detonation very rapidly making them ideal for use as primary explosives, although the extremely high sensitivity of copper and gold azides makes these impractical for use in munitions. Lead(II) azide is, in fact, the most widely used primary explosive, despite well-documented concerns over its environmental and toxicological effects.[1] Replacement of $Pb(N_3)_2$ in primers and detonators has proved to be very challenging because alternatives must have comparable explosive performance (in terms of explosive power and instantaneous response to initiation), while remaining chemically and thermally stable and compliant with existing health and safety regulations.[2] Other azides, such as NaN_3, are more difficult to initiate and decompose rapidly producing large volumes of N_2 gas, but do not detonate. This is particularly attractive for use as gas generators: NaN_3 for example has been used in automotive air-bags.[3]

Recent developments in the use of these compounds have focussed on the production of large amounts of nitrogen from a polymeric 'high-energy density material', which would be expected to burn rapidly with the release of environmentally clean by-products (i.e. $N_2(g)$ only). Peiris and Russell used the novel approach of photolysing NaN_3 under high pressure (up to 5.0 GPa) using visible light, λ = 514 nm.[4] It was hypothesised that by performing the reaction at these pressures, the azide radicals produced during photolysis would bond with other azide species to form larger molecules with high nitrogen content. Spectroscopic analysis led the authors to conclude tentatively that the product was either N_7^- or Cl_2N_6 (where $Cl^{\bullet}$ radicals originated from the NaCl pressure-transmitting medium) although the product was not recoverable to ambient pressure.

Eremets *et al*. have also reported the formation of polynitrogen species formed from sodium azide although they noted that application of pressure alone was sufficient to create a new species.[5] On the basis of their Raman spectroscopic study, they report a new phase observed above 19 GPa. The increased interaction between the azide ions at these pressures suggested a phase composed of larger clusters of nitrogen atoms. Raman measurements in the pressure range 50 – 120 GPa indicated that at these pressures an amorphous 'non-molecular' nitrogen species is formed, on the basis of the disappearance of modes attributable to the azide unit. Laser heating (up to 3300 K) and the application of large shear deformations to the sample by rotation of the diamond anvils were both found to accelerate these transitions. Although these non-molecular species could be stabilised on decompression to below 1 GPa, it was not possible to recover and characterise them at atmospheric pressure.

5.1.2 Structural Considerations

In general, azides can be broadly classified into three categories depending on their structures: molecular, ionic and co-ordinative azides.[6] Molecular azides, in which one terminal N-atom of the N_3 group is covalently bound to another atom or group (such as H, Me or a transition metal [7]), play an important role in synthetic chemistry, but are not a focus of this study.

In ionic azides the discrete cations and N_3^- anions are separated by distances greater than the sum of their respective ionic radii. Furthermore the anions are always perfectly linear and symmetric (the N-N bond lengths are equal and do not deviate significantly from 1.17 Å [8]). The electron density distribution around the N_3^- ion in sodium azide correlates well with the theoretical resonance model:

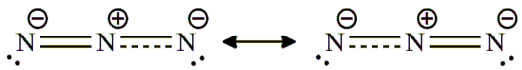

where the displaced double bond lines indicate bonding π-electrons, which lie out of the plane of the paper, perpendicular to the other bonding π-electrons,. This gives rise to a formal net positive charge on the central nitrogen of + 0.71 while the terminal N atoms each carry a charge of - 0.86.[9]

Co-ordinative azides may be considered to be an intermediate case between the ionic and molecular azides: the metal atoms are in close enough proximity to one (or more) azide group such that weak covalent interactions can occur between them, leading to polymeric networks in which the metal atoms are linked to one another *via* bridging azide units.[6] In

these cases (typically heavy metal azides) the linearity of the anion is generally retained, although some deviations have been observed (for example, in $Pb(N_3)_2$). The N-N bond lengths within the azide, however, are markedly dependent on the environments of each of the terminal N-atoms. If the terminal nitrogens are at similar distances away from two neighbouring metal atoms one would expect the N-N bond lengths to be similar, but if one N atom is only weakly interacting with one neighbouring metal, while the other N atom is surrounded by three metals, this will result in an asymmetry in the N-N bond lengths.

5.1.3 Structure and Sensitivity

Despite the rich polymorphism displayed by inorganic azides (*vide infra*), their chemical and structural simplicity makes them ideal for modelling deflagration/detonation reactions. Moreover, this family of compounds displays a wide range of sensitivities to detonation, ranging from the almost inert Group 1 azides to the very sensitive copper azides.[10] As a result, recent computational studies have focussed on understanding the electronic structure of these compounds, with a view to rationalising their explosive decompositions.[11-15] The most recent theoretical study of these important systems, however, has instead investigated the relationship between the sensitivity of a given azide and its crystal structure. Cartwright and Wilkinson report a linear correlation between impact sensitivity and the minimum non-bonded N…N distance across a wide variety of (ionic and co-ordinative) azides.[10] This is consistent with theoretical and experimental results [16], which indicate that a primary explosive should be capable of decomposition to products (in this case solid metal and $N_2(g)$) with a simple rearrangement of electrons and minimal atomic displacement.[10] While this model is appealing, primarily in its simplicity, the authors admit that no account has been made for the thermochemistry of the azides and most importantly the enthalpies of formation. Moreover their measure of sensitivity is limited to the sensitivity to impact and does not consider other initiation events such as heat, shock or friction, which may require a more nuanced description.

It is also pertinent to discussions of sensitivity to mention that temperature and/or pressure (such as in a detonation event) will undoubtedly affect the intermolecular distances and may lead to phase transitions. It is therefore absolutely critical to obtain structural information on these materials under extreme conditions in order to assess any theoretical models rigorously. Interestingly inorganic azides and diamond-anvil cell technology seem inextricably linked for this very reason. Compressibility studies on what were regarded as unstable materials were not seriously considered previously because of the danger of explosion in relatively crude large volume presses.[17] The small volume of sample required

for diamond-anvil studies meant that it became possible to carry out high-pressure X-ray diffraction studies safely. For example, Weir *et al.* reported the compressibilities of single crystals of $Pb(N_3)_2$, $Ba(N_3)_2$, KN_3, TlN_3 and NaN_3 to a maximum pressure of 2.2 GPa.[18] Subsequent high-pressure studies have utilised volumetric analysis, thermal analysis and spectroscopy to extend this field to other inorganic azides and to higher pressures. A summary of this body of work is included in the following sections.

In this study, the structural properties of a series of binary azides are to be investigated at extreme conditions: the ionic azides NaN_3, CsN_3, TlN_3 and NH_4N_3, and the co-ordinative azides AgN_3 and $Pb(N_3)_2$. This chapter focuses on the structural characterisation of the 'simple' inorganic azides (NaN_3, CsN_3 and TlN_3) by a combination of X-ray and neutron powder diffraction. The results of neutron powder diffraction studies during the compression of ammonium azide, silver azide and lead(II) azide, meanwhile, are discussed in Chapter 6.

5.2 Polymorphism of the 'Simple' Inorganic Azides

5.2.1 NaN_3

Sodium azide may adopt either of two crystal structures at atmospheric pressure, depending on temperature. The high-temperature β-form ($T > 292$ K) was shown to adopt rhombohedral symmetry ($R\bar{3}m$) by Hendricks and Pauling (1925) [19]; this structure was subsequently refined by several research groups.[8, 20-22] The rhombohedral structure of the β-form may be regarded as a distortion of the cubic NaCl structure in which the chloride anions are replaced by the rod-like azide ions (N_3^-). The azide ions lie parallel to the body diagonal of the former NaCl unit cell (see Figure 5.1) and the body diagonal thus becomes elongated. From this structure it is then preferable to re-define the unit cell in keeping with crystallographic convention and thus the rhombohedral setting is chosen. From Figure 5.1 it is also clear that β-NaN_3 may also be described as a layered structure with alternating layers of sodium and azide ions parallel to the (111) direction, which is consistent with the cubic close packing of spherical ions. Within these layers, the azide ions are aligned perpendicular to the plane of the azide layer.

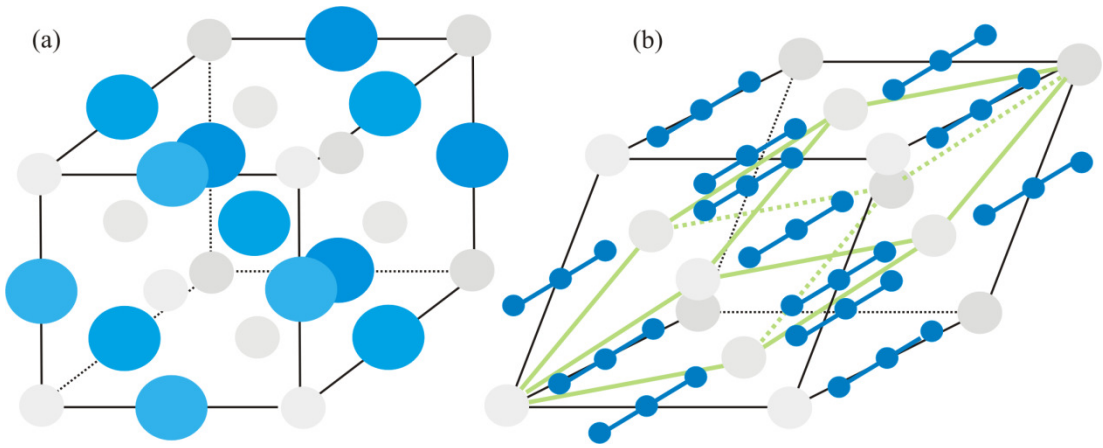

Figure 5.1 Comparison of the structures of NaCl and β-NaN_3: (a) the face-centred cubic structure of NaCl is elongated along the body diagonal upon the substitution of Cl^- with N_3^-, resulting in (b) the rhombohedral structure of β-NaN_3, the unit cell of which is shown in green. In both diagrams the Na^+ cations are shown in grey; the anions meanwhile are blue.

On the basis of their neutron diffraction measurements, in which the lateral distances between Na^+ and N_3^- units in the same layer are longer than expected and the N-N bond is shorter than expected, Choi and Prince suggest that the azide ions are tilted about the three-fold axis in a disordered manner which preserves the overall $\bar{3}m$ symmetry.[21] This model is consistent with the dynamic disorder model proposed by Iqbal, on the basis of his Raman spectroscopic observations.[23] The calculated orientational density distribution of the azide ions based on this model is in good agreement with the electron density maps of Stevens and Hope that are distinctly triangular in shape with the apexes pointing between the neighbouring Na^+ ions.[22]

It is also possible to define a monoclinic unit cell for β-NaN_3 that facilitates comparison with the low temperature α-form (*C*2/*m*), see Figure 5.2. The structure of α-NaN_3 was first determined by X-ray powder diffraction on samples cooled from the β-form.[8] (The phase transition was first observed during electron paramagnetic resonance measurements of Mn^{2+} doped crystals although the α-form was (wrongly) assumed to have orthorhombic symmetry [24]). Observations in the X-ray powder diffraction patterns led the authors to propose a displacive model for the β → α transition in which the layers of sodium atoms are sheared perpendicular to the *b*-axis and the azide ions are tilted away from the original body diagonal (see Figure 5.2). The structure of the α-form was later confirmed by a combination of X-ray single-crystal and powder diffraction.[25]

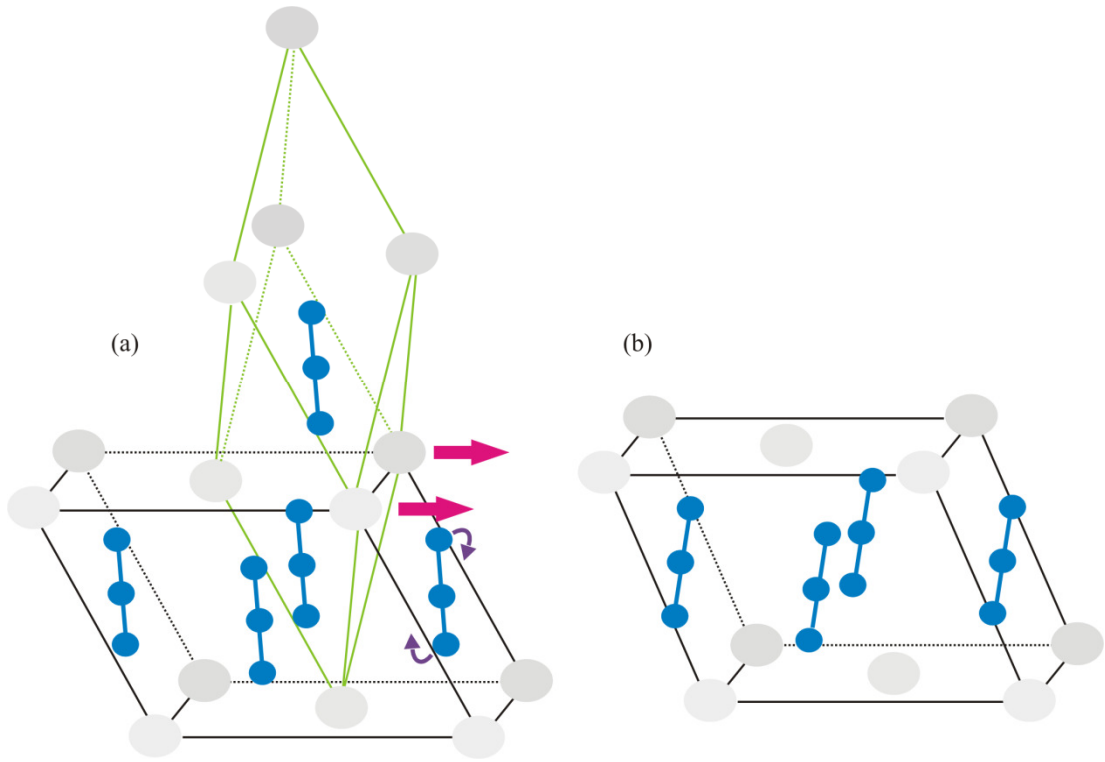

Figure 5.2 Comparison of β- and α-NaN_3: (a) in addition to the rhombohedral unit cell (shown in green), a monoclinic structure may be selected for β-NaN_3. Upon the β → α transition, the azide anions (blue) undergo a slight rotation and the cation (grey) layers are sheared. The monoclinic structure of α-NaN_3 is shown in (b).

The β → α phase transition in sodium azide (observed at a transition temperature, T_c, between 286 and 295 K [26]) has been studied by numerous analytical techniques in order to establish its true nature, *i.e.* is it weakly first order or a continuous second-order phase transition? Initially an order-disorder model was favoured, which explained the apparent second-order behaviour.[8, 27, 28] This was supported by the observation that degenerate Raman modes split [23, 26] and is consistent with the disordered model of the high-temperature phase proposed by Choi and Prince on the basis of their neutron diffraction experiments.[21]

Heat capacity measurements were unfortunately ambiguous [29, 30]: any discontinuities or thermal hysteresis loops were too small for the authors to be confident enough to exclude experimental error. Furthermore the result was significantly dependent on sample preparation – inhomogeneous strain within the sample gave rise to smearing of the specific heat, which could be mistaken for a continuous transition.[30] Midorikawa *et al.*, however, were able to observe by polarising microscopy a distinct phase front between two phase domains in a single crystal of sodium azide.[31] At the same time, Hirotsu's study of the birefringence of a single crystal also gave clear evidence for a first order transition.[32]

These contemporaneous results had a significant impact on opinion in the literature – subsequent observations have been contextualised using models that emphasise the displacive nature of the transition.[33-36]

Careful measurements of the unit cell parameters and symmetry-breaking shear strains as a function of temperature between 12 and 295 K confirmed that the transition involves a coupling of the canting of the azide anion (order-disorder) with the shearing of the sodium layers (displacive).[25] This is illustrated in Figure 5.2. As a final corroboration the authors report a small discontinuity in their measurements at 292.2 K that led them to conclude that this was the exact transition temperature, that the phase transition is ferroelastic and that it is weakly first order.

In addition to the considerable interest in the structural modifications of sodium azide within a few degrees of room temperature, there have been diffraction and spectroscopic studies undertaken at high temperatures and/or high pressure. Müller and Jöbstl observed no phase transitions from the β-form on heating to its decomposition point (548 K) at atmospheric pressure.[37] Increasing pressure at ambient temperature, however, seems to parallel the effect of cooling at ambient pressure. Bradley *et al*. first observed a splitting in their X-ray powder diffraction patterns upon increasing pressure to 0.25 GPa.[38] Although structure determination was not possible in this case, the authors note the similarity with the $\beta \rightarrow \alpha$ transition on cooling and propose that a similar transition could occur on compression. In their pioneering work on the compressibility of energetic materials, Weir *et al*. were able to apply the 'new' diamond-anvil cell technology to carry out single-crystal X-ray diffraction studies on NaN_3.[18] They obtained a monoclinic indexing for sodium azide at ~1.0 GPa, which was consistent with the low-temperature α-form.

Comparison of Raman spectra collected for the high-pressure form with those for the low-temperature α-form also confirmed that these were indeed the same phase.[36] Furthermore, it was possible to plot the linear pressure/temperature dependence of the β/α phase line between 0 - 0.3 GPa and 253 – 373 K. The pressure range for spectroscopic studies was later extended to 4.0 GPa by Christoe and Iqbal, who noted that the $\beta \rightarrow \alpha$ transition occurs at 0.07 GPa and that, once formed, the α-form remains stable to the highest pressures studied.[39] More recently neutron powder diffraction has been used to observe the structural response of α-NaN_3 to compression (up to a maximum pressure of 1.2 GPa). Rietveld refinement of data collected at 0.5 GPa shows that compression involves both a distortion of the unit cell and a tilt of the linear anions in the monoclinic plane.[40]

Finally, Pistorius and Campbell White report evidence of a third distinct phase of sodium azide obtained at elevated temperatures and pressures.[41] A volume discontinuity was observed during compression of the β-form at ~ 357 K (between 2.6 and 3.0 GPa). This β → γ transition is reported to be quite sluggish, but proceeded much more quickly when compression was performed at 373 K. It was also possible to observe a transition from the α-form to the γ-form at 333 K and 2.8 GPa but this transition was so sluggish at lower temperatures that it became 'virtually unobservable'.

The primary aim of the current study was to obtain neutron powder diffraction data of sufficient quality to allow structure solution of this high-pressure/high-temperature γ-form. Given the sluggish nature of the phase transitions *to* this form, it was also hoped that by cooling to ambient temperature before decompressing it would be possible to recover γ-NaN_3 to ambient pressure. Furthermore compression of sodium azide at ambient temperature (to 6.0 GPa) was carried out in order to assess critically the compression mechanism proposed by Knorr and Depmeier.[40]

5.2.2 CsN_3

While structures related to the NaCl structure are typical for compounds with small cations like Li^+ and Na^+, azides of larger alkali metals (K^+, Rb^+, Cs^+) adopt structures closely related to CsCl. Again the substitution of the spherical chloride anions with the rod-like N_3^- ions gives rise to a distortion of the cubic lattice, but CsN_3-II (as well as KN_3 and RbN_3) crystallises in the tetragonal space group *I*4/*mcm* at ambient temperature and pressure.[42] Figure 5.3 illustrates this tetragonal distortion and highlights the alternating layers of Cs^+ and N_3^- ions that lie perpendicular to the tetragonal *c*-axis. In contrast to NaN_3, within the azide layers the anions are oriented perpendicular to their nearest neighbours. This is electrically very favourable because the electronegative termini of the azide units are directed at the electropositive central nitrogen of the next nearest anion. Furthermore the caesium cations are surrounded by the terminal N-atoms of eight azide ions in a slightly distorted square antiprism (see Figure 5.4), which is extremely advantageous in terms of electrostatic energy.[43, 44]

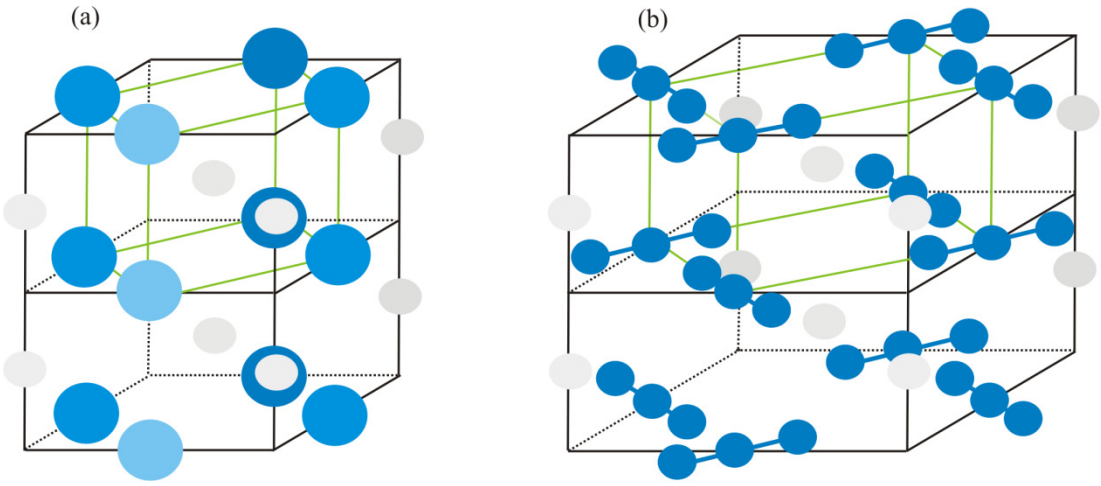

Figure 5.3 Comparison of (a) the cubic structure of CsCl and (b) the tetragonal structure of CsN_3-II. The unit cell of the cubic form is highlighted in green. The inclusion of the linear anions in CsN_3 gives rise to a lengthening of the unit cell *a*- and *b*-axes, while the alternating layers of azide layers results in a doubling of the *c*-axis.

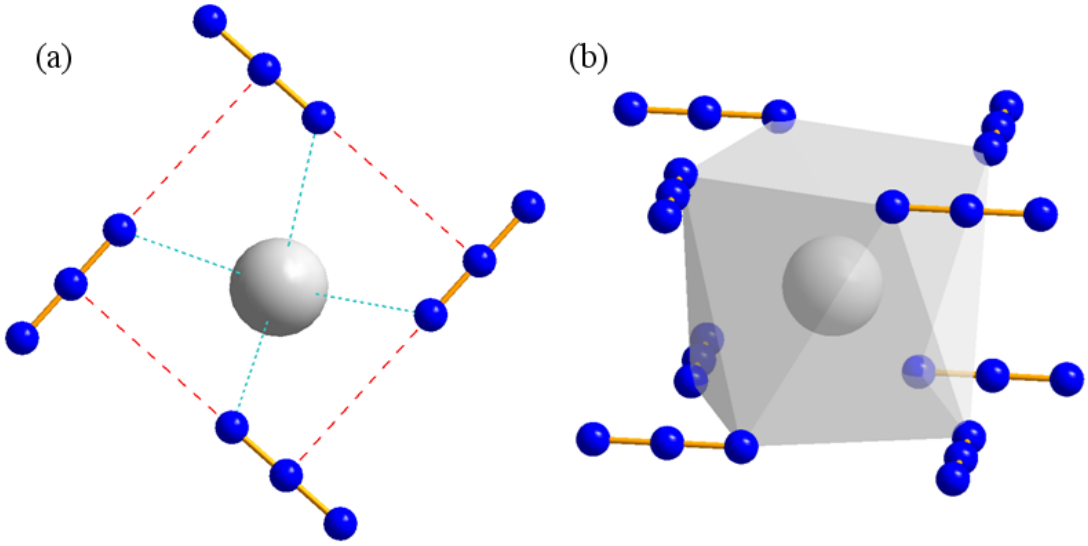

Figure 5.4 (a) Intraplanar interactions of azide anions (red) and their interactions with the cations located in the layers immediately above and below (cyan); and, (b) the square antiprism around a Cs^+ cation.

The tetragonal structure of CsN_3 has been investigated spectroscopically at ambient temperature [45] and on cooling to 20 K.[46, 47] At no point during the cooling experiment was a phase transition observed. Upon warming, however, CsN_3 undergoes a reversible transition (at 424 K) to a cubic phase CsN_3-I, first indexed by Müller and Jöbstl.[37] They were able to accurately reproduce the observed relative intensities in their X-ray powder diffraction patterns using a model based on the cubic CsCl phase ($Pm\bar{3}m$). In order to satisfy this cubic symmetry, however, the linear N_3^- ions would be required to either rotate freely or be randomly oriented. They concluded that free rotation is not likely to occur due to steric

hindrance and that instead the azide ions are oriented at random parallel to the edges of the cubic unit cell. In effect, a particular azide ion may be found (with equal probability) to align itself with any of the unit cell axes. This disorder model was later supported by differential thermal analysis and Raman spectroscopic observations.[47, 48] Entropy values for the I/II transition were too low to account for the free rotation of the anion (based on calculations by Müller and Jöbstl). Broadening of the R(E_g) mode associated with the hindered rotation of the N_3^- parallel to the *c*-axis is also consistent with a disordering process in which the azides 'jump' from one crystal site to another.[49] Recently, however, molecular dynamics simulations of this transition suggest that in the cubic phase the N_3^- ion can perform random hindered rotations about all three spatial axes.[50] In fact, these movements are observed on warming the tetragonal phase causing the lattice to expand along the tetragonal *c*-axis up to the point at which the cubic form is adopted.

In addition to the variable temperature studies at atmospheric pressure, Pistorius presented evidence for a phase transition from both the tetragonal and cubic phases to a high-pressure phase III. The transition pressure at room temperature was ~0.4 GPa although this moved to higher pressures when the compression was carried out at elevated temperatures.[48] The slope of the transition line (38 K/0.1 GPa) led the author to conclude (erroneously) that the tetragonal form should transform to the 'high-pressure phase' upon cooling at atmospheric pressure near 143 K – this has subsequently been disproven.[47] The existence of a high-pressure form was, however, substantiated by Iqbal and Christoe although their spectroscopic measurements indicated a slightly higher transition pressure (0.6 GPa at ambient temperature).[47] A further observation which may have significance for any attempts at structure solution is that CsN_3-III would consist of two sets of crystallographically non-equivalent N_3^- sites (based on splitting of vibrational modes over this transition). To date no structural information has been obtained for this form.

The current study therefore focussed on obtaining high-quality powder diffraction data during the compression of CsN_3 at ambient temperature in order to solve this high-pressure form III. A further aim was to extend the pressure range to 6.0 GPa, in order to identify and characterise any additional high-pressure forms.

5.2.3 TlN_3

Under ambient conditions, thallium azide has been found to be isostructural with CsN_3-II (*I*4/*mcm*), [42, 44, 51] with a contraction of the unit cell commensurate with the reduction in cationic radius.[43] Moreover, TlN_3 undergoes a reversible phase transition at 568 K to a high-temperature cubic form, which is reported to be analogous to CsN_3-I ($Pm\bar{3}m$) although

no unit cell parameters have been published for this form.[37] Spectroscopic measurements over this transition suggest a similar disorder model to the cubic form [52] although this has been disputed by a recent study by Liu *et al.* using molecular dynamics (MD) simulations to model the azide disorder.[53] They report a transition to the disordered cubic phase at a lower temperature than that observed experimentally (530 K), in which the tetragonal *c*-axis lengthens allowing the re-assignment of the unit cell whereby the high-temperature *c*-axis (*c*') can be related to the original tetragonal axes according to: $c'/\sqrt{2} = a,b$. Moreover they note the onset of azide disorder occurs below the phase transition, mirroring the results of an analogous simulation performed on CsN_3.[50] They suggest that this disordering of the anions on warming is accompanied by slight displacement of the thallium cations and the central nitrogen atoms, such that the Tl-Tl, Tl-N_{centre} and N_{centre}-N_{centre} radial distribution functions become uniform over the transition.[53]

Despite the uncertainty over the mechanism for this order-disorder phase transition, it is pleasing to compare analogous systems such as CsN_3 (but also RbN_3 and their related HF_2^- compounds) in order to perhaps rationalise their common phase behaviour. This has been summarised elegantly by Fuith who noted that the tetragonal → cubic transition temperature decreased with increasing cationic radius: larger cations open the structure more effectively in the tetragonal *c*-direction.[43]

In contrast to CsN_3, thallium azide also undergoes a reversible phase transition to a low temperature phase at 248 K. Mauer *et al*. were able to obtain an orthorhombic unit cell for this form (TlN_3-IV), but unfortunately space group determination and structure solution were not possible based on their X-ray powder diffraction data. Furthermore single crystals did not remain intact over this transition.[54] Studies utilising vibrational spectroscopy to investigate TlN_3 at low temperatures found supporting evidence for this transition at similar temperatures (233 – 240 K).[26, 55]

The observation that the transition to the low temperature form was rapid, with a volume change of < 0.1% [54] led Pistorius to conclude that this form was distinct from the high-pressure phase III that he reported in 1969.[48, 56] In his original high-pressure study he noted a sluggish phase transition at 0.7 GPa upon compression at room temperature (Weir *et al.* report the reconstructive phase transition to be between 0.3 and 0.54 GPa [18]). In order to compare this form with the low temperature phase IV, he subsequently carried out a similar compression study at ~ 240 K. He not only observed the transition to TlN_3-IV upon cooling but also a transition at 246 K and 0.15 GPa that was assumed to be to the high-pressure phase III.[56]

A later spectroscopic study proposed a structural model for this high-pressure phase based on the orthorhombic structure of silver azide (*vide infra*) based on more vibrational modes being observed in the Raman spectrum of the high-pressure form.[57] This lattice is derived from the tetragonal structure by means of an out-of-plane rotation of the N_3^- ions, resulting in two crystallographically distinct azide sites, hence the observed splitting. In the current study, neutron powder diffraction was utilised to structurally characterise this form (to test this hypothesis) and to investigate its phase stability up to a maximum pressure of 7.0 GPa. Furthermore, variable temperature X-ray diffraction was performed in order to allow structure solution of the low-temperature TlN_3-IV and to provide experimental evidence for the high-temperature form I, thus complementing previous computational studies.

5.2.4 A Note on Nomenclature

It should be noted that no consensus exists in the literature regarding the naming of different polymorphs of the inorganic azides. Both Greek letters and Roman numerals are used, at times interchangeably. While confusing, every effort has been made in this thesis to follow the generally accepted naming scheme for each individual compound. In order to facilitate comparison between the various forms, the important crystallographic information for each polymorph is presented in Table 5.1, along with the pressure/temperature conditions at which each form is found.

5.3 Aims

Table 5.1 highlights not only the rich polymorphism of these relatively simple materials but also the relative dearth of structural data at non-ambient conditions. The overarching aim of this study was therefore to structurally characterise this series of inorganic azides at high pressure, and, in the case of sodium azide, at high temperature *and* high pressure. Finally the ambient-pressure polymorphism of thallium azide was explored by variable temperature X-ray powder diffraction.

Polymorph	Space Group	*a* (Å)	*b* (Å)	*c* (Å)	*α* (°)	*β* (°)	*γ* (°)	Atomic positions?	*P*/*T* conditions	Ref.
α-NaN_3	*C*2/*m*	6.1654(5)	3.6350(3)	5.2634(6)	90	107.543(5)	90	Yes	Ambient *P*; *T* < 292 K *P* > 0.07 GPa; Ambient *T*	[25],[39]
β-NaN_3	$R\bar{3}m$	3.646(2)	3.646(2)	15.213(5)	90	90	120	Yes	Ambient *P*; *T* > 292 K	[8]
γ-NaN_3	-	-	-	-	-	-	-	-	*P* > 3.0 GPa; *T* > 373 K	[41]
CsN_3-I	$Pm\bar{3}m$	4.53(1)	4.53(1)	4.53(1)	90	90	90	No	Ambient *P*; *T* > 424 K	[37]
CsN_3-II	*I*4/*mcm*	6.5412(4)	6.5412(4)	8.0908(5)	90	90	90	Yes	Ambient *P*; *T* < 424 K	[44]
CsN_3-III	-	-	-	-	-	-	-	-	*P* > 0.6 GPa; Ambient *T*	[47]
TlN_3-I	$Pm\bar{3}m$	-	-	-	90	90	90	No	Ambient *P*; *T* > 568 K	[37]
TlN_3-II	*I*4/*mcm*	6.208(1)	6.208(1)	7.355(2)	90	90	90	Yes	Ambient *P*; 248 K < *T* < 568 K	[44]
TlN_3-III	-	-	-	-	-	-	-	-	*P* > 0.7 GPa; Ambient *T*	[48]
TlN_3-IV	-	8.7178(6)	8.7655(7)	7.3659(7)	90	90	90	No	Ambient *P*; *T* < 248 K	[54]

Table 5.1 Structural information for all polymorphs of sodium azide, caesium azide and thallium azide.

5.4 Experimental

5.4.1 Materials

Polycrystalline samples of NaN_3 (99.5%) and CsN_3 (99.95% purity) were purchased from Sigma-Aldrich and used as received. Thallium azide was prepared by the precipitation reaction of Tl_2SO_4 and NaN_3. Sample purity was confirmed by ambient pressure X-ray diffraction for NaN_3, CsN_3 and TlN_3.

5.4.2 High-Pressure Neutron Powder Diffraction

High-pressure neutron powder diffraction data were collected using the PEARL/HiPr diffractometer at the UK spallation neutron source, ISIS, at the STFC Rutherford Appleton Laboratory. Polycrystalline samples of each compound under investigation (NaN_3, CsN_3, and TlN_3) were loaded, in turn, into an encapsulated TiZr gasket [58] with perdeuterated methanol:ethanol (4:1) as pressure-transmitting medium and Pb as pressure calibrant.[59] The capsule assembly was then compressed with a type V3b Paris-Edinburgh (P-E) press equipped with standard single toroid anvils with cemented WC cores (Ni binder).[60] The P-E press ram pressure was monitored and varied by means of a computer-controlled hydraulic system.

Time-of-flight (ToF) neutron powder diffraction data were collected using the $2\theta = 90°$ detectors with a transverse (through-anvil) scattering geometry. The resulting summed pattern was then normalised with respect to the incident beam monitor and the scattering from a standard vanadium calibration sample. Lastly, the diffraction pattern intensity scale was corrected for the wavelength and scattering-angle dependence of the neutron attenuation by the anvil (WC) and gasket (TiZr) materials. Full-profile Rietveld refinements of the ToF neutron powder diffraction patterns were carried out using the GSAS package, in which a convolution of Gaussian (with coefficient σ_1) and Lorentzian (γ_1) functions was used to describe peak profiles (GSAS ToF profile 3).[61] Details of any restraints applied (when necessary) during refinement will be outlined in the relevant sections below.

5.4.3 High-Pressure/High-Temperature Neutron Powder Diffraction

In addition to the ambient temperature compression experiment described above, NaN_3 was investigated at high pressure *and* high temperature at the PEARL/HiPr beamline (ISIS). In this case, a Paris-Edinburgh V4 cell was equipped with a variable temperature insert to allow rapid heating and cooling *in situ*.[62] Perdeuterated methanol:ethanol (4:1) was used as the pressure-transmitting medium and pressures were calibrated to an internal Pb standard. Data were collected and processed using the procedure outlined in Section 5.4.2.

5.4.4 High-Pressure X-ray Powder Diffraction

The X-ray powder diffraction experiment on CsN_3 was performed using a Merrill-Bassett diamond-anvil cell (DAC) [63] equipped with 600 μm culet diamonds and a 250 μm thick tungsten gasket (pre-indented to a thickness of 100-150 μm) with a 300 μm hole. Pressure measurement was made by monitoring the R_1 fluorescence line of ruby spheres [64] and hydrostaticity was maintained by using methanol:ethanol (4:1) as pressure-transmitting medium. Data were collected at the Extreme Conditions Beamline (I15) at Diamond Light Source (λ = 0.44492 Å). The X-ray beam was collimated to a diameter of 50 μm and samples were exposed for 10 s. 2D diffraction patterns were collected using a Mar345 image plate, processed using FIT2D.[65] Le Bail refinements of the powder diffraction patterns were completed using GSAS.[61]

5.4.5 Ambient Pressure X-ray Powder Diffraction

The purities of NaN_3, CsN_3 and TlN_3 were confirmed by ambient pressure X-ray powder diffraction. Data were collected in reflection mode, on a Bruker D8 Advance Diffractometer (Cu $K\alpha_1$ radiation) equipped with a position sensitive detector (PSD).[66] An exposure time of 1 hr over a 2θ range of 10 – 60° was sufficient in each case to verify sample purity.

Low-temperature X-ray powder diffraction data were collected for TlN_3 in transmission mode (capillary diameter 0.5 mm) using a Bruker D8 Advance Diffractometer [67] (Cu $K\alpha_1$ radiation) equipped with a Lynxeye Si PSD detector and an Oxford Crystostream low-temperature device.[68] In order to ensure comprehensive powder averaging throughout the complete 2θ range, data were collected for 8 hrs at 293 K, and at 100 K to allow structure solution of the low-temperature TlN_3 form IV. Shorter data collections (1 hr) were performed at 20 K intervals between 80 and 280 K. Rietveld refinement of each diffraction pattern data was undertaken in GSAS in which a convolution of Gaussian (GU, GV), Lorentzian (LX, LY) and asymmetry (asym) coefficients was implemented to fit peak profiles (GSAS CW profile 2).[61]

Finally, the high-temperature phase transition in TlN_3 was investigated by X-ray powder diffraction on a Bruker D8 Advance Diffractometer (reflection mode).[66] The sample was mounted in a TTK-450 variable temperature stage [69] and data were collected using a position sensitive detector (Cu $K\alpha_1$ radiation). X-ray powder diffraction patterns were collected over a 2θ range of 15 – 60° (4 hr) at 20 K intervals between 300 and 560 K; additional data were collected in the temperature range immediately surrounding the reported transition temperature (568 K). Le Bail refinements of the powder diffraction patterns were carried out using GSAS.[61]

5.5 Results and Discussion

5.5.1 NaN_3

High-Pressure, Ambient-Temperature Neutron Diffraction Study

The initial aim of this study was to obtain an accurate value for the pressure at which the rhombohedral β-form transforms to the monoclinic α-form. For this reason, the load applied to the sample initially was minimal (6 tonnes, typically enough to seal the sample capsule without increasing sample pressure). Refinement of the unit cell parameters of the internal Pb pressure marker and comparison with its equation of state at 293 K [59] showed that the sample was indeed at atmospheric pressure. The neutron powder diffraction pattern collected at this stage showed reasonable agreement with the pattern calculated based on the structure of the β-form (see Figure 5.5). On closer inspection however there appeared to be some broadening in the two main peaks (~3.0 Å) as well as a degree of asymmetry, particularly in the peak at d = 3.1 Å.

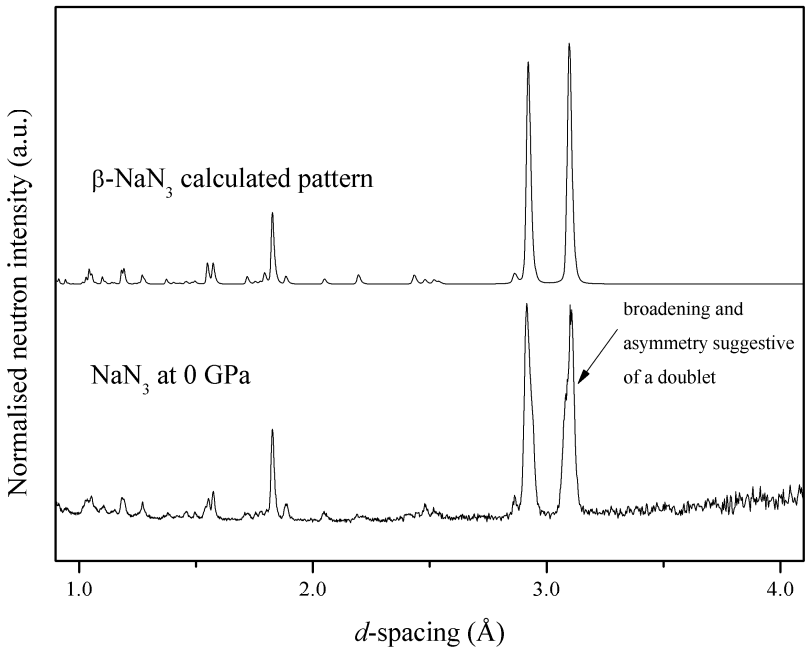

Figure 5.5 Comparison of the neutron powder diffraction pattern collected for NaN_3 at 0 GPa with the pattern calculated for β-NaN_3.

While the atmospheric temperature in the experimental hall (July) was above 293 K for the initial runs of this study, it is certainly possible that the experimental hutch may have been cooler than the rest of the facility (i.e. T < 292 K), which would result in the *thermal* phase

transition to the α-form. Using the monoclinic structure as a model for the refinement, it was then possible to achieve a much better fit to the experimental data, which was reflected in lower values for the goodness-of-fit, χ^2, (1.58 vs 3.60) and the weighted R-factor (0.048 vs 0.134). Addition of 1 tonne in load, which resulted in a pressure increase of 0.1 GPa, resulted in much better resolution of the four peaks in the region where there were only two in the rhombohedral phase (~3.0 Å), see Figure 5.6.

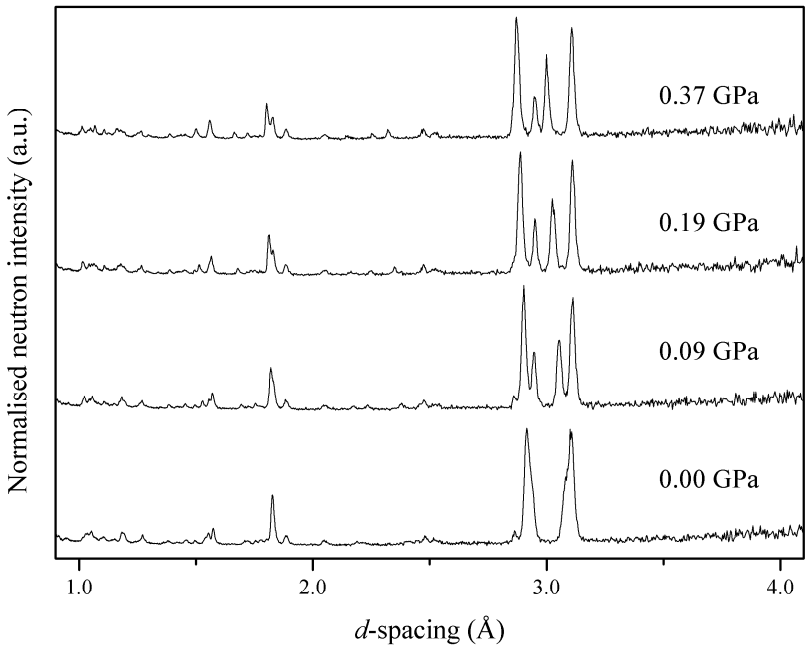

Figure 5.6 Neutron powder diffraction patterns collected for α-NaN_3 between 0.0 and 0.4 GPa, highlighting the splitting of the two peaks attributable to the rhombohedral β-form into four peaks in the monoclinic α-form.

It was then possible to use the α-structure as a model for refinement of all of the diffraction patterns collected up to the maximum pressure studied (6.06 GPa), indicating that α-NaN_3 does not undergo a phase transition in this pressure regime. A multiplot of all of the diffraction patterns collected during compression can be found in Figure 5.7, while the unit cell parameters for α-NaN_3 at each pressure are tabulated in Table 5.2 and plotted in Figure 5.8.

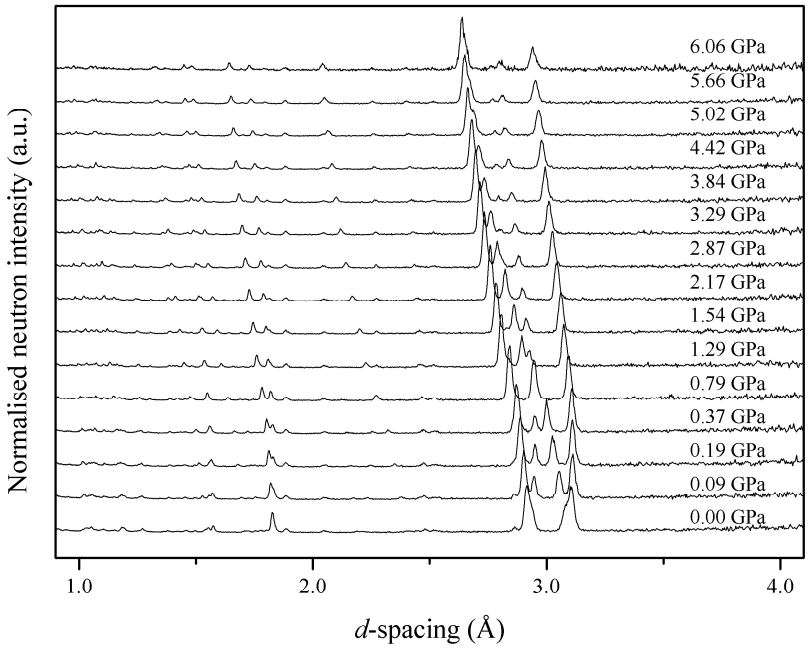

Figure 5.7 Multiplot of the neutron powder diffraction patterns collected for α-NaN_3 during compression to a maximum of 6.06 GPa. Other than the gradual movement of peaks to lower *d*-spacing with pressure, no changes indicative of a phase transition are observed.

P (GPa)	*a* (Å)	*b* (Å)	*c* (Å)	*β* (°)	*V* (Å^3)	wR_p
0.00	6.3027(4)	3.6526(2)	5.4525(8)	111.551(9)	116.748(14)	0.048
0.09	6.2785(4)	3.6552(2)	5.4070(7)	110.458(8)	116.260(12)	0.059
0.19	6.2483(4)	3.6529(2)	5.3654(7)	109.490(8)	115.445(12)	0.059
0.37	6.2169(3)	3.6478(2)	5.3284(6)	108.687(7)	114.468(11)	0.056
0.79	6.1476(4)	3.6305(2)	5.2588(6)	107.212(9)	112.114(11)	0.055
1.29	6.0720(4)	3.6069(2)	5.1935(6)	105.860(7)	109.413(11)	0.072
1.54	6.0228(4)	3.5901(2)	5.1570(5)	105.086(7)	107.664(10)	0.058
2.17	5.9664(4)	3.5689(2)	5.1160(5)	104.237(7)	105.592(10)	0.061
2.87	5.9122(4)	3.5474(2)	5.0802(5)	103.494(7)	103.607(10)	0.065
3.29	5.8687(4)	3.5298(2)	5.0536(6)	102.909(7)	102.040(10)	0.072
3.84	5.8259(4)	3.5111(2)	5.0280(6)	102.376(8)	100.460(11)	0.073
4.42	5.7879(5)	3.4931(2)	5.0061(6)	101.931(8)	99.027(11)	0.075
5.02	5.7510(5)	3.4766(2)	4.9859(7)	101.506(9)	97.683(12)	0.090
5.66	5.7175(6)	3.4606(2)	4.9685(7)	101.128(10)	96.457(13)	0.084
6.06	5.6924(12)	3.4474(5)	4.9552(14)	100.836(20)	95.51(3)	0.252

Table 5.2 Variation in the unit cell parameters of α-NaN_3 with pressure.

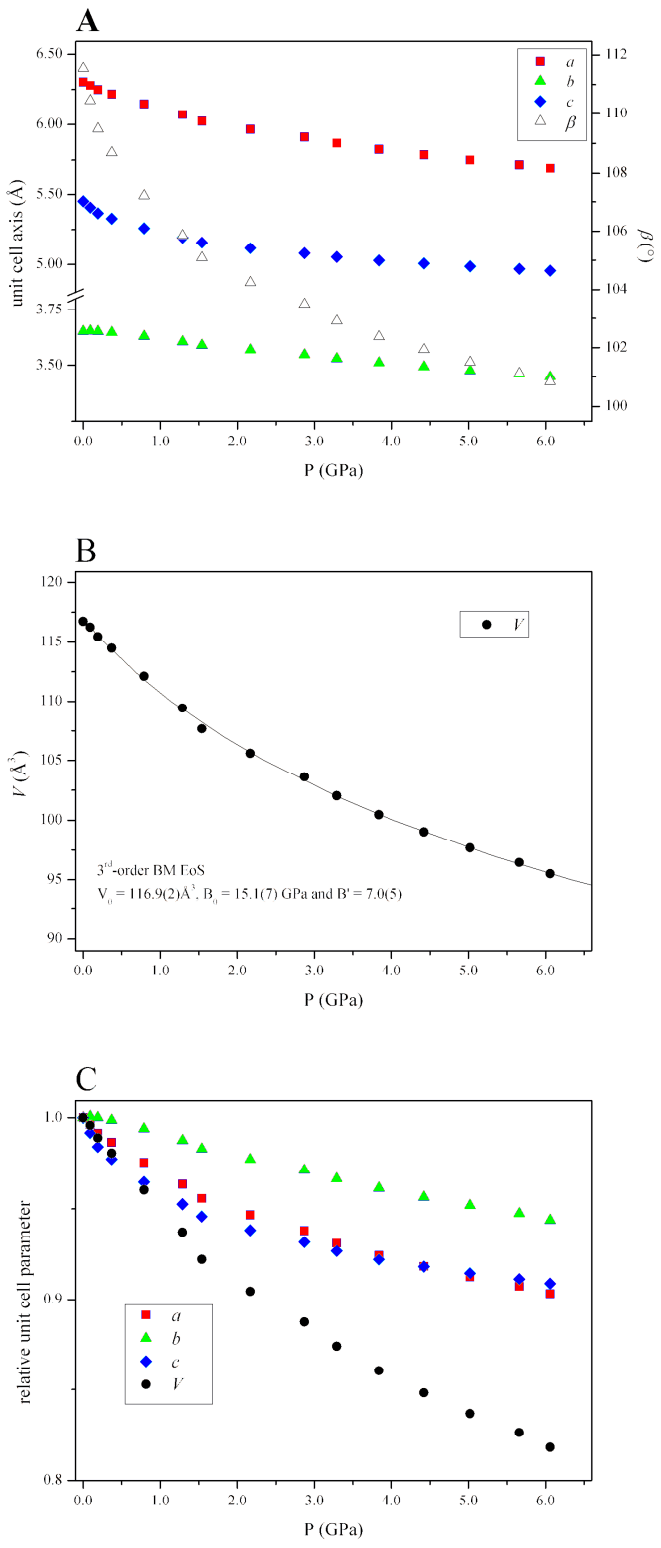

Figure 5.8 (a) Compression of the unit cell parameters (*a*, *b*, *c*, and *β)* of α-NaN_3; (b) smooth variation of unit cell volume, *V*, with pressure, including 3rd-order Birch-Murnaghan EoS; and, (c) relative compression of the unit cell parameters.

The relative compression of the unit cell axes highlights that the *b*-axis is significantly less compressible than either of the other two, which is consistent with previous compressibility measurements.[18] The greater compressibility of the *a*-axis is perhaps to be expected – this is the direction perpendicular to layers made up of alternating Na^+ and N_3^- ions (see Figure 5.9). In the case of the *c*-axis, however, its contraction is accompanied by the sharp reduction in the β-angle (from 111.5° to 100.8° over 6.0 GPa). Examination of the crystal structure allows one to rationalise the concerted contraction of the *c*-axis and the monoclinic angle in terms of a rotation of the azide ions within the *ac*-plane. Comparison of the structure determined at 5.66 GPa with the ambient pressure structure (during the same experiment) shows that the azide ion is becoming more oblique to the *c*-axis, allowing the Na^+ cations to pack more closely (see Figure 5.9). This compression mechanism is in line with that reported by Knorr and Depmeier.[40]

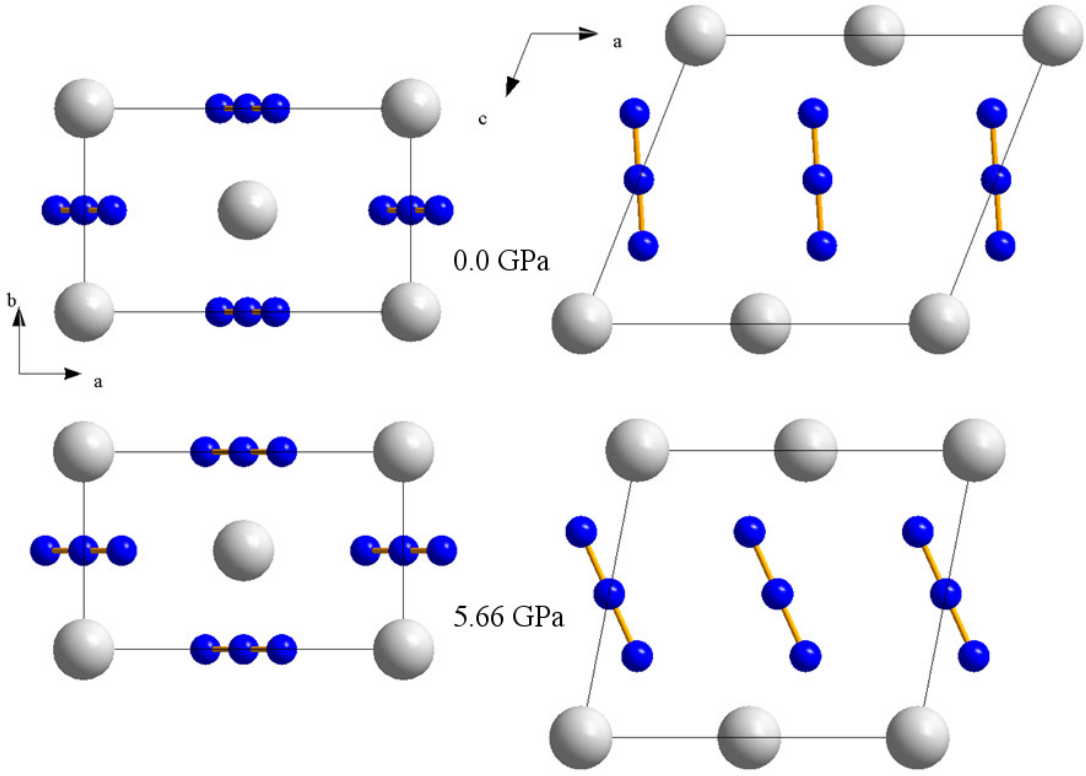

Figure 5.9 Comparison of the structures determined at 0.0 GPa and 5.66 GPa: viewed down the *c*-axis to highlight the interplanar contraction of the *a*-axis; and viewed down the *b*-axis to show the rotation of the azide anions in the monoclinic plane.

Moreover the rotation of the azide within the monoclinic plane can be represented graphically by plotting the variation in the angles created between the linear anion and the unit cell *a*- and *c*-axes throughout the compression. These can be found in Figure 5.10, which shows that this rotation does not display a linear dependence on pressure but seems to

approach a limit at the maximum pressure studied (6.06 GPa). It would therefore be very interesting to conduct further structural studies beyond this pressure range to investigate how the unit cell compression manifests itself, and whether further compression may, in fact, induce a phase transition.

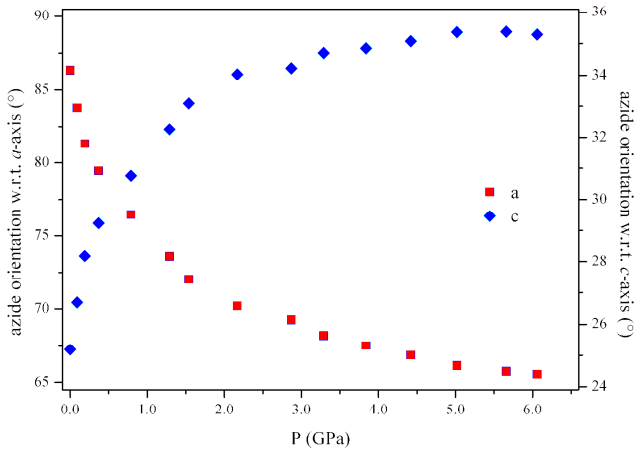

Figure 5.10 Azide ion orientation with respect to the *a*- and *c*-axes upon compression.

An interesting aspect of the compression of the *b*-axis is that it initially undergoes a small, but significant, expansion before undergoing an almost linear contraction with pressure. The exact reason for this is still unclear, although it is certainly likely that the rotation of the anions may result from or result in this small pressure-induced expansion. It is also worth noting that the change in gradient (between the initial expansion and subsequent contraction) may, in fact, be suggestive of a second-order phase transition. No discontinuity is observed in the pressure-volume plot but this may be due to the change in the *b* parameter being masked by concurrent changes in the other parameters. Such a phenomenon has been observed in high-pressure studies of minerals – a continuous phase transition was detected in lawsonite ($CaAl_2Si_2O_7(OH)_2.H_2O$) by plotting the 'normalised stress', defined as $F_E = P/3f_E(1+2f_E)^{5/2}$, against the Eulerian finite strain $f_E = ((l_0/l)^2-1)/2$, where l_0 = unit cell parameter (*a*, *b*, *c*) at zero pressure.[70] Unfortunately it has not been possible to carry out similar analyses for sodium azide due to the lack of data points in the 'low-pressure' phase. It would therefore be desirable to collect high-quality unit cell data at very low pressure (0 – 0.3 GPa) to investigate the true nature of the change in the *b*-axis within this pressure regime.

Finally a 3rd-order Birch-Murnaghan equation of state [71] has been fitted to the isothermal compression of the unit cell volume over the pressure range 0 – 6.06 GPa, assuming no

second-order phase transitions occur. Using Angel's program EoSFIT [72] the values calculated were: V_0 = 116.9(2) Å^3, B_0 = 15.1(7) GPa and B' = 7.0(5). The unit-cell volume at zero pressure (V_0) is in excellent agreement with the value obtained experimentally (116.75(1) Å^3) determined at atmospheric pressure. Furthermore, it has been possible to construct an F_E vs f_E plot analogous to that described above for the isothermal compression of the unit cell volume, see Figure 5.11. In this case it should be noted that $f_E = ((V_0/V)^{2/3}-1)/2$. All data points lie on a straight line (correlation coefficient, R^2 = 0.8597), the intercept of which represents the bulk modulus (B_0 = 15.3 GPa). The gradient, $3B_0(B'-4)/2$, is in very good agreement with the calculated value (calc. = 67.95, m = 65.0).[73] The values of B_0 and B' calculated for α-NaN_3 show that it has very similar compressibility to the isostructural LiN_3 (B_0 = 19.1(14) GPa and B' = 7.3(5))[74] and is comparable, but slightly more compressible, than the alkali halides.[75, 76]

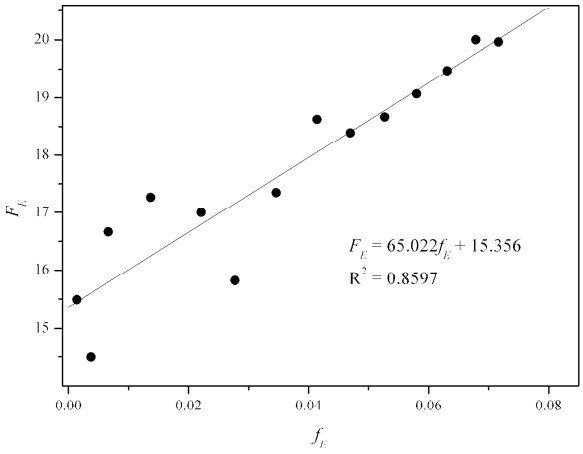

Figure 5.11 Plot of the 'normalised stress' (F_E) against Eulerian finite strain (f_E) for the isothermal compression of the unit cell volume of α-NaN_3.

High-Pressure, High-Temperature Study

In addition to characterising the high-pressure behaviour of NaN_3 at ambient temperature, the observation of a third from of sodium azide at elevated temperatures and pressures motivated further study. As in the previous study, a sample of β-NaN_3 was loaded into the sample capsule in the P-E press, but this time it was possible to characterise the pressure-induced β → α phase transition by carrying out the initial compression at 294 K. As is shown in Figure 5.12, it was possible to refine the neutron powder diffraction pattern collected at 0.13 GPa using the $R\bar{3}m$ form, but by 0.70 GPa this phase has transformed to the monoclinic α-form. The α-form was then compressed (at 294 K) to 1.91 GPa before warming and

pressurising alternately to get to the pressure-temperature regime in which Pistorius observed this new form (2.8 GPa at 333 K).[41] In accordance with the reported sluggishness of this transition, no changes in the diffraction pattern were observed during this data collection (~ 0.5 hr).

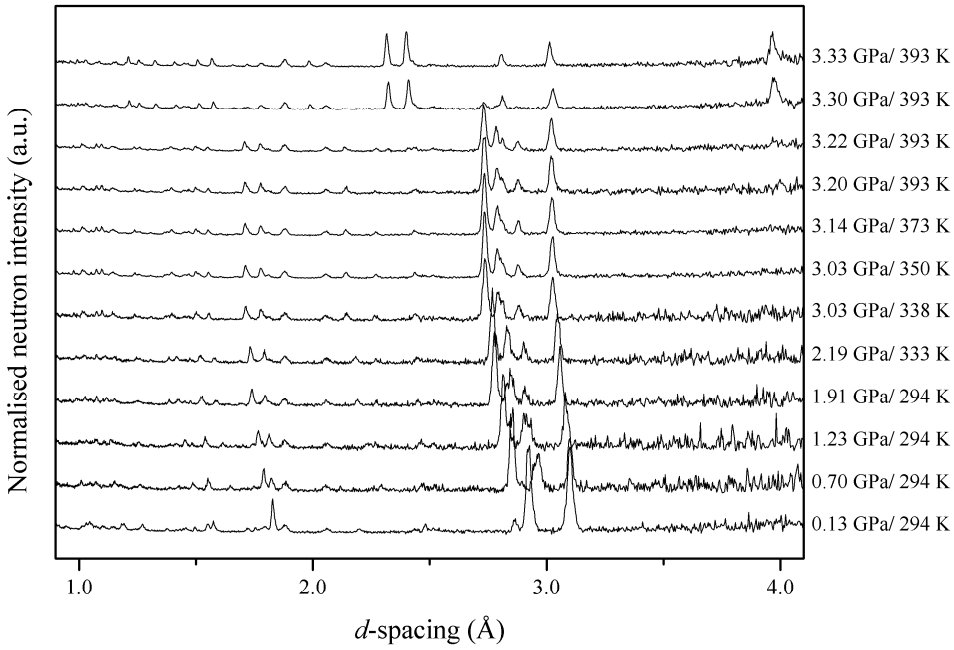

Figure 5.12 Neutron diffraction patterns collected during the compression/warming of NaN_3 to 3.33 GPa and 393 K. This multiplot shows not only the phase transition from the α-form to the γ-form, but also the β → α transition occurring between 0.13 and 0.70 GPa at 294 K.

As the rate of the α → γ transition was reported to increase at higher temperatures, the sample was warmed to 393 K at constant load, but still no changes in the diffraction patterns were evident over the course of 6 hours. Refinement of the Pb pressure marker showed, however, that the act of heating the sample resulted in an increase in sample pressure from 2.77 GPa to 3.20 GPa and it is possible that this counterbalanced the promoting influence of increasing the temperature. This is again in agreement with Pistorius's observation that the γ-form phase line has a positive slope, although according to his study, under these conditions the β-form should be present *not* the α-form.

Increasing the applied load to 40 tns at 393 K (sample pressure 3.22 GPa) resulted in the appearance of weak peaks (~2.32 and ~2.42 Å), which could not be attributed to the α-form. It was only upon further compression to 3.51 GPa, however, that a pure sample of the γ-form was observed, highlighting the significant kinetic barrier to this transition. The quality of the

diffraction pattern collected at 3.51 GPa/393 K was such that it was possible to determine the space group as *I*4/*mcm*.[77] This is the same space group adopted by the azides of the larger alkali metals and full-profile Rietveld refinement was possible using atomic co-ordinates based on the tetragonal structure of CsN_3-II. The quality of the Rietveld refinement for the γ-form is shown in Figure 5.13.

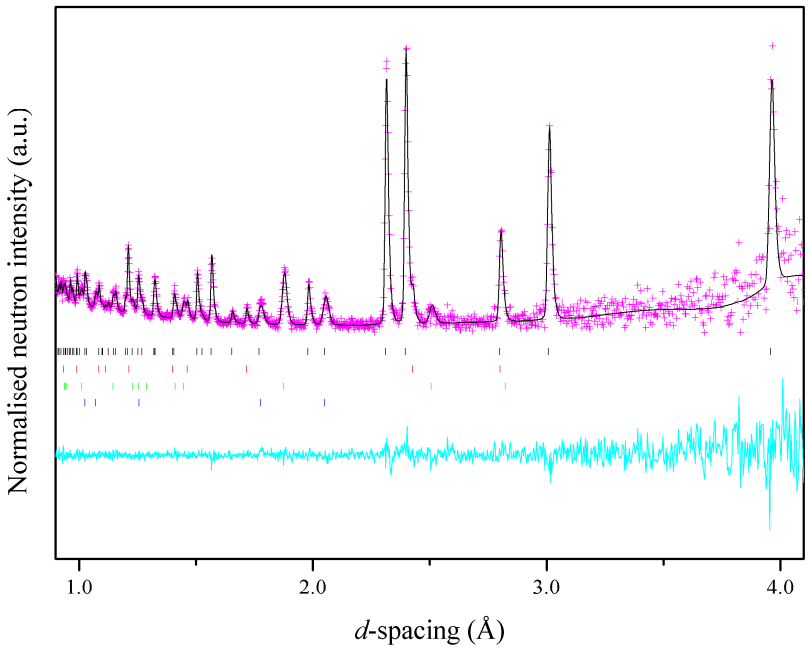

Figure 5.13 Rietveld refinement of the pattern collected for γ-NaN_3 at 3.33 GPa and 393 K. The experimental data (I_{obs}) are represented as pink crosses, the calculated pattern (I_{calc}) is shown in black and the difference (I_{obs} - I_{calc}) in cyan. Tick-marks for each phase are also shown for clarity: γ-NaN_3 (black), Pb (red), WC (green) and Ni (blue).

In the tetragonal structure of γ-NaN_3, the azide anions and sodium cations are organised intro alternating layers perpendicular to the *c*-axis. Within the layers, the azide ions are oriented normal to their nearest neighbours, resulting in the favourable interaction between the electronegative termini and electropositive central N-atom. This geometry gives rise to the square-antiprism co-ordination environment, formed by the terminal N-atoms of eight azide anions round one Na^+, rather than the very-slightly-distorted octahedral environment observed in the monoclinic form. The most significant change over the α → γ transition, however, is in the distances separating neighbouring cation layers. In α-NaN_3, each cation is surrounded by six others within the same plane (at distances of either 3.54 or 3.44 Å) and an additional two positioned directly above and below in the neighbouring layers (5.07 Å). In the tetragonal γ-form the (slight) lengthening of the intraplanar distances between

neighbouring cations (to 3.60 Å) is accompanied by a dramatic decrease in the interplanar separation (to 3.01 Å). This is highlighted in Figure 5.14. It is this dramatic shortening of the distance between the planes that results in the 7.8 % contraction of the molecular volume over the transition (between 3.22 and 3.30 GPa).

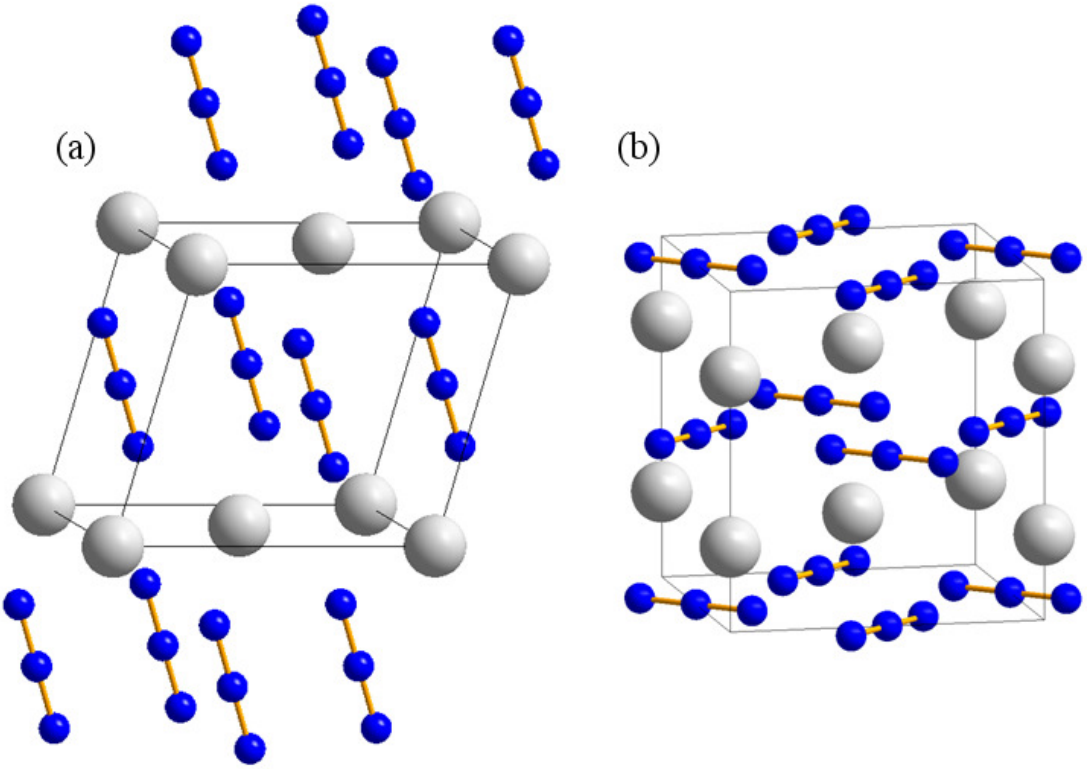

Figure 5.14 Comparison of the structures of (a) α-NaN_3 at 3.22 GPa, and (b) γ-NaN_3 at 3.30 GPa. The structures have been oriented such that the rotation of all of the azide anions over the phase transition is highlighted.

The significant amount of rearrangement in the structure (and the resultant dramatic reduction in molecular volume) explains the sluggish nature of the transition. Furthermore it suggests that the γ-form may display significant hysteresis upon cooling and subsequent decompression and may therefore be recoverable to ambient conditions. It was for this reason that we carefully monitored the cooling of γ-NaN_3 to ambient temperature (at constant load of 51 tns) as well as its decompression, in order to determine the exact conditions under which it may undergo a phase transition, most likely to the α-form.

Cooling from 393 K to 313 K (sample pressure decreased from 3.51 to 3.27 GPa) did not result in any phase transition – the unit cell parameters are tabulated below (Table 5.3). This facilitated direct comparison between the α-form obtained in the ambient temperature compression study above and the γ-form in the present study. The molecular volume of the

α-form at 3.29 GPa (293 K) is 102.909(7) Å^3, compared to 93.889(17) Å^3 obtained for the γ-form at 3.27 GPa (313 K). This clearly shows that the γ-form is the denser form (by 8.8%).

T (K)	*P* (GPa)	Form	*a* (Å)	*b* (Å)	*c* (Å)	*β* (°)	*V* (Å^3)	wR_p
294	0.13	β	3.64684(17)		15.222(3)		175.32(3)	0.106
294	0.70	α	6.1721(11)	3.6373(6)	5.2817(19)	107.66(3)	113.00(4)	0.199
294	1.23	α	6.0907(12)	3.6139(6)	5.2061(18)	106.11(2)	110.10(4)	0.314
294	1.91	α	6.0055(10)	3.5826(5)	5.1422(14)	104.82(2)	106.96(3)	0.174
333	2.19	α	5.9838(11)	3.5749(5)	5.1316(15)	104.57(2)	106.24(3)	0.211
333	2.46	α	5.9224(10)	3.5493(5)	5.0836(14)	103.64(2)	103.85(3)	0.202
338	3.03	α	5.9139(9)	3.5476(5)	5.0841(14)	103.59(2)	103.68(3)	0.199
350	3.03	α	5.9118(5)	3.5459(2)	5.0802(7)	103.55(1)	103.53(1)	0.063
373	3.14	α	5.9091(5)	3.5439(2)	5.0802(7)	103.53(1)	103.41(1)	0.066
393	3.20	α	5.9073(7)	3.5430(3)	5.0802(10)	103.53(1)	103.37(2)	0.130
393	3.22	α	5.9019(6)	3.5414(3)	5.0732(9)	104.45(1)	103.12(2)	0.083
393	3.30	γ	5.6114(3)		6.0418(4)		190.24(2)	0.082
393	3.33	γ	5.5965(3)		6.0136(4)		188.35(2)	0.082
383	3.47	γ	5.5962(4)		6.0092(6)		188.20(3)	0.195
373	3.34	γ	5.5957(4)		6.0093(5)		188.17(3)	0.146
363	3.35	γ	5.5950(3)		6.0096(4)		188.13(2)	0.089
353	3.24	γ	5.5947(4)		6.0076(5)		188.04(2)	0.205
343	3.29	γ	5.5943(3)		6.0063(5)		187.97(2)	0.149
333	3.28	γ	5.5937(3)		6.0047(4)		187.88(2)	0.077
313	3.27	γ	5.5932(3)		6.0023(4)		187.78(2)	0.078
300	2.47	γ	5.6169(4)		6.0553(6)		191.04(3)	0.116
		α	5.933(3)	3.5512(2)	5.079(5)	103.96(7)	103.85(9)	
300	1.32	α	6.068(2)	3.6006(9)	5.187(3)	105.85(4)	109.02(6)	0.207
300	0.00	α	6.2957(14)	3.6573(8)	5.434(2)	110.70(3)	117.04(5)	0.134

Table 5.3 Unit cell parameters (*a*, *c* and *V*) obtained NaN_3 throughout the variable temperature and pressure neutron powder diffraction study. The pattern collected at 300 K and 2.47 GPa was successfully refined as a mixed phase of both the α- and γ-forms; structural data for both forms is presented under these conditions.

It was only upon decompression that the first indications of a phase transition were observed – the pattern collected at 2.63 GPa (300 K) was successfully refined as a mixed phase of the α- and γ-forms. Further decompression to 1.32 GPa resulted in a clean pattern of the α-form, which remained upon decompression to atmospheric pressure. These patterns, however,

showed significant peak broadening when compared to the lowest pressure pattern obtained for the *same* form during compression (shown in Figure 5.15). Although the shorter data collection time for the recovered form has certainly resulted in a lower signal-to-noise ratio, this would be not be expected to have an effect on the observed peak-widths. Peak broadening in this case is therefore indicative of significant strain within the sample, arising from the considerable re-arrangement required during the $\gamma \rightarrow \alpha$ transition.

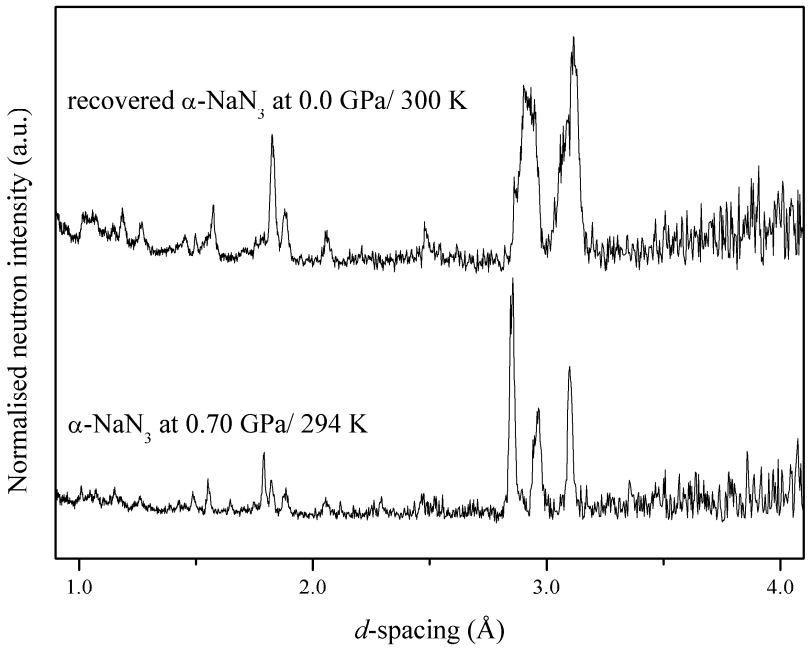

Figure 5.15 Comparison of the neutron powder diffraction patterns collected for α-NaN_3 before the high-pressure/high-temperature phase transition to the γ-form (bottom) and after decompression and cooling (top). The peak broadening in the recovered pattern is clear evidence of significant strain within the sample following the $\gamma \rightarrow \alpha$ transition.

Summary: NaN_3

The ambient-temperature, high-pressure behaviour of NaN_3 has been characterised to a maximum pressure of 6.06 GPa. It was not possible to characterise the pressure-induced $\beta \rightarrow \alpha$ phase transition, but once formed the α-form has been shown to be stable to the limit of this study. The compression mechanism involves a rotation of the azide ions within the monoclinic plane, although this seems to approach a limit at the highest pressures studied. It would therefore be intriguing to perform diffraction studies at even higher pressure to examine whether this, in fact, results in a phase transition.

In addition, the high-pressure, high-temperature polymorph of NaN_3 has been structurally characterised for the first time. This γ-form has been shown to adopt a tetragonal structure analogous to the structure adopted by the other ionic azides at ambient conditions (e.g. CsN_3 and TlN_3). In this way, the application of pressure may be regarded as being analogous to moving down a group in the periodic table, by forcing smaller metal cations to adopt higher co-ordination numbers. The considerable structural rearrangement (and dramatic reduction in volume) results in a significant kinetic barrier for the α → γ transition, which is also reflected in the hysteresis observed during cooling and decompression. Furthermore phase history has a marked effect on sample quality – samples of α-NaN_3 recovered from the γ-form show evidence of considerable crystallographic strain. Of particular importance is the effect this may have on performance characteristics, such as sensitivity.

5.5.2 CsN_3

High-Pressure Neutron Powder Diffraction Study

The ambient-temperature, high-pressure polymorphism of caesium azide has been investigated by both X-ray and neutron powder diffraction. In a similar study to the compression study of NaN_3 above, the initial aim of this experiment was to identify the transition pressure from CsN_3-II to the high-pressure form III that has previously been observed spectroscopically.[47] In contrast to the above study, not only was a transition to this form observed (at 0.32 GPa), but two further high-pressure polymorphs have also been identified. A multiplot of the neutron powder diffraction patterns collected during compression, including patterns representative of these forms, is shown in Figure 5.16.

Polycrystalline CsN_3-II (*I*4/*mcm*) was loaded into the sample capsule and its structure was confirmed by Rietveld refinement of the neutron powder diffraction pattern collected at 0.13 GPa. Compression to 0.32 GPa resulted in the appearance of weak peaks at ~2.9 and 3.1 Å which could not be fit by the tetragonal structural model. It was possible to drive this transition to completion by increasing the applied load from 8 to 9.5 tns (resulting in an increase in sample pressure to 0.54 GPa).

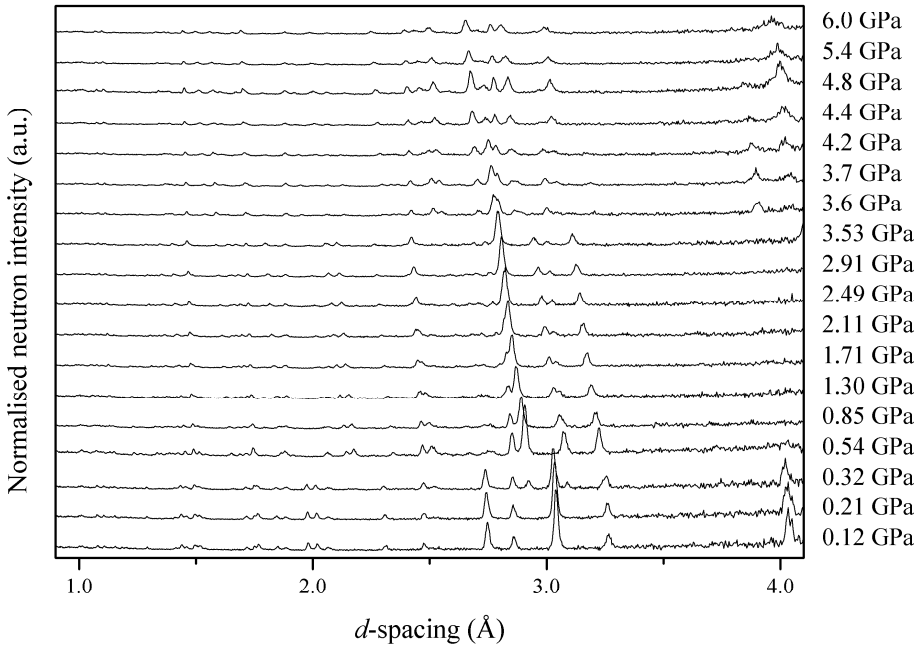

Figure 5.16 Multiplot of neutron powder diffraction patterns collected for CsN_3. The pattern collected at 0.32 GPa has features attributable to forms II and III – this transition is completed in the next pattern (0.54 GPa). Since it has not been possible to perform full-profile refinements on the patterns collected above 3.53 GPa, the pressures have been estimated based on the position of the Pb (200) and (111) peaks and are therefore less precise.

The neutron powder diffraction data collected at 0.54 GPa (3 hrs) were of sufficient quality to allow CsN_3-III to be indexed to a monoclinic unit cell; subsequent Le Bail refinement of the powder pattern using this unit cell then facilitated space-group determination ($P2_1/c$). Atomic positions were initially generated by a monoclinic distortion of the original tetragonal unit cell and subsequent Rietveld refinement. Using this structure it was possible to carry out full-profile Rietveld refinements on all of the neutron powder diffraction patterns collected for CsN_3-III, up to a maximum pressure of 3.53 GPa. It should be noted that while bond angle restraints [180(2)°] were initially applied to each of the two individual azide groups, the final cycle of refinement could be undertaken without this restraint. The unit cell parameters obtained during refinement of the neutron powder diffraction patterns are tabulated in Table 5.4 and represented graphically in Figure 5.18(a).

Comparison of the monoclinic structure of CsN_3-III with the tetragonal form II (see Figure 5.17) clearly shows that the layered structure is largely retained over the transition, although half of the azide anions undergo a 45° rotation out of the *bc*-plane. This results in alternate layers of 'flat' and 'canted' azide anions, thus accounting for previous spectroscopic

observations of two different azide environments.[47] Within the flat layer of anions each azide retains its perpendicular orientation with respect to its nearest neighbours, thus maintaining the electrostatically favourable interactions between the negative termini and positive central nitrogens. Moreover, the cations remain situated in the pocket formed by the arrangement of four terminal nitrogen atoms, although the displacement of the cation from (0.25, 0.5, *z*) results in four discrete Cs…N distances (ranging from 3.155 to 3.227 Å at 0.54 GPa). This feature, along with the rotation of alternate anion layers, gives rise to a considerable distortion of the octahedral co-ordination sphere around each cation; the 8 nearest azide termini now no longer reside in two parallel planes but in planes oriented at ~17° to one another. It is interesting to note that this angle does not vary significantly throughout compression, a feature that is reflected in the relative contraction of the Cs…N and interplanar Cs…Cs distances. No particular interaction appears to be more susceptible to compression throughout the stability range of CsN_3-III.

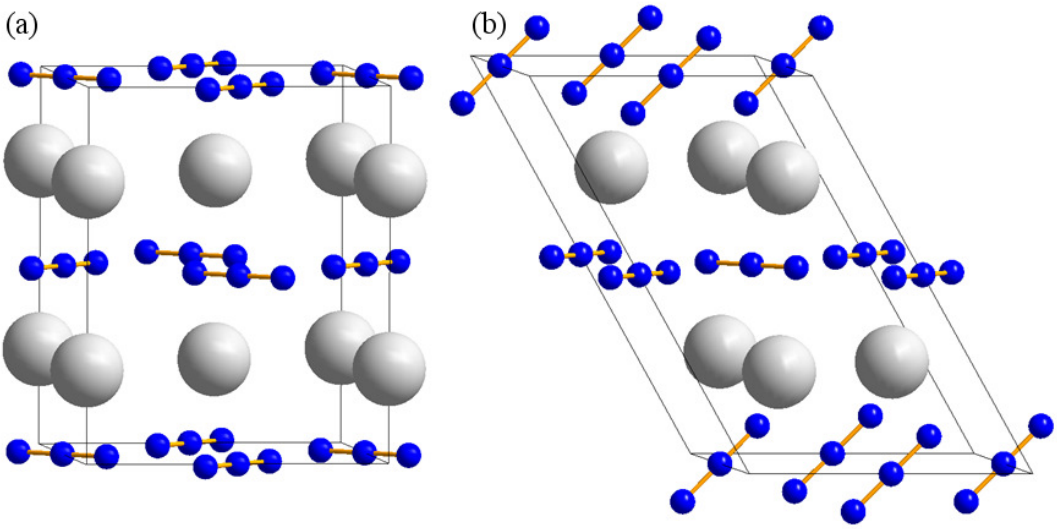

Figure 5.17 Comparison of (a) CsN_3-II and (b) CsN_3-III, highlighting the retention of the layered structure, meanwhile showing the rotation of half of the azide anions.

Compression of the unit cell appears to manifest itself primarily in the contraction of the unit cell *a*- and *b*-axes, while the *c*-axis is more resistant to compression, see Figure 5.18(c). It is likely, however, that the resistance of the *c*-axis to compression can be attributed to two competing effects; the pressure-induced contraction is partially compensated by expansion along the same direction due to the slight shearing of the layers (illustrated by the increase in the β-angle). It should also be noted that compression is not accompanied by any appreciable rotation of the azide groups with respect to the unit cell axes.

From these data it has also been possible to describe the smooth variation in unit cell volume with pressure by a 3rd-order Birch-Murnaghan equation of state (EoS) for this polymorph. In this case, V_0 has been fixed to be the unit cell volume determined by refinement of the pattern collected at 0.54 GPa (the first pressure at which pure form III is observed); all of the higher pressures have been normalised to this. The coefficients calculated in this way were: V_0 = 325.98 Å^3, B_0 = 19.7(10) GPa and B' = 5.8(11), which are consistent with values reported for caesium halides.[78] It should be noted, however, that the first pressure at which this form was observed was 0.32 GPa and it would therefore be worthwhile collecting more diffraction data over the II/III phase transition in order to determine accurately the unit cell volume (V_0) of CsN_3-III at this pressure. This would not be expected to change the absolute values of B_0 or B' dramatically and one can therefore be confident about comparisons drawn between this study and those on analogous systems.

P (GPa)	*a* (Å)	*b* (Å)	*c* (Å)	*β* (°)	*V* (Å^3)	wR_p
0.54	9.8858(8)	6.1327(7)	6.2119(10)	120.054(8)	325.98(4)	0.048
0.85	9.8325(9)	6.0968(7)	6.1949(11)	120.073(9)	321.37(5)	0.060
1.30	9.7630(10)	6.0520(7)	6.1690(11)	120.074(9)	315.43(5)	0.065
1.71	9.6986(8)	6.0084(5)	6.1449(9)	120.110(7)	309.76(3)	0.053
2.11	9.6449(10)	5.9736(7)	6.1249(11)	120.159(9)	305.12(4)	0.063
2.49	9.6005(11)	5.9457(7)	6.1076(11)	120.183(9)	301.36(4)	0.063
2.91	9.5470(8)	5.9143(5)	6.0891(9)	120.227(7)	297.07(3)	0.045
3.53	9.4861(10)	5.8756(7)	6.0686(11)	120.275(9)	292.11(4)	0.060

Table 5.4 Unit cell parameters obtained during the high-pressure neutron diffraction study of CsN_3-III.

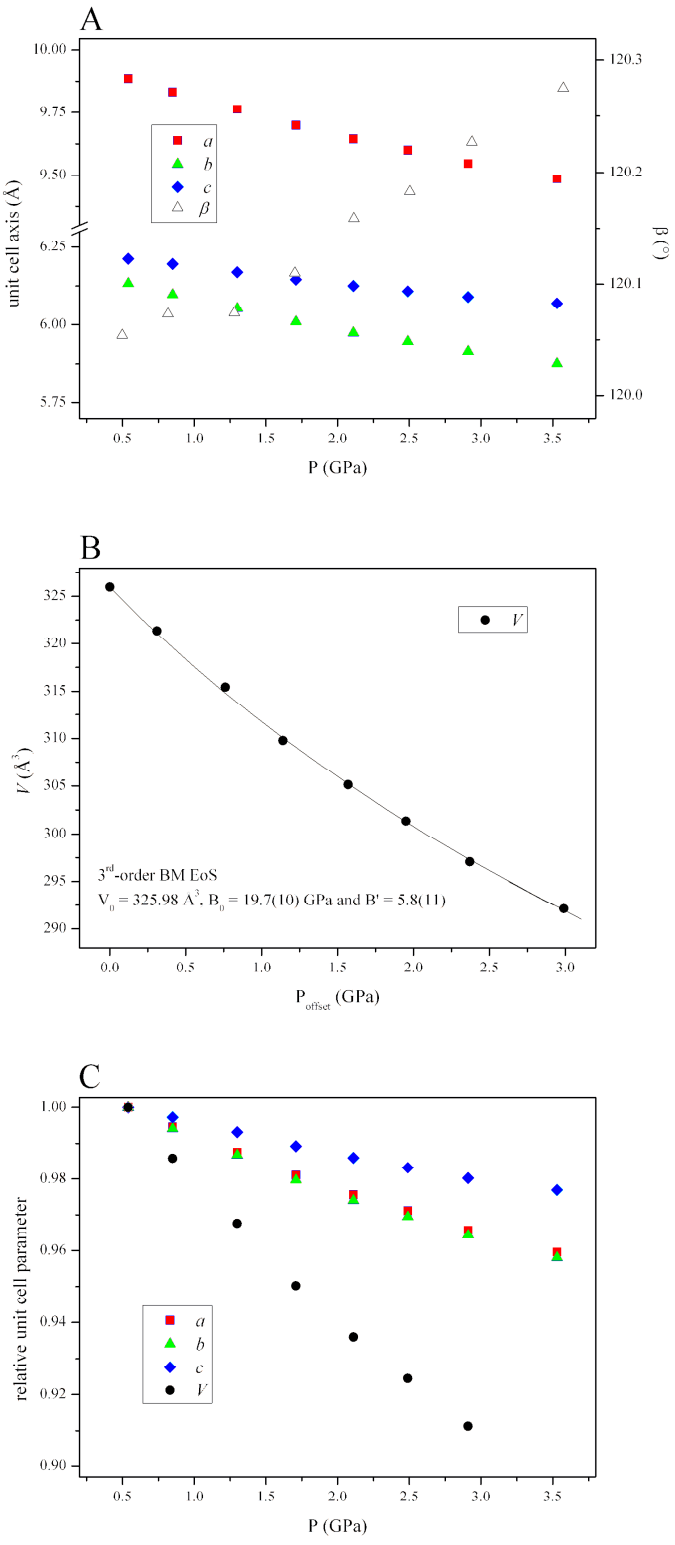

Figure 5.18 (a) compression of the unit cell parameters (a, b, c and β) of CsN_3-III over its stability range; (b) relative compression of the unit cell axes and unit cell volume (normalised to P = 0.54 GPa); and, (c) PV-plot for CsN_3-III and its representative 3rd-order Birch-Murnaghan EoS.

The pattern collected at the next pressure point (3.6 GPa[8]) showed a dramatic change, indicative of a phase transition. Further compression of this phase (CsN_3-IV) showed that its stability was limited to a pressure range of only ~1.0 GPa – a third high-pressure phase transition was observed to commence at 4.4 GPa. A clean pattern was collected for a pure form of CsN_3-V at 4.8 GPa. No further changes were observed up to the maximum pressure studied (6.0 GPa). Current efforts are focussed on obtaining unambiguous unit cells for these high-pressure phases and it is hoped that structure solution will be possible based on the neutron powder diffraction data presented herein and complementary high-pressure X-ray powder studies (*vide infra*).

Unfortunately the time constraints of this experiment meant that it was not possible to examine the decompression behaviour sufficiently to determine any hystereses. Nevertheless, examination of the diffraction pattern collected at atmospheric pressure confirmed that the tetragonal form II had been recovered and, in contrast to NaN_3 above, showed no evidence of internal strain.

High-Pressure X-ray Powder Diffraction Study

In order to complement the above neutron diffraction study, powder X-ray diffraction data were collected during the compression of caesium azide (to 3.9 GPa) at the Extreme Conditions Beamline (I15), Diamond Light Source. Diffraction patterns collected during this experiment, representative of forms II-IV, are shown in Figure 5.19. Comparison of the diffraction patterns obtained experimentally for CsN_3-III with those calculated using the structural model presented above highlighted a number of intensity mismatches, particularly in the peaks located at d = 2.11, 2.42, 2.97 and 4.22 Å in the pattern collected at 2.1 GPa (Figure 5.20). Visual inspection of the sample after data collection showed that considerable radiation damage had occurred – this dramatic effect is presented in Figure 5.21. The light colouration of the sample caused by sample centring (green lines) is thought to be due to the formation of F-centres upon irradiation – a well-documented phenomenon in alkali metal azides.[79, 80] This effect became more noticeable upon irradiation for longer exposure times (red spots correspond to 10 s; dark blue spot in Figure 5.21(b) after irradiation for 90 s) and thus is perhaps indicative of sample decomposition. This phenomenon has also previously been observed in, for example, TlN_3 (in which the unit cell volume was observed to increase after X-ray irradiation [81]) and in NaN_3 (in which 'trapped' N atoms were

[8] It should be noted that the pressures reported for the three high-pressure phases have been estimated based on the *d*-spacing of the Pb (200) and (111) peaks. In some cases these peaks were overlapped by sample peaks and the uncertainty in pressure is therefore larger than patterns for which Rietveld refinement was possible.

observed by ESR spectroscopy [82]). Furthermore it is analogous to the high-pressure photolysis (λ = 514 nm) of sodium azide reported by Peiris and Russell who propound this method for the generation of novel polynitrogen species.[4]

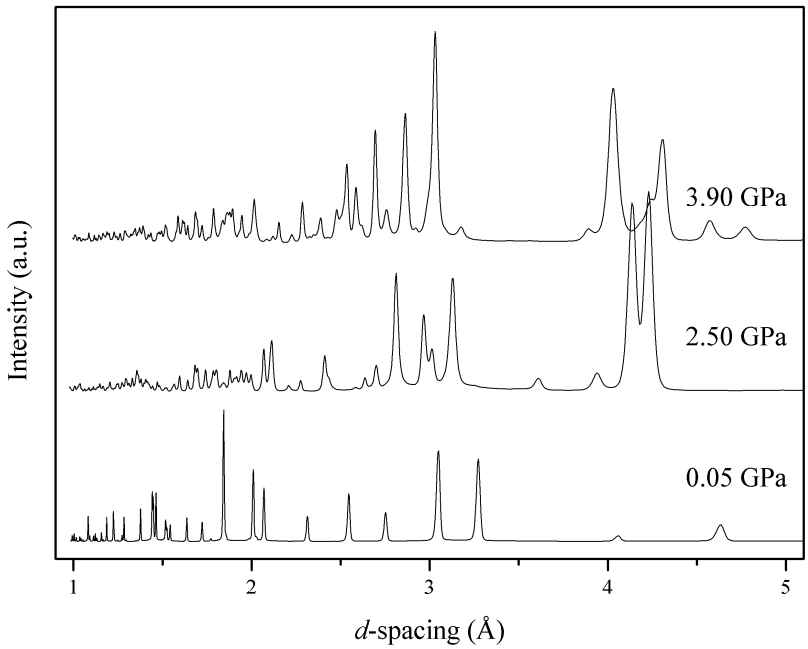

Figure 5.19 X-ray powder diffraction patterns collected for CsN_3-II (0.05 GPa), CsN_3-III (2.50 GPa) and CsN_3-IV (3.90 GPa) collected at the Extreme Conditions Beamline (I15), Diamond Light Source.

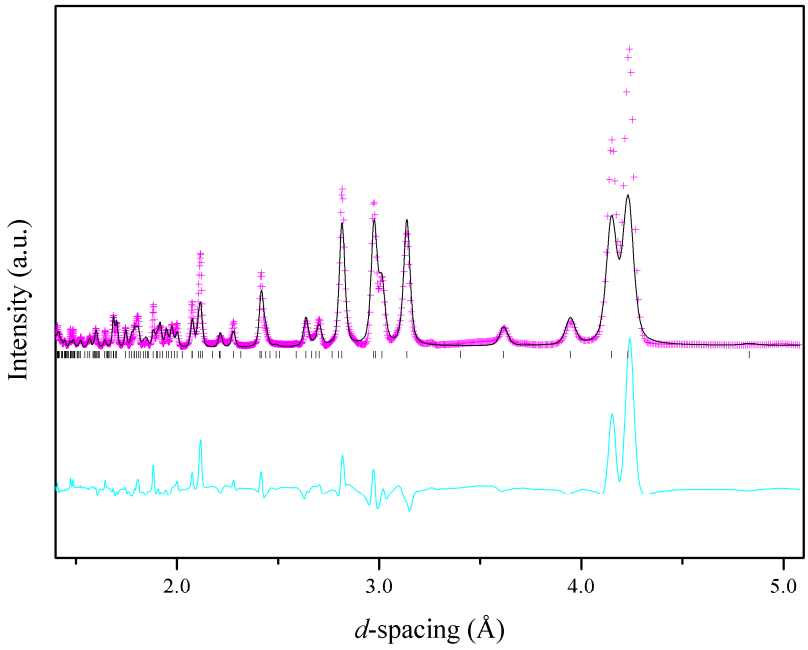

Figure 5.20 Refinement of the X-ray powder diffraction pattern collected for CsN_3 at 2.1 GPa using the CsN_3-III structural model (black tick marks). The observed intensities (I_{obs}) are represented as pink crosses and the calculated pattern (I_{calc}) is shown as a black line. The difference curve ($I_{obs} - I_{calc}$) is shown in cyan – this highlights numerous intensity mismatches in this pattern, particularly at d = 2.11, 2.42, 2.97 and 4.22 Å.

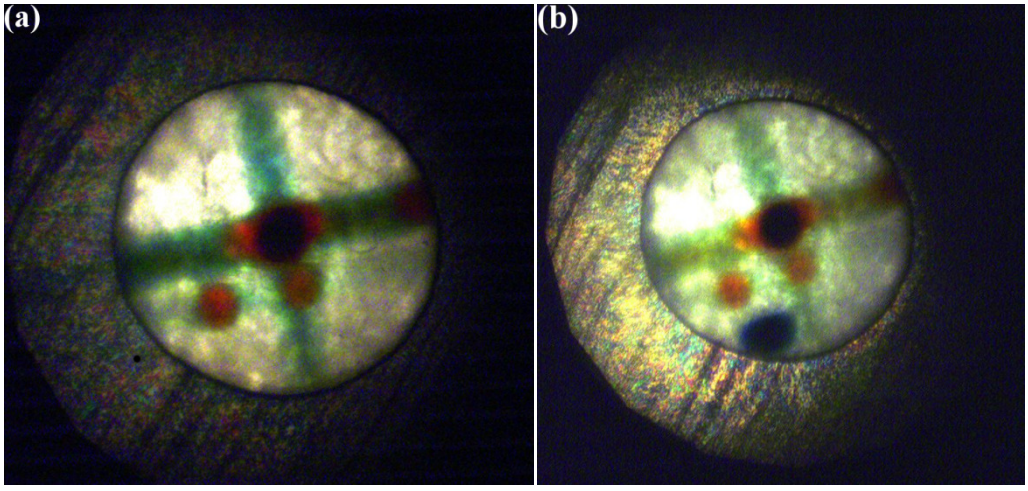

Figure 5.21 Optical microscope images of the radiation damage of CsN_3 at constant pressure (a) before and (b) after 90 second exposure. The green lines in each image are due to exposure of the sample to X-ray during alignment of the diamond-anvil cell; the red dots were produced during shorter data collections (10 s); the blue dot present in (b) is an effect of exposure of a fresh sample of CsN_3 to synchrotron radiation for 90 sec.

This dramatic evidence of sample deterioration in the synchrotron beam prompted the investigation of possible (crystalline) decomposition products which may be present in

sufficient quantities to contribute to the Bragg scattering. The majority of the intensity mismatches are coincident with diffraction peaks arising from caesium metal ($Im\bar{3}m$) although the relative intensities of these peaks do not correspond with the calculated pattern based on the cubic structure of Cs(s). This is perhaps not surprising as one would expect the small quantities of metal deposited in this way to be under extreme strain and to exhibit preferred orientation. Furthermore the deposition of caesium metal also implies the formation of a (or various) polynitrogen species, which may be expected to have an effect on the relative intensities of the diffraction peaks observed in this experiment. It would therefore be beneficial to repeat these studies and characterise the products of photolysis by a number of methods, particularly vibrational spectroscopy. Once identified and characterised at pressure, the recoverability of these products to ambient conditions should then become a priority in order to explore this avenue as a route to synthesising novel, 'greener' energetic materials.

Unfortunately the uncertainty over the effect of irradiation on CsN_3 has meant that it has not been possible to structurally characterise the second high-pressure polymorph, for which X-ray powder diffraction patterns were also collected. It would therefore also be worthwhile repeating this study using short exposure times in order to obtain high-resolution X-ray powder diffraction data on CsN_3-IV and CsN_3–V, while minimising sample decomposition.

Summary: CsN_3

The compression of caesium azide has been studied to a maximum pressure of 6.0 GPa by a combination of X-ray and neutron powder diffraction: evidence of three high-pressure polymorphs is presented. The structure of the first high-pressure form (CsN_3-III) has been determined by a combination of X-ray and neutron powder diffraction. In addition, evidence of two further high-pressure polymorphs is presented and current efforts are being directed at the structural characterisation of these forms. An unexpected result of the X-ray powder diffraction study was the observation of photolysis at pressure, resulting in Cs metal and, possibly, polynitrogen species. These studies should therefore be supplemented by a more rigorous study in order to asses the sample composition critically and to investigate the possibility of the recovery of the product materials to ambient pressure.

5.5.3 TlN_3

High-Pressure Neutron Diffraction Study

The initial aim of the structural investigation of thallium azide was to obtain high quality diffraction data on the high-pressure polymorph, TlN_3-III. A multiplot of the neutron powder

diffraction patterns collected during this experiment is shown in Figure 5.22. Since the phase transition from the tetragonal form II to the high-pressure form was reported to be *ca* 0.7 GPa, the initial increases in sample pressure were small (0.05 – 0.1 GPa increments). In this way it was possible to carry out Rietveld refinements on the powder diffraction patterns collected for TlN_3-II in this lower pressure regime (unit cell parameters may be found in Table 5.5). A 2nd order Birch-Murnaghan EoS has been fitted to the smooth compression of unit cell volume with V_0 (refined) 283.0(9) Å^3, B_0 = 21(3) GPa and B'(fixed) = 4. Unfortunately the relatively narrow stability range of TlN_3-II meant that any scatter in the data was magnified and thus it was not possible to determine a higher-order EoS and the e.s.d calculated for the bulk modulus is larger than desired. Despite this, the value of B_0 is consistent with other metal azides and the calculated V_0 compares favourably with the volume at ambient conditions (282.6(1) Å^3) determined experimentally by X-ray powder diffraction.

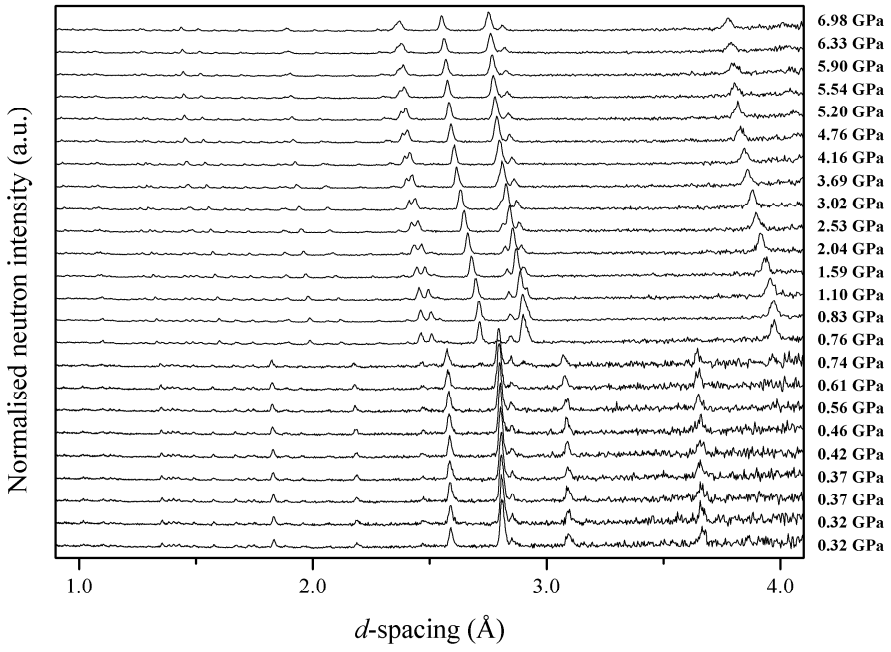

Figure 5.22 Multiplot of neutron powder diffraction patterns collected during the compression of TlN_3. The patterns collected below 0.76 GPa display a lower signal-to-noise ratio, since shorter collection times were utilised in these cases (*ca* 1 hr compared to 4 hrs for the later patterns).

Comparison of the structure determined at 0.74 GPa with that obtained from the initial pattern (0.32 GPa) shows that the compression of the unit cell is not accompanied by any rotation of the N_3^- anions and is surprisingly isotropic. Plots of the relative compression of

the unit cell axes (Figure 5.23) show that the compression within the layers of N_3^- and Cs^+ (*ab*-plane) is comparable to compression normal to the layer (*c*-axis).

P (GPa)	*a*, *b* (Å)	*c* (Å)	*V* (Å^3)	wR_p
0.32	6.1775(5)	7.3155(6)	279.17(4)	0.121
0.32	6.1762(6)	7.3141(8)	279.00(5)	0.151
0.37	6.1742(5)	7.3062(7)	278.52(4)	0.205
0.37	6.1707(5)	7.3022(7)	278.05(4)	0.125
0.42	6.1661(5)	7.3005(7)	277.57(4)	0.133
0.46	6.1604(5)	7.2957(7)	276.87(4)	0.124
0.56	6.1571(5)	7.2889(7)	276.33(4)	0.116
0.61	6.1472(6)	7.2847(8)	275.27(5)	0.146
0.74	6.1398(7)	7.2793(9)	274.41(5)	0.168

Table 5.5 Unit cell parameters determined during the compression of TlN_3-II, to a maximum pressure of 0.74 GPa.

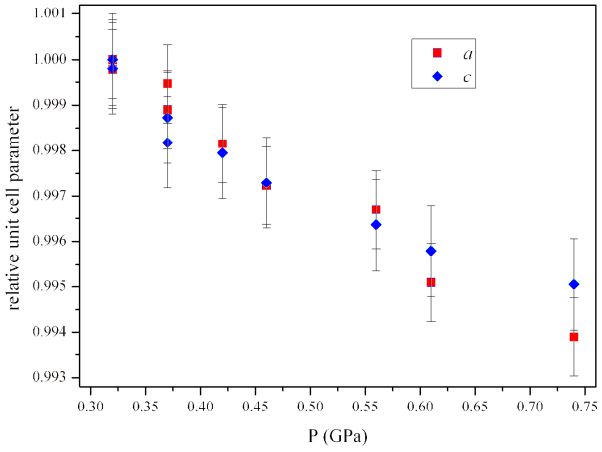

Figure 5.23 Relative compression of the unit cell axes in TlN_3-II to a maximum pressure of 0.74 GPa.

Another advantage of increasing the sample pressure in very small increments is the accurate determination of the II/III transition pressure (to within 0.2 GPa). The diffraction pattern collected at 0.76 GPa shows striking differences when compared to the pattern collected at 0.74 GPa; this is clear evidence of a phase transition. The quality of the diffraction pattern (after 2.5 hours) meant that it was possible to obtain an orthorhombic unit cell (*Immm*) for this high-pressure form. It was possible to carry out full-profile Rietveld refinement on this pattern and all subsequent patterns collected during the compression to a maximum pressure

of 6.98 GPa. It should be noted that the axes have been chosen to facilitate comparison with the ambient pressure tetragonal form.

Comparison of the structure of TlN_3-III determined at 0.76 GPa with the tetragonal structure immediately preceding the phase transition highlights the dramatic rearrangement that the azide anions undergo over this transition. As is illustrated in Figure 5.24, the phase transition involves an out-of-plane rotation of half of the azides (type I) to lie parallel to the orthorhombic *c*-axis, while the other azides (type II) are re-oriented parallel to the *a*-axis. As a result there are two independent azide units, an observation which is reflected in the splitting of vibrational modes noted by previous investigators.[57] These independent azides are arranged perpendicular to one another in chains that run parallel to the *c*-axis: the negative terminal N-atom of one is aligned with the positive central N-atom of its nearest neighbour, at a distance of 3.03 Å.

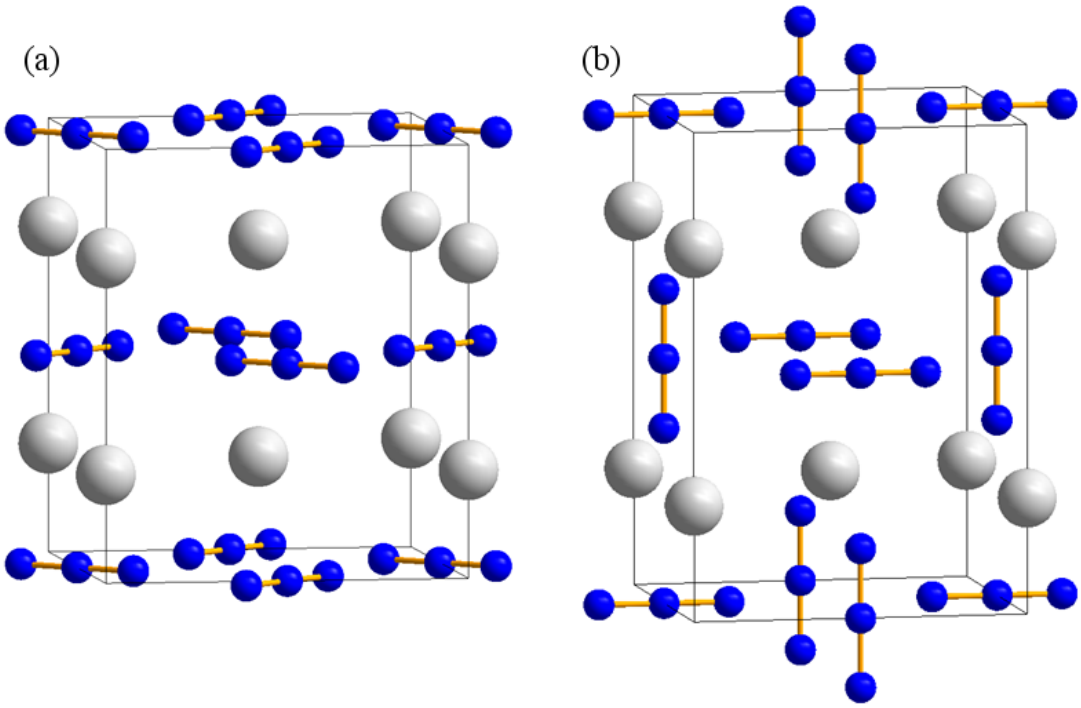

Figure 5.24 Comparison of the structures of (a) TlN_3-II and (b) TlN_3 –III clearly demonstrating the out-of-plane rotation of half of the azide anions over the high-pressure phase transition.

This arrangement of the azides results in each adopting a different co-ordination environment. In Type I each terminus lies in close proximity to four Tl cations (2.90 and 3.02 Å) in the layers immediately above and below the azide. Looking down the length of the N_3^- unit, these cations lie directly above one another resulting in a cuboidal configuration (see Figure 5.25 (a)). In contrast, Type II are co-planar with their four nearest Tl cations,

giving rise to the bifurcated N…Tl interactions shown in Figure 5.25(b). The co-ordination environment of the thallium cations can be thought of as a greatly distorted octahedron involving the termini of four Type I azides (2.90 and 3.02 Å) and two of Type II (2.88 Å). This is illustrated in Figure 5.26(a). Furthermore, it should be noted that the cations do not order themselves in perfectly linear chains; when viewed down the *b*-axis the alternating arrangement of Type I and Type II results in a wave-like distribution of Tl^+ cations (Figure 5.26(b)), which becomes more pronounced throughout compression (from 3.8° at 0.76 GPa to 6.3° at 6.98 GPa).

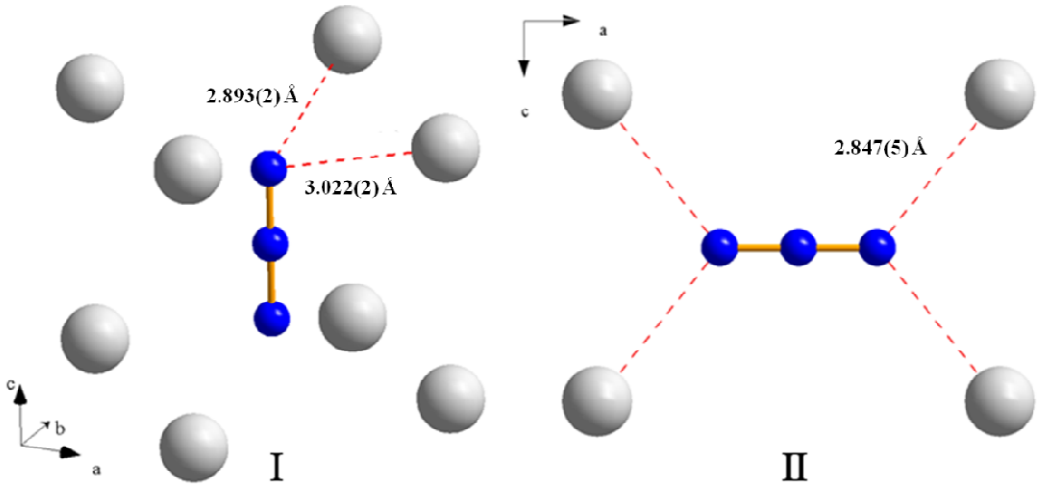

Figure 5.25 Co-ordination environments of the independent azides in TlN_3 (Type I and Type II) at 0.76 GPa.

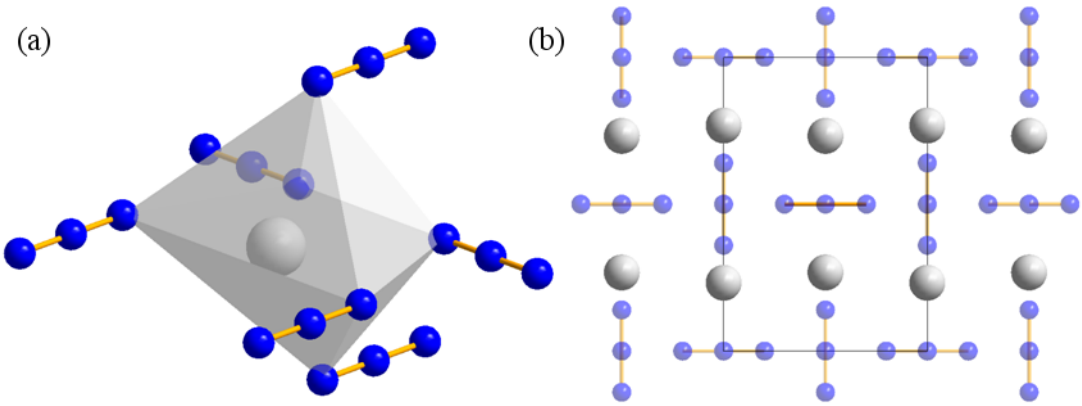

Figure 5.26 Co-ordination environment of the Tl cations in TlN_3 (a) the distorted O_h round one cation, and (b) the wave-like distribution of cations in unit cell viewed down the *a*-axis.

The unit cell parameters over the course of the experiment (from 0.32 to 6.98 GPa) have been tabulated in Table 5.6 and plotted in Figure 5.27. This shows that the lengthening of the tetragonal axis is outweighed by the shortening of the *a*- and *b*-axes, resulting in a 2.7%

reduction in unit cell volume over the phase transition. This sizeable contraction and the considerable degree of re-organisation within the structure explain the reconstructive nature of this phase transition noted during single-crystal studies.[18]

P (GPa)	a (Å)	b (Å)	c (Å)	V (Å^3)	wR_p
0.76	5.8274(6)	5.4141(3)	8.4670(7)	267.14(3)	0.057
0.83	5.8261(4)	5.4097(3)	8.4589(5)	266.61(3)	0.034
1.10	5.8145(5)	5.3840(3)	8.4224(7)	263.66(4)	0.050
1.59	5.7943(5)	5.3472(3)	8.3703(6)	259.34(3)	0.044
2.04	5.7743(5)	5.3137(3)	8.3227(7)	255.37(3)	0.045
2.53	5.7549(4)	5.2817(3)	8.2777(6)	251.61(3)	0.048
3.02	5.7353(4)	5.2520(3)	8.2354(6)	248.07(3)	0.047
3.69	5.7120(4)	5.2207(3)	8.1901(6)	244.23(3)	0.044
4.16	5.6933(4)	5.1981(3)	8.1595(6)	241.47(3)	0.049
4.76	5.6742(5)	5.1712(3)	8.1217(7)	238.31(3)	0.050
5.20	5.6607(5)	5.1548(3)	8.0995(7)	236.34(3)	0.054
5.54	5.6492(5)	5.1400(4)	8.0789(8)	234.59(4)	0.061
5.90	5.6402(5)	5.1268(4)	8.0628(9)	233.15(4)	0.073
6.33	5.6266(6)	5.1123(4)	8.0428(9)	231.35(4)	0.061
6.98	5.6098(6)	5.0923(4)	8.0137(9)	228.93(4)	0.070

Table 5.6 Unit cell parameters obtained by Rietveld refinement of neutron powder diffraction patterns collected for TlN_3-III.

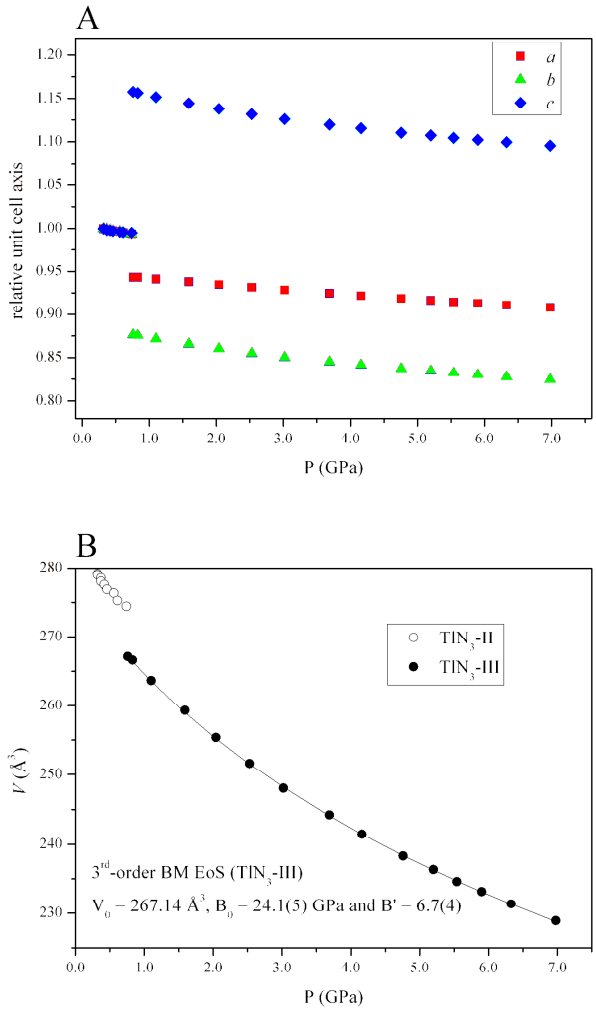

Figure 5.27 (a) relative compression of the unit cell axes of TlN_3 between 0.3 and 7.4 GPa, highlighting the lengthening of the tetragonal *c*-axis over the II/III transition; and, (b) the contraction of the unit cell volume over the same pressure regime, with clear evidence of the first-order transition.

The variation in the unit cell volume with pressure can be described by a 3rd-order Birch Murnaghan EoS with $V_0 = 267.14$ Å^3 (fixed), $B_0 = 24.1(5)$ GPa and B' = 6.7(4). It should be noted that for this high-pressure phase, the volume at the first pressure (0.76 GPa) where it was observed has been taken as V_0; all pressures were therefore normalised to this. The coefficients of the EoS have been verified by construction of an *Ff*-plot and are consistent with the compression characteristics observed for the other metal azides in this study. The larger value of the bulk modulus for this polymorph compared to TlN_3-II shows that this form is less compressible than the ambient pressure form, although it should be noted that the large error in the bulk modulus of TlN_3-II means that it is unadvisable to draw any further conclusions.

The relative shortening of the unit cell axes in TlN_3-III (shown in Figure 5.27) allows one to assess the compression mechanism critically. This figure clearly shows that the *a*-axis is most resistant to compression – while the shortening of the *a*-axis does result in shorter interactions between the cations and the azide termini within the same plane, this is accompanied by an increase in the angle formed between the Type II azide and its two thallium neighbours which would be expected to reduce the efficacy of any cohesive interactions (see Figure 5.28a). Contraction of the *c*-axis results in a significant shortening of the interaction between the termini of Type I azides and the central atom of Type II (~7% over the pressure range studied). Interestingly the parallel interactions between neighbouring cations are compressed by either ~2% or ~ 10% over the same pressure range (Figure 5.28b), resulting in the observed wave-like distribution becoming more pronounced at higher pressures. This differential contraction would therefore suggest that, at some finite pressure, TlN_3-III would undergo a symmetry-breaking phase transition. The direction aligned with the interplanar separation (*b*-axis) is, as expected, the most compressible axis.

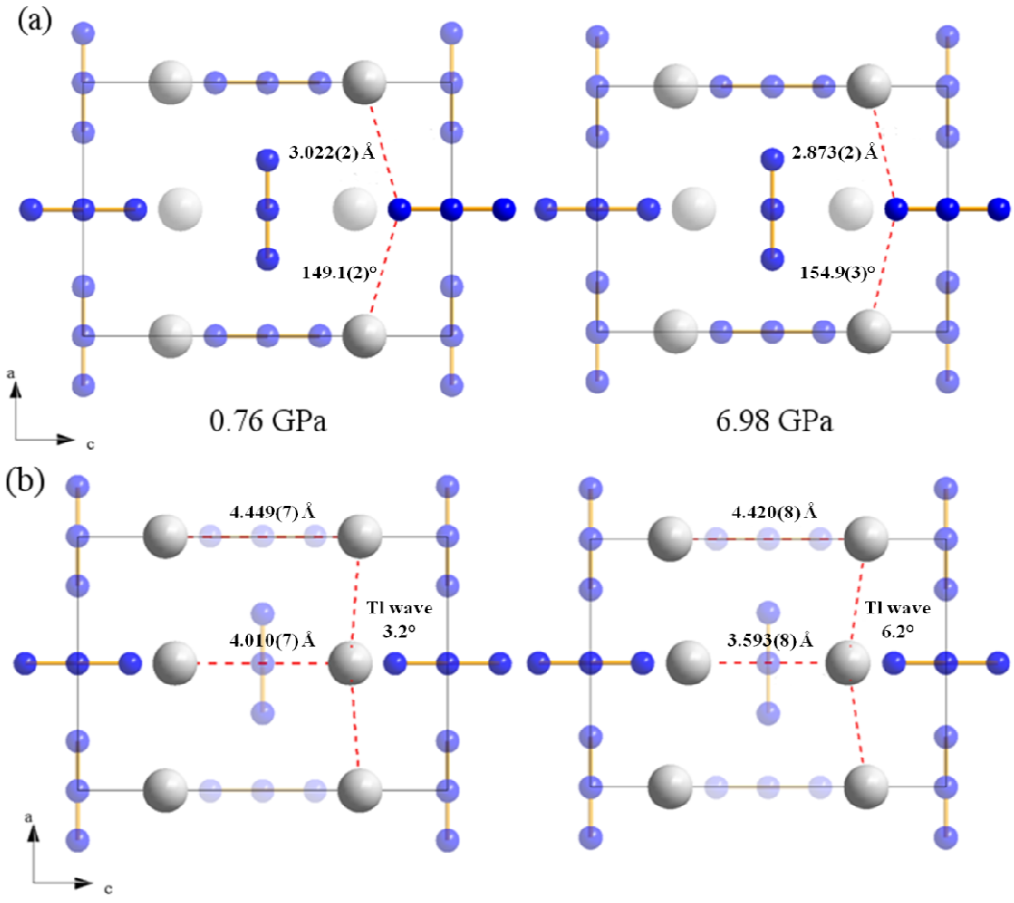

Figure 5.28 (a) Compression along the *a*-axis, highlighting the increased angle between Tl-N-Tl, (b) compression along the *c*-axis, which has been shown to result in the differential contraction of Tl…Tl and N…N interactions.

Finally it should be noted that a weak reflection (2.32 Å) is observed in the patterns collected above 3.69 GPa which could not be accurately described by the current structural model. This peak persists during compression, but the only other significant change in the diffraction pattern is a slight reduction in intensity of the peak at 2.60 Å; no other extra peaks are observed (Figure 5.29). For this reason it has not been possible to determine whether this is indicative of a new phase, perhaps as a result of a monoclinic distortion of the orthorhombic form III, or in fact is evidence of a decomposition product. Unfortunately mechanical failure of the gasket during decompression resulted in complete evacuation of the sample chamber. This meant that it was impossible to collect a neutron powder diffraction pattern at atmospheric pressure to examine the reversibility of the II/III phase transition and no material could be recovered for subsequent analysis to assess sample purity. It would therefore be worthwhile to investigate the high-pressure polymorphism of TlN_3 using high resolution X-ray diffraction, primarily to determine if a phase transition does occur above 3.69 GPa, but also to characterise the decompression behaviour fully.

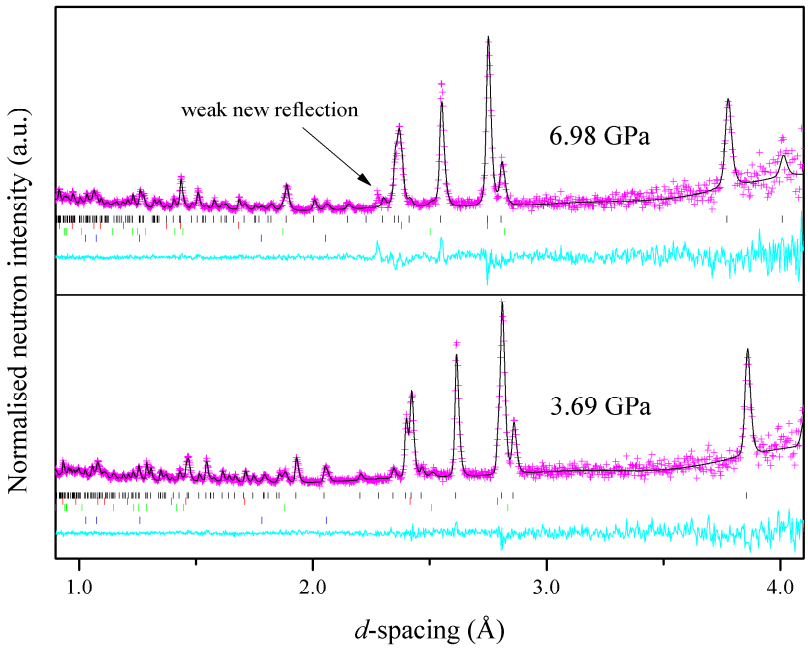

Figure 5.29 Rietveld refinement of the patterns collected at 6.98 GPa and 3.69 GPa to show the emergence of the weak peak *ca* 2.3 Å in the higher pressure pattern. In both cases the experimental data (I_{obs}) are represented as pink crosses, the calculated pattern (I_{calc}) is superimposed as a black line and the difference between these ($I_{obs} - I_{calc}$) is shown in cyan. Tick marks for each phase are also shown for clarity: TlN_3 (black), Pb (red), WC (green) and Ni (blue).

In addition to examining the high-pressure behaviour of thallium azide at ambient temperature, the low temperature phase (TlN_3-IV) was investigated at ambient pressure by X-ray powder diffraction. Due to concerns previously raised [55] over the effect of sample aging upon the phase behaviour of TlN_3, high-quality X-ray powder diffraction data were collected (2θ range of 2 – 140°) for a freshly-prepared sample at room temperature to confirm sample purity. The quality of the diffraction data (and the Rietveld refinement of this pattern using the tetragonal TlN_3-II structure) is highlighted in Figure 5.30, which clearly shows that no contamination from a decomposition product or other impurity occurred. The sample was subsequently cooled to 100 K, at which point diffraction data were collected over a period of 8 hours to ensure effective powder-averaging throughout the whole 2θ range and therefore to facilitate structure solution. X-ray powder patterns were then collected at 20 K intervals between 80 and 280 K (1 hr exposure), although smaller temperature increments were employed in the range of 230 – 245 K in order to determine accurately the TlN_3-II → IV transition temperature. A multiplot of the X-ray powder diffraction patterns collected during this experiment is shown in Figure 5.31.

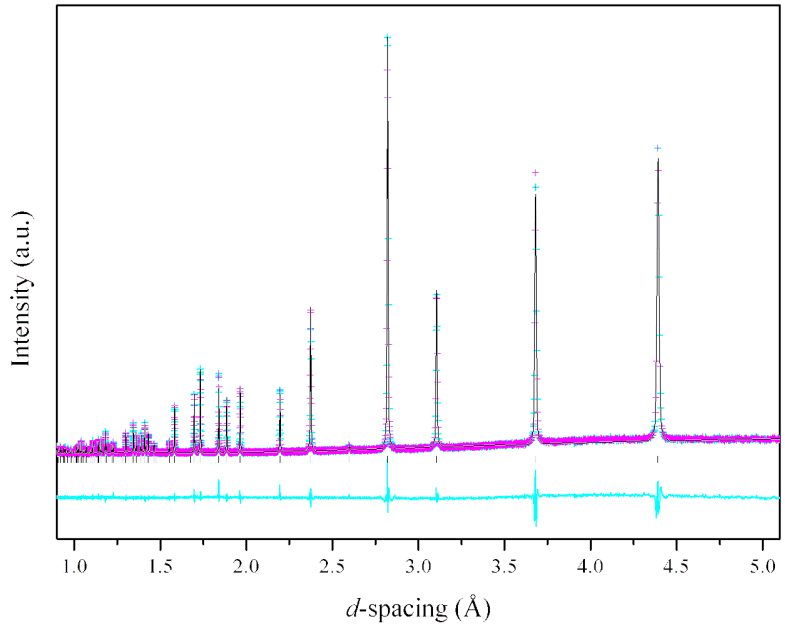

Figure 5.30 Rietveld refinement of the X-ray powder diffraction pattern collected for TlN_3-II (black tick marks) at room temperature, highlighting the quality of the data and the sample. The experimental data (I_{obs}) are shown as pink crosses, the calculated pattern (I_{calc}) as a black line and the difference curve ($I_{obs} - I_{calc}$) in cyan.

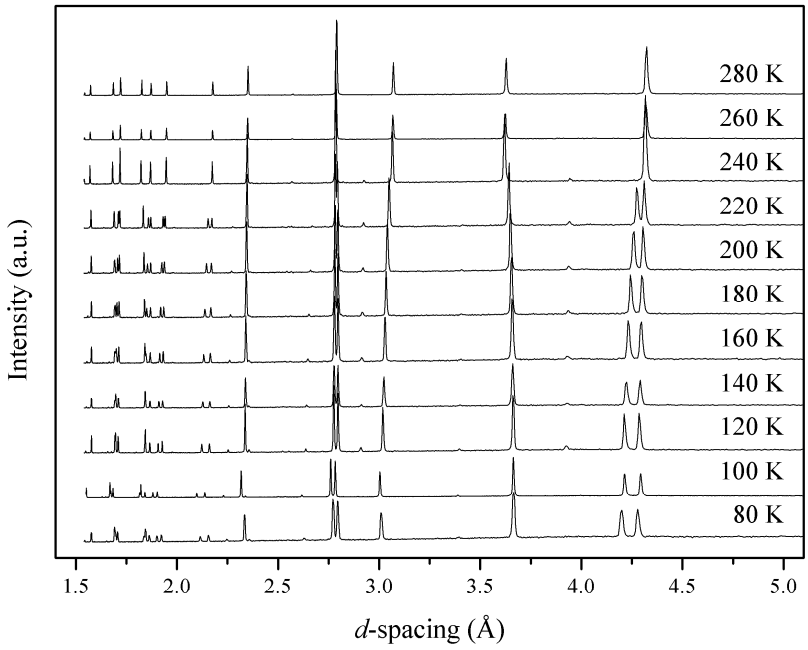

Figure 5.31 Mulitplot of the X-ray powder diffraction patterns collected during the variable temperature study of TlN_3 (intensities scaled for clarity). The TlN_3-II → IV transition between 240 and 220 K is evident in the splitting of peaks *ca* 2.15, 2.75 and 4.40 Å.

Close inspection of the diffraction patterns collected at 235 and 240 K, particularly in the region $d < 2.2$ Å, shows splitting of the diffraction peaks, characteristic of a phase transition between these temperatures, see Figure 5.32. This transition temperature is in accordance with that observed by Iqbal and Christoe during the spectroscopic measurements [55], but is significantly lower than the transition temperature (248 ± 5 K) reported by Mauer *et al.* in their X-ray powder diffraction study. It should be noted, however, that Mauer *et al*. based their determination of the transition temperature on a discontinuity in the slope of a plot of the unit cell parameters *versus* temperature and remarked that 'the change in the X-ray pattern is subtle, and it is difficult to establish the transition temperature accurately'.[54] The quality of the data reported herein, however, has allowed the accurate determination of the transition temperature to be between 235 and 240 K – the pattern collected at 240 K exhibits no peak broadening and the characteristic peaks are suitably modelled by singlets. A more detailed study in this temperature range using high-resolution powder diffraction is currently underway in order to determine the transition temperature more precisely.

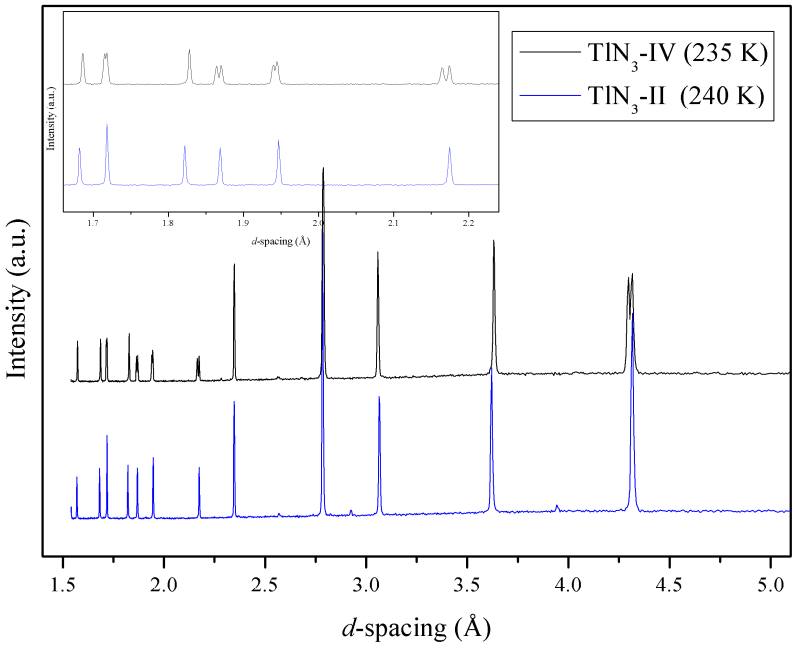

Figure 5.32 Comparison of the diffraction patterns collected for TlN_3 at 240 and 235 K. The tetragonal → orthorhombic transition is indicated by the splitting of numerous peaks, particularly those highlighted in the inset.

The splitting observed in the characteristic peaks (such as (004) and (400) at d ~ 2.2 Å) is indicative of a phase transition from the tetragonal structure of TlN_3-II to an orthorhombic structure, in accordance with conclusions drawn from previous diffraction studies.[54] In the present study, however, the quality of the 100 K data allowed space group determination (*Cmcm*) and subsequent structure solution. The structure of TlN_3-IV was solved by Dr S. Margadonna (School of Chemistry, University of Edinburgh), using the simulated annealing program Powder Solve within Materials Studio.[83] The positions of the heavy atoms were determined initially (using $P\bar{1}$ symmetry) before global optimisation, throughout which the azide anions were treated as rigid bodies. It was then possible to carry out full-profile Rietveld refinement of all diffraction patterns collected for this form, the quality of which is typified by that shown in Figure 5.33 for the pattern collected at 100 K. Throughout refinement the angles N1-N2-N1 and N3-N4-N3 were restrained to be 180(2)° by the insertion of a 'dummy' atom at positions equivalent to N1' and N3' (with zero occupancy) and defining each restraint in terms of N1-N2-N1' and N3-N4-N3'.[84]

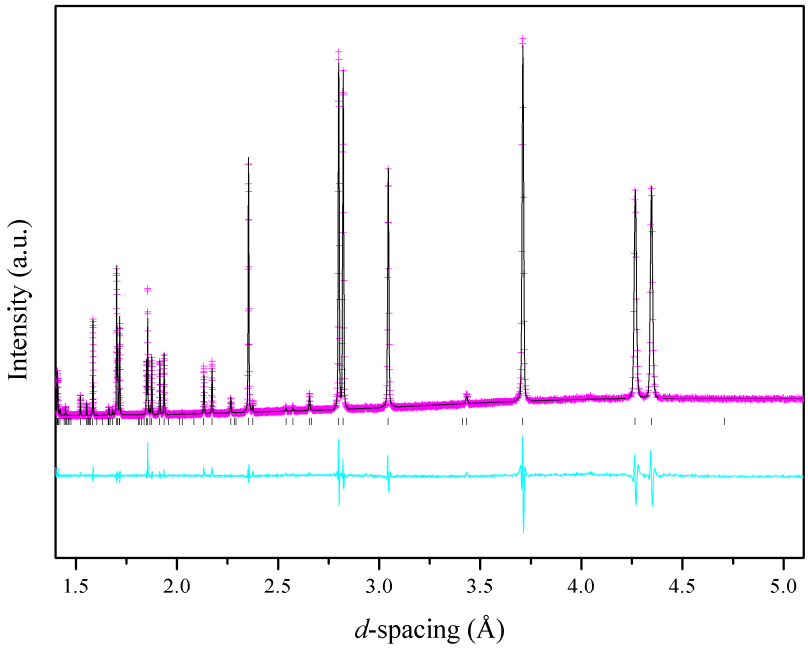

Figure 5.33 Rietveld refinement of the diffraction pattern collected at 100 K using the TlN3-IV structural model (black tick marks). The experimental data (I_{obs}) are shown as pink crosses, the calculated pattern (I_{calc}) as a black line and the difference between these models ($I_{obs} - I_{calc}$) is shown in cyan.

A summary of the unit cell parameters determined throughout this experiment can be found in Table 5.7 and in Figure 5.34(a), which clearly shows the phase transition between the tetragonal form II and the orthorhombic form IV. In order to provide a direct comparison between the different forms, also presented in Figure 5.34(a) are values calculated for $a_{ortho}/\sqrt{2}$ and $c_{ortho}/\sqrt{2}$, since the *a*- and *c*-axes in the orthorhombic cell correspond to the face diagonals of the original tetragonal cell. Furthermore, as the transition involves a doubling of the unit cell, it has been necessary to scale the volume of TlN_3-IV by 0.5 to facilitate comparison of the thermal expansion of each form, presented graphically in Figure 5.34(b). The volumetric thermal expansion of TlN_3-IV has been determined for the temperature range 80 – 235 K: α_v = [6.0(3) + 0.0519(20) T] x 10^{-5} K^{-1}; in comparison, α_v = [-0.9(5) + 0.0039(18) T] x 10^{-3} K^{-1} for TlN_3-II in the range 240 – 293 K.

T (K)	a (Å)	b (Å)	c (Å)	V (Å^3)	wR_p
293	6.21108(3)	6.21108(3)	7.36070(4)	283.958(3)	0.089
280	6.20331(5)	6.20331(5)	7.34648(6)	282.701(4)	0.097
260	6.19934(4)	6.19934(4)	7.33636(6)	281.950(4)	0.083
245	6.19578(5)	6.19578(5)	7.33129(7)	281.432(4)	0.074
240	6.19415(5)	6.19415(5)	7.32956(7)	281.217(4)	0.085
235	8.71953(13)	7.35130(9)	8.75930(13)	561.686(12)	0.074
230	8.70298(12)	7.36344(8)	8.75621(12)	561.139(10)	0.070
220	8.67820(14)	7.37495(9)	8.75079(14)	560.063(11)	0.087
200	8.64169(14)	7.39067(9)	8.73969(14)	558.185(10)	0.079
180	8.61319(14)	7.40098(9)	8.72927(14)	556.457(11)	0.082
160	8.58947(15)	7.40814(9)	8.71948(15)	554.837(11)	0.078
140	8.56829(15)	7.41281(10)	8.71018(15)	553.228(11)	0.074
120	8.54919(12)	7.41814(7)	8.70142(12)	551.836(9)	0.092
100	8.53315(5)	7.42110(3)	8.69385(5)	550.541(4)	0.095
80	8.52053(19)	7.42222(12)	8.68620(20)	549.327(15)	0.090

Table 5.7 Unit cell parameters obtained during the low-temperature X-ray powder diffraction experiment conducted on TlN_3.

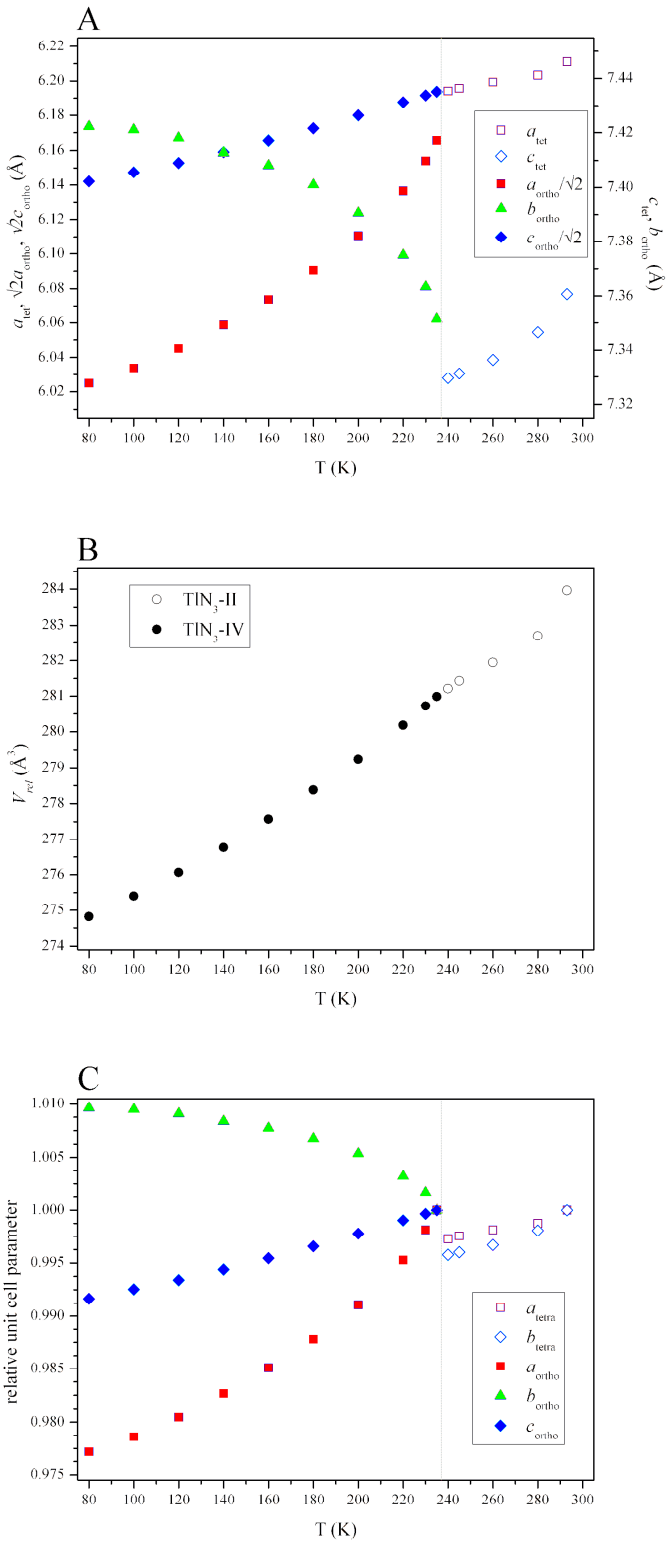

Figure 5.34 (a) Response of the unit cell parameters (*a*, *b* and *c*) to cooling presented alongside $a_{ortho}/\sqrt{2}$ and $c_{ortho}/\sqrt{2}$ to facilitate comparison with the tetragonal cell; (b) the relative volume contraction upon cooling; and, (c) the relative unit cell contraction/expansion throughout the experiment.

The relative contraction or expansion of the unit cell parameters is highlighted in Figure 5.34(c). It should be noted that the unit cell parameters have been normalised to their values at the maximum temperature at which each form has been studied (i.e. 235 K for form IV and 293 K form TlN_3-II). This clearly shows the anomalous expansion of the orthorhombic *b*-axis (corresponding to the *c*-axis in the indexing put forward by Mauer *et al.* [54]), which led previous authors to suggest a transition mechanism involving the 'rotation of one set of the N_3 groups out of the (001) plane' [*sic*].[55] Comparison of the structure of TlN_3-IV at 235 K with the tetragonal form at 240 K (see Figure 5.35), however, shows that there is very little re-arrangement required over this transition, a fact that is reflected in the rapid nature of the transition and the very small volume contraction reported by previous authors.[54, 56] This is in direct contrast to the II → III at 0.7 GPa which does involve an out-of-plane rotation of half the azide units. One would therefore expect a similar transition mechanism to occur upon compression of the low-temperature form IV into the high-pressure regime of form III.

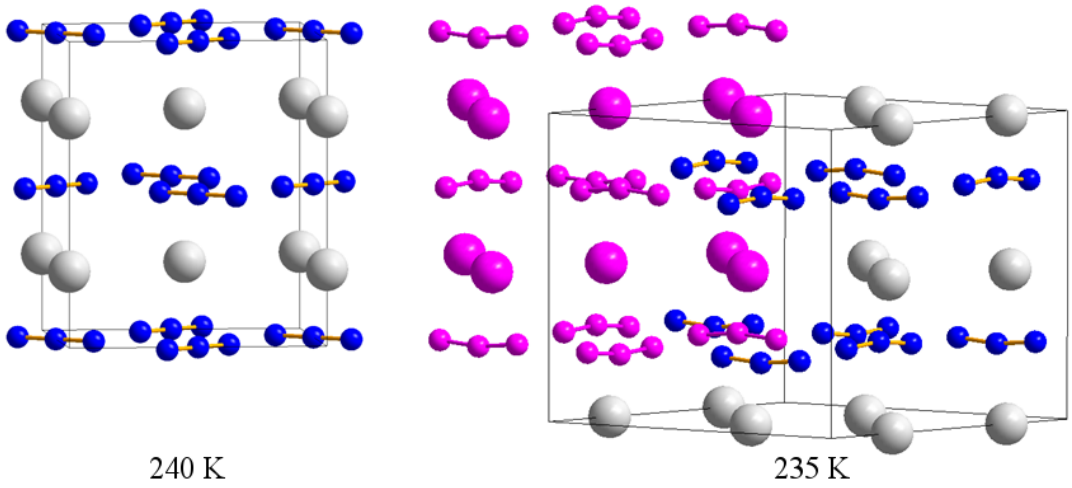

Figure 5.35 The crystal structures determined for TlN_3-II (at 240 K) and TlN_3-IV (at 235 K). In order to facilitate comparison between the related structures, the original tetragonal unit cell has been highlighted in pink in the orthorhombic structure. The deviation from linearity that is observed for the anions in TlN_3-IV may also be seen in the 235 K structure.

The orthorhombic distortion over the II → IV transition is, however, accompanied by a slight displacement of the Tl atoms resulting in a wave-like distribution. This feature becomes more pronounced upon cooling (4° at 235 K to 8° at 80 K), mirroring the behaviour observed throughout compression of TlN_3-III. This results in the appearance of small peaks in the diffraction pattern, which can only be modelled by the displacement of the thallium atoms away from (0.75, *y*, *z*), as depicted in Figure 5.36. It should also be noted that neither of the azide groups are linear (despite the restraints applied to these groups), although it has

been difficult to refine the positions of the nitrogen atoms due to the minimal contribution they make to the total X-ray scattering in this case.

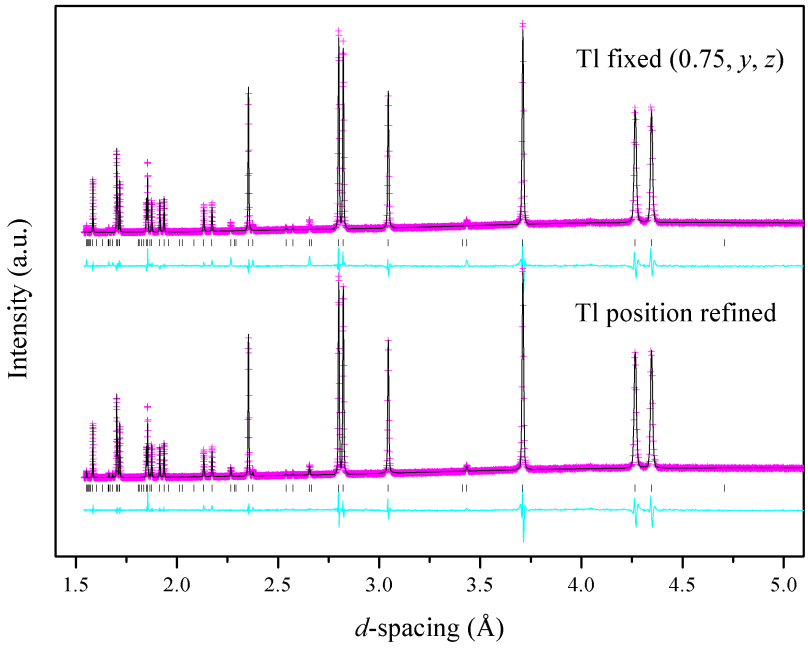

Figure 5.36 Comparison of the Rietveld refinements in which the thallium positions are refined and are fixed (bottom and top, respectively). In both cases, the observed intensities (I_{obs}) are plotted in pink, the calculated pattern (I_{calc}) in black and the difference curve ($I_{obs} - I_{calc}$) is shown in cyan. It should be noted that the top refinement (Tl fixed) does not accurately re-create the observed intensities at d = 2.25, 2.65 and 3.45 Å, corresponding to the (023), (221) and (021) reflections, respectively.

The exact reason for the anomalous expansion of the *b*-axis is still to be determined – one would expect a planar structure such as this to exhibit a preferential contraction of the interplanar distance, rather than expansion along it. Moreover, the observation that a single crystal did not survive the low-temperature transition is surprising, especially given the structural similarities between the two forms in the temperature range immediately surrounding the transition point. This perhaps indicates a more complex transition mechanism involving the azide groups. It would therefore be extremely desirable to conduct an analogous low-temperature neutron diffraction study in order to accurately determine the nitrogen positions. This would also allow an accurate assessment of the linearity (and symmetry) of the azide groups, thus providing an important insight into the interactions between the anions and the thallium cations.

Ambient-Pressure, High-Temperature Study

In order to provide complementary experimental evidence of the II → I transition at high temperatures, X-ray powder diffraction data were collected upon warming a freshly prepared sample of TlN_3 between 320 and 575 K. The diffraction patterns collected over the phase transition are presented in Figure 5.37, in which two important features are highlighted. First, the abrupt loss in intensity of the (004) and (114) peaks at d = 1.87 and 1.72 Å, respectively, upon warming from 550 to 560 K; secondly, the appearance of a new peak at d = 2.76 Å in the pattern collected at 570 K, becoming more prominent in the 575 K pattern. The latter feature is perhaps indicative of partial sample decomposition; the peak at 2.76 Å coincides with the strongest peak of the cubic high-temperature form of thallium metal ($Im\bar{3}m$) [85, 86], although it should be noted that no other peaks attributable to β-Tl are present in the 575 K pattern. Unfortunately the relatively low signal-to-noise ratio has made the determination of the temperature at which sample decomposition first occurs difficult. It would therefore be advantageous to repeat this study using either longer data collection times, high-resolution X-ray powder diffraction (as in the low-temperature study above) or neutron powder diffraction, thus providing an invaluable insight into the thermal stability of TlN_3.

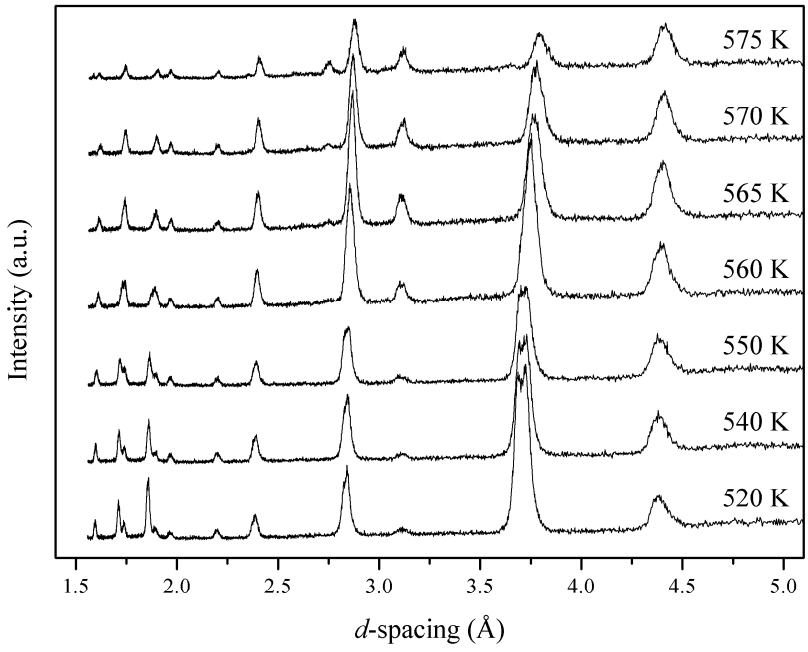

Figure 5.37 X-ray powder diffraction patterns collected for TlN_3 over the II – I phase transition (520 – 575 K).

The reduction in intensity of the (004) and (114) peaks is more likely indicative of a phase transition within the sample. Thus the TlN_3-II → I transition has been observed to occur between 550 and 560 K, below the previous experimental transition temperature (568 K reported by Müller and Jöbstl [37]) and above that observed in Molecular Dynamics (MD) simulations (530 K).[53] Supporting evidence for the phase transition occurring between 550 and 560 K can be found by plotting the unit cell parameters determined by Le Bail refinement of each of the diffraction patterns. In addition, these data have been corroborated manually by fitting Pseudo-Voigt functions to (002), (004), (110) and (220) peaks. A summary of all the data can be found in Table 5.8 and Figure 5.38. It should be noted that in this case, the phase transition has simply been modelled by a marked lengthening of the unit cell axes (primarily the *c*-axis), while maintaining the space group symmetry. This is in accordance with the procedure followed by Liu *et al.* who describe the high-temperature cubic form as a distortion of the original tetragonal cell.[53] The unit cell axes are shown in Figure 5.38 to undergo a thermal expansion of < 1.0% in the temperature range 320 – 550 K; in the high-temperature form, however, the relative expansion between 550 and 575 K *ca* 1.5 times this.

T (K)	a, b (Å)	c (Å)	V (Å^3)	R_p
320	6.1981(7)	7.3810(9)	283.55(9)	0.103
340	6.2062(6)	7.3571(6)	283.38(6)	0.137
360	6.2073(7)	7.3649(6)	283.77(7)	0.187
380	6.2049(7)	7.3723(5)	283.84(6)	0.183
400	6.2076(6)	7.3764(4)	284.25(5)	0.117
420	6.2030(7)	7.3779(4)	283.88(6)	0.195
440	6.2048(7)	7.3837(4)	284.26(6)	0.138
460	6.2066(7)	7.3906(4)	284.70(6)	0.176
480	6.2056(8)	7.4032(9)	285.10(7)	0.243
500	6.2023(6)	7.4071(5)	284.94(6)	0.252
520	6.2087(6)	7.4126(4)	285.74(6)	0.153
540	6.2089(6)	7.4247(4)	286.22(5)	0.135
550	6.2083(5)	7.4378(5)	286.67(5)	0.157
560	6.2094(5)	7.4922(5)	288.87(4)	0.163
565	6.2139(5)	7.5313(7)	290.81(5)	0.196
570	6.2135(5)	7.5569(8)	291.75(5)	0.260
575	6.2220(8)	7.5812(13)	293.50(8)	0.202

Table 5.8 Unit cell parameters (a, c, V) determined by Le Bail refinement of the X-ray powder diffraction patterns. R_p factors are reported in this case since it has not been possible to carry out full-profile refinements of the X-ray powder diffraction patterns collected, resulting in larger than desirable values of χ^2 and hence wR_p.

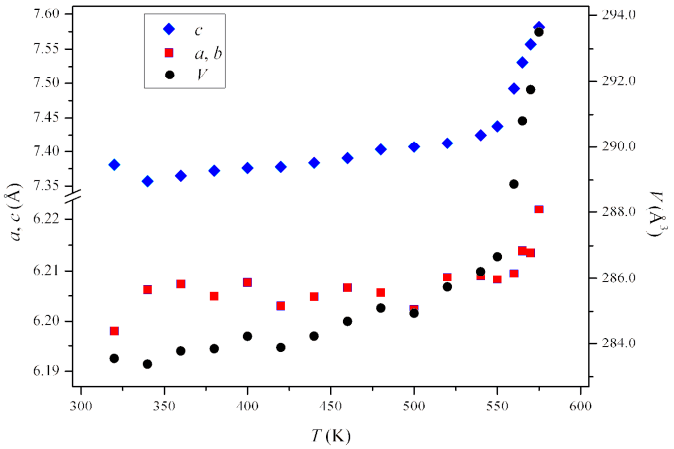

Figure 5.38 Expansion of the unit cell parameters (a, c, V) with temperature, as determined by Le Bail refinement.

A further interesting aspect of this variable temperature study, which may have significant implications for the treatment of the disorder model proposed for this system, is the reduction of the intensities of the (002) and (004) peaks 90 K below the proposed phase transition. Again Pseudo-Voigt functions have been fitted to each peak and their intensities have been normalised to (a) the intensity of each peak at 320 K, and (b) the (112) peak at each temperature, the intensity of which was observed not to vary considerably up to 550 K. A plot of the normalised intensities versus temperature can be found in Figure 5.39, alongside a representation of the diminishing intensity of the (004) peak. It should be noted that the intensity of each peak does not vary significantly upon warming to 460 K, indicating the temperature effect on the diffraction intensities to be negligible. The selective reduction in intensity of some of the Bragg peaks between 460 and 550 K would rather seem to suggest a degree of internal disorder, preceding the phase transition. The exact nature of this disorder is still to be fully explored experimentally. However, the observation that the (002) peak (corresponding to the *hkl* plane, in which half the azide anions are situated) and the (004) peak (affected solely by thallium atoms) are *both* diminished would indicate that the disorder mechanism involves motion of both the anions and the cations.

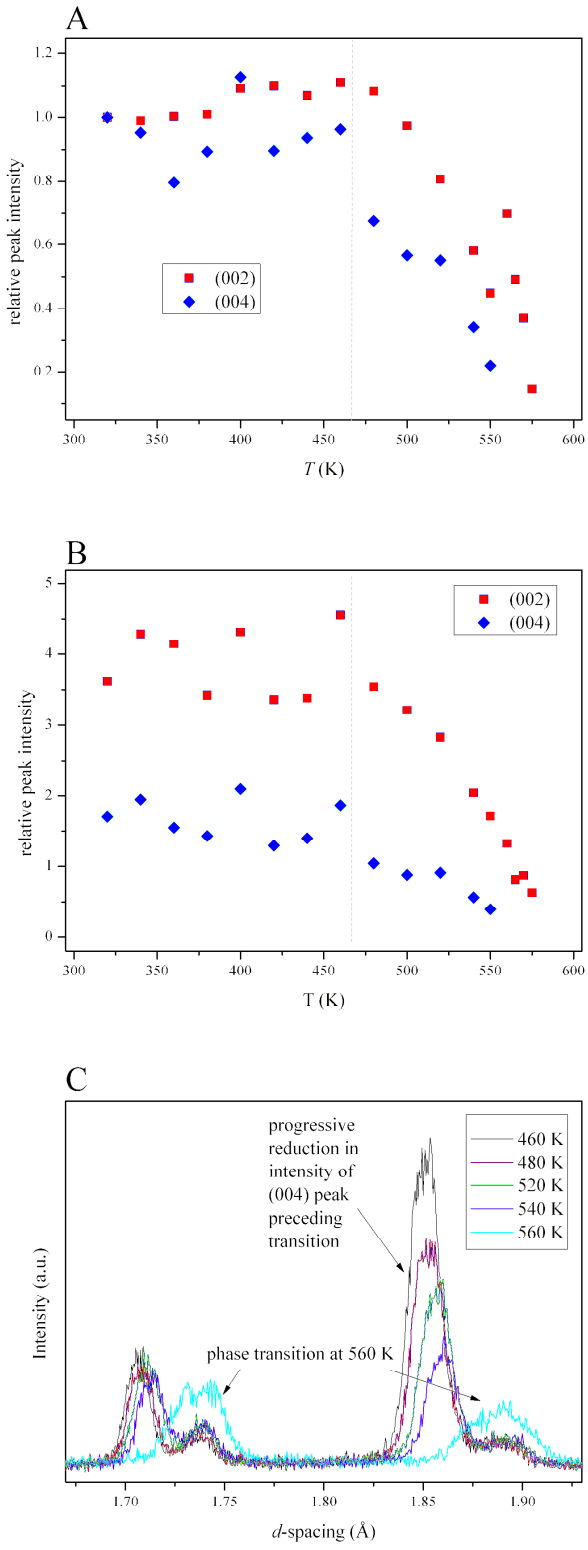

Figure 5.39 Plots of (a) the intensity of the (002) and (004) peaks with respect to their intensities in the 320 K pattern, and (b) the intensity relative to the (112) peak. It should be noted that the (004) peak cannot be distinguished from the background above 550 K. The dashed line represents the temperature at which the disorder is proposed to commence. The reduction in intensity of the (004) on warming is shown in (c) alongside the pattern collected at 560 K, after the phase transition.

Finally in this study, the recoverability of the high-temperature form I was explored by cooling the sample back to 300 K over *ca* 12 hrs. A comparison of the diffraction pattern collected for the recovered phase with those collected at 575 and 320 K is presented in Figure 5.40. In order to ensure that complete transformation to this phase had occurred, additional data collections were performed after 12 and 24 hrs. No significant changes in peak position or intensity were observed over this timeframe. Visual inspection of the diffraction patterns suggests that the recovered pattern shares similarities with both the pattern collected at 320 K (form I) and that collected at 575 K (form II), indicating the presence of either a mixed phase, or perhaps a novel polymorph obtained upon cooling. Unfortunately the low resolution of the diffraction pattern and the unsatisfactory signal-to-noise ratio has meant that it has not been possible to exclude the possibility of sample decomposition at elevated temperatures. Diffraction peaks attributable to the hexagonal ambient temperature form of thallium metal (at d = 2.62, 2.74 and 2.99 Å) are either overlapped by TlN_3 sample peaks or may not be suitably distinguished from the background. High-resolution X-ray powder diffraction on the recovered sample is currently being investigated, with a view to providing conclusive evidence for the presence (or otherwise) of Tl(s) and to allow indexing of the remaining TlN_3 sample.

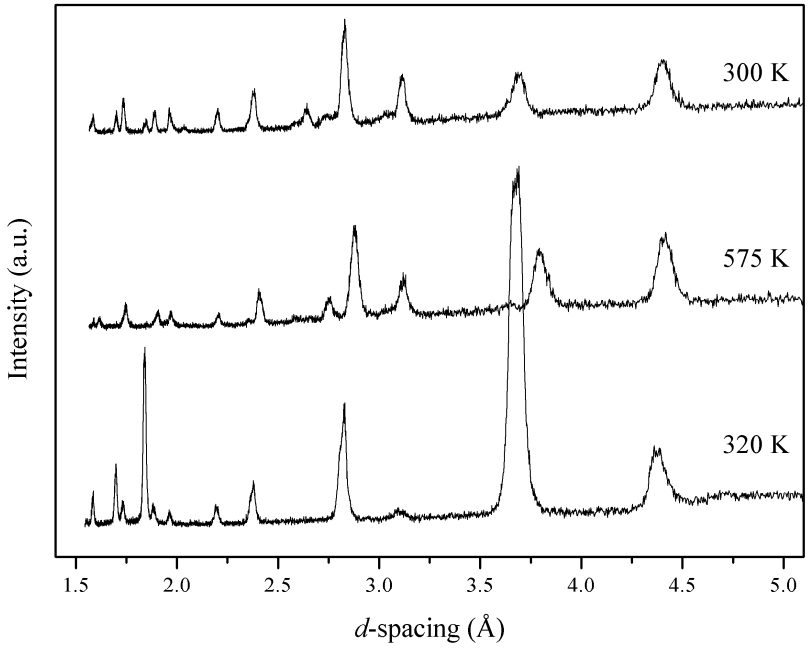

Figure 5.40 Comparison of the X-ray powder diffraction patterns collected at 320 and 575 K, along with the pattern collected for the recovered sample (at 300 K).

Summary: TlN_3

The high-pressure, ambient-temperature behaviour of thallium azide has been investigated by neutron powder diffraction. TlN_3-II has been shown to remain stable upon compression to a maximum of 0.74 GPa: in this region compression is surprisingly isotropic and is not accompanied by any significant rotation of the azide anions. Structure solution of TlN_3-III (*Immm*) has shown that a dramatic re-arrangement of the anions occurs over the II → III transition (at 0.76 GPa). This high-pressure form III has been shown to remain stable up to the maximum pressure studied (6.98 GPa) although the appearance of a new peak in the neutron powder diffraction patterns collected above 3.69 GPa may be indicative of a subtle phase transition at this pressure.

In addition to the high-pressure form III, the structure of the low-temperature form-IV (*Cmcm*) has been determined for the first time. The cell-doubling associated with the phase transition is in accordance with previous experimental data [54, 55], but no significant re-organisation of the anions is observed, on the basis of our X-ray powder diffraction data. Moreover the thallium cations are distributed in a wave-like fashion, similar to TlN_3-III, but in contrast the azide anions deviate significantly from linearity. Neutron powder diffraction experiments are planned to confirm this structural model.

Finally the high-temperature phase transition (II → I) has been shown to occur between 550 and 560 K. This transition temperature is lower than that observed in the only previous experimental report (568 K) [37], although it is possible that Müller and Jöbstl were actually observing partial sample decomposition, which we observe to commence ~ 570 K. The variable temperature X-ray powder diffraction study presented herein has provided experimental evidence to complement the MD simulations reported by Liu *et al.* [53] Both studies indicate that a significant degree of disorder occurs preceding the II → I transition, although neutron diffraction experiments are advised to obtain an accurate description of the atomic thermal motions in this temperature regime.

5.6 Summary and Conclusions

Given the relative structural simplicity of the inorganic azides, particularly the compounds studied in this chapter, the polymorphism they display is remarkable. The fact that each of NaN_3, CsN_3 and TlN_3 have been found to adopt *at least* three different crystal structures at extreme conditions highlights the dramatic effect that even modest pressure (*ca* 0.5 GPa) has on the relative energies of different crystalline systems. These results will therefore be invaluable to solid state chemists and physicists who seek to create accurate computational

models for these systems. Furthermore, it is hoped that the structural characterisation of these materials under a range of pressure and temperature conditions will provide an insight into their energetic performance and may facilitate the rationalisation of their respective sensitivities. The table of structural information for these three compounds has been updated to reflect the advances made in this study. This is presented in Table 5.9 below.

The α-form of sodium azide has been shown to remain stable during compression at ambient temperature. However, the combined effects of temperature and pressure were sufficient to prompt a phase transition to a tetragonal γ-form. Interestingly, this form is isostructural with CsN_3 and RbN_3 and, in this case, one may therefore consider pressure to be acting to force sodium to behave like a larger group 1 element, adopting a larger co-ordination number. Furthermore, the considerable structural re-arrangement required for a $\gamma \rightarrow \alpha$ transition results in significant kinetic barrier to this transition, which is reflected in the observed hysteresis behaviour. Upon complete decompression to ambient pressure, a sample of the α-form was recovered, although considerable crystallographic strain was evident in the neutron powder diffraction pattern. This dramatic reduction in sample quality may have implications for sensitivity, particularly if further phase transitions were to occur at even higher pressures and/or temperatures during detonation events.

The ambient-pressure, high-pressure polymorphism of CsN_3 has been found to be unexpectedly rich – three high-pressure forms have been identified, although only one of these has been structurally characterised. X-ray powder diffraction studies of these high-pressure forms, meanwhile, have been hampered by sample decomposition in the high-energy synchrotron beam. This apparent photolysis at pressure, however, may prove to be an even more exciting prospect since this may present a relatively facile route to highly desirable polynitrogen species. It will therefore be essential to conduct rigorous studies not only to determine the structure of the parent CsN_3 species at extreme conditions but also to characterise the photolysis products and their recoverability.

Finally, the high-pressure and the low-temperature structures (forms III and IV, respectively) of thallium azide have been determined. While the low-temperature phase transition has been observed to involve a simple orthorhombic distortion of the tetragonal TlN_3-II, the $II \rightarrow III$ transition involves a more holistic rearrangement. In addition to these new forms, the high-temperature form I was investigated by X-ray powder diffraction. Although the quality of the diffraction data was not sufficient to allow Rietveld refinement of the structure during warming, striking evidence of a phase transition was observed between 550 and 560 K. Furthermore, it is suggested that the reduction in intensity of select peaks in the diffraction

Polymorph	Space Group	*a* (Å)	*b* (Å)	*c* (Å)	*α* (°)	*β* (°)	*γ* (°)	Atomic positions?	*P*/*T* conditions	Ref.
α-NaN_3	*C*2/*m*	6.1654(5)	3.6350(3)	5.2634(6)	90	107.543(5)	90	Yes	Ambient *P*; *T* < 292 K *P* > 0.07 GPa; Ambient *T*	[25],[39]
β-NaN_3	$R\bar{3}m$	3.646(2)	3.646(2)	15.213(5)	90	90	120	Yes	Ambient *P*; *T* > 292 K	[8]
γ-NaN_3	***I4/mcm***	**5.6114(3)**	**5.6114(3)**	**6.0418(4)**	**90**	**90**	**90**	**Yes**	***P* > 3.12 GPa; *T* > 393 K**	**this study**
CsN_3-I	$Pm\bar{3}m$	4.53(1)	4.53(1)	4.53(1)	90	90	90	No	Ambient *P*; *T* > 424 K	[37]
CsN_3-II	*I*4/*mcm*	6.5412(4)	6.5412(4)	8.0908(5)	90	90	90	Yes	Ambient *P*; *T* < 424 K	[44]
CsN_3-III	***P*2$_1$/*c***	**9.8858(8)**	**6.1327(7)**	**6.2119(10)**	**90**	**120.054(8)**	**90**	**Yes**	**0.54 GPa < *P* < 3.6 GPa; Ambient *T***	**this study**
CsN_3-IV	-	-	-	-	-	-	-	-	**3.6 GPa < *P* < 4.8 GPa; Ambient *T***	**this study**
CsN_3-V	-	-	-	-	-	-	-	-	***P* > 4.8 GPa; Ambient *T***	**this study**
TlN_3-I	$Pm\bar{3}m$	-	-	-	90	90	90	No	Ambient *P*; *T* > 568 K	[37]
TlN_3-II	*I*4/*mcm*	6.208(1)	6.208(1)	7.355(2)	90	90	90	Yes	Ambient *P*; 248 K < *T* < 568 K	[44]
TlN_3-III	***Immm***	**5.8274(6)**	**5.4141(3)**	**8.4670(7)**	**90**	**90**	**90**	**Yes**	***P* > 0.76 GPa; Ambient *T***	**this study**
TlN_3-IV	***Cmcm***	**8.71953(13)**	**7.35130(9)**	**8.75930(13)**	**90**	**90**	**90**	**Yes**	**Ambient *P*; *T* < 235 K**	**this study**

Table 5.9 Structural information for all polymorphs of sodium azide, caesium azide and thallium azide, including the structural data determined in this study (emboldened).

pattern commencing at 460 K is indicative of the initiation of a disorder model although planned neutron powder diffraction studies are expected to elucidate this behaviour.

5.7 Suggestions for Further Work

The X-ray powder diffraction experiments conducted in this work, although instructive, have been hampered by the dominance of the scattering from the heavy metals (Cs and Tl). It has therefore been proposed that variable temperature neutron powder diffraction studies be conducted. This will not only allow the definitive structure solution of the low-temperature form of TlN_3 by the refinement of the nitrogen positions but will also facilitate the thorough examination of the high-temperature behaviour of TlN_3 and CsN_3. It is hoped that it will be possible to characterise any disorder preceding the tetragonal → cubic (II → I) phase transition, as well as obtaining structural data on the high-temperature forms of each compound.

Furthermore, it would be worthwhile re-examining the high-pressure behaviour of TlN_3, in order to determine whether the presence of the additional peak above 3.69 GPa is actually evidence of a further phase transition. Unfortunately, it was not possible to explore the decompression behaviour of TlN_3 and this should therefore be investigated at the earliest possible opportunity. This will provide important information on the recoverability of the high-pressure phase(s) *and* the effect these transitions have on sample quality.

As has been stated above, the opportunity of obtaining polynitrogen species by the photolysis of simple azides at elevated pressures is particularly exciting. The initial focus of these experiments should certainly be the identification and characterisation of the photolysis products, as well as the conditions necessary for photolysis to occur. It is also recommended that such studies should not be limited to CsN_3. While X-ray powder diffraction has been successful in these initial studies, a range of analytical techniques should be explored in future. It is expected that vibrational spectroscopy may be particularly sensitive to the formation of 'non-molecular' nitrogen species, as it will be relatively straightforward to identify any spectral bands that cannot be attributed to the azide anions. Should this method be successful, the focus of these studies will naturally shift to the recovery of these species to ambient conditions.

Finally, it would also be interesting to examine the anomalous compression behaviour of sodium azide at very low pressures. While it is reasonable to suggest that the lengthening of the *b*-axis between 0.0 and 0.5 GPa simply arises due to a particularly anisotropic compression mechanism, such behaviour may also be indicative of a subtle structural

modification. In order to characterise this compression behaviour fully, a gas cell experiment using high-resolution neutron powder diffraction is advised. The gas cell is recommended since it allows the compression to be performed in small, and exact, pressure increments. Meanwhile, the increased resolution of a beamline such as POLARIS (ISIS) would highlight any structural nuances that may not have been detected during the present work.

5.8 References

1. J. Giles, *Nature*, 2004, **427**, 580.
2. M.H.V. Huynh, M.A. Hiskey, T.J. Meyer, and M. Wetzler, *Proc. Nat. Acad. Sci. USA*, 2006, **103**, 5409.
3. E.W. Sidebottom, *US Patent Appl. 05/375,654*, 1973
4. S.M. Peiris and T.P. Russell, *J. Phys. Chem. A*, 2003, **107**, 944.
5. M.I. Eremets, M.Y. Popov, I.A. Trojan, V.N. Denisov, R. Boehler, and R.J. Hemley, *J. Chem. Phys.*, 2004, **120**, 10618.
6. U. Müller, *Strukturchemie der Azide*, in *Structure and Bonding, Inorganic Chemistry, Vol. 14*, 1973, Springer, Berlin/Heidelberg.
7. I.C. Tornieporth-Oetting and T.M. Klapötke, *Angew. Chem. Int. Ed.*, 1995, **34**, 511.
8. G.E. Pringle and D.E. Noakes, *Acta Cryst.*, 1968, **B24**, 262.
9. I.D. Campbell and C.K. Coogan, *J. Chem. Phys.*, 1966, **44**, 2075.
10. M. Cartwright and J. Wilkinson, *Propellants, Explos., Pyrotech.*, 2010, **35**, 326.
11. A.B. Gordienko, Y.N. Zhuravlev, and A.S. Poplavnoi, *Phys. Status Solidi B*, 1996, **198**, 707.
12. A.B. Gordienko and A.S. Poplavnoi, *Russ. Phys. J.*, 2004, **47**, 1056.
13. W. Zhu, J. Xiao, and H. Xiao, *J. Phys. Chem. B*, 2006, **110**, 9856.
14. W. Zhu and H. Xiao, *J. Phys. Chem. B*, 2006, **110**, 18196.
15. W. Zhu and H. Xiao, *J. Comput. Chem.*, 2008, **29**, 176.
16. V. Lisitsyn, Y. Zhuravlev, V. Oleshko, D. Fedorov, and V. Tsipilev, *High Energy Chem.*, 2006, **40**, 218.
17. G.J. Piermarini, *J. Res. Natl. Inst. Stand. Technol.*, 2001, **106**, 889.
18. C.E. Weir, S. Block, and G.J. Piermarini, *J. Chem. Phys.*, 1970, **53**, 4265.
19. S.B. Hendricks and L. Pauling, *J Am. Chem. Soc.*, 1925, **47**, 2904.
20. J.I. Bryant, *J. Chem. Phys.*, 1964, **40**, 3195.
21. C.S. Choi and E. Prince, *J. Chem. Phys.*, 1976, **64**, 4510.
22. E.D. Stevens and H. Hope, *Acta Cryst.*, 1977, **A33**, 723.
23. Z. Iqbal, *J. Chem. Phys.*, 1973, **59**, 1769.
24. B.S. Miller and G.J. King, *J. Chem. Phys.*, 1963, **39**, 2779.
25. S.R. Aghdaee and A.I.M. Rae, *Acta Cryst.*, 1984, **B40**, 214.
26. Z. Iqbal, *Advances in Raman Spectroscopy*, 1972, **1**, 188.
27. J.C. Raich and N.S. Gillis, *J. Chem. Phys.*, 1976, **65**, 2088.
28. J.C. Raich and A. Huller, *J. Chem. Phys.*, 1979, **70**, 3669.
29. R.C. Carling and E.F. Westrum Jnr., *J. Chem. Thermodynamics*, 1976, **8**, 565.
30. S. Hirotsu, M. Miyamota, and K. Ema, *J. Phys. C: Solid State Physics*, 1983, **16**, L661.
31. M. Midorikawa, H. Orihara, Y. Ishibashi, T. Minato, and H. Terauchi, *J. Phys. Soc. Jpn*, 1983, **52**, 3833.
32. S. Hirotsu, *J. Phys. C: Solid State Physics*, 1983, **16**, L1103.
33. K.R. Jeffrey, *J. Chem. Phys.*, 1977, **66**, 4677.
34. S.R. Aghdaee and A.I.M. Rae, *J. Chem. Phys.*, 1983, **79**, 4558.
35. T. Kushida and R.W. Terhune, *Phys. Rev. B: Condens. Matter*, 1986, **34**, 5791.
36. G.J. Simonis and C.E. Hathaway, *Phys. Rev. B: Condens. Matter*, 1974, **10**, 4419.

37. H.J. Müller and J.A. Jöbstl, *Z. Kristallogr.*, 1965, **121**, 385.
38. R.S. Bradley, J.D. Grace, and D.C. Munro, *Z. Kristallogr.*, 1964, **120**, 349.
39. C.W. Christoe and Z. Iqbal, *Chem. Phys. Lett.*, 1976, **39**, 511.
40. K. Knorr and W. Depmeier, *High Pressure Res.*, 2000, **17**, 297
41. C.W.F.T. Pistorius and A.J. Campbell White, *High Temperatures - High Pressures*, 1970, **2**, 507.
42. T.C. Waddington, *J. Chem. Soc*, 1959, 2499.
43. A. Fuith, *Phase Transitions*, 1997, **62**, 1
44. U. Müller, *Z. Anorg. Allg. Chem.*, 1972, **392**, 159.
45. J.I. Bryant, *J. Chem. Phys.*, 1966, **45**, 689.
46. C.E. Hathaway and P.A. Temple, *Phys. Rev. B: Condens. Matter*, 1971, **3**, 3497.
47. Z. Iqbal and C.W. Christoe, *J. Chem. Phys.*, 1975, **62**, 3246.
48. C.W.F.T. Pistorius, *J. Chem. Phys.*, 1969, **51**, 2604.
49. P. da R. Andrade, A.D.P. Rao, R.S. Katiyar, and S.P.S. Porto, *Solid State Commun.*, 1973, **12**, 847.
50. M.M. Ossowski, J.R. Hardy, and R.W. Smith, *Phys. Rev. B: Condens. Matter*, 1999, **60**, 15094.
51. O. Reckeweg and A. Simon, *Z. Naturforsch.*, 2003, **58**, 1097.
52. F.J. Owens, *J. Phys. C: Solid State Physics*, 1979, **12**, 2255.
53. J. Liu, C.G. Duan, M.M. Ossowski, W.N. Mei, R.W. Smith, and J.R. Hardy, *Mater. Res. Bull.*, 2001, **36**, 2035.
54. F.A. Mauer, C.R. Hubbard, and T.A. Hahn, *J. Chem. Phys.*, 1973, **59**, 3770.
55. Z. Iqbal and C.W. Christoe, *Chem. Phys. Lett.*, 1974, **29**, 623.
56. C.W.F.T. Pistorius, *J. Chem. Phys.*, 1974, **60**, 3720.
57. C.W. Christoe and Z. Iqbal, *Solid State Commun.*, 1974, **15**, 859.
58. W.G. Marshall and D.J. Francis, *J. Appl. Crystallogr.*, 2002, **35**, 122.
59. A.D. Fortes, PhD Thesis, 2004, Department of Earth Sciences, University College, London, UK.
60. J.M. Besson, R.J. Nelmes, G. Hamel, J.S. Loveday, G. Weill, and S. Hull, *Physica B*, 1992, **180-181**, 907.
61. R. Von Dreele and A.C. Larson, *General Structure Analysis System (GSAS)*, 1986.
62. W.G. Marshall, D.J. Francis, C.J. Barry, O. Kirichek, C.R. Pulham, and M.G. Tucker, *manuscript in preparation*, 2010.
63. L. Merrill and W.A. Bassett, *Rev. Sci. Instrum.*, 1974, **45**, 290.
64. G.J. Piermarini, S. Block, J.D. Barnett, and R.A. Forman, *J. Appl. Phys.*, 1975, **46**, 2774.
65. A.P. Hammersley, S.O. Svensson, M. Hanfland, A.N. Fitch, and D. Hausermann, *High Press. Res.*, 1996, **14**, 235
66. Bruker-AXS, *D8-Advance*, Madison, WI, USA, 2002.
67. Bruker-AXS, *D8-Advance*, Madison, WI, USA, 2010.
68. J. Cosier and A.M. Glazer, *J. Appl. Crystallogr.*, 1986, **19**, 105.
69. Anton-Paar, *TTK-450*, Graz, Austria, 1998.
70. T. Boffa-Ballaran and R.J. Angel, *Eur. J. Mineral.*, 2003, **15**, 241.
71. F. Birch, *Phys. Rev.*, 1947, **71**, 809.
72. R.J. Angel, *EOS-FIT V5.2*, Department of Geological Sciences, Virginia Tech., Blacksburg, VA, USA, 2001.
73. R.J. Angel, *Equations of State*, in *Reviews in Mineralogy and Geochemistry, 41: High-Temperature and High-Pressure Crystal Chemistry*, R.M. Hazen and R.T. Downs, Editors, 2000, Mineralogical Society of America, Washington, D.C., USA.
74. S.A. Medvedev, I.A. Trojan, M.I. Eremets, T. Palasyuk, T.M. Klapötke, and J. Evers, *J. Phys. Condens. Matter*, 2009, **21**, 195404.
75. H. Spetzler, C.G. Sammis, and R.J. O'Connell, *J. Phys. Chem. Solids*, 1972, **33**, 1727.

76. J.L. Feldman, M.J. Mehl, L.L. Boyer, and N.C. Chen, *Phys. Rev. B*, 1988, **37**, 4784.
77. D. Louër and A. Boultif, *Z. Kristallogr. Suppl.*, 2007, **26**, 191.
78. S. Zhang, H. Li, H. Li, S. Zhou, and X. Cao, *J. Phys. Chem. B*, 2007, **111**, 1304.
79. F.C. Tompkins and D.A. Young, *Proc. R. Soc. London, Ser. A*, 1956, **236**, 10.
80. H.A. Papazian, *J. Phys. Chem. Solids*, 1965, **27**, 906.
81. B.H. Krause, *J. Chem. Phys.*, 1963, **39**, 1706.
82. G.J. King, F.F. Carlson, B.S. Miller, and R.C. McMillan, *J. Chem. Phys.*, 1961, **34**, 1499.
83. Accelrys, *Materials Studio*, Sand Diego, CA, USA, 2010.
84. R. Von Dreele, *personal communication*, 2010.
85. H. Lipson and A.R. Stokes, *Nature*, 1941, **148**, 437.
86. E.G. Ponyatovskii and A.I. Zakharov, *Kristallografiya*, 1962, **7**, 461.

Chapter 6

Structural Investigation of a Series of Inorganic Azides

Part 2: NH_4N_3, AgN_3 and $Pb(N_3)_2$

6 Structural Investigation of a Series of Inorganic Azides (Part 2)

6.1 Polymorphism of the 'More Complex' Inorganic Azides

6.1.1 NH_4N_3

The structure of ammonium azide is also based on a modification of the basic CsCl cubic structure although hydrogen bonding plays a dominant role in the distortion. The azide anions are broadly organised into layers, but half of the anions are rotated out of the plane to allow hydrogen bonding between the ammonium ion and the negative termini of the azide ions. This results in half of the anions lying parallel to the *a*-axis (Type I), while the other half lie perpendicular to *a* (Type II), thus allowing a tetrahedral arrangement of azide termini around a single cation (Figure 6.1).

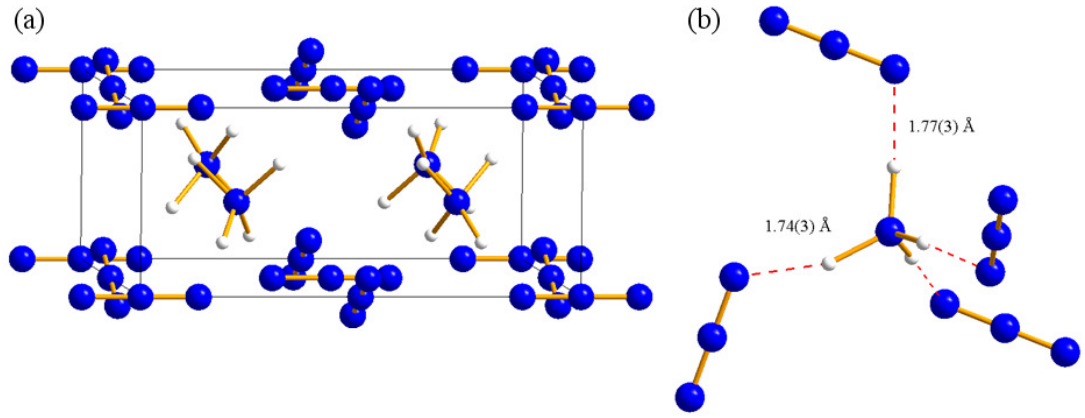

Figure 6.1 (a) Structure of ammonium azide, highlighting the layers of azide anions, in which the anions that are normal to the *a*-axis are rotated out of the *ac*-plane; and, (b) the N-H…N hydrogen bonding interactions.

The space group (*Pmna*) and nitrogen positions were determined in 1936 and from these data it was possible to infer the existence of strong H-bonds and that the ammonium ion adopts a definite orientation at room temperature, which is not spherically averaged.[1] This was subsequently confirmed spectroscopically.[2] A full structural refinement was subsequently performed using single-crystal neutron diffraction.[3] NH_4N_3 has recently been used as a test case for *ab initio* structure solution from X-ray powder diffraction using synchrotron radiation.[4] The authors successfully (re)-determined the structure of this light-atom structure, including hydrogen positions – their structural model was in good agreement with the structure obtained from single-crystal neutron data. Single-crystal X-ray diffraction results published in 2003 were also in accordance with the proposed structure.[5]

Low temperature spectroscopic measurements indicate that no phase transitions occur upon cooling to 68 K [6] and thermal analysis up to the sublimation point (408 K) showed no anomalies indicative of a phase transition to a high-temperature form.[7] No variable pressure studies have ever been reported in the open literature. This study therefore aims to be the first such investigation and uses neutron powder diffraction to characterise the compression behaviour of ND_4N_3 to a maximum pressure of 4.9 GPa.

6.1.2 AgN_3

Silver azide may be regarded as an intermediary between the ionic azides described above and the co-ordinative azides of other heavy metals (such as copper and lead).[8] In common with the ionic azides, the unit cell is based on the CsCl cubic structure and the N_3^- ions are linear and symmetric. In fact, the orthorhombic (*Ibam*) structure adopted at ambient temperature and pressure is in many regards consistent with the tetragonal structure found in CsN_3 and TlN_3, although a lengthening of the crystallographic *b*-axis reduces the symmetry to an orthorhombic cell.[9-12] This leads to a significant change in the environment of the Ag^+ cations: instead of the square anti-prism found in CsN_3, the orthorhombic distortion means that four of the terminal N-atoms are moved closer to the silver ions, resulting in two different Ag-N interactions. This gives rise to a distorted tetrahedral primary co-ordination environment around each cation formed by the azide termini within the same layer, while secondary Ag-N interactions exist between the layers (see Figure 6.2). The reduction in symmetry and the two crystallographically distinct N_3^- anions are reflected in the vibrational spectra: more vibrational modes are evident for AgN_3 than for the tetragonal forms of CsN_3 and TlN_3.[13, 14]

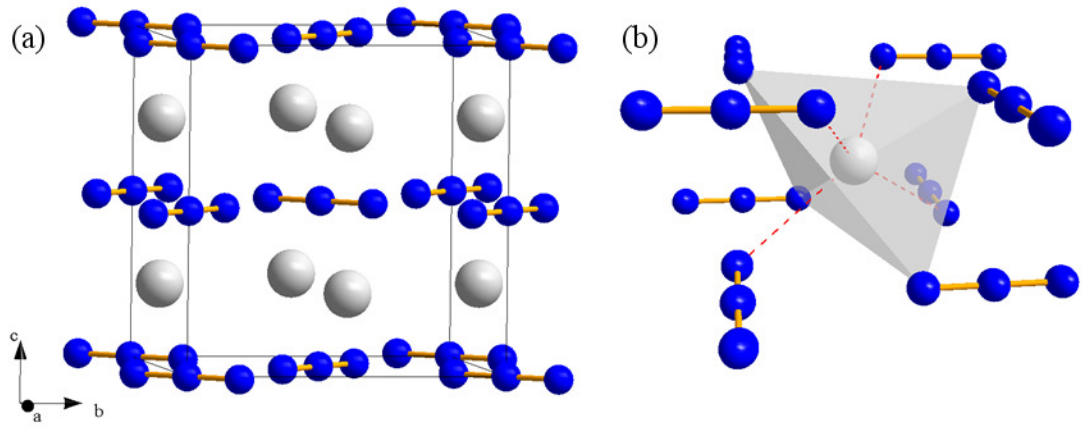

Figure 6.2 (a) Crystal packing in AgN_3 showing the similarity with the *I*4/*mcm* structures of CsN_3-II and TlN_3-II; and, (b) the cationic co-ordination environment – the primary 'tetrahedral' environment is shown in grey, while secondary Ag-N interactions are in red.

Raman studies of silver azide down to 10 K have shown that there is no phase transition to a low-temperature phase over this temperature range.[15] Warming to a maximum temperature of 443 K, however, results in a very sluggish phase transition to a monoclinic ($P2_1/c$) form that can be recovered to room temperature, as characterised by X-ray powder diffraction.[16] In this high-temperature form, the silver cation is surrounded by four nitrogen termini within the same layer (at distances ranging from 2.32 to 2.47 Å) in a distorted square geometry. Two further interactions (2.72 and 3.00 Å) with the azide groups above and below the plane of this layer give rise to a highly distorted 4 + 2 octahedral co-ordination environment (Figure 6.3). It is interesting to note that this phase transition is irreversible and that the high-temperature form is retained even after annealing the sample at 423 K.[16] This prompted the authors to perform density functional theory (DFT) calculations on both this form and the room temperature polymorph. Both represented minima on the calculated energy surface although it was not possible to determine which structure represented the global minimum.

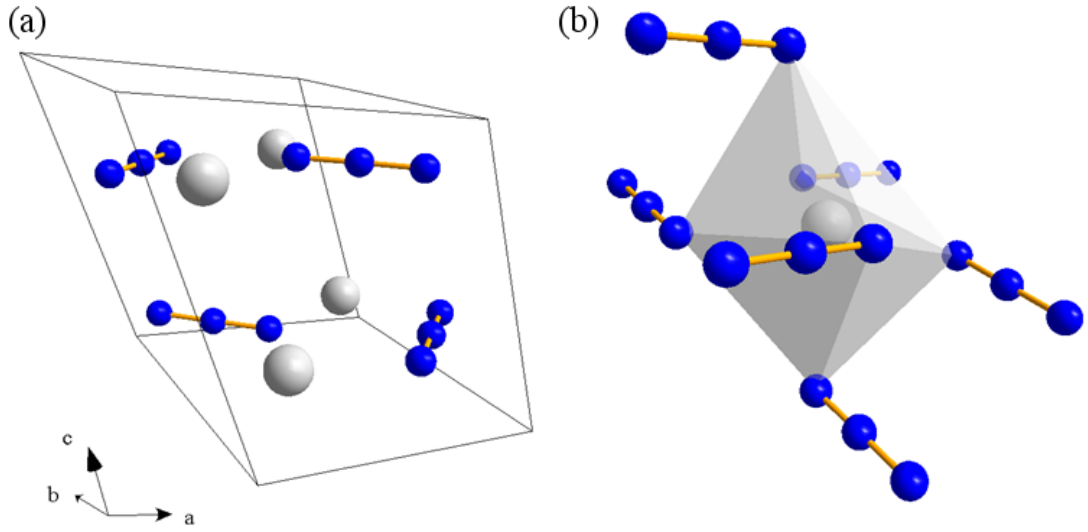

Figure 6.3 High-temperature modification of silver azide: (a) the crystal packing, and (b) the 4 + 2 co-ordination environment of the silver.

Experimental studies of the high-pressure behaviour of silver azide have been limited to a maximum pressure of 0.4 GPa – no evidence of a phase transition is observed from electrical conductivity [17] or spectroscopic measurements.[18] A DFT study on the structural and vibrational properties of AgN_3 under high pressure indicated the presence of an energetically favourable high-pressure phase above 7.0 GPa.[19] This high-pressure phase is predicted to adopt the tetragonal $I4/mcm$ symmetry of the CsN_3 and TlN_3 at ambient pressure and is considered to remain stable under hydrostatic compression to the limit of the study (500 GPa). No experimental study of silver azide has ever been undertaken in this pressure range and it was therefore a primary aim of the current work to obtain experimental evidence to

complement the theoretical predictions. Moreover the stability of the 'high-temperature form' at room temperature presents further evidence of the possibility of using a thermodynamic variable (such as temperature or, as reported herein, pressure) to obtain new materials that may be recovered to ambient conditions. This provided further motivation to investigate the high-pressure behaviour of silver azide.

6.1.3 $Pb(N_3)_2$

Four polymorphs of lead (II) azide have been identified, although only α-$Pb(N_3)_2$ has been thoroughly investigated crystallographically. The crystallisation of a monoclinic γ-form and a triclinic δ-form is reported to be favoured by low pH and/or the presence of additives such as polyvinyl alcohol. Both can be isolated as single crystals although no structural information (beyond tentative unit cell parameters) is available in the open literature.[20] Crystals of the monoclinic β-form, crystallised from aqueous solutions containing additives such as dextrin or by slow diffusion, are sufficiently metastable at ambient temperature such that they remain unchanged for years and may even be heated (473 K) for short periods with no obvious change. [21] However, the presence of small crystals of the more stable α-form results in a rapid solvent-mediated transition.[22] Detailed crystallographic investigations on β-$Pb(N_3)_2$ have been hampered by the tendency for spontaneous detonation during crystallisation.[23] As a result of the difficulties in growing single crystals of the different polymorphs, only the α-form has been structurally characterised.

The unit cell of the α-form was first determined by X-ray diffraction, although space group assignment was based primarily on the positions of the lead atoms.[21, 24, 25] In order to determine the atomic co-ordinates of the nitrogens accurately, and therefore to obtain an unambiguous space group, it was necessary to utilise neutron diffraction.[26-28] α-$Pb(N_3)_2$ crystallises in orthorhombic symmetry (*Pnma*) with four crystallographically distinct azide groups, all of which are distorted from the linear, symmetric configuration found in the ionic azides above. This is reflected in the complicated vibrational spectra, with numerous modes attributed to the different azide units.[14, 29] Bond lengths and angles within each of the azide groups and distances to the neighbouring Pb atoms are summarised in Figure 6.4.

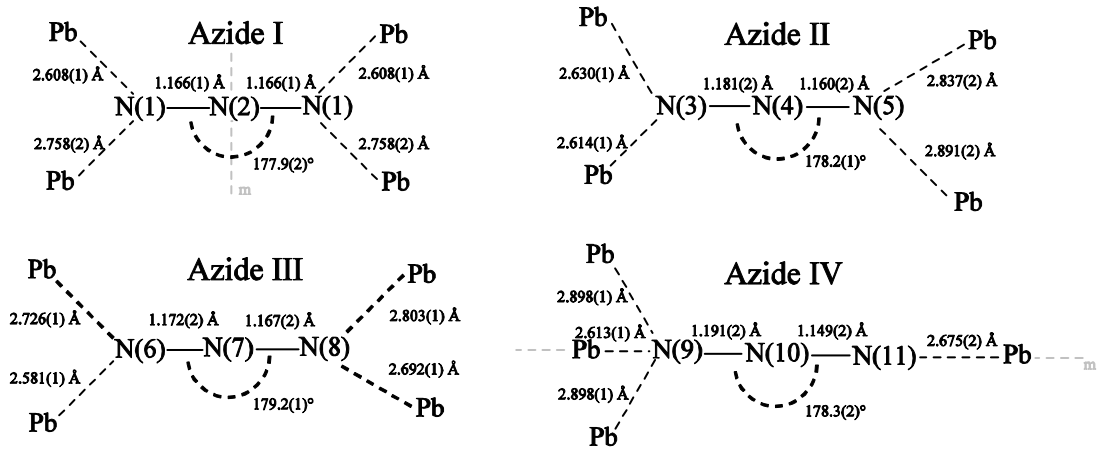

Figure 6.4 The four independent azide groups within α-$Pb(N_3)_2$ and their immediate Pb environment, as determined by Choi *et al.*[28] Azide I is situated over a mirror plane perpendicular to the N-N bonds, while IV occupies a mirror plane along with two Pb. The mirror planes are denoted m in the above scheme.

As illustrated in Figure 6.4, all of the azide groups are slightly bent and are asymmetric with the exception of azide I, which is situated across a mirror plane. Moreover the distortions within the azide groups are reflected in the Pb…N distances: the terminal nitrogen of the shortest N-N bond is in contact with only one neighbouring lead atom, while the other end of this azide group (with the longest N-N distance) is in close proximity to three Pb atoms. The asymmetric bonding within the azide groups and the related variation in Pb…N distances have been rationalised in terms of a degree of covalency between the metal and the azide groups.[28, 30]

Examination of the crystal packing shows that the azide ions arrange themselves into layers perpendicular to the crystallographic *c*-axis, with Pb atoms separating the layers. Azide types I and II occupy one sheet while the other is composed of azide types III and IV. Mauer *et al.* subsequently used this approach to explain the significant anisotropy in the thermal expansion of α-$Pb(N_3)_2$.[31] Over the temperature range 102 – 423 K, the linear expansion of the *c*-axis was found to be ~20 times that for the *b*-axis and four times that of the *a*-axis. They note that expansion in the direction normal to the azide layers would be expected to be larger than expansion within the layers, which would have to occur by either rotation or elongation of the individual azides. Weir *et al.* also note that the *c*-axis is the most compressible in α-$Pb(N_3)_2$ to a maximum pressure of 2.2 GPa.[32] It is important to note that neither group observed any phase transitions, although no structural refinements have been performed for $Pb(N_3)_2$ under extreme conditions.

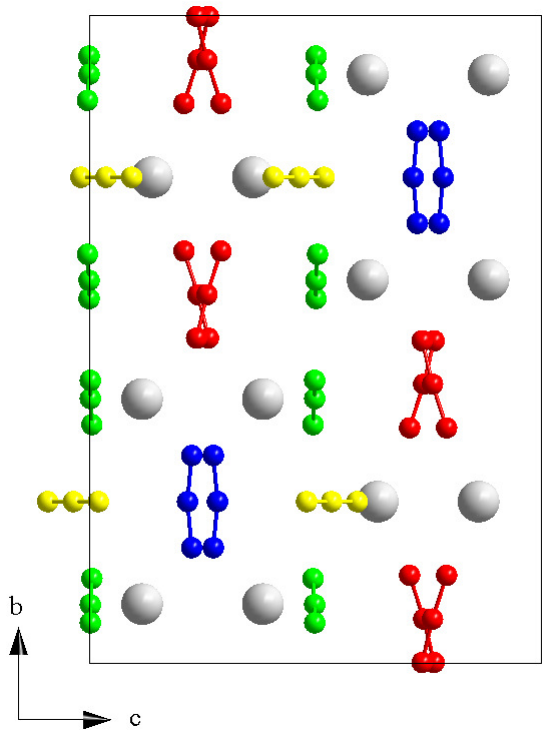

Figure 6.5 Crystal packing of α-$Pb(N_3)_2$, in which each independent azide group is clearly distinguished: Type I (blue), Type II (red), Type III (green) and Type IV (blue).

It was therefore proposed to obtain high quality neutron powder diffraction data during the compression of α-$Pb(N_3)_2$ to a maximum pressure of 5.74 GPa in order to understand qualitatively the compression mechanism, to obtain an equation of state for this material (for comparison with *ab initio* calculations [33]) and to investigate any new high-pressure forms.

6.2 Aims

Reference to Table 6.1 not only shows the structural variety of these compounds under ambient conditions, but also highlights the lack of structural information under extreme conditions, particularly at elevated pressures. The aim of the current study is therefore to explore the effect of high pressure on ammonium azide, silver azide and lead(II) azide by neutron powder diffraction. The results of these studies will provide valuable information on the compressibilities of these materials, as well as identifying and characterising any high-pressure polymorphs that may be obtained.

Polymorph	Space Group	*a* (Å)	*b* (Å)	*c* (Å)	*α* (°)	*β* (°)	*γ* (°)	Atomic positions?	*P*/*T* conditions	Ref.
NH_4N_3	*Pmna*	8.948(3)	3.808(2)	8.659(3)	90	90	90	Yes	Ambient *P*/*T*	[3]
α-AgN_3	*Ibam*	5.600(1)	5.980(6)	5.998(1)	90	90	90	Yes	Ambient *P*; *T* < 443 K	[11]
β-AgN_3	$P2_1/c$	6.0756(2)	6.1663(2)	6.5729(2)	90	114.19(0)	90	Yes	Ambient *P*; *T* > 443 K Recovered to ambient *P*/*T*	[16]
α-$Pb(N_3)_2$	*Pnma*	6.63	16.25	11.31	90	90	90	Yes	Ambient *P*/*T*	[24],[28]
β-$Pb(N_3)_2$	-	18.31	8.88	5.12	90	107.5	90	No	Ambient *P*/*T*	[22]
γ-$Pb(N_3)_2$	-	12.060	10.507	6.505	90	95.75	90	No	Ambient *P*/*T*; low pH/additives	[20]
δ-$Pb(N_3)_2$	-	13.163	10.532	6.531	90.53	98.12	112.67	No	Ambient *P*/*T*; low pH/additives	[20]

Table 6.1 Structural information for all polymorphs of the inorganic azides (where no esd is tabulated, no values were given in the primary literature).

6.3 Experimental

6.3.1 Materials

Due to concerns over their sensitivity to detonation, samples (*ca* 100 mg) of AgN_3 and $Pb(N_3)_2$ were prepared at the ISIS Neutron and Muon Source immediately prior to the high-pressure neutron diffraction experiments. AgN_3 was prepared by mixing equimolar solutions of silver nitrate and sodium azide at room temperature and subsequent washing with deionised water. Lead(II) azide was produced by the solution-phase reaction of $Pb(NO_3)_2$ and NaN_3 (purchased from Sigma-Aldrich, 99.5% purity). NH_4N_3 was prepared by the metathetic reaction of ammonium chloride and sodium azide as reported by Richter.[34] Equimolar amounts of NH_4Cl and NaN_3 were distilled with a small quantity of water; the product NH_4N_3 volatised at 433 K with water vapour and solidified in the condenser tube. Recovery of small crystallites of NH_4N_3 was complicated by its propensity to deliquesce at room temperature – the pure product was precipitated from aqueous solution at ~ 278 K and removed to a desiccator for storage. ND_4N_3 for neutron powder diffraction was prepared by the analogous reaction of ND_4Cl and NaN_3 (in D_2O) by Dr P. Szilagyi (School of Chemistry, University of Edinburgh).

Sample purity was confirmed by neutron powder diffraction at minimal sample pressure for AgN_3, $Pb(N_3)_2$ and ND_4N_3.

6.3.2 High-Pressure Neutron Powder Diffraction

High-pressure neutron powder diffraction data were collected using the PEARL/HiPr diffractometer at the UK spallation neutron source, ISIS, at the STFC Rutherford Appleton Laboratory. Polycrystalline samples of each compound under investigation (ND_4N_3, AgN_3 and $Pb(N_3)_2$) were loaded, in turn, into an encapsulated TiZr gasket [35] with perdeuterated methanol:ethanol (4:1) as pressure-transmitting medium and Pb as pressure calibrant.[36] The capsule assembly was then compressed with a type V3b Paris-Edinburgh (P-E) press equipped with standard single toroid anvils with cemented WC cores (Ni binder).[37] The P-E press ram pressure was monitored and varied by means of a computer-controlled hydraulic system.

Time-of-flight (ToF) neutron powder diffraction data were collected using the $2\theta = 90°$ detectors with a transverse (through-anvil) scattering geometry. The resulting summed pattern was then normalised with respect to the incident beam monitor and the scattering from a standard vanadium calibration sample. Lastly, the diffraction pattern intensity scale was corrected for the wavelength and scattering-angle dependence of the neutron attenuation

by the anvil (WC) and gasket (TiZr) materials. Full-profile Rietveld refinements of the ToF neutron powder diffraction patterns were carried out using the GSAS package, in which a convolution of Gaussian (with coefficient σ_1) and Lorentzian (γ_1) functions was used to describe peak profiles (GSAS ToF profile 3).[38] Details of any restraints applied (when necessary) during refinement will be outlined in the relevant sections below.

6.4 Results and Discussion

6.4.1 NH_4N_3

High-Pressure Neutron Diffraction Study of ND_4N_3

In the first ever such study, the high-pressure polymorphism of ND_4N_3 was investigated by neutron powder diffraction to a maximum pressure of 4.9 GPa. The diffraction patterns collected during this experiment are presented in Figure 6.6. In order to ensure sample purity it was necessary to collect a diffraction pattern at low initial load (6 tns, sample pressure = 0.07 GPa). Full-profile Rietveld refinement confirmed the orthorhombic structure and the data were of such high quality (after 2 hours exposure) that it was possible to refine the thermal parameters of the deuterium atoms anisotropically. Figure 6.7 shows how the thermal ellipsoids of two of the deuteriums are elongated along the direction of the hydrogen bonds to the nearest azide anions, while the longest axis in the ellipsoids of the other two are normal to their hydrogen bonds. This results in a scissor-type motion of the tetrahedral cations. As has been observed in previous studies, the tetrahedra do not rotate freely about their positions in the lattice.

Shorter data collection times were utilised in later runs in order to maximise the pressure range studied; thermal parameters at these pressures were therefore refined isotropically. As is evident from Figure 6.6, the α-form remains stable upon compression to 2.39 GPa, but at the next pressure (2.6 GPa) the diffraction pattern changes dramatically. This pattern persisted to the highest pressure studied (4.9 GPa). It should be noted that, since it has not been possible to carry out Rietveld refinements of the patterns collected for this high-pressure β-form, pressures have been determined using estimations of the *d*-spacings of the Pb (200) and (111) peaks and will therefore have a larger error associated with them.

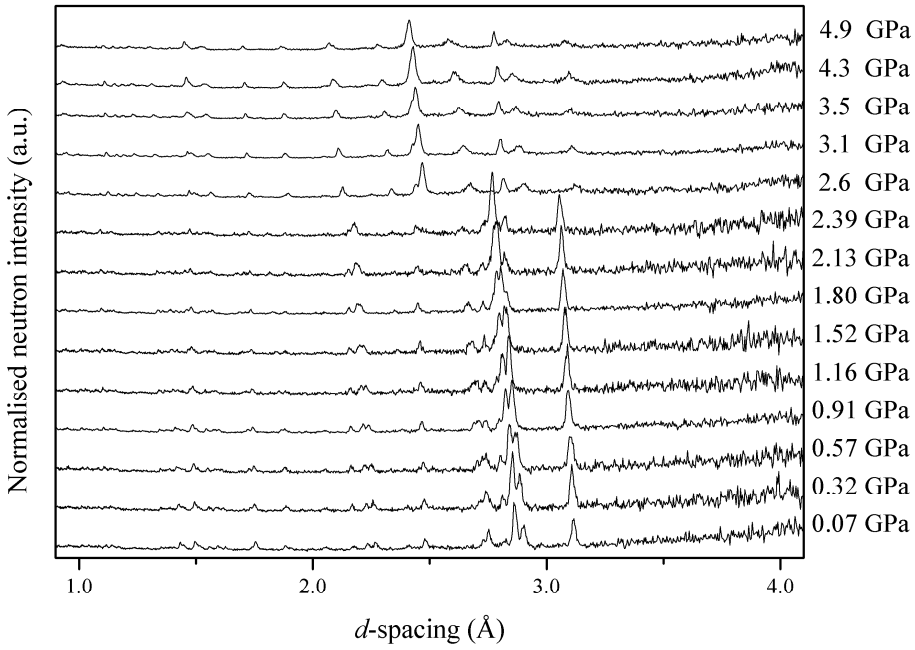

Figure 6.6 Multiplot of the neutron powder diffraction patterns collected for ND_4N_3. Since it has not been possible to perform full-profile Rietveld refinements on the patterns collected for the high-pressure β-form, pressures have been estimated based on the position of the Pb (002) and (111) peaks.

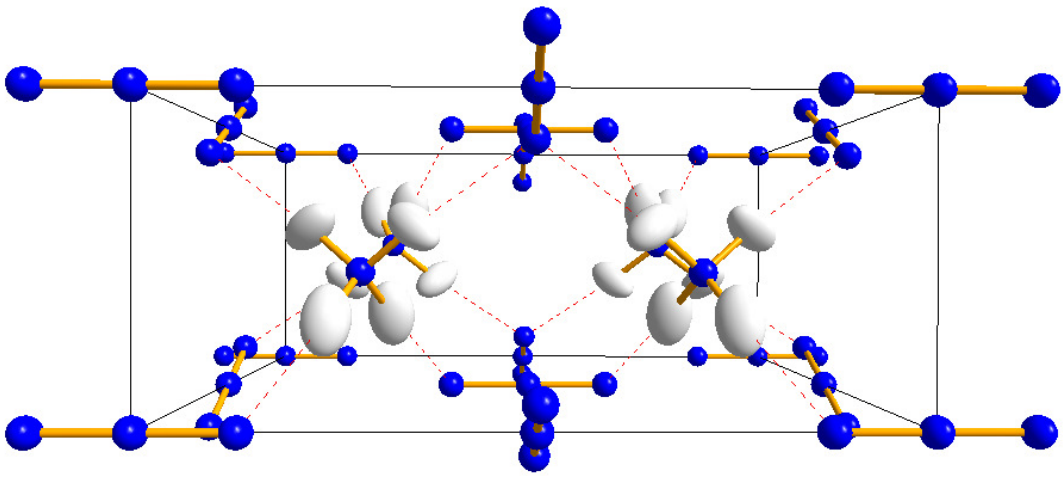

Figure 6.7 Crystal structure of ND_4N_3 at 0.07 GPa, in which the anisotropic displacement parameters of the deuterium atoms have been shown (50 % level). The thermal parameters of the nitrogen atoms were refined isotropically.

The unit cell parameters determined during the compression of α-ND_4N_3 have been tabulated in Table 6.2 and are presented graphically in Figure 6.8. The relative compressibilities of the unit cell axes are also presented. This shows that the *c*-axis is the least compressible, while the *b*-axis is the most compressible. Both of these features may be explained by a

compression mechanism which involves the rotation of the azide anions that lie normal to the *a*-axis (Type II). During the compression of α-ND_4N_3 these azides become more parallel with the *c*-axis: this would therefore counter the effects of pressure on the *c*-axis while also explaining the more rapid decrease in the *b*-axis as the wave-like planes of N_3^- anions flatten out. The rotation of these azides with respect to the *c*-axis is plotted in Figure 6.9. Compression along the *a*-axis would increase the interactions between the terminal N-atoms of Type I azides and the central N-atom of Type II, but this is balanced by repulsion between the tetrahedral cations. It is also interesting to note that during compression the central nitrogen atoms of the NH_4^+ ions become more eclipsed; using the *ac*-plane as reference, the degree of stagger has been calculated at each pressure and is plotted in Figure 6.10.

P (GPa)	*a* (Å)	*b* (Å)	*c* (Å)	*V* (Å^3)	wR_p
0.07	8.9282(18)	3.8033(8)	8.6646(19)	294.22(7)	0.065
0.32	8.9052(18)	3.7764(8)	8.6510(19)	290.93(7)	0.121
0.57	8.8745(18)	3.7530(7)	8.6405(18)	287.78(7)	0.109
0.91	8.8421(12)	3.7242(5)	8.6231(12)	283.96(5)	0.071
1.16	8.8118(19)	3.6964(8)	8.6142(18)	280.58(8)	0.138
1.52	8.7797(19)	3.6713(8)	8.6056(18)	277.39(8)	0.152
1.80	8.7454(11)	3.6474(5)	8.5924(11)	274.08(5)	0.089
2.13	8.7093(18)	3.6219(7)	8.5883(17)	270.91(7)	0.220
2.39	8.6517(20)	3.5954(7)	8.5969(20)	267.42(7)	0.173

Table 6.2 Unit cell parameters obtained during the compression of α-ND_4N_3.

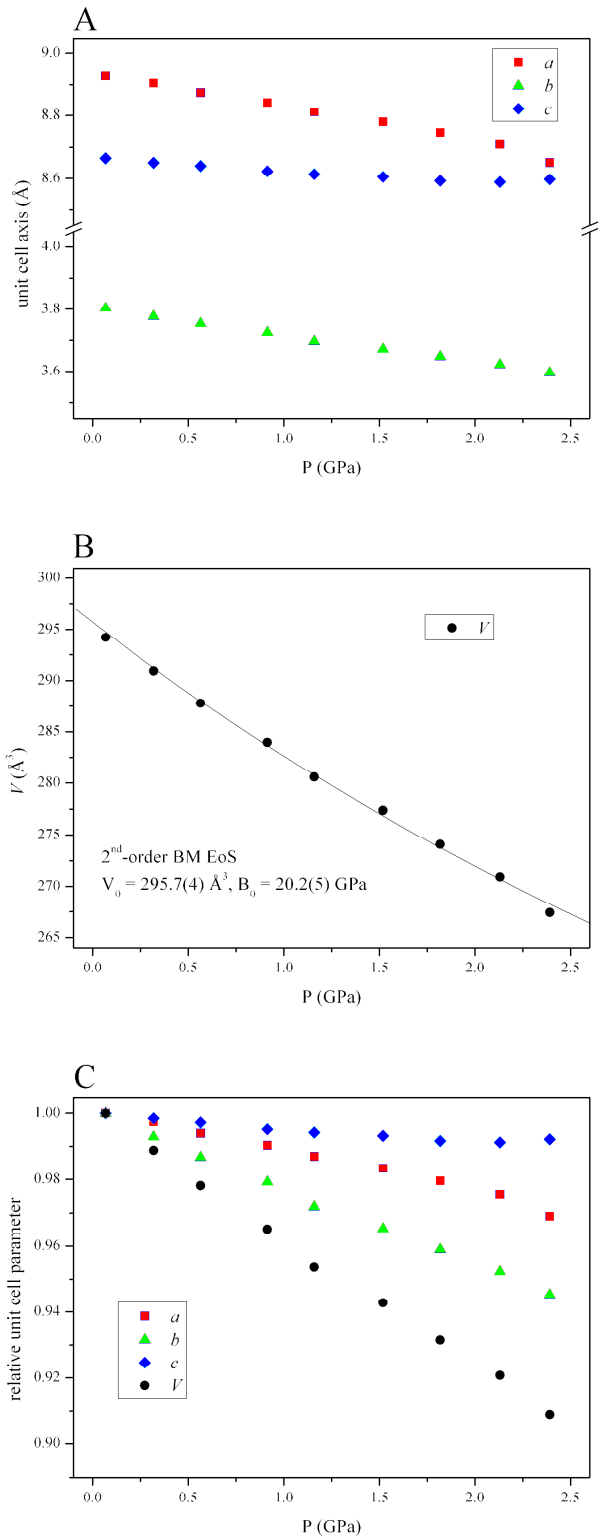

Figure 6.8 (a) Contraction of the unit cell parameters of α-ND_4N_3 indicating that the *a*- and *c*-axes become more equivalent at higher pressures; (b) the 2nd-order Birch-Murnaghan *PV*-plot for compression of α-ND_4N_3; and, (c) the relative contraction of the unit cell parameters.

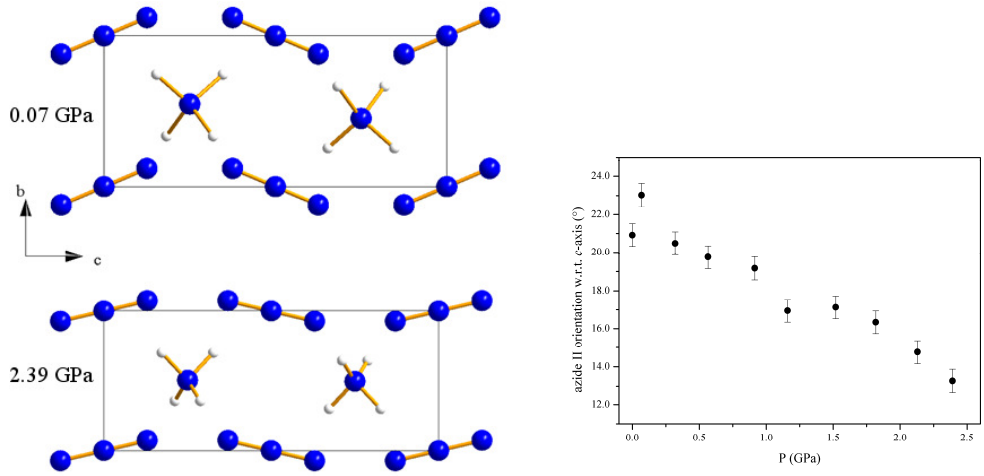

Figure 6.9 (a) Rotation of azide (Type II) w.r.t. *c*-axis between 0.07 and 2.39 GPa. This has been represented graphically in (b) [e.s.d. = 0.6°].

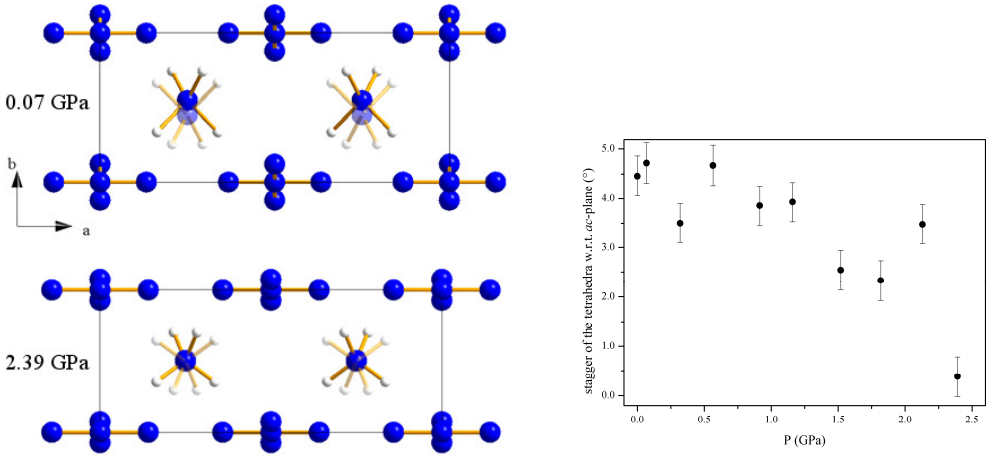

Figure 6.10 (a) Stagger of tetrahedral cations – the foremost tetrahedra have been lightened to allow them to be distinguished. This gradual reduction in the tetrahedral stagger during compression has also been represented graphically in (b) [e.s.d. = 0.4°].

Data-points in the plot of the normalised pressure (F_E) against Eulerian strain (f_E) were found to lie on a horizontal line indicating that the compression of unit cell volume would be adequately described by a 2nd-order Birch-Murnaghan EoS.[39] The coefficient were calculated to be: V_0 = 295.7(4) Å^3 and B_0 = 20.2(5) GPa and are in good agreement with the experimentally determined volume at ambient pressure (295.05 Å^3) [3] and the intercept of the *Ff*-plot (19.7).

The dramatic change in the neutron powder diffraction patterns upon increasing sample pressure from 2.39 GPa to 2.6 GPa was indicative of a phase transition. This new β-ND_4N_3 was then compressed to a maximum pressure of 4.9 GPa; no further phase transitions were

observed. Moreover this high-pressure polymorph was observed to persist during decompression to 2.1 GPa, *i.e.* below the upstroke transition pressure; the sample was observed to have transformed to the α-form at 1.52 GPa.

Unfortunately it has not been possible to obtain an unambiguous indexing for the high-pressure β-form. It should be noted that, despite the apparent convergence of the unit cell a- and *c*-axis during compression of the α-form, Le Bail refinement of the patterns collected for the high-pressure form indicates that this transition does not appear to result in a tetragonal unit cell. The process of obtaining unambiguous unit cell indexings is complicated based on neutron powder diffraction patterns due to the limited range of *d*-spacing accessible and the overlap of sample peaks with peaks due to the Pb pressure calibrant and WC and Ni from the PE-press anvils. An analogous powder diffraction study using synchrotron radiation is therefore planned to obtain complementary data on this high-pressure phase. It is also hoped that single crystals of this material are sufficiently stable under ambient conditions to permit their loading into a diamond-anvil cell for X-ray single-crystal diffraction experiments. Moreover, an X-ray study on the hydrogenous material would also highlight any deuteration effects on the transition pressure or compression mechanism.

Summary: ND_4N_3

The structure of ammonium azide has been investigated under high pressure. The compression of the α-form, which remains stable to a pressure of 2.39 GPa, is characterised by a rotation of half of the azide anions and an alignment of the tetrahedral cations. The β-form, which is still to be structurally characterised, remains stable to the maximum pressure studied (4.9 GPa) and displays hysteresis during decompression. Complementary X-ray powder diffraction studies on the hydrogenous material are planned and the possibility of loading single crystals of NH_4N_3 into a diamond-anvil cell for high-pressure single-crystal X-ray diffraction is currently being explored.

6.4.2 AgN_3

The interesting polymorphism of silver azide at high temperature (and the recovery of this high-temperature form to ambient pressure) motivated the study of this material at high pressure by means of neutron powder diffraction. A freshly prepared sample of AgN_3 was therefore compressed to a maximum of 5.17 GPa, which was sufficient pressure to induce a phase transition (observed at 0.80 GPa). This is in contrast to theoretical predictions of the same phase transition occurring at 7.0 GPa.[19] A multiplot of the neutron powder diffraction patterns collected throughout this study is shown in Figure 6.11.

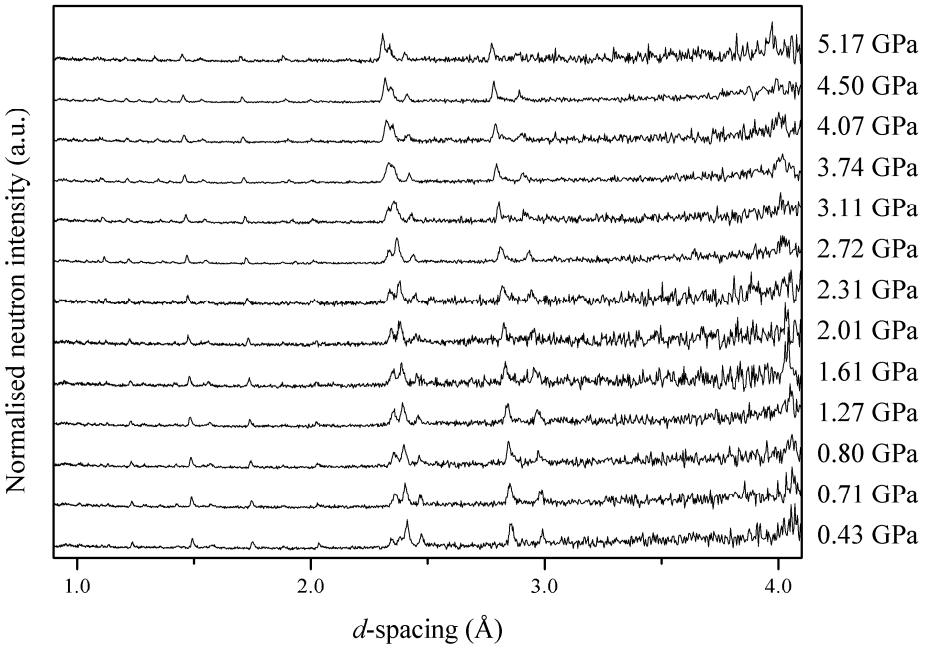

Figure 6.11 Multiplot of the neutron powder diffraction patterns collected during the compression of AgN_3.

Using the ambient pressure α-structure (orthorhombic, *Ibam*) it was possible to carry out full-profile Rietveld refinements on the patterns collected at 0.43 and 0.71 GPa. In order to assess the compression of this phase fully, these data are presented along with the ambient pressure unit cell parameters reported by Guo *et al*. in Table 6.3. This clearly shows that, while the orthorhombic *c*-axis shows limited compressibility (~1%), the *b*-axis shortens dramatically (~4%) and the *a*-axis actually lengthens. The contraction of the *b*-axis may be rationalised in terms of a shortening of the interplanar distance, which one would expect to be more compressible than either of the intraplanar axes. Interestingly, however, the expansion along *a* is not due to any rotation of the azide anions; the angle between the long axis of the azide and the *a*-axis does not change significantly in this pressure region. The relative change in the unit cell parameters, however, does result in a change in the co-ordination of the silver cations. Rather than there being two very distinct Ag-N distances, as in the ambient pressure structure, by 0.71 GPa the silver co-ordination sphere becomes almost, but not quite, a perfect square antiprism. The interplanar distance shortens from 2.80 Å at 0.0 GPa to 2.69 Å at 0.71 GPa; the intraplanar distance meanwhile increases from 2.56 to 2.62 Å.

P (GPa)	a (Å)	b (Å)	c (Å)	V (Å^3)	wR_p
0.00	5.600(1)	5.980(6)	5.998(1)	200.86(20)	Ref. [11]
0.43	5.659(2)	5.830(3)	5.9701(13)	196.95(8)	0.114
0.71	5.704(3)	5.760(3)	5.9512(14)	195.52(8)	0.118

Table 6.3 Unit cell parameters obtained during compression of α-AgN_3, presented alongside literature values obtained at ambient pressure (293 K).

This continuing distortion, or rather removal of an orthorhombic distortion, by the application of pressure eventually results in a phase transition to the tetragonal structure of γ-AgN_3 (*I*4/*mcm*). This structure is analogous to the structures adopted by CsN_3 and TlN_3 at ambient conditions and NaN_3 at elevated temperatures and pressures. It was therefore relatively straightforward to perform Rietveld refinements on all of the diffraction patterns collected for this form, up to a maximum pressure of 5.17 GPa. The unit cell parameters obtained during these refinements are presented in Table 6.4 and Figure 6.12.

P (GPa)	a, b (Å)	c (Å)	V (Å^3)	wR_p
0.80	5.7239(11)	5.9338(14)	194.41(7)	0.110
1.27	5.7146(11)	5.9231(14)	193.43(7)	0.106
1.61	5.7087(17)	5.9026(20)	192.36(11)	0.310
2.01	5.6965(15)	5.8818(20)	190.86(9)	0.223
2.31	5.6885(17)	5.8727(20)	190.03(11)	0.306
2.72	5.6804(12)	5.8483(15)	188.71(8)	0.109
3.11	5.6714(13)	5.8183(16)	187.14(8)	0.165
3.74	5.6637(13)	5.7936(17)	185.84(9)	0.120
4.07	5.6565(14)	5.7820(18)	185.00(9)	0.162
4.50	5.6431(9)	5.7695(13)	183.73(6)	0.130
5.17	5.6191(15)	5.7509(19)	181.58(10)	0.271

Table 6.4 Unit cell parameters during compression of γ-AgN_3

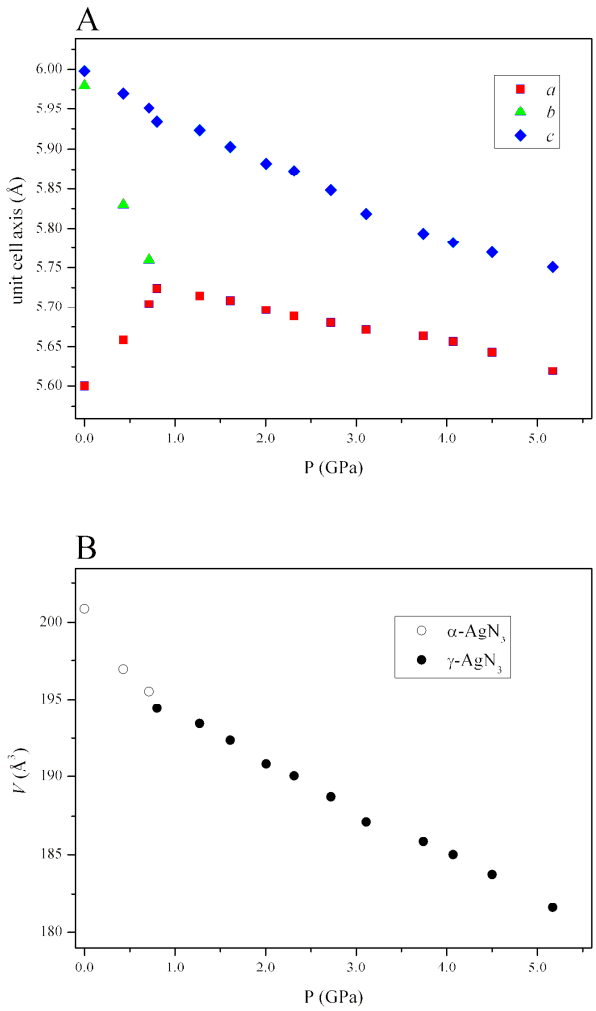

Figure 6.12 (a) Variation of the unit cell parameters throughout compression, highlighting the orthorhombic/tetragonal transition at 0.80 GPa; and, (b) compression of the unit cell volume across the α → γ transition.

As in the other tetragonal azides, the Ag^+ and N_3^- ions are arranged in layers normal to the *c*-axis; within these layers the azide ions lie perpendicular to their nearest neighbours. It is therefore not surprising that the *c*-axis is the most compressible (Figure 6.13). The compression of the *ab*-plane manifests itself in the shortening of the $N_{central}$-$N_{terminal}$ interactions between neighbouring azides - in this pressure range the azides do not rotate and thus the 4-fold rotational symmetry is maintained. Moreover, a result of the phase transition is that the co-ordination environment of the cations becomes a regular square-antiprism with 8 equivalent Ag-N interactions (2.67 Å at 0.80 GPa). This arrangement is maintained throughout compression of the γ-form: the contraction of the *c*-axis is mirrored in the shortening of these interactions.

An interesting feature of the compression of γ-AgN_3 is the slightly convex nature of the *PV*-plot (Figure 6.13), which indicates that the structure becomes more compressible at higher pressures. Although rare, such behaviour has been observed during the compression of network solids, particularly those that have been noted to exhibit negative thermal expansion, such as $Zn(CN)_2$ [40] and ZIF-8, a zinc imidazolate framework.[41] The exact reasons for this behaviour in the case of silver azide are, as yet, unknown but this anomalous compression behaviour is most affected by the contraction of the *c*-axis. This is also reflected in the variation of the interplanar Ag…Ag and Ag-N interactions. One may therefore suggest that argentophilic (Ag…Ag) interactions compound the applied compression along the *c*-axis leading to a greater than expected contraction along this direction. In order to be confident in this conclusion, however, it would be advisable to extend the pressure range of the current study to validate the current observations and to examine the compression mechanism at higher pressures. This would also allow further refinement of the EoS for γ-AgN_3. Furthermore, DFT calculations have been planned to investigate whether it is possible to re-create this anomalous compression behaviour computationally.

The data presented in Figure 6.13 have been fitted to both a 3rd-order Birch-Murnaghan [B_0 = 70(3) GPa, B' = -1.4(14)] and a Vinet [B_0 = 71(4) GPa, B' = -2.5(19)] equation of state.[42] As for TlN_3-III above, the value of V_0 (194.14 Å^3) has been fixed to the experimentally determined volume at 0.80 GPa; all subsequent pressures have been scaled to this value. The large errors associated with the values of B' are a reflection of the relatively poor fit to the data. Both equations, however, accurately describe the marginally convex volume curve (negative B') and show relatively good agreement on the values of the bulk modulus. Should the negative values of B' be verified by future studies, this would mean that AgN_3 is dramatically more resistant to compression than the ionic azides above. This has previously been attributed to the degree of covalency displayed by silver azide, in contrast to the purely ionic alkali metal azides.[19]

In order to test the sensitivity of the coefficients B_0 and B' to the value of V_0, 3rd-order Birch-Murnaghan and Vinet equations of state were also fit using the unit cell volume of α-AgN_3 (200.86 Å^3 [11]) at atmospheric pressure as V_0. Furthermore, in a third set of least-squares regression the value of V_0 was refined. A summary of these regressions may be found in Table 6.5. It is interesting to note that, of the three case presented, the worst fit to the *PV* data is obtained by fixing V_0 to be the same as in the α-form, although this does result in values of B_0 and B' (*ca* 27 GPa and 15, respectively) that are in accordance with the other metal azides presented in this work. The quality of the fit improves markedly upon allowing

V_0 to refine (for example, R_w is reduced from 4.735% to 1.918% in the 3rd-order Birch-Murnaghan EoS) although this is accompanied by an equally dramatic increase in B_0 (26.2 to 60 GPa). Furthermore, one may suggest that the error associated with the extrapolation of V_0 may be much larger than that indicated by the standard error presented in Table 6.5 due to the highly-correlated nature of the coefficients of these regressions. Such observations suggest that extreme caution should be taken when fitting equations of state, particularly to high-pressure phases for which V_0 cannot be accurately determined. For this reason, it is suggested that this study be repeated with particular emphasis on the collection of high-quality diffraction data at low pressure, in order to obtain a sufficient number of *PV* data-points for a reliable equation of state.

Assumption	Model	Coefficients	Fitting Statistics
$V_0 = V_{0.80\ GPa}$	3rd-order Birch-Murnaghan	V_0 = 194.14 Å^3 (fixed) B_0 = 70(3) GPa B' = -1.4(14)	R_u = 3.601% χ^2_u = 0.0125 R_w = 4.118% χ^2_w = 3.6983
	Vinet	V_0 = 194.14 Å^3 (fixed) B_0 = 71(4) GPa B' = -2.5(19)	R_u = 3.566% χ^2_u = 0.0122 R_w = 4.072% χ^2_w = 3.6114
$V_0 = V_{0(\alpha\text{-form})}$	3rd-order Birch-Murnaghan	V_0 = 200.86 Å^3 (fixed) B_0 = 26.2(25) GPa B' = 17(4)	R_u = 3.901% χ^2_u = 0.0251 R_w = 4.735% χ^2_w = 7.4663
	Vinet	V_0 = 200.86 Å^3 (fixed) B_0 = 27.9(21) GPa B' = 13.2(19)	R_u = 3.987% χ^2_u = 0.0273 R_w = 4.968% χ^2_w = 8.2143
V_0 refined	3rd-order Birch-Murnaghan	V_0 = 197.2(4) Å^3 B_0 = 60(5) GPa B' = 1.3(15)	R_u = 1.918% χ^2_u = 0.0063 R_w = 2.187% χ^2_w = 1.9145
	Vinet	V_0 = 197.2(4) Å^3 B_0 = 60(6) GPa B' = 0.9(20)	R_u = 1.925% χ^2_u = 0.0063 R_w = 2.185% χ^2_w = 1.9134

Table 6.5 Coefficients of the equations of state determined for γ-AgN_3 highlighting their dependence on the assumptions used. The quality of the fit in each case may be assessed by comparison of the fitting statistics calculated during the least-squares regression (obtained from the EoSFIT output file).[39]

The current experimental study provides complementary data to a previous computational study on the structural properties of silver azide up to 500 GPa. While this theoretical study correctly predicts a phase transition to the tetragonal (*I*4/*mcm*) structure, the transition pressure was grossly overestimated (7 GPa compared to 0.8 GPa in this work). Furthermore the calculations do not correctly represent the compression of the unit cell volume or the individual parameters: the expansion of the orthorhombic *a*-axis is not predicted to occur until > 5 GPa; the *c*-axis in γ-AgN_3 is predicted to be the short axis; and the value of B' is predicted to be positive. This should therefore underscore the importance of carrying out

experimental high-pressure studies on these materials, in order to test rigorously and, ultimately, improve computational models of their properties under extreme conditions.

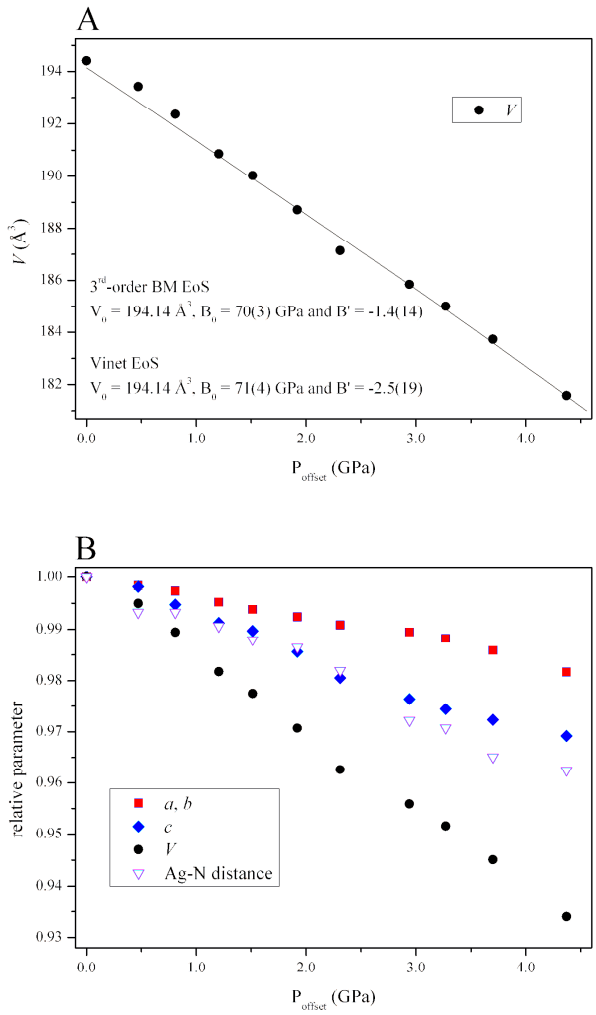

Figure 6.13 (a) Compression of γ-AgN_3 – the marginally convex character to the *PV*-plot is reflected in the negative values of B' for both the 3rd-order Birch-Murnaghan and Vinet equations of state; and, (b) the relative compression of the unit cell axes and volume presented alongside the contraction of the Ag-N distance.

The observation that the high-temperature β-form could be recovered to ambient temperature meant that the decompression of the γ-form was of great interest in the present study. Unfortunately the time constraints of the neutron diffraction experiment meant that data could not be collected at a series of pressures during decompression. It was, however, possible to collect a diffraction pattern of the sample at atmospheric pressure (shown in Figure 6.14 alongside patterns collected for both the α- and γ-forms). The diffraction pattern collected at 0 GPa shows no Bragg peaks other than the Pb, WC and Ni from the sample environment. Despite this, the observation that the sample remained in the capsule during

decompression is indicative of sample amorphisation during decompression, rather than leakage from the gasket. Visual inspection of the recovered sample found that it had darkened considerably from the initial loading; this grey colouration was found to permeate the whole sample and was not limited to a surface effect. A significant rise in vacuum pressure in the sample chamber was also observed upon reducing the load to below 2 tns, suggesting the release of a gaseous decomposition product.

The reason for this apparent amorphisation is not yet clear, although one would not expect the subtle transition from the tetragonal γ-form to the related orthorhombic α-form to cause a great deal of structural rearrangement. However, at this time it is not possible to exclude the possibility of a further polymorph obtained during decompression. An alternative mechanism may be the photolytic decomposition of AgN_3 (resulting from the cumulative effects of γ-radiation) to produce amorphous Ag(s) and N_2(g). Throughout the course of the experiment the sample may have been exposed to periodic flashes of γ-radiation from the spallation target, although one may reasonably expect a considerable portion of this to have been absorbed by the sample environment. In fact, it is perhaps more likely that the sample itself becomes a source of γ-radiation due to neutron absorption by the silver atoms and their subsequent decay.

Numerous silver salts, particularly the silver halides, have been observed to be susceptible to photolytic decomposition to metallic silver.[43-45] Indeed the effect of radiation absorption on the decomposition of silver azide has been documented for over a century [46], although recent interest has focussed on the targeted precipitation of silver nanoparticles by exposure of silver salts, such as AgN_3, to high-energy radiation.[47, 48] It is therefore reasonable to suggest that exposure of the sample to γ-radiation may result in an accumulation of crystal defects that would impact greatly on the stability of the crystal lattice during decompression.

Of course, the observed amorphisation upon decompression may be attributable to a combination of the mechanical and chemical processes outlined. It would therefore be highly desirable to conduct a more detailed decompression study to highlight: any further phase transitions; the development of crystal strain within the sample; or, any changes in sample composition (by the reduction of Bragg peak intensities).

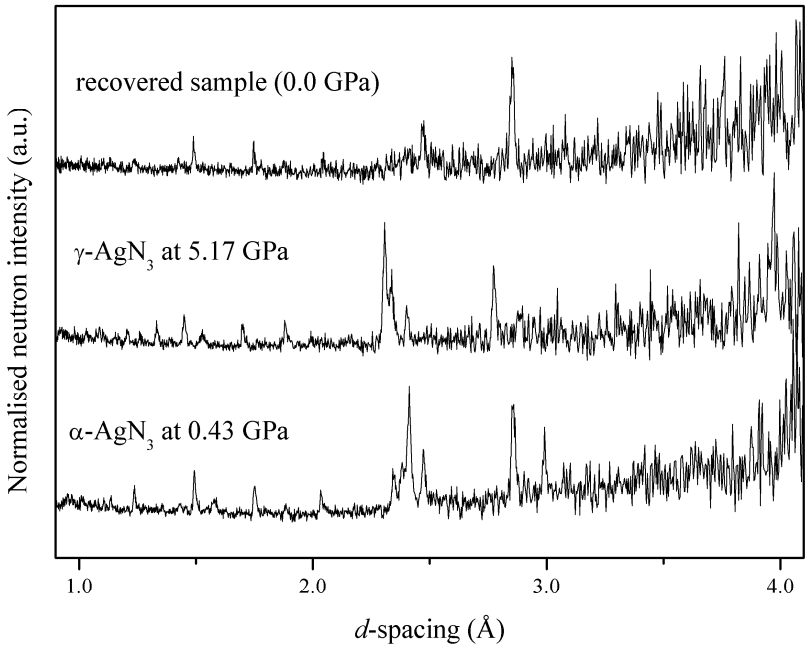

Figure 6.14 Comparison of the neutron powder diffraction pattern collected after decompression with those collected for the α-form (at the lowest pressure, 0.43 GPa) and the γ-form (immediately prior to decompression, 5.17 GPa). Apart from contributions from the Pb pressure marker and the WC and Ni from the sample environment, no Bragg peaks are observed.

Summary: AgN_3

The high-pressure polymorph of silver azide (γ-AgN_3) has been structurally characterised. This is the first experimental evidence for a form that was predicted theoretically, although several discrepancies arise between the theoretical study and the results presented herein (primarily the transition pressure). γ-AgN_3 has been found to adopt the same space group (*I*4/*mcm*) as the azides of the larger alkali metals at ambient conditions and has been shown to be the result of the gradual reduction of an orthorhombic distortion by the application of pressure.

The application of pressure to the γ-form is manifested mainly in the contraction of the tetragonal *c*-axis by reduction of the interplanar distance and is perhaps enhanced by increased argentophilic interactions between the layers. This results in a slightly convex compression curve (characterised by a negative value of B'), although this should be verified by further study. A more detailed study of the decompression of γ-AgN_3 and characterisation of the recovered product would provide a valuable insight into the observed amorphisation.

6.4.3 $Pb(N_3)_2$

The last of this series of inorganic azides to be investigated under high pressure was lead(II) azide. After obtaining a high-quality neutron powder diffraction pattern at minimal applied load (sample pressure of 0 GPa as determined by Pb calibrant) to confirm sample purity, the compression of the α-form was studied to 2.38 GPa. At the next pressure (2.60 GPa) a new reflection was observed at ~2.36 Å, although there was very little change in the rest of the pattern. This reflection persisted, and in fact grew in intensity, during further compression to the highest pressure studied (5.8 GPa), as is shown in Figure 6.15. Subsequent decompression to ambient pressure confirmed that the sample had not undergone decomposition and that this phase transition to a distinct ε-form is reversible. No additional peaks were observed during the Rietveld refinement of the ambient pressure pattern using the α-$Pb(N_3)_2$ structural model.

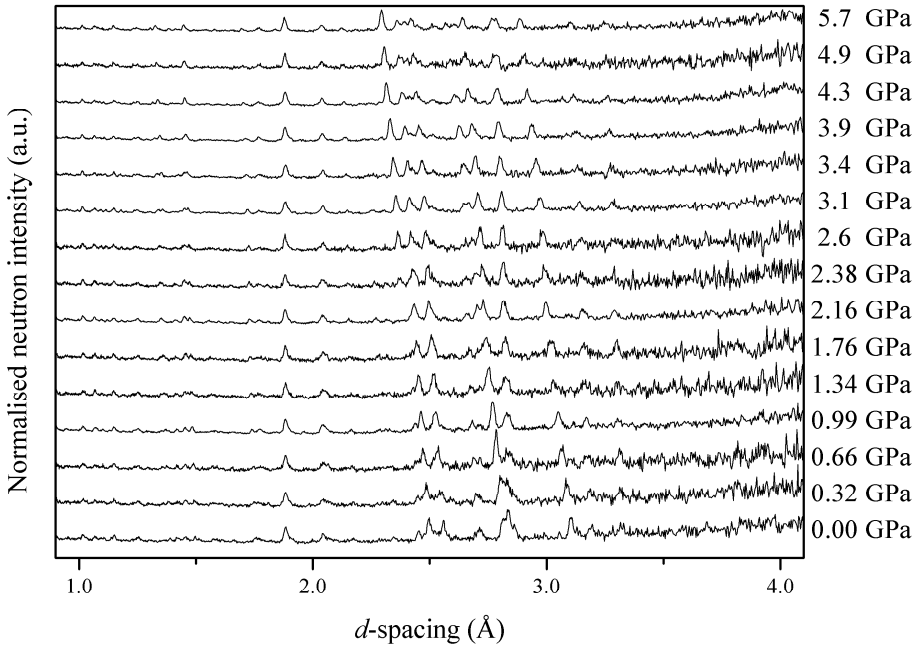

Figure 6.15 Multiplot of the neutron powder diffraction patterns collected for $Pb(N_3)_2$ up to 5.7 GPa. Since it has not been possible to perform full-profile refinements on the ε-$Pb(N_3)_2$ patterns (*i.e.* above 2.6 GPa), the pressures in these runs have been estimated by the position of the Pb (200) peak.

The structure is the most complex of the series – $Pb(N_3)_2$ contains four independent azide groups, none of which is completely linear and symmetric. This structural complexity, along with the limited range of *d*-spacing accessible during a high-pressure neutron diffraction experiment, meant that Rietveld refinement of the patterns collected during the compression

of the α-form was laborious. Refinements were initially attempted without the application of restraints to bond distances and bond angles, an approach that has been possible for all other refinements in this chapter. Unfortunately, this resulted in chemically unreasonable values for some N-N bond distances (for example, bond distances less than 1.00 Å in some cases).

In order to balance the need for the structure to remain chemically reasonable with an accurate description of the intermolecular and intramolecular interactions it was then decided to apply restraints to the bond distances and bond angles of the azide groups, with large enough standard deviations to allow sufficient variation to indicate any structural effects of the applied pressure. The N-N bond distances were restrained to 1.165(10) Å, while the N-N-N bond angles in azides II-IV were restrained to be 180(2)°. The bond angle within azide I (N1-N2-N1) was restrained by including a dummy atom (N1') as in TlN_3-IV.[49] However, refinements of the powder patterns did not converge successfully when these restraints were applied, particularly at higher pressures. On closer inspection this was found to be due to violation of the bond angle restraints that prevented convergence of the refinements.

It was therefore decided to conduct the refinements without the bond angle restraints, while maintaining the restraints applied to the bond distances. In this case the refinements successfully converged and the resulting bond distances and angles remained chemically reasonable throughout.

In order to critically assess the non-linearity of the azide units, a further refinement strategy that was employed was to restrain the distance between the two termini of each azide (II – IV) to be comparable to the ambient pressure distance, 2.340(20) Å. By the application of this restraint, in conjunction with the N-N bond distance restraint outlined above, it was hoped that linearity could be maintained without the requirement of an explicit angle restraint. In this case, convergence was successfully attained although the values of χ^2 and wR_p increased marginally (see Table 6.6 for a summary of all the refinement procedures). Despite these restraints, however, it should be noted that the azide groups still deviate significantly from linearity. For example, azide III adopts an angle of 172° and therefore one can conclude that this procedure is no more appropriate than the application of bond restraints alone, although this may be worthwhile for better quality data-sets. For this reason, the latter refinement procedure has been applied to all of the high-pressure data collections for α-$Pb(N_3)_2$. The values of the unit cell parameters obtained in this way can be found in Table 6.7 and Figure 6.16.

Bond Restraint $N_{terminal}$-$N_{central}$	Angle Restraint N-N-N (II – IV)	Length Restraint $N_{terminal}\ldots N_{terminal}$ (II – IV)	Quality of Fit
-	-	-	$\chi^2 = 1.140$ $wR_p = 0.0447$
1.165(10) Å	-	-	$\chi^2 = 1.142$ $wR_p = 0.0457$
-	180(2)°	-	did not converge
1.165(10) Å	180(2)°	-	did not converge
1.165(10) Å	-	2.340(20) Å	$\chi^2 = 1.146$ $wR_p = 0.0459$
1.165(10) Å	180(2)°	2.340(20) Å	did not converge

Table 6.6 Restraints applied during the refinement of the neutron powder diffraction pattern collected for α-$Pb(N_3)_2$ at 0.0 GPa with an assessment of the quality of the fits obtained. Convergence was not attained during any refinement involving an angle restraint. Although the best fitting statistics were obtained during the refinement in which no restraints were applied, this resulted in chemically unreasonable bond distances and angles. The application of bond *and* length restraints did not have the desired effect of maintaining the linearity of the azide group and therefore were not performed for the higher-pressure data.

P (GPa)	*a* (Å)	*b* (Å)	*c* (Å)	*V* (Å^3)	wR_p
0.0	6.6363(13)	16.277(4)	11.3203(20)	1222.9(3)	0.046
0.32	6.6277(14)	16.265(5)	11.231(2)	1210.7(3)	0.058
0.66	6.6130(16)	16.248(5)	11.125(2)	1195.4(4)	0.075
0.99	6.6046(9)	16.241(3)	11.0464(13)	1184.9(2)	0.031
1.34	6.5943(20)	16.236(6)	10.946(3)	1171.9(5)	0.074
1.76	6.5894(20)	16.204(6)	10.874(3)	1161.0(5)	0.070
2.16	6.5755(10)	16.192(3)	10.7848(15)	1148.2(2)	0.034
2.38	6.5727(20)	16.185(6)	10.754(3)	1144.0(4)	0.083

Table 6.7 Unit cell parameters determined during compression of α-$Pb(N_3)_2$.

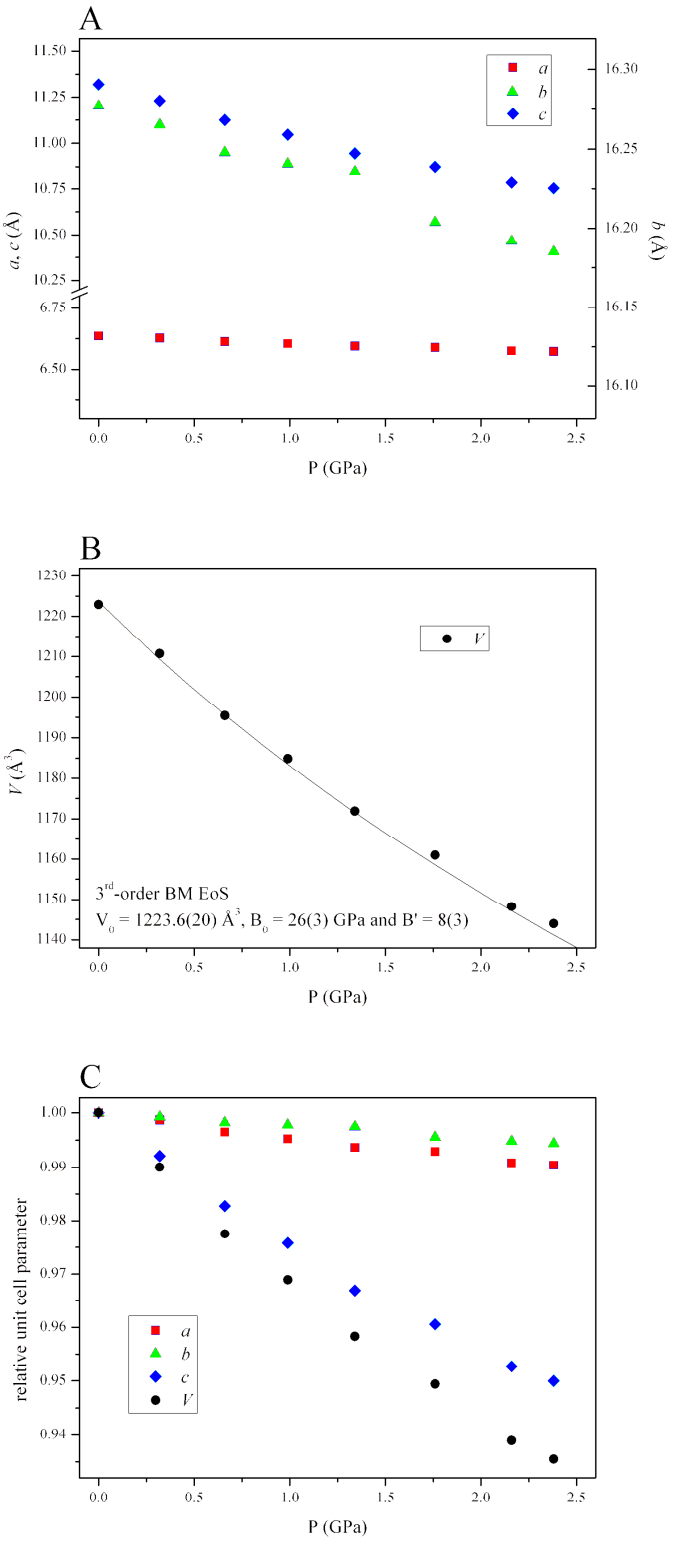

Figure 6.16 (a) Unit cell compression of α-$Pb(N_3)_2$; (b) Birch-Murnaghan *PV*-plot; and, (c) relative compression of the unit cell parameters, clearly showing the *c*-axis to be the most compressible.

While the structure remained chemically reasonable throughout, unfortunately no appreciable correlation between compression and structural parameters (such as the N-N and Pb…N distances, the N-N-N bond angles and the relative symmetry of each of the azides) was observed upon close inspection of the data. However, a plot of the relative contraction of the unit cell axes is illuminating (see Figure 6.16(c)). This clearly shows that the *c*-axis is considerably more compressible than either of the other axes, which is consistent with the relative thermal expansions of the axes at ambient pressure. This can be rationalised by noting that while one azide group aligns itself parallel to the *c*-axis, the other azides are completely perpendicular to this axis (Types I and III) or, in the case of Type II, almost perpendicular to it. This is shown in Figure 6.17. During compression the angle formed between a line drawn between the termini of Type II azides and the *c*-axis does gradually reduce, indicating that it is becoming more parallel with this axis, although this is still *ca* 25° at the upper pressure limit of the α-form.

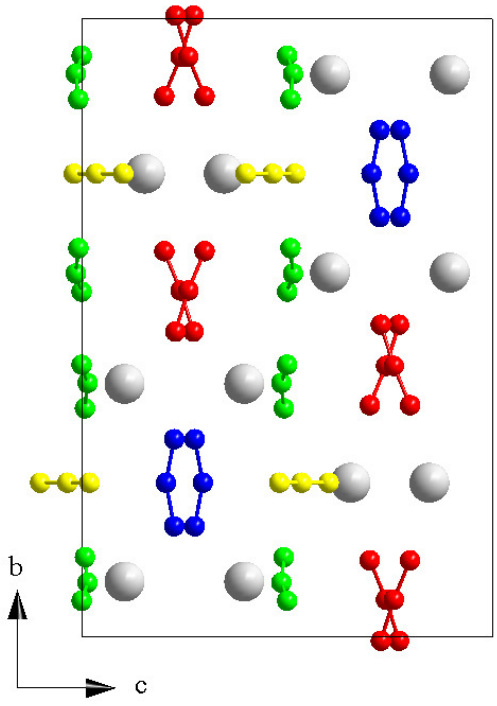

Figure 6.17 $Pb(N_3)_2$ viewed down the *a*-axis highlighting the orientation of the different azide groups. While three of the azide groups align themselves normal to the *c*-axis, only one (Type IV) is parallel to it.

The variation in the unit cell volume of α-$Pb(N_3)_2$ with increasing pressure has been fitted to a 3rd-order Birch-Murnaghan equation of state (EoS) with V_0 = 1223.6(20) Å^3, B_0 = 26(3) GPa and B' = 8(3). These values represent excellent agreement with our experimental result for V_0 (1222.9(3) Å^3) and the coefficients of the calculated Vinet EoS and F_E vs f_E plot. It is

also noteworthy that the bulk modulus for α-$Pb(N_3)_2$ is much closer to the bulk moduli reported for the ionic azides (NaN_3, CsN_3, TlN_3 and NH_4N_3) than that calculated for silver azide. This is despite both AgN_3 and $Pb(N_3)_2$ being regarded as co-ordinative azides, with a significant degree of covalency in their bonding. This observation may therefore suggest a more sophisticated classification of these compounds which accounts for their compression behaviour.

The observation of a new reflection in the diffraction pattern (at ~2.36 Å) with very little change in the rest of the diffraction pattern is clear evidence of a phase transition, most likely to a related structure. It is important to note that this peak is not coincident with any reflections in the neutron powder diffraction pattern calculated from the hexagonal ($P6_3/mmc$) structure of β-N_2 at 2.9 GPa.[50, 51] This, coupled with the observation that decompression to ambient pressure results in the recovery of the α-form, would suggest that this subtle change in the diffraction pattern is indicative of a phase transition to a new polymorph (ε-$Pb(N_3)_2$) rather than sample decomposition. Unfortunately the limited data range and the large unit cell volume have meant that it has so far been impossible to obtain an unambiguous indexing for this high-pressure polymorph. It would therefore be extremely useful to carry out complementary X-ray measurements, particularly on single crystals should they remain intact over this phase transition, to provide additional information. This would then allow Rietveld refinement of the neutron powder diffraction data collected in this study. This will provide extremely valuable information on the compression behaviour of ε-$Pb(N_3)_2$ to a maximum pressure of 5.8 GPa.

Summary: $Pb(N_3)_2$

The compression of α-$Pb(N_3)_2$ has been characterised by neutron powder diffraction and has been shown to manifest itself in the preferred contraction of the *c*-axis. Unfortunately the quality of the data obtained during this high-pressure experiment proved to be insufficient to allow one to make qualitative remarks about the inter- and intra-molecular interactions during compression, particularly the linearity and symmetry of the different azide groups. These data do, however, represent the first high-pressure study of this important energetic material. Furthermore, it is difficult to imagine a dramatic increase in data quality, especially within the time constraints of a typical neutron diffraction experiment; X-ray experiments may provide useful information (primarily unit cell parameters and Pb positions), but would be unlikely to aid in the refinement of the azide groups.

Another important result of this experiment has been the observation of another polymorph of lead(II) azide stable above 2.60 GPa, the structure of which has yet to be determined. This should therefore become a priority in the high-pressure study of these materials as this will aid in the understanding of the behaviour of $Pb(N_3)_2$ under operational conditions.

6.5 Summary and Conclusions

As in the more simple azides of sodium, caesium and thallium, the application of pressure has been particularly successful in inducing phase transitions in NH_4N_3, AgN_3 and $Pb(N_3)_2$. Each of these compounds has been found to adopt a new crystal structure at elevated pressure, although to date only γ-AgN_3 has been solved. These are significant observations, since polymorphic transitions may be expected to adversely affect the performance of these materials under detonation conditions. This is especially true for $Pb(N_3)_2$, which is still used extensively as a primary explosive. It is expected, therefore, that these studies will be of key importance to those who seek to improve the efficacy of predictive models of energetic performance (*i.e.* sensitivity, detonation velocity, *etc*). Moreover, the high-quality structural information will also be crucial for theoretical studies examining high-energy processes, such as the transition to detonation. The recent advances in the structural characterisation of these compounds have been reflected in an updated Table 6.8.

The ambient pressure structure of ND_4N_3 (α-form) has been observed to remain stable to 2.39 GPa. Up to this pressure, the compression is manifested in a rotation of half of the azide anions and an alignment of the tetrahedral cations. Further compression, however, results in a high-pressure phase transition at 2.6 GPa. Unfortunately, the structure solution of this β-form has been hampered by the limited range of *d*-spacing available and the relatively low resolution of the data obtained in these studies. Complementary X-ray powder and single-crystal diffraction studies are planned and it is expected that these experiments will be sufficient to elucidate the structure of β-NH_4N_3.

Interestingly, the compression of α-AgN_3 results in the removal of an orthorhombic distortion observed in the ambient-pressure structure – γ-AgN_3 adopts the archetypal tetragonal structure observed for CsN_3 and TlN_3 at under ambient conditions. Although this phase transition was predicted theoretically, the transition pressure was considerably higher than that observed experimentally. The most intriguing aspect of this study, however, was the slightly convex nature to the *PV*-plot obtained during compression of the γ-form. Such a feature, which suggests that the structure actually becomes more compressible at higher pressures, is unexpected, although previous observations of this behaviour have been

reported for network solids. Nevertheless, complementary high-pressure X-ray powder diffraction studies are suggested in order to confirm this result.

Finally, the high-pressure neutron diffraction study of lead(II) azide has been shown to yield a further polymorph, denoted ε-$Pb(N_3)_2$. Although subtle, the change in the diffraction patterns upon compression from 2.38 to 2.6 GPa is significant. It is therefore suggested that this transition involves a slight reduction in symmetry, or perhaps a monoclinic distortion of the orthorhombic unit cell. High-pressure X-ray powder diffraction studies would be beneficial in the structural characterisation of this ε-form by providing information on the unit cell parameters and heavy atom positions, thus complementing the neutron diffraction results presented herein.

6.6 Suggestions for Further Work

The primary focus of any high-pressure study of ammonium azide should be the collection of X-ray diffraction data. Although structure solution may be possible based on a combination of X-ray and neutron powder diffraction data, it is suggested that NH_4N_3 is a prime candidate for single-crystal compression studies. Provided single crystals are sufficiently stable at room temperature to allow their loading into a diamond-anvil cell, one would hope that refinement of single-crystal data would be straightforward. However, it should be noted that high-pressure phase transitions in the inorganic azides are often reconstructive in nature and it is currently not possible to predict whether single crystals would remain intact over the $\alpha \rightarrow \beta$ transition in NH_4N_3. Nevertheless, it would be interesting to conduct parallel studies on NH_4N_3 and ND_4N_3, since this will provide important information on the relative strengths of the hydrogen bonding interactions in these analogues, and whether deuteration results in any significant modifications to the compression behaviour of ammonium azide.

Further examination of the compression of silver azide by X-ray and neutron diffraction is also recommended, in order to corroborate the unusual compressibility curve observed in this work. Should this be the case, however, this clearly demonstrates the complexity of these systems and suggests that current theoretical models require some improvement. It would therefore be intriguing to conduct density functional theory (DFT) calculations with a view to re-creating the experimental compression behaviour. Furthermore, since the previous examples of structures with this anomalous compressibility also display negative thermal expansion at ambient pressure, a low temperature diffraction study is planned for AgN_3. Comparison of the material's thermal expansion at increasing pressure would be fascinating.

Finally, the high-pressure polymorph of lead(II) azide requires characterisation. Provided that the determination of the unit cell parameters is possible from future X-ray diffraction experiments, it is expected that structure solution may be viable on the basis of the neutron powder data collected in this work. A more complex undertaking may, in fact, be the crystallisation of the three other polymorphs that have been observed at ambient pressure (β, γ and δ). It would be particularly pleasing to solve the structure of the triclinic δ-form, as this represents a significant departure from the structures of many of the other azides in this study, the majority of which adopt orthorhombic symmetry or higher.

Polymorph	Space Group	*a* (Å)	*b* (Å)	*c* (Å)	*α* (°)	*β* (°)	*γ* (°)	Atomic positions?	*P*/*T* conditions	Ref.
α-NH_4N_3	*Pmna*	8.948(3)	3.808(2)	8.659(3)	90	90	90	Yes	Ambient *P*/*T*	[3]
β-NH_4N_3	-	-	-	-	-	-	-	-	***P* > 2.6 GPa; Ambient *T***	**this study**
α-AgN_3	*Ibam*	5.600(1)	5.980(6)	5.998(1)	90	90	90	Yes	Ambient *P*; *T* < 443 K	[11]
β-AgN_3	$P2_1/c$	6.0756(2)	6.1663(2)	6.5729(2)	90	114.19(0)	90	Yes	Ambient *P*; *T* > 443 K Recovered to ambient *P*/*T*	[16]
γ-AgN_3	***I4/mcm***	**5.7239(11)**	**5.7239(11)**	**5.9338(14)**	**90**	**90**	**90**	**Yes**	***P* > 0.80 GPa; Ambient *T***	**this study**
α-$Pb(N_3)_2$	*Pnma*	6.63	16.25	11.31	90	90	90	Yes	Ambient *P*/*T*	[24],[28]
β-$Pb(N_3)_2$	-	18.31	8.88	5.12	90	107.5	90	No	Ambient *P*/*T*	[22]
γ-$Pb(N_3)_2$	-	12.060	10.507	6.505	90	95.75	90	No	Ambient *P*/*T*; low pH/additives	[20]
δ-$Pb(N_3)_2$	-	13.163	10.532	6.531	90.53	98.12	112.67	No	Ambient *P*/*T*; low pH/additives	[20]
ε-$Pb(N_3)_2$	-	-	-	-	-	-	-	-	***P* > 2.6 GPa; Ambient *T***	**this study**

Table 6.8 Structural data for ammonium, silver and lead(II) azides at variable temperature and pressure. The results of the current study (bold) have been included alongside previous reports.

6.7 References

1. L.K. Frevel, *Z. Kristallogr.*, 1936, **94**, 197.
2. T.C. Waddington, *J. Chem. Soc.*, 1958, 4340.
3. E. Prince and C.S. Choi, *Acta Cryst.*, 1978, **B34**, 2606.
4. H.S. de Amorim, M.R. do Amaral Jr., P. Pattison, I.P. Ludka, and J.C. Mendes, *Rev. Soc. Quim. Mex.*, 2002, **4**, 313.
5. O. Reckeweg and A. Simon, *Z. Naturforsch.*, 2003, **58**, 1097.
6. D.A. Dows, E. Whittle, and G.C. Pimentel, *J. Chem. Phys.*, 1955, **23**, 1475.
7. W.L. Ng and J.E. Field, *Thermochim. Acta*, 1985, **84**, 133.
8. U. Müller, *Strukturchemie der Azide*, in *Structure and Bonding, Inorganic Chemistry, Vol. 14*, 1973, Springer, Berlin/Heidelberg.
9. T.C. Waddington, *J. Chem. Soc*, 1959, 2499.
10. H.E. Marr, III and R.H. Stanford, Jnr, *Acta Cryst.*, 1962, **15**, 1313.
11. G.C. Guo, Q.M. Wang, and T.C.W. Mak, *J. Chem. Crystallogr.*, 1999, **29**, 561.
12. C.D. West, *Z. Kristallogr.*, 1936, **95**, 421.
13. J.I. Bryant and R.L. Brooks, *J. Chem. Phys.*, 1971, **54**, 5315.
14. K. Dehnicke, *Z. Anorg. Allg. Chem.*, 1974, **409**, 311.
15. C.M. Pereira and M.M. Chaudhri, 1988, **57**, 173
16. C.L. Schmidt, R. Dinnebier, U. Wedig, and M. Jansen, *Inorg. Chem.*, 2007, **46**.
17. G.M. Diamant, A.E. Saprykin, and Y.Y. Sidorin, *Reactivity of Solids*, 1989, **7**, 375.
18. C.M. Pereira and M.M. Chaudhri, *J. Energetic Mater.*, 1989, **7**, 297
19. W. Zhu and H. Xiao, *J. Solid State Chem.*, 2007, **180**, 3521.
20. S. Lamnevik and R. Söderquist, *FOA Report A 1174 - F110*, 1964.
21. F.D. Miles, *J. Chem. Soc.*, 1931, 2532.
22. K. Hattori and W. McCrone, *Anal. Chem.*, 1956, **28**, 1792.
23. G.W.C. Taylor and A.T. Thomas, *J. Cryst. Growth*, 1968, **3-4**, 391.
24. L.V. Azaroff, *Z. Kristallogr.*, 1956, **107**, 362.
25. K. Hattori and W. McCrone, *Anal. Chem.*, 1956, **28**, 1791.
26. C.S. Choi and H.P. Boutin, *Acta Cryst.*, 1969, **B25**, 982.
27. G.L. Glen, *J Am. Chem. Soc.*, 1963, **85**, 3892.
28. C.S. Choi, E. Prince, and W.L. Garrett, *Acta Cryst.*, 1977, **B33**, 3536.
29. Z. Iqbal, W. Garrett, C.W. Brown, and S.S. Mitra, *J. Chem. Phys.*, 1971, **55**, 4528.
30. W. Zhu and H. Xiao, *J. Phys. Chem. B*, 2006, **110**, 18196.
31. F.A. Mauer, C.R. Hubbard, and T.A. Hahn, *J. Chem. Phys.*, 1974, **60**, 1341.
32. C.E. Weir, S. Block, and G.J. Piermarini, *J. Chem. Phys.*, 1970, **53**, 4265.
33. W.F. Perger, *Int. J. Quantum Chem.*, 2010, **110**, 1916.
34. T.A. Richter, *Synthesis and Chemical Properties*, in *Energetic Materials 1: Physics and Chemistry of the Inorganic Azides*, H.D. Fair and R.F. Walker, Editors, 1977, Plenum Press, New York.
35. W.G. Marshall and D.J. Francis, *J. Appl. Crystallogr.*, 2002, **35**, 122.
36. A.D. Fortes, PhD Thesis, 2004, Department of Earth Sciences, University College, London, UK.
37. J.M. Besson, R.J. Nelmes, G. Hamel, J.S. Loveday, G. Weill, and S. Hull, *Physica B*, 1992, **180-181**, 907.
38. R. Von Dreele and A.C. Larson, *General Structure Analysis System (GSAS)*, 1986.
39. R.J. Angel, *Equations of State*, in *Reviews in Mineralogy and Geochemistry, 41: High-Temperature and High-Pressure Crystal Chemistry*, R.M. Hazen and R.T. Downs, Editors, 2000, Mineralogical Society of America, Washington, D.C., USA.
40. K.W. Chapman and P.J. Chupas, *J. Am. Chem. Soc.*, 2007, **129**, 10090.
41. K.W. Chapman, G.J. Halder, and P.J. Chupas, *J. Am. Chem. Soc.*, 2009, **131**, 17546.
42. P. Vinet, J. Ferrante, J.R. Smith, and J.H. Rose, *J. Phys. C: Solid State Phys.*, 1986, **19**, L467.

43. S.E. Sheppard and W. Vanselow, *J. Phys. Chem.*, 1929, **33**, 250.
44. J.P. Abid, A.W. Wark, P.F. Brevet, and H.H. Girault, *Chem. Commun.*, 2002, **38**, 792.
45. O.V. Mikhailov, A.V. Kondakov, and R.I. Krikunenko, *High Energy Chem.*, 2005, **39**, 324.
46. L. Wohler, *Chem. Ztg*, 1912, **35**, 1096.
47. E.P. Surovoi, S.M. Sirik, Y.A. Zakharov, L.N. Bugerko, and I.K. Kilina, *Zhurnal Nauchnoi i Prikladnoi Fotografii*, 2000, **45**, 14.
48. E.P. Surovoi, S.M. Sirik, and L.N. Bugerko, *Materialovedenie*, 2008, **5**, 40.
49. R. Von Dreele, *personal communication*, 2010.
50. D. Schiferl, D.T. Cromer, R.R. Ryan, A.C. Larson, R. LeSar, and R.L. Mills, *Acta Cryst.*, 1983, **C39**, 1151.
51. J. Belak, R. LeSar, and R.D. Etters, *J. Chem. Phys.*, 1990, **92**, 5430.

Chapter 7

General Remarks

7 General Remarks

This study highlights the importance of obtaining high-quality structural information on energetic materials over a range of temperatures and pressures. The high-pressure/high-temperature polymorph of RDX has been determined and has been shown to be distinct from the highly metastable β-form at ambient conditions, with which is it has previously been confused. This has led to it being re-named the ε-form. Furthermore, an equation of state has been obtained for RDX up to a maximum pressure of 23 GPa. At no point during this study was a transition to δ-RDX observed, contrary to previous spectroscopic results.

The high-pressure behaviour of another high explosive, CL-20, has also been investigated. It was found that compression of ε-CL-20 (the most thermodynamically stable form at ambient conditions) to 7.2 GPa, did not result in any polymorphic transitions. The γ-form, however, was found to be more susceptible to pressure-induced phase transitions and, moreover, the nature of these transitions depended upon the pressure-transmitting medium used. For example, compression of γ-CL-20 in Fluorinert produced the ζ polymorph, while compression in MeOH:EtOH resulted in pressure-induced solvate formation.

Finally, a series of metal azides (NaN_3, CsN_3, TlN_3, NH_4N_3, AgN_3 and $Pb(N_3)_2$) have been shown to display remarkable polymorphism at variable temperatures and pressures. All have been observed to undergo at least one phase transition, and a total of 10 new polymorphs have been identified.

The number of high-pressure polymorphs identified in this work is a reflection, not only of the powerful role that pressure plays in dramatically altering the relative energies of different crystal structures, but also the technical advances which have facilitated the collection and refinement of complementary high-pressure structural data. Furthermore, the success of these studies highlights the unrivalled opportunity for obtaining novel materials that high-pressure studies provide and the exciting prospect of the recovery of high-pressure phases to ambient conditions. This has been proposed as an effective way of improving performance of energetic materials (such as crystal density, reduced sensitivity, etc) without the need for changing their molecular structure.

It would therefore be advised to extend these studies to other energetic materials, in the first instance HMX, FOX-7 and octanitrocubane. Indeed high-pressure techniques may provide a viable route to the denser form of octanitrocubane that has been predicted theoretically (see Section 1.2.2). Should this be the case, recovery of this form to ambient conditions would be a remarkable achievement and would emphasise the importance of such experiments to the

energetics community. An alternative approach to the structural modification of energetic materials is to co-crystallise them with simple organic molecules, with a view to tailoring their detonation characteristics, particularly sensitivity. Although not actively explored in this research, it has been observed that the crystal structure of CL-20 is sufficiently porous to allow the formation of a 2:1 CL-20:MeOH solvate at pressure, which is recoverable to ambient conditions. Thus the possibility of obtaining co-crystals of CL-20, HMX and various other energetic materials should be explored.

Naturally, the performance characteristics of recovered high-pressure forms and co-crystals will need to be rigorously assessed. It will therefore be necessary to collaborate with defence scientists who have experience conducting sensitivity studies. Other collaborative projects may involve theoreticians and shock physicists. It is anticipated that the experimental data presented in this work will complement theoretical studies focussed on the predictive modelling of energetic performance, particularly detonation velocities and sensitivities. In a more general sense, however, these high-pressure studies will also prove to be excellent candidates to test the validity of intermolecular potentials used to describe these materials. Meanwhile, the spectroscopic identification of new high-pressure polymorphs may be possible at the very high pressures attainable in shock compression studies, although their structural solution is far more problematic. The results of these experiments, however, may guide diffraction studies like those conducted in the present work.

Finally, it is also hoped that the rich polymorphism of the metal azides (NaN_3, CsN_3, TlN_3, NH_4N_3, AgN_3 and $Pb(N_3)_2$) at extreme conditions will lead to the extension of this study to include other metal azides (such as KN_3, RbN_3) as well as analogous binary systems, for example metal bifluorides (MHF_2), cyanates (MOCN) and thiocyanates (MSCN).

In addition, the photolysis of CsN_3 to produce Cs metal and, potentially, polynitrogen species has opened up a further avenue for the application of high-pressure techniques in the synthesis of ‘high-energy density materials’. In the immediate future the identification of the optimum conditions for photolysis and the characterisation of the photolysis products are advised. However, it is anticipated that these studies may then be extended to more complex azides containing a greater proportion of nitrogen, for example $[Cr(III)(N_3)_6]^{3-}$. Of course rigorous studies will have to be completed on the synthesis of such complexes, their structures and their reactivities. Furthermore, detailed investigations of the product species must also be conducted before their application in munitions.

Appendix

Crystallographic Information

Conferences and Lecture Course Attended

Publications

8 Appendix

8.1 Crystallographic Information

8.1.1 Chapter 3

X-ray Single Crystal Data	**β-RDX at 273 K**
Crystal Data	
Chemical Formula	C3 H6 N6 O6
M_r	222.12
Cell setting, space group	Orthorhombic, $Pca2_1$
Temperature (K)	273
a, b, c (Å)	15.0972(7), 7.5463(4), 14.4316(6)
V (Å^3)	1644.16(13)
Z	8
D_c (Mg m^{-3})	1.795
Radiation type	Mo-Kα
No. reflections for cell parameters	2672
θ range (°)	3-23
μ (mm^{-1})	0.171
Crystal form, colour	Lathe, colourless
Crystal size (mm)	0.05 x 0.20 x 0.45
Data Collection	
Diffractometer	Bruker SMART
Data collection method	ω
Absorption correction	Multiscan
T_{min}	0.67
T_{max}	0.97
No. of measured, independent and observed reflections	10137, 1244
Criterion for observed reflections	$I > 2.00u(I)$
R_{int}	0.055
θ_{max} (°)	23.312
Range of h, k, l	-16 → h → 16 -8 → k → 8 -16 → l → 15
Refinement	
Refinement on	F^2
$R[F^2 > 2\sigma(F^2)]$, $wR(F^2)$, S	0.0975, 0.1405, 0.7647
No. of reflections	1244
No. of parameters	271
H-atom treatment	Constrained to parent
Weighting scheme	Calculated $w = 1/[\sigma^2(F^2) + (0.08P)^2 + 0.56P]$ where $P = (\max(F_o^2,0) + 2F_c^2)/3$
(Δ/σ)max	0.000045
$\Delta\rho_{max}$, $\Delta\rho_{min}$ (e Å^{-3})	0.52, -0.43

X-ray Single Crystal Data	β-RDX at 150 K
Crystal Data	
Chemical Formula	C3 H6 N6 O6
M_r	222.12
Cell setting, space group	Orthorhombic, $Pca2_1$
Temperature (K)	150
a, b, c (Å)	15.1267(11), 7.4563(6), 14.3719(11)
V (Å^3)	1621.0(2)
Z	8
D_c (Mg m^{-3})	1.820
Radiation type	Mo-Kα
No. reflections for cell parameters	2888
θ range (°)	3-24
μ (mm^{-1})	0.0173
Crystal form, colour	Block, colourless
Crystal size (mm)	0.15 x 0.23 x 0.38
Data Collection	
Diffractometer	Bruker SMART
Data collection method	ω
Absorption correction	Multiscan
T_{min}	0.85
T_{max}	0.97
No. of measured, independent and observed reflections	10899, 2097
Criterion for observed reflections	$I > 2.00u(I)$
R_{int}	0.038
θ_{max} (°)	28.425
Range of h, k, l	-20 → h → 14 -8 → k → 9 -19 → l → 14
Refinement	
Refinement on	F^2
$R[F^2 > 2\sigma(F^2)]$, $wR(F^2)$, S	0.0465, 0.0847, 0.8136
No. of reflections	2097
No. of parameters	271
H-atom treatment	Constrained to parent
Weighting scheme	Calculated $w = 1/[\sigma^2(F^2) + (0.03P)^2 + 0.00P]$ where $P = (\max(F_o^2,0) + 2F_c^2)/3$
(Δ/σ)max	0.000149
$\Delta\rho_{max}$, $\Delta\rho_{min}$ (e Å^{-3})	0.48, -0.34

X-ray Single Crystal Data	ε-RDX at 293(2) K, 5.70(5) GPa
Crystal Data	
Chemical Formula	C3 H6 N6 O6
M_r	222.12
Cell setting, space group	Orthorhombic, $Pca2_1$
Temperature (K)	293(2)
a, b, c (Å)	7.0324(11), 10.530(3), 8.7909(11)
V (Å^3)	651.0(2)
Z	8
D_c (Mg m^{-3})	2.266
Radiation type	Mo-Kα
No. reflections for cell parameters	430
θ range (°)	3-19
μ (mm^{-1})	0.216
Crystal form, colour	Block, colourless
Crystal size (mm)	0.05 x 0.05 x 0.10
Data Collection	
Diffractometer	Bruker Nonius APEX II
Data collection method	ω
Absorption correction	Multiscan
T_{min}	0.86
T_{max}	0.99
No. of measured, independent and observed reflections	3740, 333
Criterion for observed reflections	$I > 2.00u(I)$
R_{int}	0.0916
θ_{max} (°)	26.910
Range of h, k, l	$-8 \rightarrow h \rightarrow 8$ $-6 \rightarrow k \rightarrow 5$ $-11 \rightarrow l \rightarrow 10$
Refinement	
Refinement on	F^2
$R[F^2 > 2\sigma(F^2)]$, $wR(F^2)$, S	0.0578, 0.1102, 1.0337
No. of reflections	333
No. of parameters	61
H-atom treatment	Constrained to parent
Weighting scheme	Calculated $w = 1/[\sigma^2(F^2) + (0.06P)^2 + 0.92P]$ where $P = (\max(F_o^2,0) + 2F_c^2)/3$
(Δ/σ)max	0.000051
$\Delta\rho_{max}$, $\Delta\rho_{min}$ (e Å^{-3})	0.44, -0.47

8.1.2 Chapter 4

X-ray Single Crystal Data	**ζ-CL-20 at 293(2) K, 3.30(5) GPa**
Crystal Data	
Chemical Formula	C6 H6 N12 O12
M_r	438.19
Cell setting, space group	Monoclinic, $P2_1/n$
Temperature (K)	293(2)
a, b, c (Å)	12.579(2), 7.7219(19), 14.1260(15)
β (°)	111.218(10)
V (Å^3)	1279.1(4)
Z	4
D_c (Mg m^{-3})	2.275
Radiation type	Mo-Kα
No. reflections for cell parameters	676
θ range (°)	3-22
μ (mm^{-1})	0.218
Crystal form, colour	Block, colourless
Crystal size (mm)	0.05 x 0.05 x 0.10
Data Collection	
Diffractometer	Bruker Nonius APEX II
Data collection method	ω
Absorption correction	Multiscan
T_{min}	0.99
T_{max}	0.99
No. of measured, independent and observed reflections	5107, 935
Criterion for observed reflections	$I > 2.00u(I)$
R_{int}	0.128
θ_{max} (°)	23.345
Range of h, k, l	-13 → h → 13 -5 → k → 5 -15 → l → 15
Refinement	
Refinement on	F
$R[F^2 > 2\sigma(F^2)]$, $wR(F^2)$, S	0.0877, 0.0885, 1.1244
No. of reflections	515
No. of parameters	121
H-atom treatment	Constrained to parent
Weighting scheme	Calculated $w = 1.0/[A_0T_0(x) + A_1T_1(x) + A_{n-1}T_{n-1}(x)]$, where A_i are the Chebychev coefficients (A_i = 1.17, 0.787, 0.789) and $x = F_{calc}/F_{max}$
(Δ/σ)max	0.0000906
$\Delta\rho_{max}$, $\Delta\rho_{min}$ (e Å^{-3})	-0.54, 0.48

X-ray Single Crystal Data	CL-20:MeOH (2:1) solvate at 100 K
Crystal Data	
Chemical Formula	2(C6 H6 N12 O12): (CO)
M_r	448.19
Cell setting, space group	Orthorhombic, *Pbca*
Temperature (K)	100
a, b, c (Å)	9.6445(5), 13.2186(7), 23.3407(8)
V (Å^3)	2975.6(2)
Z	8
D_c (Mg m^{-3})	2.001
Radiation type	Cu-Kα
No. reflections for cell parameters	6542
θ range (°)	2-73
μ (mm^{-1})	5.097
Crystal form, colour	Block, colourless
Crystal size (mm)	0.0722 x 0.0918 x 0.2600
Data Collection	
Diffractometer	OD Supernova
Data collection method	ω
Absorption correction	Multiscan
T_{min}	0.52533
T_{max}	1.00000
No. of measured, independent and observed reflections	16053, 2920
Criterion for observed reflections	$I > 2.00u(I)$
R_{int}	0.066
θ_{max} (°)	73.212
Range of h, k, l	-11 → h → 11 -16 → k → 11 -28 → l → 28
Refinement	
Refinement on	F^2
$R[F^2 > 2\sigma(F^2)]$, $wR(F^2)$, S	0.0756, 0.1991, 0.9563
No. of reflections	2920
No. of parameters	286
H-atom treatment	Constrained to parent
Weighting scheme	Calculated $w = 1/[\sigma^2(F^2) + (0.12P)^2 + 9.25P]$ where $P = (\max(F_o^2,0) + 2F_c^2)/3$
(Δ/σ)max	0.0000915
$\Delta\rho_{max}$, $\Delta\rho_{min}$ (e Å^{-3})	0.79, -0.47

8.2 Quality of Fit: Equations of State

Polymorph	Model	Coefficients	Fitting Statistics*
ε-RDX-d_6	Murnaghan	V_0 = 808(4) Å^3 B_0 = 10.3(8) GPa B' = 7.8(3)	R_u = 1.179% χ^2_u = 0.0019 R_w = 1.469% χ^2_w = 0.7676
γ-RDX-h_6 (MeOH:EtOH)	3rd-order Birch-Murnaghan	V_0 = 1632 Å^3 (fixed) B_0 = 14(3) GPa B' = 8.4(18)	R_u = 5.597% χ^2_u = 0.8619 R_w = 6.238% χ^2_w = 0.8532
γ-RDX-h_6 (no medium)	3rd-order Birch-Murnaghan	V_0 = 1632 Å^3 (fixed) B_0 = 11(6) GPa B' = 8(4)	R_u = 2.887% χ^2_u = 0.4630 R_w = 3.468% χ^2_w = 0.4526
ε-CL-20	3rd-order Birch-Murnaghan	V_0 = 1431.8 Å^3 (fixed) B_0 = 9.5(22) GPa B' = 27(8)	R_u = 5.542% χ^2_u = 0.0877 R_w = 5.888% χ^2_w = 11.9400
CL-20:MeOH (2:1)	3rd-order Birch-Murnaghan	V_0 = 3120.6 Å^3 (fixed) B_0 = 4.6(5) GPa B' = 27(4)	R_u = 1.092% χ^2_u = 0.0017 R_w = 1.156% χ^2_w = 0.6292
	Vinet	V_0 = 3120.6 Å^3 (fixed) B_0 = 6.6(5) GPa B' = 13.6(8)	R_u = 2.068% χ^2_u = 0.0039 R_w = 1.995% χ^2_w = 0.0039
	3rd-order Birch-Murnaghan (P_{offset} = 0.57 GPa)	V_0 = 2922.0 Å^3 (fixed) B_0 = 17.2(10) GPa B' = 10.1(12)	R_u = 0.394% χ^2_u = 0.0001 R_w = 0.366% χ^2_w = 0.0458
	Vinet (P_{offset} = 0.57 GPa)	V_0 = 2922.0 Å^3 B_0 = 17.5(8) GPa B' = 9.2(8)	R_u = 0.353% χ^2_u = 0.0001 R_w = 0.337% χ^2_w = 0.0043
α-NaN_3	3rd-order Birch-Murnaghan	V_0 = 116.9(2) Å^3 B_0 = 15.1(7) GPa B' = 7.0(5)	R_u = 1.366% χ^2_u = 0.0028 R_w = 1.489% χ^2_w = 1.1315
CsN_3-III	3rd-order Birch-Murnaghan (P_{offset} 0.54 GPa)	V_0 = 325.98 Å^3 (fixed) B_0 = 19.7(10) GPa B' = 5.8(11)	R_u = 1.358% χ^2_u = 0.0007 R_w = 1.377% χ^2_w = 0.2862
TlN_3-II	2nd-order Birch-Murnaghan	V_0 = 283.0(9) Å^3 B_0 = 21(3) GPa B' = 4 (fixed)	R_u = 4.404% χ^2_u = 0.0008 R_w = 4.508% χ^2_w = 0.3015
TlN_3-III	3rd-order Birch-Murnaghan (P_{offset} = 0.76 GPa)	V_0 = 267.14 Å^3 (fixed) B_0 = 24.1(5) GPa B' = 6.7(4)	R_u = 0.566% χ^2_u = 0.0005 R_w = 0.574% χ^2_w = 0.1827
α-ND_4N_3	2nd-order Birch-Murnaghan	V_0 = 295.7(4) Å^3 B_0 = 20.2(5) GPa B' = 4 (fixed)	R_u = 2.813% χ^2_u = 0.0022 R_w = 2.876% χ^2_w = 0.8566
γ-AgN_3	3rd-order Birch-Murnaghan	V_0 = 200.86 Å^3 (fixed) B_0 = 26.2(25) GPa B' = 17(4)	R_u = 3.901% χ^2_u = 0.0251 R_w = 4.735% χ^2_w = 7.4663
	Vinet	V_0 = 200.86 Å^3 (fixed) B_0 = 27.9(21) GPa B' = 13.2(19)	R_u = 3.987% χ^2_u = 0.0273 R_w = 4.968% χ^2_w = 8.2143
	3rd-order Birch-Murnaghan	V_0 = 197.2(4) Å^3 B_0 = 60(5) GPa B' = 1.3(15)	R_u = 1.918% χ^2_u = 0.0063 R_w = 2.187% χ^2_w = 1.9145

Polymorph	Model	Coefficients	Fitting Statistics*
γ-AgN_3 (contd)	Vinet	V_0 = 197.2(4) Å^3 B_0 = 60(6) GPa B' = 0.9(20)	R_u = 1.925% χ^2_u = 0.0063 R_w = 2.185% χ^2_w = 1.9134
	3rd-order Birch-Murnaghan (P_{offset} = 0.80 GPa)	V_0 = 194.14 Å^3 (fixed) B_0 = 70(3) GPa B' = -1.4(14)	R_u = 3.601% χ^2_u = 0.0125 R_w = 4.118% χ^2_w = 3.6983
	Vinet (P_{offset} = 0.80 GPa)	V_0 = 194.14 Å^3 (fixed) B_0 = 71(4) GPa B' = -2.5(19)	R_u = 3.566% χ^2_u = 0.0122 R_w = 4.072% χ^2_w = 3.6114
α-$Pb(N_3)_2$	3rd-order Birch-Murnaghan	V_0 = 1223.6(20) Å^3 B_0 = 26(3) GPa B' = 8(3)	R_u = 2.029% χ^2_u = 0.0006 R_w = 1.741% χ^2_w = 0.0006

* Fitting statistics obtained from EoSFIT output file.

8.3 Conferences and Lecture Courses Attended

8.3.1 Year 1

Oral Presentation

David I.A. Millar, Adam S. Cumming, Duncan J. Francis, William G. Marshall, Iain D.H. Oswald and Colin R. Pulham, **High-Pressure Structural Studies of Energetic Materials**, *Neutron and Muon User Meeting: Young Scientist Talks*, Nottingham, UK, March 2008.

Poster Presentations

David I.A. Millar, Adam S. Cumming, Duncan J. Francis, William G. Marshall, Iain D.H. Oswald and Colin R. Pulham, **High-Pressure Structural Studies of Energetic Materials**, *British Crystallographic Association: Spring Meeting*, York, UK, April 2008.

David I.A. Millar, Adam S. Cumming, Duncan J. Francis, William G. Marshall, Iain D.H. Oswald and Colin R. Pulham, **High-Pressure Structural Studies of Energetic Materials**, *Gordon Research Conference: Energetic Materials*, Tilton, NH, USA, June 2008.

David I.A. Millar, Adam S. Cumming, Duncan J. Francis, William G. Marshall, Iain D.H. Oswald and Colin R. Pulham, **The Crystal Structure of β-RDX: An Elusive Form of an Explosive Revealed**, *ISIS Crystallography Group: User Meeting*, Abingdon, Oxon., UK, November 2008.

Courses Attended

EaStCHEM: Academic Paper Writing, St Andrews, UK, April 2008.

Scottish Universities Summer School in Physics (Number 63): High-Pressure Physics, Skye, UK, May 2008.

8.3.2 Year 2

Oral Presentation

David I.A. Millar, Adam S. Cumming, Duncan J. Francis, William G. Marshall, Iain D.H. Oswald and Colin R. Pulham, **Pressure-Cooking Explosives: A Tale of Two Polymorphs**, *British Crystallographic Association: Young Crystallographers' Satellite Meeting*, Loughborough, UK, April 2009.

Poster Presentations

David I.A. Millar, Adam S. Cumming, Duncan J. Francis, William G. Marshall, Iain D.H. Oswald and Colin R. Pulham, **Pressure-Cooking Explosives: A Tale of Two Polymorphs**, *British Crystallographic Association: Spring Meeting*, Loughborough, UK, April 2009.

Courses Attended

12th BCA/CCG Intensive Training School in X-ray Structure Analysis, Durham, UK, April 2009.

41st Course on High-Pressure Crystallography: From Novel Experimental Approaches to Applications in Cutting-Edge Technologies, Erice, Italy, June 2009.

DLS Workshop: Defects in Structural Materials, Didcot, UK, September 2009.

Transkills: Introduction to UNIX, Edinburgh, UK, November 2009.

8.3.3 Year 3

Oral Presentation

David I.A. Millar, Christopher Barry, Adam S. Cumming, Duncan J. Francis, Annette K. Kleppe, William G. Marshall, Helen E. Maynard-Casely, Iain D.H. Oswald and Colin R. Pulham, **Energetic Materials at Extreme Conditions: RDX and CL-20**, *Edinburgh Postgraduate Seminar*, May 2010.

Poster Presentation

David I.A. Millar, Adam S. Cumming, Craig A. Henderson, Anna Muszkiewicz and Colin R. Pulham, **Co-Crystallisation of Energetic Materials: A Step Towards Tailored**

Munitions, *British Crystallographic Association: Spring Meeting*, Warwick, April 2010. **[Awarded International Centre for Diffraction Data (ICDD) Bursary]**

David I.A. Millar, Christopher Barry, Adam S. Cumming, Duncan J. Francis, Annette K. Kleppe, William G. Marshall, Helen E. Maynard-Casely, Iain D.H. Oswald and Colin R. Pulham, **Energetic Materials at Extreme Conditions: The Power of Pressure**, *Gordon Research Conference: Energetic Materials*, Tilton, NH, USA, June 2010.

Courses Attended

Transkills: Publishing with LaTeX, Edinburgh, UK, December 2009.

8.4 Publications

Alistair J. Davidson, Iain D.H. Oswald, Duncan J. Francis, Alistair R. Lennie, William G. Marshall, David I.A. Millar, Colin R. Pulham, John E. Warren and Adam S. Cumming, **Explosives under pressure – the crystal structure of γ-RDX as determined by high-pressure X-ray and neutron diffraction**, *CrystEngComm*, 2008, **10**(2), 162-165. **[Highlighted in *Chemical Science*, December 2007]**

David I.A. Millar, Iain D.H. Oswald, Duncan J. Francis, William G. Marshall, Colin R. Pulham and Adam S. Cumming, **The crystal structure of β-RDX – an elusive form of an explosive revealed**, *Chem. Commun*., 2009, **45**(5), 562-564.

David I.A. Millar, William G. Marshall, Iain D.H. Oswald and Colin R. Pulham, **High-pressure structural studies of energetic materials**, *Crystallogr. Rev*., 2010, **16**(2), 115-132.

David I.A. Millar, Helen E. Maynard-Casely, Annette K. Kleppe, William G. Marshall, Colin R. Pulham and Adam S. Cumming, **Putting the squeeze on energetic materials – structural characterisation of a high-pressure phase of CL-20**, *CrystEngComm*, 2010, **12**, 2524-2527.

David I.A. Millar, Iain D.H. Oswald, Christopher Barry, Duncan J. Francis, William G. Marshall, Colin R. Pulham and Adam S. Cumming, **Pressure-cooking explosives – the crystal structure of ε-RDX as determined by X-ray and neutron diffraction**, *Chem. Commun.*, 2010, **46**(31), 5662-5664. **[Hot Article]**